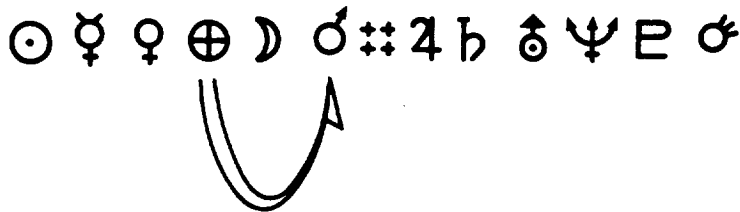




Interplanetary Mission Design Handbook, Volume I, Part 2

Earth to Mars Ballistic Mission Opportunities,
1990-2005

Andrey B. Sergeyevsky
Gerald C. Snyder
Ross A. Cunniff



September 15, 1983



National Aeronautics and
Space Administration

Jet Propulsion Laboratory
California Institute of Technology
Pasadena, California

(NASA-CR-173306) INTERPLANETARY MISSION
DESIGN HANDBOOK. VOLUME 1, PART 2: EARTH
TO MARS BALLISTIC MISSION OPPORTUNITIES,
1990-2005 (Jet Propulsion Lab.) 176 p
HC A09/MF A01

N84-18226

Unclass
18207

CSCL 22A G3/12

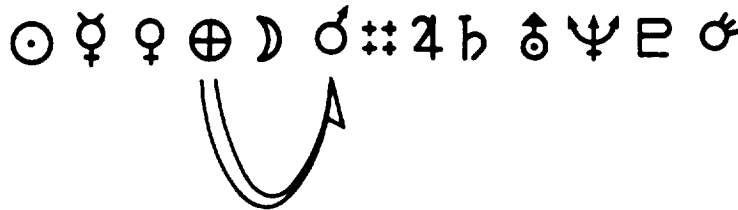
TECHNICAL REPORT STANDARD TITLE PAGE

1. Report No. 82-43, Vol. I, Pt. 2	2. Government Accession No.	3. Recipient's Catalog No.	
4. Title and Subtitle Interplanetary Mission Design Handbook, Volume I, Part 2: Earth to Mars Ballistic Mission Opportunities, 1990-2005		5. Report Date September 15, 1983	
		6. Performing Organization Code	
7. Author(s) A.B. Sergeevsky, G.C. Snyder, R.A. Cunniff		8. Performing Organization Report No.	
9. Performing Organization Name and Address JET PROPULSION LABORATORY California Institute of Technology 4800 Oak Grove Drive Pasadena, California 91109		10. Work Unit No.	
		11. Contract or Grant No. NAS 7-100	
		13. Type of Report and Period Covered JPL Publication	
12. Sponsoring Agency Name and Address NATIONAL AERONAUTICS AND SPACE ADMINISTRATION Washington, D.C. 20546		14. Sponsoring Agency Code RD4/P-186-30-03-11-00	
15. Supplementary Notes			
16. Abstract <p>This document contains graphical data necessary for the preliminary design of ballistic missions to Mars. Contours of launch-energy requirements, as well as many other launch and Mars-arrival parameters, are presented in launch-date/arrival-date space for all launch opportunities from 1990 through 2005. In addition, an extensive text is included which explains mission-design methods, from launch-window development to Mars-probe and orbiter-arrival design, utilizing the graphical data in this volume as well as numerous equations relating various parameters. This is one of a planned series of mission-design documents which will apply to all planets and some other bodies in the solar system.</p>			
17. Key Words (Selected by Author(s)) Astronautics Astrodynamics Launch Vehicles and Space Vehicles Lunar and Planetary Exploration		18. Distribution Statement Unclassified - Unlimited	
19. Security Classif. (of this report) Unclassified	20. Security Classif. (of this page) Unclassified	21. No. of Pages 176	22. Price

Interplanetary Mission Design Handbook, Volume I, Part 2

Earth to Mars Ballistic Mission Opportunities,
1990-2005

Andrey B. Sergeyevsky
Gerald C. Snyder
Ross A. Cunniff



September 15, 1983



National Aeronautics and
Space Administration

Jet Propulsion Laboratory
California Institute of Technology
Pasadena, California

The research described in this publication was carried out by the Jet Propulsion Laboratory, California Institute of Technology, under contract with the National Aeronautics and Space Administration.

Abstract

This document contains graphical data necessary for the preliminary design of ballistic missions to Mars. Contours of launch energy requirements, as well as many other launch and Mars arrival parameters, are presented in launch date/arrival date space for all launch opportunities from 1990 through 2005. In addition, an extensive text is included which explains mission design methods, from launch window development to Mars probe and orbiter arrival design, utilizing the graphical data in this volume as well as numerous equations relating various parameters. This is one of a planned series of mission design documents which will apply to all planets and some other bodies in the solar system.

Preface

This publication is one of a series of volumes devoted to interplanetary trajectories of different types. Volume I deals with ballistic trajectories. The present publication is Part 2 and describes ballistic trajectories to Mars. Part 3, which was published in 1982, treated ballistic trajectories to Jupiter. Part 4, which was published earlier in 1983, described ballistic trajectories to Saturn. Parts 1 and 5, which will be published in the near future, will treat ballistic trajectories to Venus and Mars-to-Earth return trajectories, respectively.

Contents

I. Introduction	1
II. Computational Algorithms	1
A. General Description	1
B. Two-Body Conic Transfer	1
C. Pseudostate Method	3
III. Trajectory Characteristics	4
A. Mission Space	4
B. Transfer Trajectory	5
C. Launch/Injection Geometry	9
1. Launch Azimuth Problem	9
2. Daily Launch Windows	10
3. Range Angle Arithmetic	15
4. Parking Orbit Regression	16
5. Dogleg Ascent	17
6. Tracking and Orientation	17
7. Post-Launch Spacecraft State	18
8. Orbital Launch Problem	18
D. Planetary Arrival Synthesis	18
1. Flyby Trajectory Design	18
2. Capture Orbit Design	24
3. Entry Probe and Lander Trajectory Design	28
E. Launch Strategy Construction	31
IV. Description of Trajectory Characteristics Data	32
A. General	32
B. Definition of Departure Variables	32
C. Definition of Arrival Variables	32
V. Table of Constants	33
A. Sun	33
B. Earth/Moon System	33
C. Mars System	33

D. Sources	33
Acknowledgments	33
References	33
Figures	
1. The Lambert problem geometry	2
2. Departure geometry and velocity vector diagram	2
3. Pseudostate transfer geometry	3
4. Mission space in departure/arrival date coordinates, typical example ..	5
5. Effect of transfer angle upon inclination of trajectory arc	6
6. Nodal transfer geometry	6
7. Mission space with nodal transfer	7
8. Broken-plane transfer geometry	8
9. Sketch of mission space with broken-plane transfer effective energy requirements	8
10. Launch/injection trajectory plane geometry	9
11. Earth equator plane definition of angles involved in the launch problem	10
12. Generalized relative launch time t_{RLT} vs launch azimuth Σ_L and departure asymptote declination δ_∞	11
13. Permissible regions of azimuth vs asymptote declination launch space for Cape Canaveral	12
14. Typical launch geometry example in celestial (inertial) Mercator coordinates	12
15. Central range angle Θ between launch site and outgoing asymptote direction vs its declination and launch azimuth	13
16. Typical example of daily launch geometry (3-dimensional) as viewed by an outside observer ahead of the spacecraft	14
17. Basic geometry of the launch and ascent profile in the trajectory plane	15
18. Angle from perigee to departure asymptote	16
19. Definition of cone and clock angle	17
20. Planetary flyby geometry	19
21. Definition of target or arrival B -plane coordinates	20
22. Two T -axis definitions in the arrival B -plane	21
23. Definition of approach orientational coordinates ZAPS and ETSP, ZAPE and ETEP	22

24. Phase angle geometry at arrival planet	22
25. Typical entry and flyby trajectory geometry	23
26. Coapsidal and cotangential capture orbit insertion geometries	25
27. Coapsidal capture orbit insertion maneuver ΔV requirements for Mars	26
28. Coapsidal and intersecting capture orbit insertion geometries	27
29. Characteristics of intersecting capture orbit insertion and construction of optimal burn envelope at Mars	29
30. Minimum ΔV required for insertion into Mars capture orbit of given apsidal orientation	30
31. General satellite orbit parameters and precessional motion due to oblateness coefficient J_2	31
32. Voyager (MJS77) trajectory space and launch strategy	31
 Mission Design Data Contour Plots, Earth to Mars Ballistic Mission Opportunities, 1990–2005	 35
1990 Opportunity	37
1992 Opportunity	49
1994 Opportunity	61
1996/7 Opportunity	73
1998/9 Opportunity	85
2000/1 Opportunity	109
2002/3 Opportunity	133
2005 Opportunity	157

I. Introduction

The purpose of this series of Mission Design Handbooks is to provide trajectory designers and mission planners with graphical trajectory information, sufficient for preliminary interplanetary mission design and evaluation. In most respects the series is a continuation of the previous three volumes of the Mission Design Data, TM 33-736 (Ref. 1) and its predecessors (e.g., Ref. 2); it extends their coverage to departures through the year 2005 A.D.

The entire series is planned as a sequence of volumes, each describing a distinct mission mode as follows:

- Volume I: Ballistic (i.e., unpowered) transfers between Earth and a planet, consisting of one-leg trajectory arcs. For Venus and Mars missions the planet-to-Earth return trajectory data are also provided.
- Volume II: Gravity-Assist (G/A) trajectory transfers, comprising from two to four ballistic interplanetary legs, connected by successive planetary swingbys.
- Volume III: Delta-V-EGA (Δ VEGA) transfer trajectories utilizing an impulsive deep-space phasing and shaping burn, followed by a return to Earth for a G/A swingby maneuver taking the spacecraft (S/C) to the eventual target planet.

Each volume consists of several parts, describing trajectory opportunities for missions toward specific target or swingby bodies.

This Volume I, Part 2 of the series is devoted to ballistic transfers between Earth and Mars. It describes trajectories taking from 100 to 500 days of flight time for the 8 successive mission opportunities, departing Earth in the following years: 1990, 1992, 1994, 1996/7, 1998/9, 2000/1, 2002/3, and 2005.

Individual variables presented herein are described in detail in subsequent sections and summarized again in Section IV. Suffice it to say here that all the data are presented in sets of 11 contour plots each, displayed on the launch date/arrival date space for each opportunity. Required departure energy C_3 , departure asymptote declination and right ascension, arrival V_∞ and its equatorial directions, as well as Sun and Earth direction angles with respect to the departure/arrival asymptotes, are presented.

It should be noted that parts of the launch space covered may require launcher energies not presently (1983) available,

but certainly not unrealistic using future orbital assembly techniques.

A separate series of volumes (Ref. 3) is being published concurrently to provide purely geometrical (i.e., trajectory-independent) data on planetary positions and viewing/orientation angles, experienced by a spacecraft in the vicinity of these planetary bodies. The data cover the time span through 2020 A.D., in order to allow sufficient mission duration time for all Earth departures, up to 2005 A.D.

The geometric data are presented in graphical form and consist of 26 quantities, combined into eight plots for each calendar year and each target planet. The graphs display equatorial declination and right ascension of Earth and Sun (planetocentric), as well as those of the target planet (geocentric); heliocentric (ecliptic) longitude of the planet, its heliocentric and geocentric distance; cone angles of Earth and Canopus, clock angle of Earth (when Sun/Canopus-oriented); Earth-Sun-planet, as well as Sun-Earth-planet angles; and finally, rise and set times for six deep-space tracking stations assuming a 6-deg horizon mask. This information is similar to that in the second part of each of the volumes previously published (Ref. 1).

II. Computational Algorithms

A. General Description

The plots for the entire series were computer-generated. A minimum of editorial and graphic support was postulated from the outset in an effort to reduce cost.

A number of computer programs were created and/or modified to suit the needs of the Handbook production.

The computing effort involved the generation of arrays of transfer trajectory arcs connecting departure and arrival planets on a large number of suitable dates at each body. Algorithms (computational models) to solve this problem can vary greatly as to their complexity, cost of data generated, and resulting data accuracy. In light of these considerations, the choice of methods used in this effort has been assessed.

B. Two-Body Conic Transfer

Each departure/arrival date combination represents a unique transfer trajectory between two specified bodies, if the number of revolutions of the spacecraft about the primary (e.g., the Sun) is specified. The Lambert Theorem provides a suitable framework for the computation of such primary-centered trajectories, but it is of practical usefulness only if restricted two-body conic motion prevails.

Restricted two-body motion implies that the dynamical system consists of only two bodies, one of which, the primary,

is so much more massive than the other, that all of the system's gravitational attraction may be assumed as concentrated at a point—the center of that primary body. The secondary body of negligible mass (e.g., the spacecraft) then moves in Keplerian (conic) orbits about the primary (e.g., the Sun) in such a way that the center of the primary is located at one of the foci of the conic (an ellipse, parabola, or hyperbola).

The Lambert Theorem states that given a value of the gravitational parameter μ (also known as GM) for the central body, the time of flight between two arbitrary points in space, R_1 and R_2 , is a function of only three independent variables: the sum of the distances of the two points from the focus, $|R_1| + |R_2|$, the distance between the two points $C = |R_2 - R_1|$, and the semimajor axis, a , of the conic orbital flight path between them (Fig. 1.)

Detailed algorithm descriptions of the Lambert method, including necessary branching and singularity precautions, are presented in numerous publications, e.g., Refs. 2 and 4. The computations result in a set of conic classical elements ($a, e, i, \Omega, \omega, v_1$) and the transfer angle, Δv_{12} , or two equivalent spacecraft heliocentric velocity vectors, $V_{hS/C\ i}$ —one at departure, the other at the arrival planet. Subtraction of the appropriate planetary heliocentric velocity vector, $V_{hPLANET\ i}$, at the two corresponding times from each of these two spacecraft velocity vectors results in a pair of planetocentric velocity states "at infinity" with respect to each planet (Fig. 2):

$$V_{\infty\ i} = V_{hS/C\ i} - V_{hPLANET\ i} \quad (1)$$

where $i = 1$ and 2 refer to positions at departure and arrival, respectively. The scalar of this V_{∞} vector is also referred to as

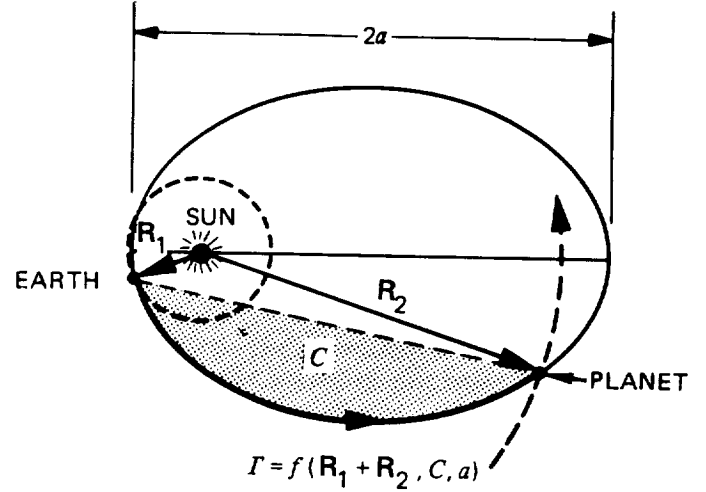


Fig. 1. The Lambert problem geometry

the hyperbolic excess velocity, "V-infinity" or simply "speed" (e.g., Ref. 4). The V_{∞} represents the velocity of the spacecraft at a great distance from the planet (where its gravitational attraction is practically negligible). It is attained when the spacecraft has climbed away from the departure planet, following injection at velocity V_I :

$$V_{\infty\ 1} = \sqrt{V_I^2 - \frac{2\mu_1}{r_I}} \quad , \text{ km/s} \quad (2)$$

or before it starts its fall into the arrival planet's gravity well, where it eventually reaches a closest approach (periapse, C/A) velocity V_P :

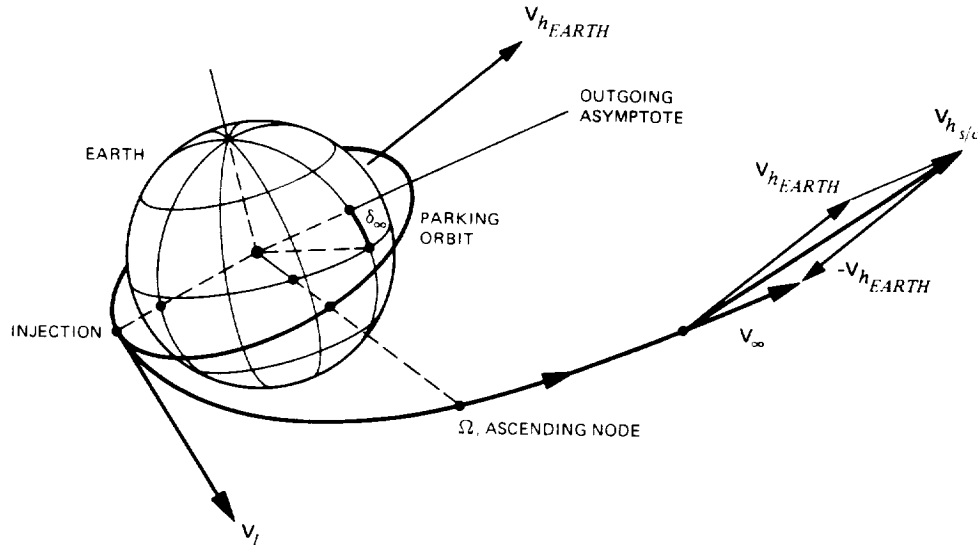


Fig. 2. Departure geometry and velocity vector diagram

$$V_P = \sqrt{V_{\infty 2}^2 + \frac{2\mu_2}{r_p}}, \text{ km/s} \quad (3)$$

The variables r_I and r_p refer to the departure injection and arrival periapse planetocentric radii, respectively. Values for the gravitational parameter μ (or GM) are given in subsequent Section V on constants.

The V_{∞} vectors, computed by the Lambert method, represent a body center to body center transfer. They can, however, be translated parallel to themselves at either body without excessive error due to the offset, and a great variety of realistic departure and arrival trajectories may thus be constructed through their use, to be discussed later. The magnitude and direction of V_{∞} as well as the angles that this vector forms with the Sun and Earth direction vectors at each terminus are required for these mission design exercises.

Missions to the relatively small terrestrial planets such as Mars are suited to be analyzed by the Lambert method, as the problem can be adequately represented by the restricted two-body formulation, resulting in flight time errors of less than 1 day — an accuracy that cannot even be read from the contour plots presented in this document.

C. Pseudostate Method

Actual precision interplanetary transfer trajectories, especially those involving the giant outer planets, do noticeably violate the assumptions inherent in the Lambert Theorem. The restricted two-body problem, on which that theorem is based, is supposed to describe the conic motion of a massless secondary (i.e., the spacecraft) about the point mass of a primary attractive body (i.e., the Sun), both objects being placed in an otherwise empty Universe. In reality, the gravitational attraction of either departure or target body may significantly alter the entire transfer trajectory.

Numerical N -body trajectory integration could be called upon to represent the true physical model for the laws of motion, but would be too costly, considering the number of complete trajectories required to fully search and describe a given mission opportunity.

The pseudostate theory, first introduced by S. W. Wilson (Ref. 5) and modified to solve the three-body Lambert problem by D. V. Byrnes (Ref. 6), represents an extremely useful improvement over the standard Lambert solution. For the giant planet missions, it can correct about 95 percent of the three-body errors incurred, e.g., up to 30 days in flight time on a typical Jupiter-bound journey.

Pseudostate theory is based on the assumption that for modest gravitational perturbations the spacecraft conic motion about the primary and the pseudo-conic displacement due to a third body may be superimposed, if certain rules are followed.

The method, as applied to transfer trajectory generation, does not provide a flight path—only its end states. It solves the original Lambert problem, however, not between the true planetary positions themselves, but instead, between two computed "pseudostates." These are obtained by iteration on two displacement vectors off the planetary ephemeris positions on the dates of departure and arrival. By a suitable superposition with a planetocentric rectilinear impact hyperbola and a constant-velocity, "zero gravity," sweepback at each end of the Lambertian conic (see Fig. 3), a satisfactory match is obtained.

Of the five arcs involved in the iteration, the last three (towards and at the target planet) act over the full flight time, ΔT_{12} , and represent:

- (1) Conic heliocentric motion between the two pseudostates R_1^* and R_2^* (capital R is used here for all heliocentric positions),
- (2) The transformation of R_2^* to a planetocentric position, r_2^* (lower case r is used for planetocentric positions), performed in the usual manner is followed by a "constant-velocity" sweepback in time to a point $r_a^* = r_2^* - V_{\infty 2} \times \Delta T_{12}$, correcting the planetocentric position r_2^* to what it would have been at T_1 , had there been no solar attraction during ΔT_{12} , and finally,
- (3) The planetocentric rectilinear incoming hyperbola, characterized by: incoming V -infinity $V_{\infty 2}$, a radial

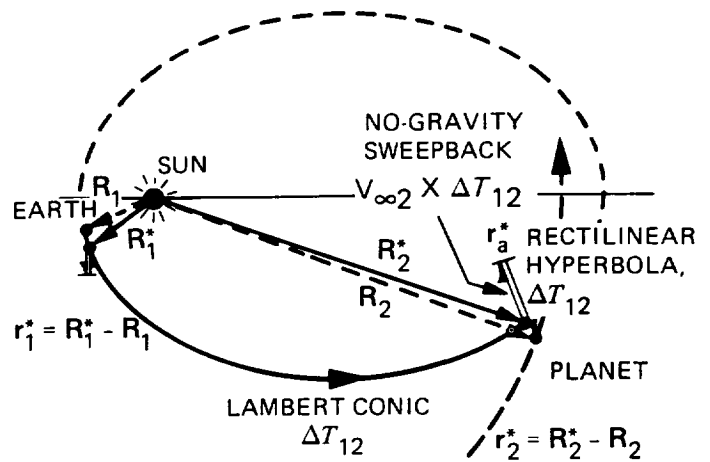


Fig. 3. Pseudostate transfer geometry

target planet impact, and a trip-time ΔT_{12} from \mathbf{r}_a^* to periape, which can be satisfied by iteration on the \mathbf{r}_2^* -magnitude and thus also on \mathbf{R}_2^* .

This last aspect provides for a great simplification of the formulation as the \mathbf{R}_2^* end-point locus now moves only along the $\mathbf{V}_{\infty} \parallel \mathbf{r}_2^*$ vector direction. The resulting reduction in computing cost is significant, and the equivalence to the Lambert point-to-point conic transfer model is attractive.

The first two segments of the transfer associated with the departure planet may be treated in a like manner. If the planet is Earth, the pseudostate correction may be disregarded (i.e., $\mathbf{R}_1^* = \mathbf{R}_1$), or else the duration of Earth's perturbative effect may be reduced to a fraction of ΔT_{12} . It can also be set to equal a fixed quantity, e.g., $\Delta T_i = 20$ days. The latter value was in fact used at the Earth's side of the transfer in the data generation process for this document.

The rectilinear pseudostate method described above and in Ref. 7 thus involves an iterative procedure, utilizing the standard Lambert algorithm to obtain a starting set of values for \mathbf{V}_{∞} at each end of the transfer arc. This first guess is then improved by allowing the planetocentric pseudostate position vector \mathbf{r}_i^* to be scaled up and down, using a suitable partial at either body, such that ΔT_{REQ} , the time required to fall along the rectilinear hyperbola through \mathbf{r}_a^* (the sum of the sweep-back distance $\mathbf{V}_{\infty} \times \Delta T_i$ and the planetocentric distance $|\mathbf{r}_i^*|$), equal the gravitational perturbation duration, ΔT_i . Both \mathbf{r}_i^* and \mathbf{V}_{∞} , along which the rectilinear fall occurs, are continuously reset utilizing the latest values of magnitude and direction of \mathbf{V}_{∞} at each end, i , of the new Lambert transfer arc, as the iteration progresses. The procedure converges rapidly as the hyperbolic trip time discrepancy, $\Delta \Delta T = \Delta T_{REQ} - \Delta T_i$, falls below a preset small tolerance. Once the \mathbf{V}_{∞} vectors at each planet are converged upon, the desired output variables can be generated and contour plotted by existing standard algorithms.

As mentioned before, the pseudostate method was found to be unnecessary for the accuracy of this Mars-oriented handbook. The simpler Lambert method was used instead in the data-generation process.

III. Trajectory Characteristics

A. Mission Space

All realistic launch and injection vehicles are energy-limited and impose very stringent constraints on the interplanetary mission selection process. Only those transfer opportunities which occur near the times of a minimum Earth departure energy requirement are thus of practical interest. On either side of such an optimal date, departure energy increases, first slowly, followed by a rapid increase, thus requiring either a greater launch capability, or alternatively a lower allowable

payload mass. A "launch period," measured in days or even weeks, is thus definable: on any day within its confines the capability of a given launch/injection vehicle must equal or exceed the departure energy requirement for a specified payload weight.

In the course of time these minimum departure energy opportunities do recur regularly, at "synodic period" intervals reflecting a repetition of the relative angular geometry of the two planets. If ω_1 and ω_2 are the orbital angular rates of the inner and outer of the two planets, respectively, moving about the Sun in circular orbits, then the mutual configuration of the two bodies changes at the following rate:

$$\omega_{12} = \omega_1 - \omega_2, \text{ rad/s} \quad (4)$$

If a period of revolution, P , is defined as

$$P = \frac{2\pi}{\omega}, \text{ s} \quad (5)$$

then

$$\frac{1}{P_S} = \frac{1}{P_1} - \frac{1}{P_2} \quad (6)$$

where P_S , the synodic period, is the period of planetary geometry recurrence, while P_1 and P_2 are the orbital "sidereal (i.e., inertial) periods" of the inner (faster) and the outer (slower) planet considered, respectively.

Since planetary orbits are neither exactly circular nor coplanar, launch opportunities do not repeat exactly, some years being better than others in energy requirements or in other parameters. A complete repeat of trajectory characteristics occurs only when exactly the same orbital geometry of departure and arrival body recurs. For negligibly perturbed planets approximately identical inertial positions in space at departure and arrival imply near-recurrence of transfer trajectory characteristics. Such events can rigorously be assessed only for nearly resonant nonprecessing planetary orbits, i.e., for those whose periods can be related in terms of integer fractions. For instance, if five revolutions of one body correspond to three revolutions of the other, that time interval would constitute the "period of repeated characteristics." Near-integer ratios provide nearly repetitive configurations with respect to the lines of apsides and nodes. The Earth-relative synodic period of Mars is 779.935 days, i.e., about 2.14 years. Each cycle of 7 consecutive Martian mission opportunities amounts to 5459.55 days and is nearly repetitive, driven by 8 Martian sidereal periods of 686.9804 days. It is obvious that for an identical mutual angular geometry Mars would be found short of its inertial position in the previous cycle by 36.3 days worth of motion (19.02 deg), while Earth would have completed $5459.55/365.25 = 14.947$ revolutions, being short of the old mark by the same angular amount as Saturn.

A much closer repetition of characteristics occurs at 17 full Martian revolutions (11678.667 days), after 15 Mars-departure opportunities (11699.031 days = 32.0302 years), showing an inertial position excess of only 10.7 degs., 20.4 days worth of Mars motion beyond the original design arrival point.

A variety of considerations force the realistic launch period not to occur at the minimum energy combination of departure and arrival dates. Launch vehicle readiness status, procedure slippage, weather anomalies, multiple launch strategies, arrival characteristics—all cause the launch or, more generally, the departure period to be extended over a number of days or weeks and not necessarily centered on the minimum energy date.

For this document, a 160-day departure date coverage span was selected, primarily in order to encompass launch energy requirements of up to a $C_3 = 50 \text{ km}^2/\text{s}^2$ contour, where $C_3 = V_{\infty}^2$, i.e., twice the injection energy per unit mass. $E_I = V_{\infty}^2/2$. Arrival date coverage was set at 400 days to display missions from 100–400 days of flight time.

The matrix of departure and arrival dates to be presented comprises the “mission space” for each departure opportunity.

B. Transfer Trajectory

As previously stated, each pair of departure/arrival dates specifies a unique transfer trajectory. Each such point in the mission space has associated with it an array of descriptive variables. Departure energy, characterized by C_3 , is by far the most significant among these parameters. It increases towards

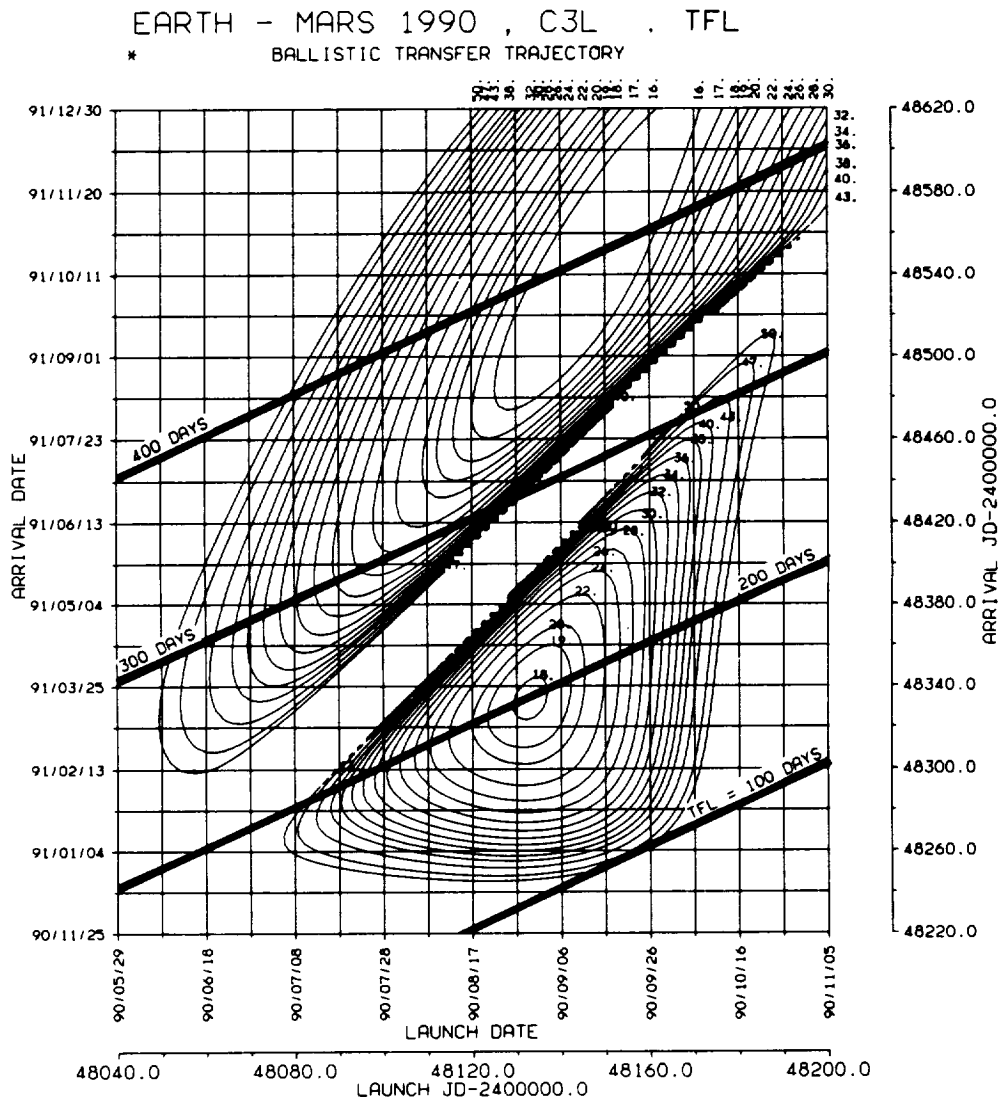


Fig. 4. Mission space in departure/arrival date coordinates, typical example

the edges of the mission space, but it also experiences a dramatic rise along a "ridge," passing diagonally from lower left to upper right across the mission space (Fig. 4). This disturbance is associated with all diametric, i.e., near-180-deg, transfer trajectories (Fig. 5).

In 3-dimensional space the fact that all planetary orbits are not strictly coplanar causes such diametric transfer arcs to require high ecliptic inclinations, culminating in a polar flight path for an exact 180-deg ecliptic longitude increment between departure and arrival points. The reason for this behavior is, as shown in Fig. 5, that the Sun and both trajectory end points must lie in a single plane, while they are also lining up along the same diameter across the ecliptic. The slightest target planet orbital inclination causes a deviation

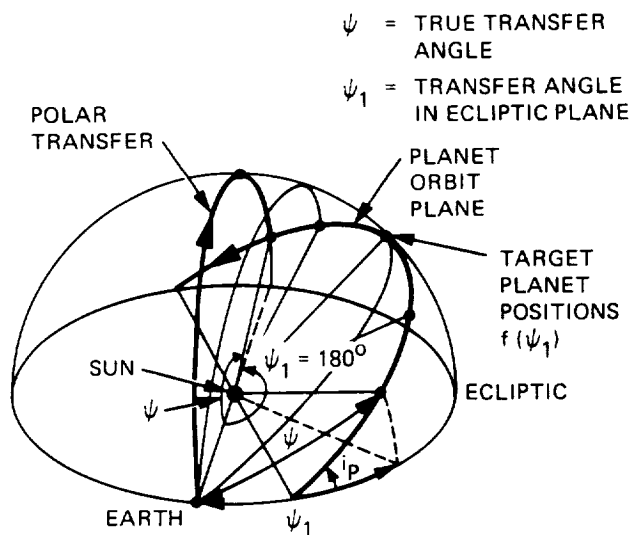


Fig. 5. Effect of transfer angle upon inclination of trajectory arc

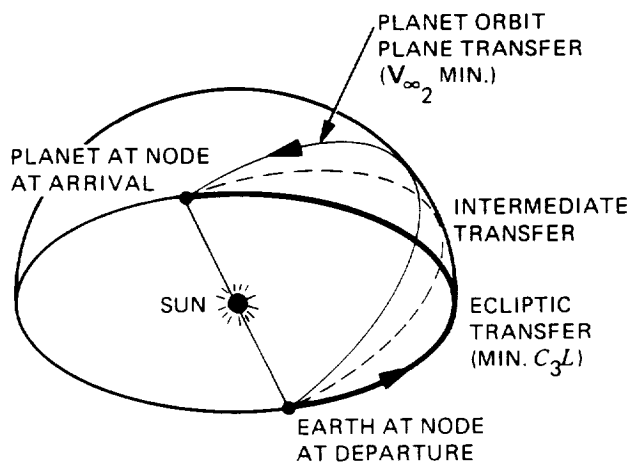


Fig. 6. Nodal transfer geometry

out of the ecliptic and forces a polar 180-deg transfer, in order to pick up the target's vertical out-of-plane displacement.

The obvious sole exception to this rule is the nodal transfer mission, where departure occurs at one node of the target planet orbit plane with the ecliptic, whereas arrival occurs at the opposite such node. In these special cases, which recur every half of the repeatability cycle, discussed in the preceding paragraph, the transfer trajectory plane is indeterminate and may as well lie in the departure planet's orbit plane, thus requiring a lesser departure energy (Fig. 6). The opposite strategy (i.e., a transfer in the arrival planet's orbit plane) may be preferred if arrival energy, $V_{\infty 2}$, is to be minimized (Fig. 7).

It should be noted that nodal transfers, being associated with a specific Mars arrival date, may show up in the data on several consecutive Martian mission opportunity graphs (e.g., 1992-1998), at points corresponding to the particular nodal arrival date. Their mission space position moves, from opportunity to opportunity, along the 180-deg transfer ridge, by gradually sliding towards shorter trip times and earlier relative departure dates. Only one of these opportunities would occur at or near the minimum departure energy or the minimum arrival V_{∞} date, which require a near-perihelion to near-aphelion transfer trajectory. These pseudo-Hohmann nodal transfer opportunities provide significant energy advantages, but represent singularities, i.e., single-time-point missions, with extremely high error sensitivities. Present-day mission planning does not allow single fixed-time departure strategies; however, future operations modes, e.g., space station "on-time" launch, or alternately Earth gravity assist (repeated) encounter at a specific time, may allow the advantages of a nodal transfer to be utilized in full.

The 180-deg transfer ridge subdivides the mission space into two basic regions: the Type I trajectory space below the ridge, exhibiting less than 180-deg transfer arcs, and the Type II space whose transfers are longer than 180 deg. In general the first type also provides shorter trip times.

Trajectories of both types are further subdivided in two parts—Classes 1 and 2. These are separated, generally horizontally, by a boundary representing the locus of lowest C_3 energy for each departure date. Classes separate longer duration missions from shorter ones within each type. Type I, Class 1 missions could thus be preferred because of their shorter trip times.

Transfer energies become extremely high for very short trip times, infinite if launch date equals arrival date, and of course, meaningless for negative trip times.

The reason that high-inclination transfers, as found along the ridge, also require such high energy expenditures at depar-

ORIGINAL PAGE IS
OF POOR QUALITY

EARTH - MARS 1996/7, C3L TFL

* BALLISTIC TRANSFER TRAJECTORY

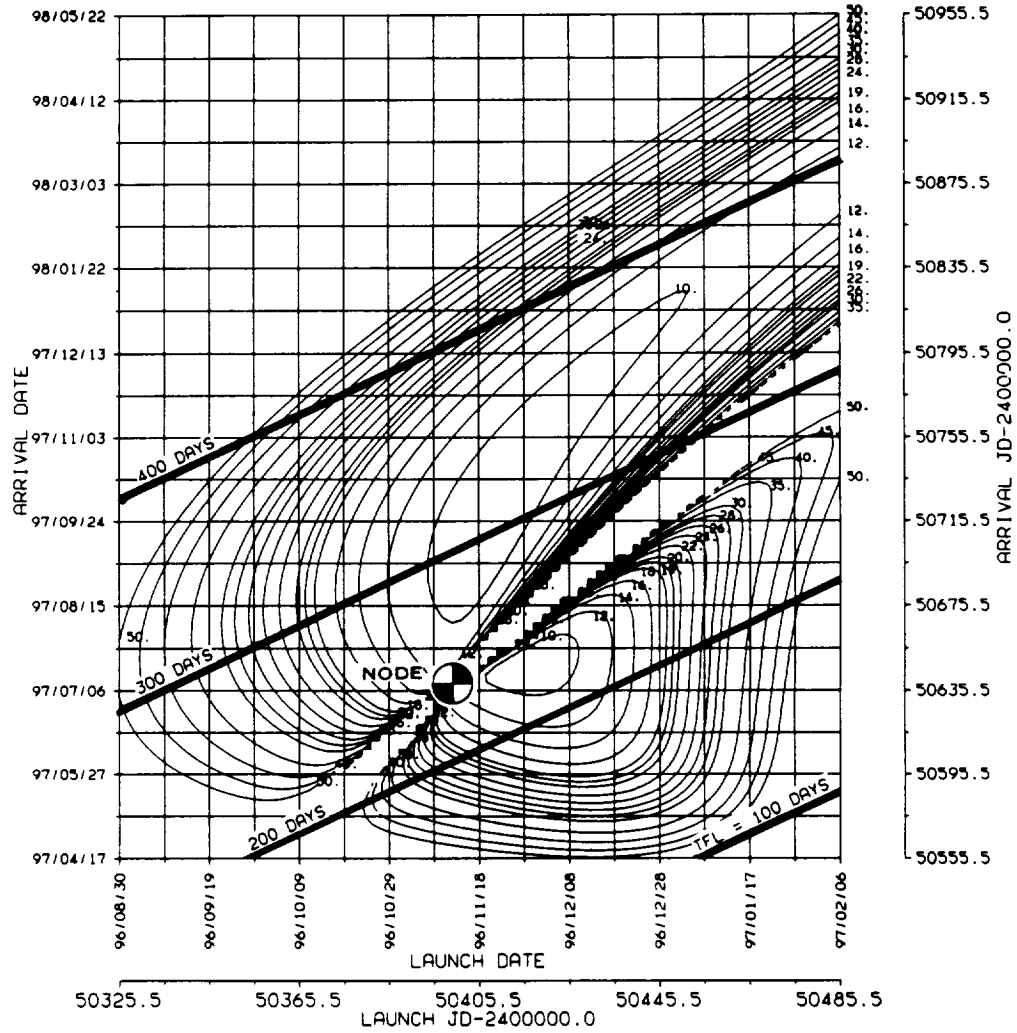


Fig. 7. Mission space with nodal transfer

ture is that the spacecraft velocity vector due to the Earth's orbital velocity must be rotated through large angles out of the ecliptic in addition to the need to acquire the required transfer trajectory energy. The value of C_3 on the ridge is large but finite; its saddle point minimum value occurs for a pseudo-Hohmann (i.e., perihelion to aphelion) polar transfer, requiring

$$C_3 = V_E^2 \left(\frac{2a_p}{1+a_p} + 1 \right) \approx 1950 \text{ km}^2/\text{s}^2 \quad (7)$$

where $V_E = 29.766 \text{ km/s}$, the Earth's heliocentric orbital velocity, and $a_p = 1.49 \text{ AU}$, Mars's (the arrival planet's) semi-major axis. By a similar estimate, it can be shown that for a true nodal pseudo-Hohmann transfer, the minimum energy required would reduce to

$$C_{3\text{NODAL}} = V_E^2 \left[\left(\frac{2a_p}{1+a_p} \right)^{1/2} - 1 \right]^2 \approx 7.83 \text{ km}^2/\text{s}^2 \quad (8)$$

This is the lowest value of C_3 required to fly from Earth to Mars, assuming circular planetary orbits.

Arrival V -infinity, $V_{\infty A}$, is at its lowest when the transfer trajectory is near-coplanar and tangential to the target planet orbit at arrival.

Both C_3 and $V_{\infty A}$ near the ridge can be significantly lowered if deep-space deterministic maneuvers are introduced into the mission. The "broken-plane" maneuvers are a category of

such ridge-counteracting measures, which can nearly eliminate all vestiges of the near-180-deg transfer difficulties.

The basic principle employed in broken-plane transfers is to avoid high ecliptic inclinations of the trajectory by performing a plane change maneuver in the general vicinity of the halfway point, such that it would correct the spacecraft's aim toward the target planet's out-of-ecliptic position (Fig. 8).

Graphical data can be presented for this type of mission, but it requires an optimization of the sum of critical ΔV expenditures. The decision on which ΔV s should be included must be based on some knowledge of overall staging and arrival intentions, e.g., departure injection and arrival orbit insertion vehicle capabilities and geometric constraints or objectives contemplated. As an illustration, a sketch of resulting contours of C_3 is shown in Fig. 9 for a typical broken-plane opportunity represented as a narrow strip covering the riuge area (Class 2 of Type I and Class 1 of Type II) on a nominal 1990

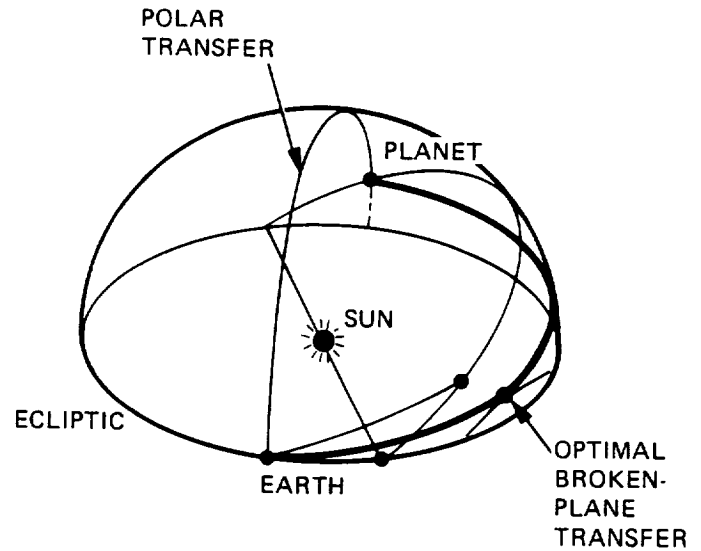


Fig. 8. Broken-plane transfer geometry

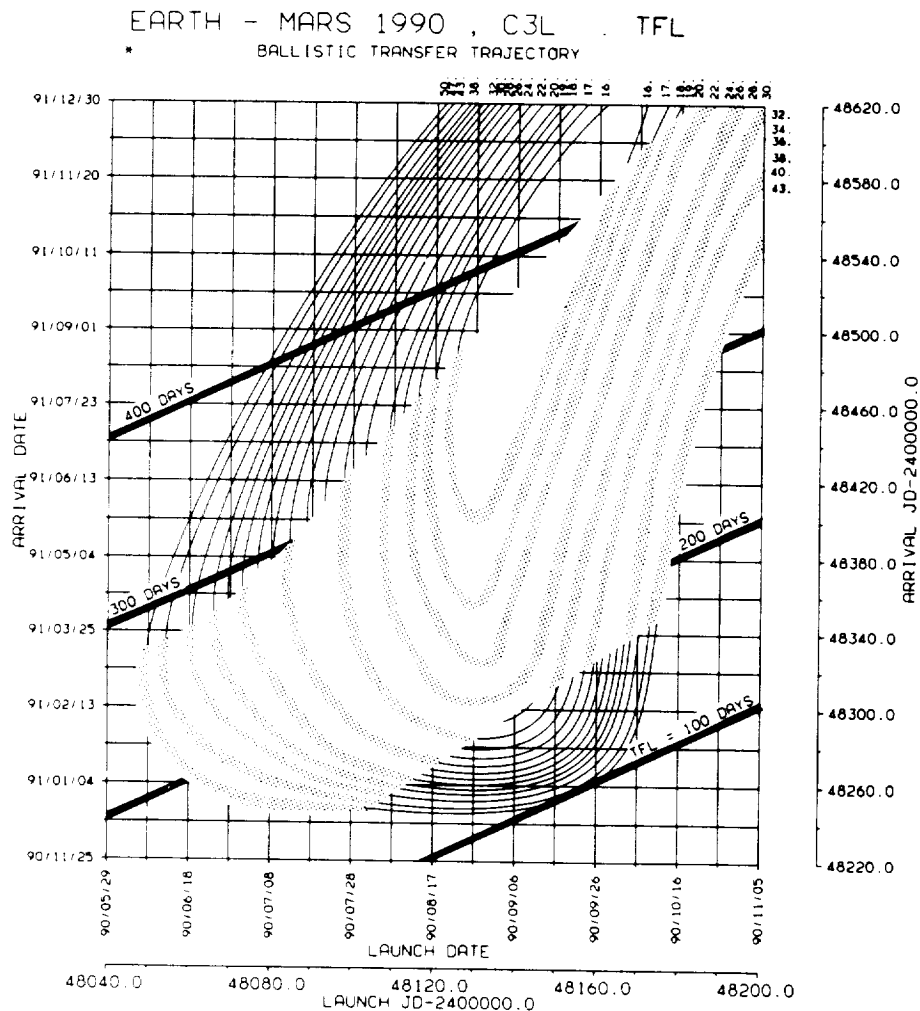


Fig. 9. Sketch of mission space with broken-plane transfer, effective energy requirements

launch/arrival date C_3 contour plot. The deep-space maneuver ΔV_{BP} is transformed into a C_3 equivalent by converting the new broken-plane C_{3BP} to an injection velocity at parking orbit altitude, adding ΔV_{BP} , and converting the sum to a new and slightly larger C_3 value at each point on the strip.

C. Launch/Injection Geometry

The primary problem in departure trajectory design is to match the mission-required outgoing V -infinity vector, \mathbf{V}_∞ , to the specified launch site location on the rotating Earth. The site is defined by its geocentric latitude, ϕ_L , and geographic east longitude, λ_L (Figs. 10 and 11).

Range safety considerations prohibit overflight of populated or coastal areas by the ascending launch vehicle. For each launch site (e.g., Kennedy Space Center, Western Test Range, or Guiana Space Center), a sector of allowed azimuth firing directions Σ_L is defined (measured in the site's local horizontal plane, clockwise from north). For each launch vehicle, the allowed sector may be further constrained by other safety considerations, such as spent stage impact locations down the range and/or down-range significant event tracking capabilities.

The outgoing V -infinity vector is a slowly varying function of departure and arrival date and may be considered constant for a given day of launch. It is usually specified by its energy

magnitude $C_3 = |\mathbf{V}_\infty|^2$, called out as C_3L in the plots and representing twice the kinetic energy (per kilogram of injected mass) which *must* be matched by launch vehicle capabilities, and the V -infinity direction with respect to the inertial Earth Mean Equator and equinox of 1950.0 (EME50) coordinate system: the declination (i.e., latitude) of the outgoing asymptote δ_∞ (called DLA), and its right ascension (i.e., equatorial east longitude from vernal equinox, Υ) α_∞ (or RLA). These three quantities are contour-plotted in the handbook data presented in this volume.

1. Launch azimuth problem. The first requirement to be met by the trajectory analyst is to establish the orientation of the ascent trajectory plane (Ref. 8). In its simplest form this plane *must contain the outgoing V-infinity (DLA, RLA) vector, the center of Earth, and the launch site at lift-off* (Fig. 10). As the launch site partakes in the sidereal rotation of the Earth, the continuously changing ascent plane manifests itself in a monotonic increase of the launch azimuth, Σ_L , with lift-off time, t_L , (or its angular counterpart, $\alpha_\infty - \alpha_L$, measured in the equator plane):

$$\cotan \Sigma_L = \frac{\cos \phi_L \times \tan \delta_\infty - \sin \phi_L \times \cos(\alpha_\infty - \alpha_L)}{\sin(\alpha_\infty - \alpha_L)} \quad (9)$$

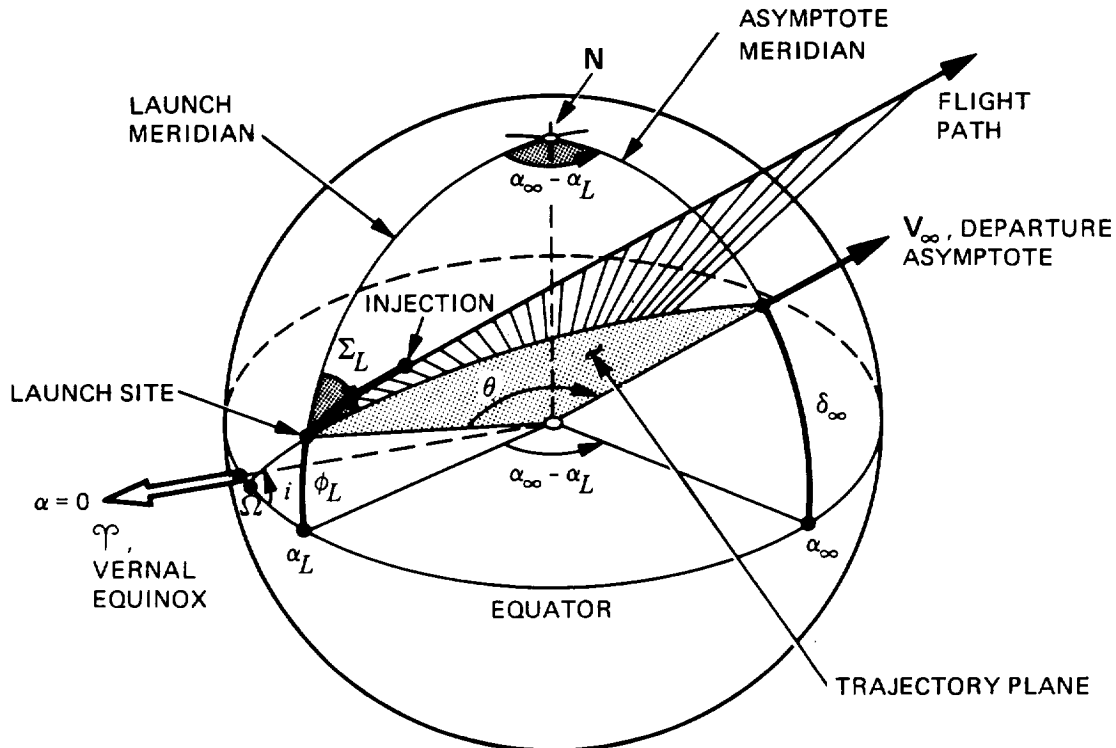


Fig. 10. Launch/injection trajectory plane geometry

The daily time history of azimuth can be obtained from Eq. (9) for a given α_∞ , δ_∞ departure asymptote direction by following quadrant rules explained below and using the following approximate expressions (see Fig. 11):

$$\alpha_L = \lambda_L + GHA_{DATE} + \omega_{EARTH} \times t_L \quad (10)$$

$$GHA_{DATE} = 100.075 + 0.9856123008 \times d_{50} \quad (11)$$

where

α_L = Right ascension of launch site (ϕ_L , λ_L) at t_L (deg)

GHA_{DATE} = Greenwich hour angle at 0^h GMT of any date, the eastward angle between vernal equinox and the Greenwich meridian (deg), assumes equator is EME50.0

ω_{EARTH} = sidereal (inertial) rotation rate of Earth (15.041067179 deg/h of mean solar time)

d_{50} = launch date in terms of full integer days elapsed since 0^h Jan. 1, 1950 (days)

t_L = lift-off time (h, GMT, i.e., mean solar time)

A relative launch time, t_{RLT} , measured with respect to an inertial reference (the departure asymptote meridian's right ascension α_∞), can be defined as a sidereal time (Earth's rotation rate is 15.0 deg/h of sidereal time, exactly):

$$t_{RLT} = 24.0 - \frac{\alpha_\infty - \alpha_L}{15.0}, \text{ h} \quad (12)$$

This time represents a generalized sidereal time of launch, elapsed since the launch site last passed the departure asymptote meridian, α_∞ .

The actual Greenwich Mean (solar) Time (GMT) of launch, t_L , may be obtained from t_{RLT} by transforming it to mean solar time and adding a date, site, and asymptote-dependent adjustment:

$$t_L = \frac{t_{RLT} \times 15.0}{\omega_{EARTH}} + \frac{\alpha_\infty - GHA_{DATE} - \lambda_L (EAST)}{\omega_{EARTH}} \quad (13)$$

The expression for Σ_L (Eq. 9) must be used with computational regard for quadrants, singular points, and sign conventions. If the launch is known to be direct (i.e., eastward), then Σ_L , when $\cotan \Sigma_L$ is negative, must be corrected to $\Sigma_L = \Sigma_{LNEG} + 180.0$. For retrograde (westward) launches, 180.0 deg must be added in the third (when $\cotan \Sigma$ is posi-

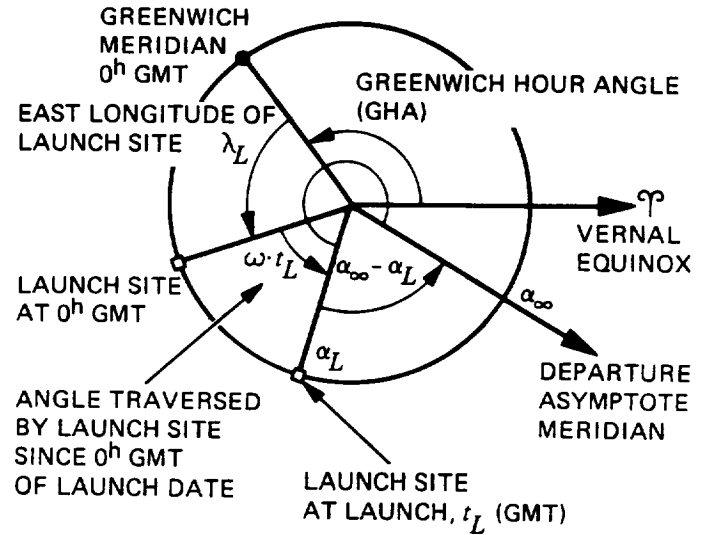


Fig. 11. Earth equator plane definition of angles involved in the launch problem

tive) and 360.0 deg in the fourth quadrant (when $\cotan \Sigma$ is negative).

A generalized plot of relative launch time t_{RLT} vs launch azimuth Σ_L can be constructed based on Eqs. (9) and (12), if a fixed launch site latitude is adopted (e.g., $\phi_L = 28.3$ deg for Kennedy Space Flight Center at Cape Canaveral, Florida). Such a plot is presented in Fig. 12 with departure asymptote declination δ_∞ as the contour parameter. The plot is applicable to any realistic departure condition, independent of α_∞ , date, or true launch time t_L (Ref. 9).

2. Daily launch windows. Inspection of Fig. 12 indicates that generally two contours exist for each declination value (e.g., $\delta_\infty = -10$ deg), one occurring at t_{RLT} during the a.m. hours, the other in the p.m. hours of the asymptote relative "day."

Since lift-off times are bounded by preselected launch-site-dependent limiting values of launch azimuth Σ_L (e.g., 70 deg and 115 deg), each of the two declination contours thus contains a segment during which launch is permissible—"a launch window." The two segments on the plot do define the two available daily launch windows.

As can be seen from Fig. 12, for $\delta_\infty = 0$, the two daily launch opportunities are separated by exactly 12 hours; with an increasing $|\delta_\infty|$ they close in on each other, until at $|\delta_\infty| = |\phi_L|$ they merge into a single daily opportunity. For $|\delta_\infty| > |\phi_L|$, a "split" of that single launch window occurs, disallowing an ever-increasing sector of azimuth values. This sector is symmetric about east and its limits can be determined from

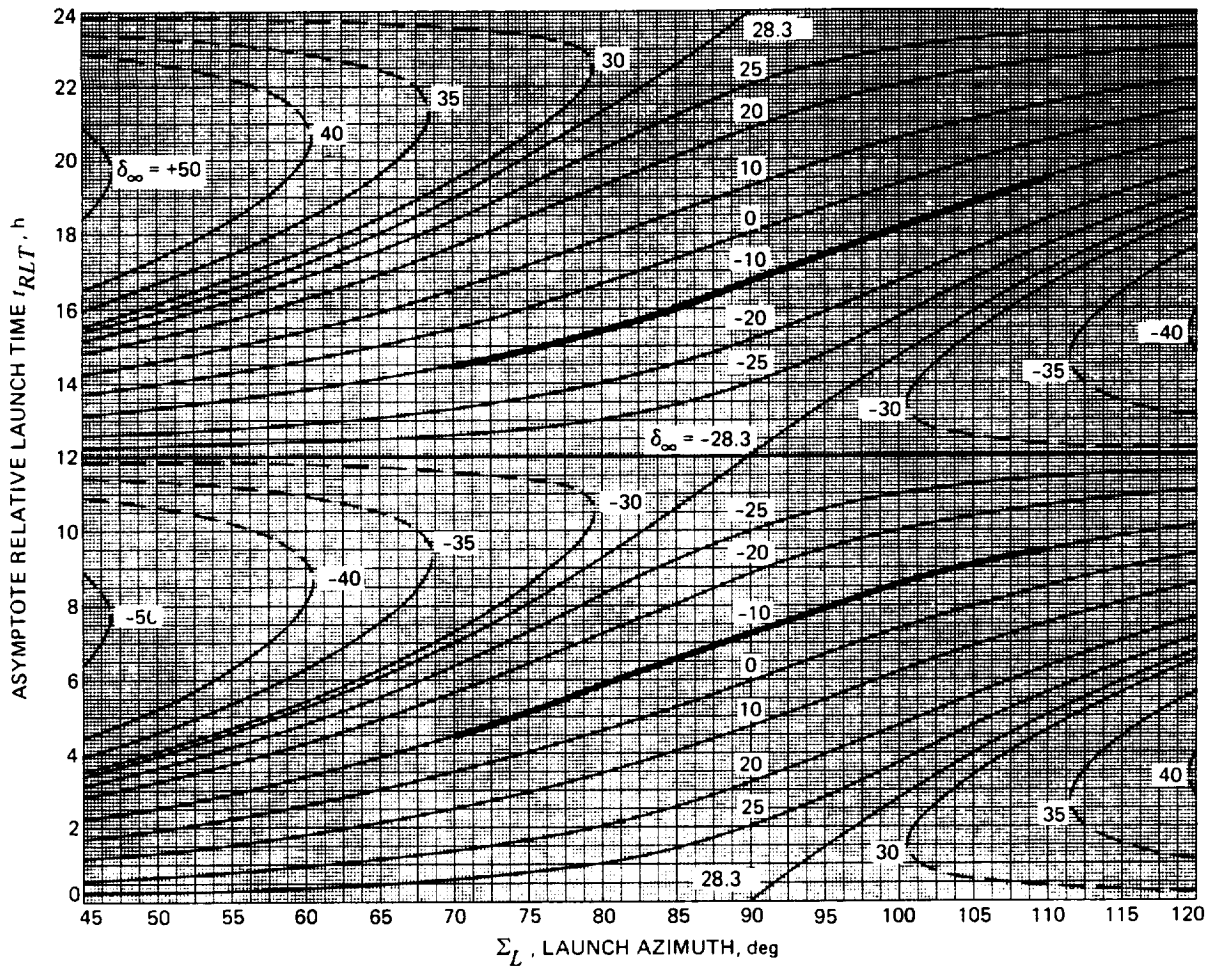


Fig. 12. Generalized relative launch time t_{RLT} vs launch azimuth Σ_L and departure asymptote declination δ_∞ .
Pair of typical example launch windows for $\delta_\infty = -10$ deg shown by bold curve segments
(reproduced from Ref. 9).

$$\sin \Sigma_{L \text{ LIMIT}} = \pm \frac{\cos \delta_\infty}{\cos \phi_L} \quad (14)$$

As δ_∞ gets longer, the sector of unavailable launch azimuths reaches the safety boundaries of permissible launches, and planar launch ceases to exist (Fig. 13). This subject will be addressed again in the discussion of "dogleg" ascents.

Figure 14 is a sketch of a typical daily launch geometry situation, shown upon a Mercator map of the celestial sphere. The two launch windows exhibit a similar geometry since the inclinations of the ascent trajectory planes are functions of launch site latitude ϕ_L and azimuth Σ_L only:

$$\cos i = \cos \phi_L \times \sin \Sigma_L \quad (15)$$

The two daily opportunities do differ greatly, however, in the right ascension of the ascending node Ω of the orbit and in the length of the traversed in-plane arc, the range angle θ .

The angular equatorial distance between the ascending node and the launch site meridian is given by

$$\sin(\alpha_L - \Omega) = \frac{\sin \phi_L \times \sin \Sigma_L}{\sin i} \quad (16)$$

Quadrant rules for this equation involve the observation that a negative $\cos \Sigma_L$ places $(\alpha_L - \Omega)$ into the second or third quadrant, while the sign of $\sin(\alpha_L - \Omega)$ determines the choice between them.

The range angle θ is measured in the inertial ascent trajectory plane from the lift-off point at launch all the way to the departure asymptote direction, and can be computed for a given launch time t_L or $\alpha_\infty - \alpha_L(t_L)$ and an azimuth Σ_L already known from Eq. (9) as follows:

$$\cos \theta = \sin \delta_\infty \times \sin \phi_L + \cos \delta_\infty \times \cos \phi_L \times \cos(\alpha_\infty - \alpha_L) \quad (17)$$

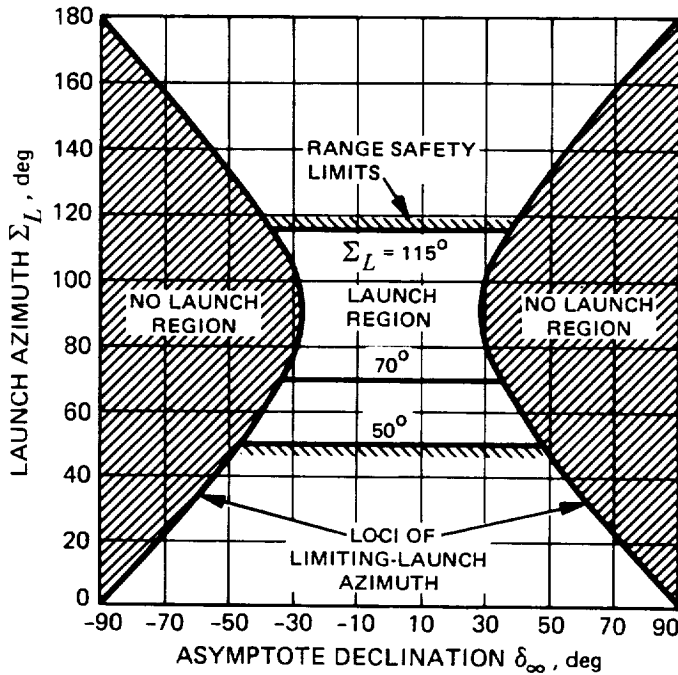


Fig. 13. Permissible regions of azimuth vs asymptote declination launch space for Cape Canaveral

$$\sin \theta = \frac{\sin (\alpha_{\infty} - \alpha_L) \times \cos \delta_{\infty}}{\sin \Sigma_L} \quad (18)$$

The extent of range angle θ can be anywhere between 0 deg and 360 deg, so both $\cos \theta$ and $\sin \theta$ may be desired in its determination. The range angle θ is related to the equatorial plane angle, $\Delta\alpha = \alpha_{\infty} - \alpha_L$, discussed before. Even though the two angles are measured in different planes, they both represent the angular distance between launch and departure asymptote, and hence they traverse the same number of quadrants.

Figure 15 represents a generally applicable plot of central range angle θ vs the departure asymptote declination and launch azimuth, computed using Eqs. (17) and (18) and a launch site latitude $\phi_L = 28.3$ (Cape Canaveral). The twin daily launch opportunities are again evident, showing the significant difference in available range angle when following a vertical, constant δ_{∞} line.

It is sometimes convenient to reverse the computational procedure and determine launch azimuth from known range angle θ and t_{RLT} , i.e., $\Delta\alpha = \alpha_{\infty} - \alpha_L$, as follows:

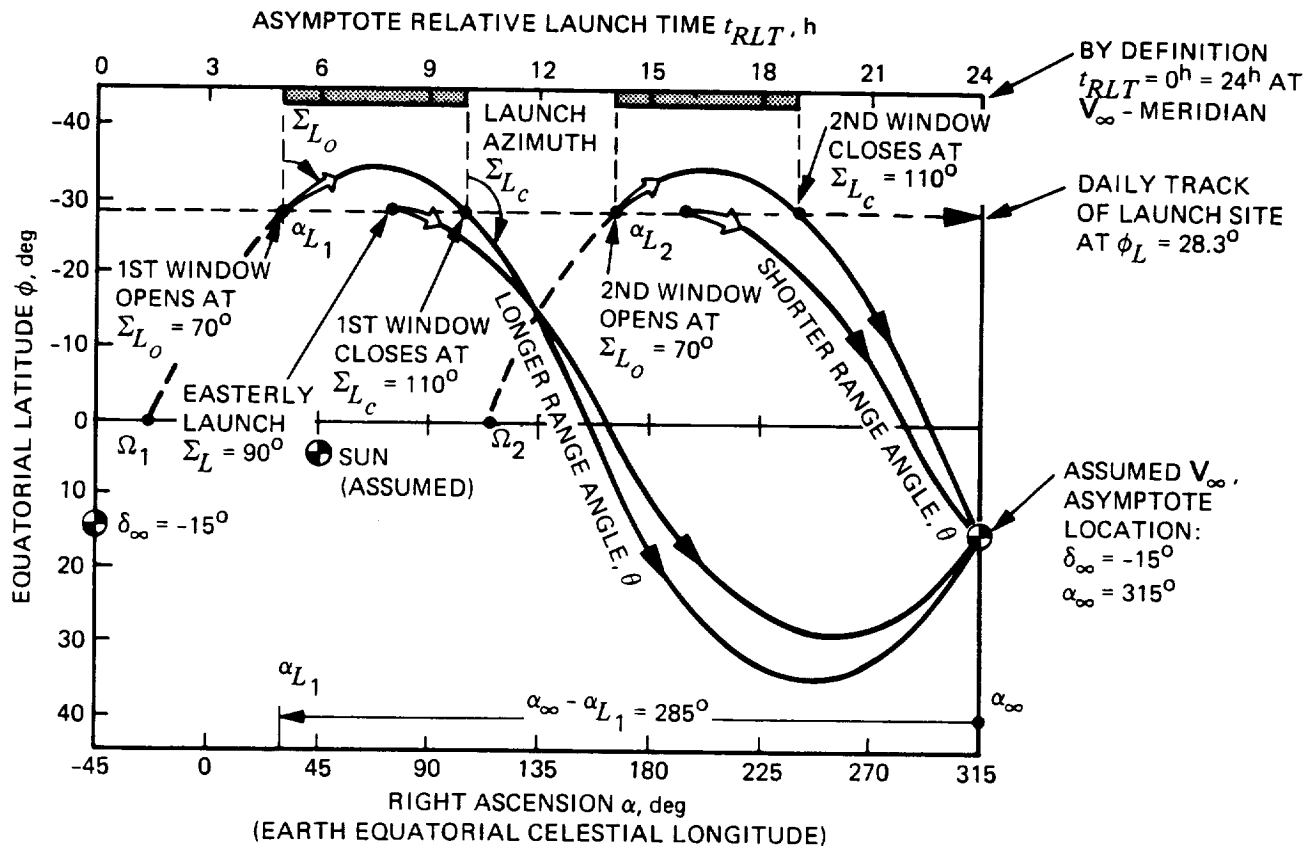


Fig. 14. Typical launch geometry example in celestial (inertial) Mercator coordinates

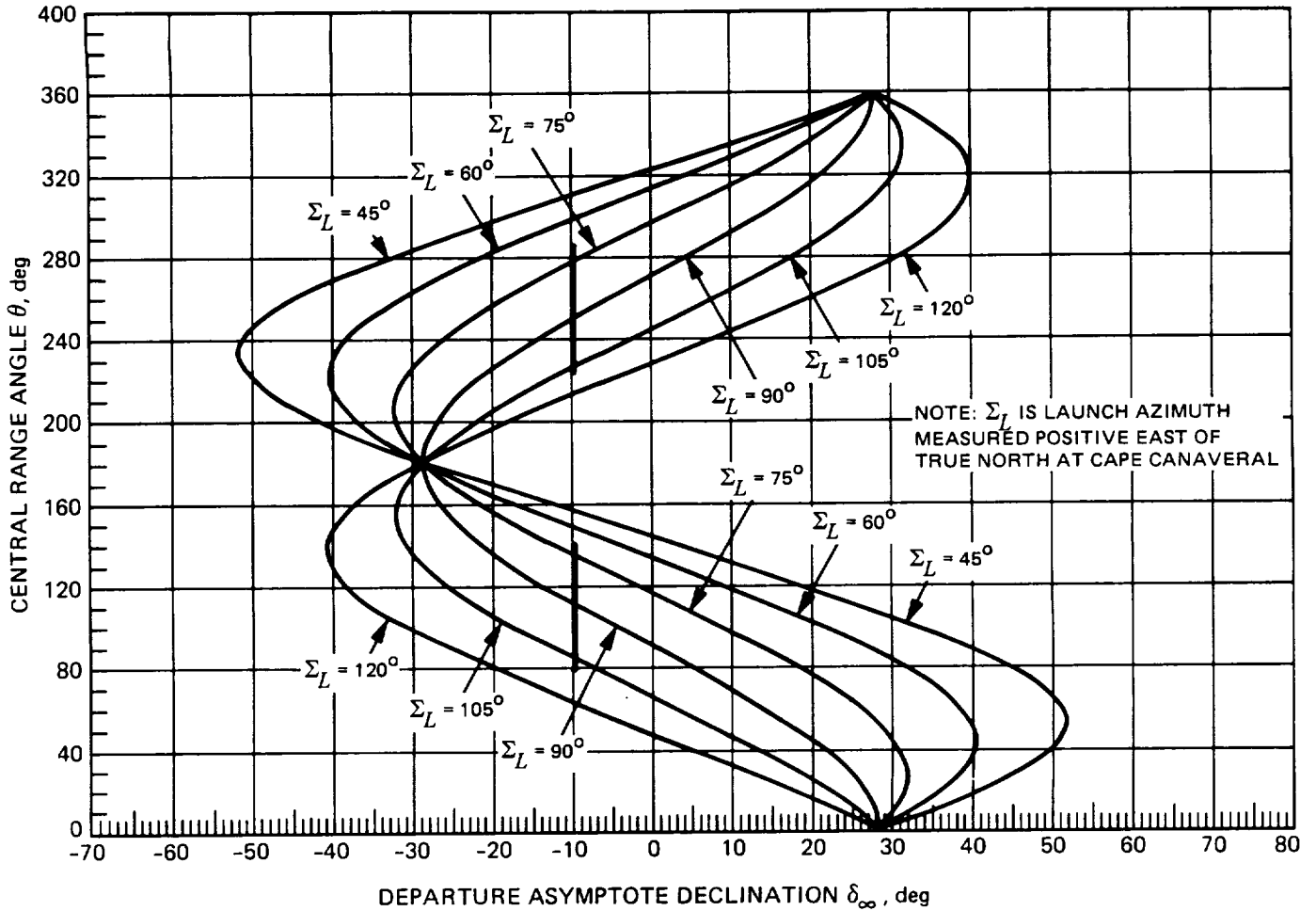


Fig. 15. Central range angle θ between launch site and outgoing asymptote direction vs its declination and launch azimuth. Pair of typical example launch windows for $\delta_{\infty} = -10$ deg shown by bold line segments (reproduced from Ref. 8).

$$\sin \Sigma_L = \frac{\cos \delta_{\infty} \times \sin (\alpha_{\infty} - \alpha_L)}{\sin \theta} \quad (19)$$

$$\cos \Sigma_L = \frac{\sin \delta_{\infty} - \cos \theta \times \sin \phi_L}{\sin \theta \times \cos \phi_L} \quad (20)$$

with the lighting conditions at lift-off and consequently allows a lighting profile analysis along the entire ascent arc.

The angle ZALS, displayed in Fig. 16, is defined as the angle between the departure V_{∞} vector and the Sun-to-Earth direction vector. It allows some judgment on available ascent lighting.

Figure 16 displays a 3-dimensional spatial view of the same typical launch geometry example shown previously in map format in Fig. 14. The difference in available range angles as well as orientation of the trajectory planes for the two daily launch opportunities clearly stands out. In addition, the figure illustrates the relationship between the "first" and "second daily" launch windows, defined in asymptote-relative time, t_{RLT} , as contrasted with "morning" or "night" launches, defined in launch-site-local solar time. The latter is associated

The length of the range angle required exhibits a complex behavior—the first launch window of the example in Figs. 14 and 16 offers a longer range angle than the second, but the second launch window opens up with a range angle so short that direct ascent into orbit is barely possible. Further launch delay shortens the range even further, forcing the acceptance of a very long coast (one full additional revolution in parking orbit) before transplanetary departure injection. A detailed analysis of required arc lengths for the various sub-arcs of the

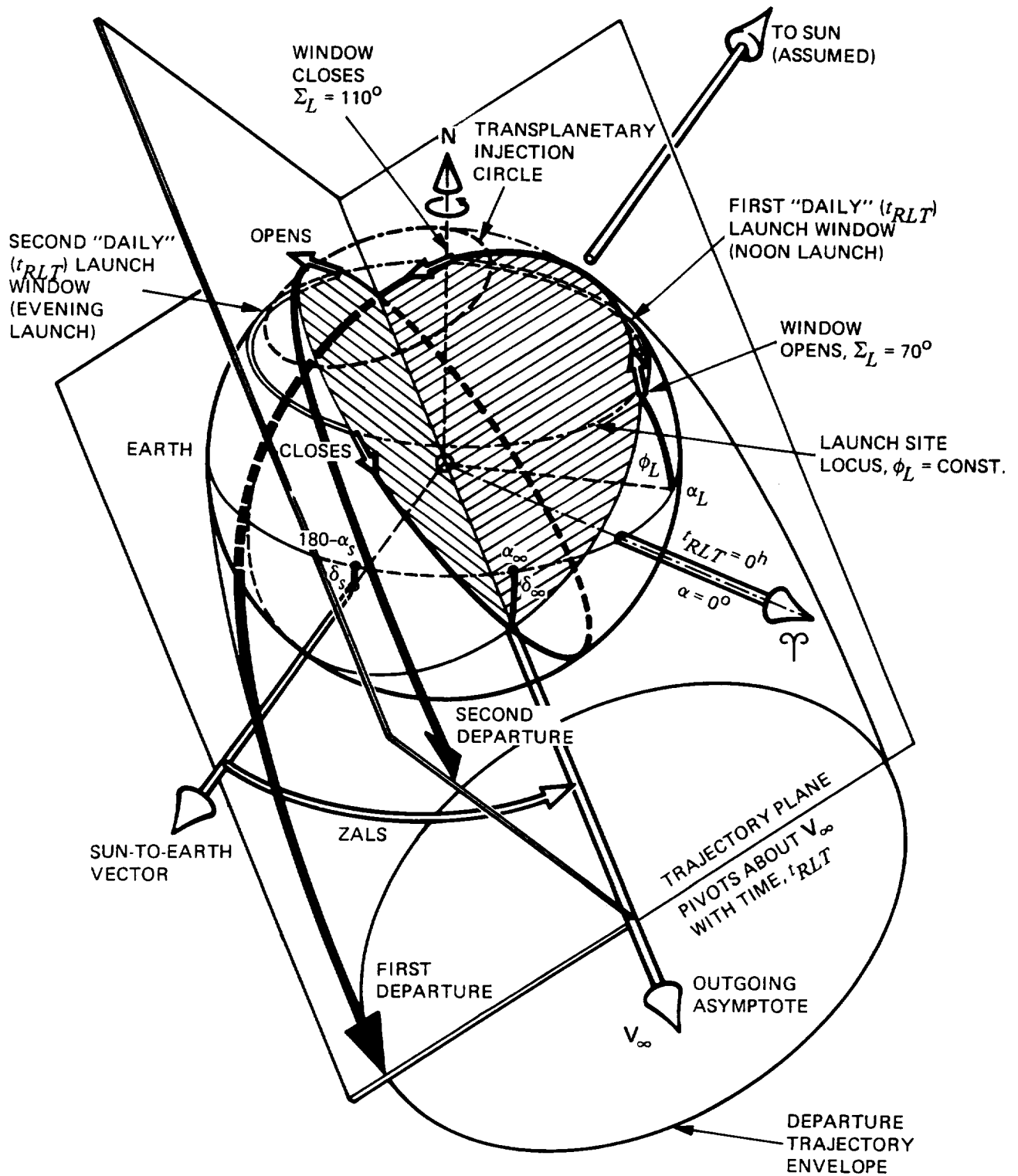
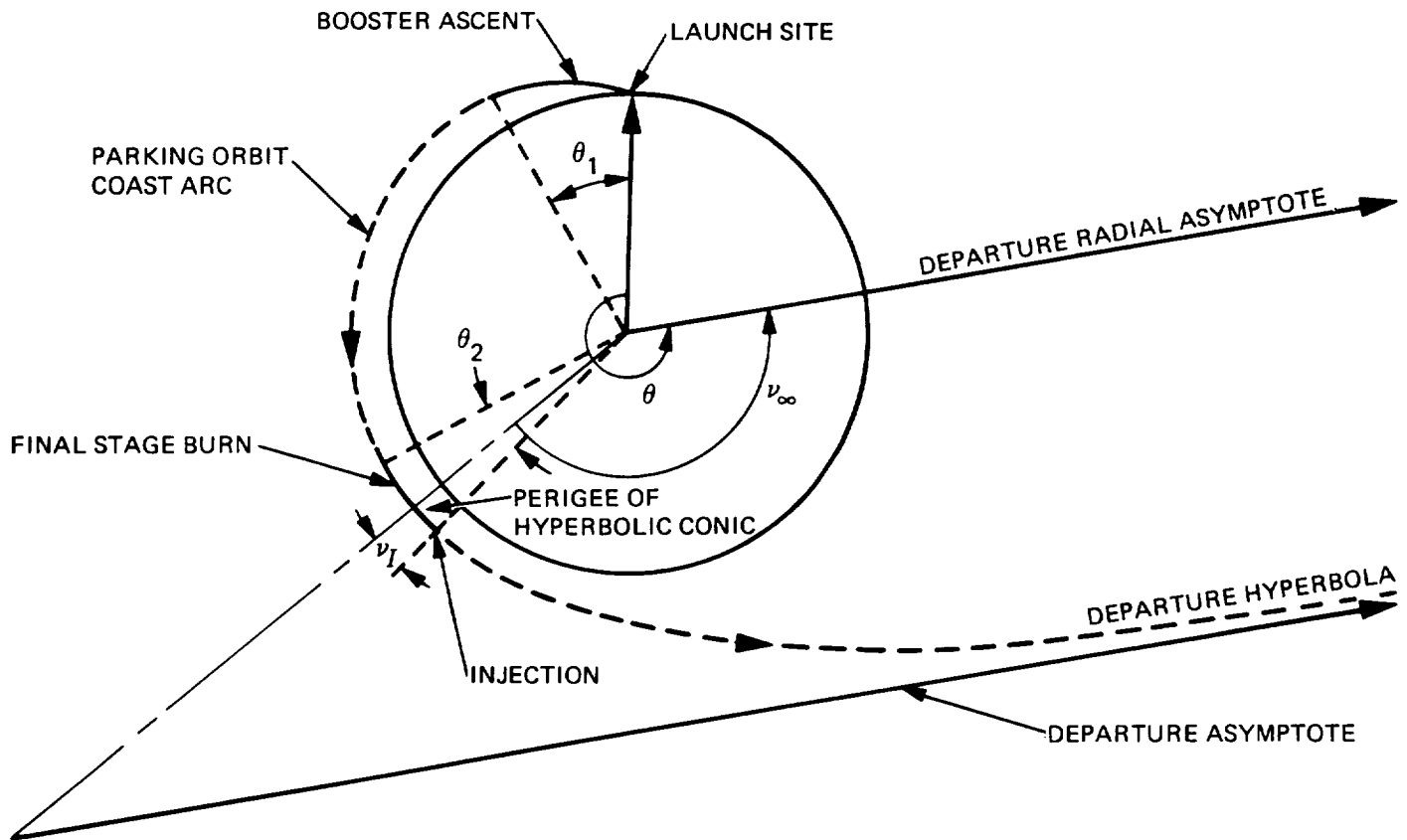


Fig. 16. Typical example of daily launch geometry (3-dimensional) as viewed by an outside observer ahead of the spacecraft



- θ_1 BURNING ARC OF BOOSTER VEHICLES INTO PARKING ORBIT
 θ_2 BURNING ARC OF FINAL STAGE THRUST
 θ RANGE ANGLE BETWEEN LAUNCH SITE AND DEPARTURE RADIAL ASYMPTOTE
 ν_∞ ANGLE BETWEEN PERIGEE AND DEPARTURE RADIAL ASYMPTOTE
 ν_I TRUE ANOMALY OF INJECTION

Fig. 17. Basic geometry of the launch and ascent profile in the trajectory plane (after Ref. 9)

departure trajectory is thus a trajectory design effort of paramount importance (Fig. 17)

3. **Range angle arithmetic.** For a viable ascent trajectory design, the range angle θ must first of all accommodate the twin burn arcs θ_1 and θ_2 , representing ascent into parking orbit and transplanetary injection burn into the departure hyperbola. In addition, it must also contain the angle from periape to the V_∞ direction, called "true anomaly of the asymptote direction" (Fig. 18):

$$\cos \nu_\infty = \frac{-1}{1 + \frac{C_3 \times r_p}{\mu_E}} \quad (21)$$

where:

r_p = periape radius, typically 6563 km, for a horizontal injection from a 185-km (100-nmi) parking orbit

μ_E = GM , gravitational parameter of Earth (refer to the Table of Constants, Section V).

The proper addition of these trajectory sub-arcs also requires adjustment for nonhorizontal injection (i.e., for the flight path angle $\gamma_I > 0$), especially significant on direct ascent missions (no coast arc) and missions with relatively low thrust/weight ratio injection stages. The adjustment is accomplished as follows:

$$\theta = \theta_1 + \theta_{COAST} + \theta_2 + \nu_\infty - \nu_I \quad (22)$$

where:

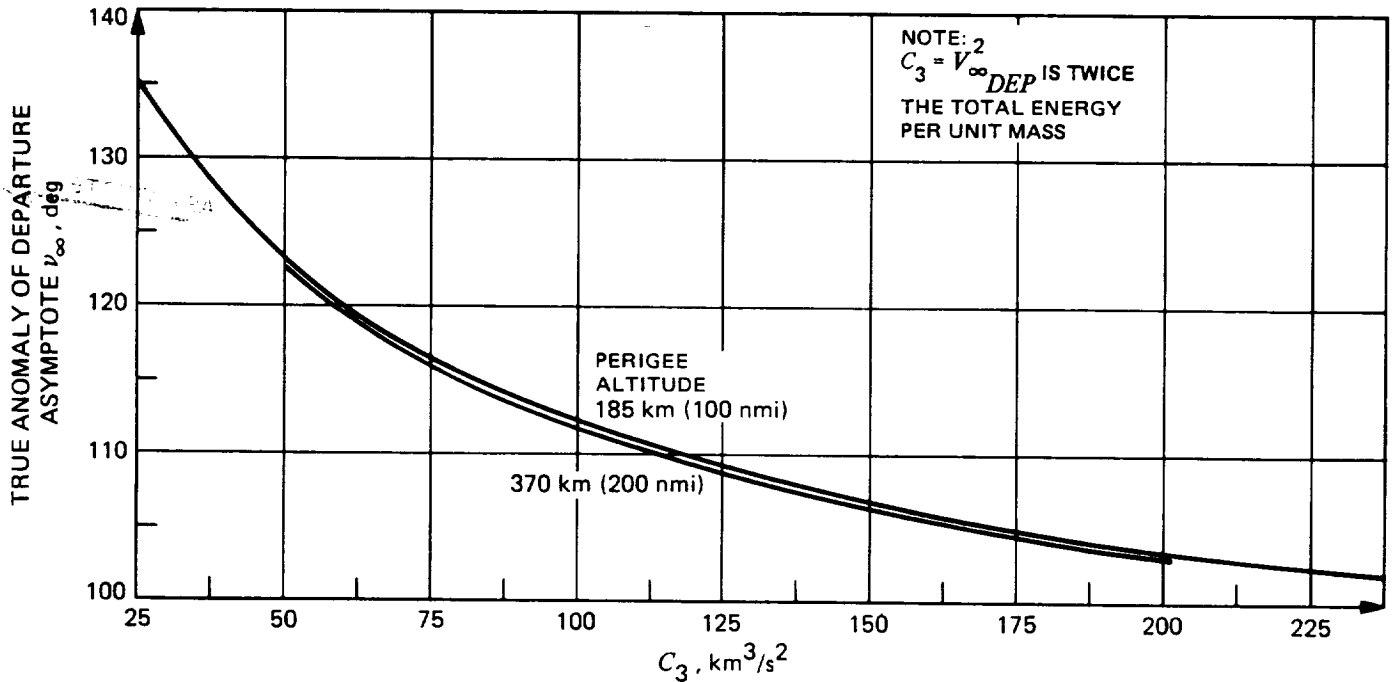


Fig. 18. Angle from perigee to departure asymptote

ν_I = is the true anomaly of the injection point, usually is near 0 deg, and can be computed by iteration using:

$$\tan \gamma_I = \frac{e_H \sin \nu_I}{1 + e_H \cos \nu_I} \quad (23)$$

γ_I = injection flight path angle above local horizontal, deg

e_H = eccentricity of the departure hyperbola:

$$e_H = 1 + \frac{C_3 \times r_p}{\mu_E} \quad (24)$$

To make Eq. (22) balance, the parking orbit coast arc, θ_{COAST} , must pick up any slack remaining, as shown in Fig. 17. A negative θ_{COAST} implies that the Σ_L -solution was too short-ranged. A direct ascent with positive injection true anomaly ν_I (i.e., upward climbing flight path angle, γ_I , at injection) with attendant sizable gravity losses, may be acceptable, or even desirable (within limits) for such missions. Alternately, the other solution for Σ_L , exhibiting the longer range angle θ , and thus a longer parking orbit coast, θ_{COAST} , should be implemented. An extra revolution in parking orbit may be a viable alternative. Other considerations, such as desire for a lightside launch and/or injection, tracking ship location and booster impact constraints, may all play a signif-

icant role in the ascent orbit selection. A limit on maximum coast duration allowed (fuel boil-off, battery life, guidance gyro drift, etc.) may also influence the long/short parking orbit decision. In principle, any number of additional parking orbit revolutions is permissible. Shuttle launches of interplanetary missions (e.g., Galileo) are in fact required to use such additional orbits for cargo bay door opening and payload deployment sequences. In such cases, however, the precessional effects of Earth's oblateness upon the parking orbit, primarily the regression of the orbital plane, must be considered.

4. Parking orbit regression. The average regression of the nodes (i.e., the points of spacecraft passage through the equator plane) of a typical direct (prograde) circular parking orbit of 28.3-deg inclination with the Earth's equator, due to Earth's oblateness, amounts to about 0.46 deg of westward nodal motion per revolution and can be approximately computed from

$$\dot{\Omega} = \frac{540^\circ \times r_s^2 \times J_2 \times \cos i}{r_o^2}, \text{ deg/revolution} \quad (25)$$

where

r_s = Earth equatorial surface radius, 6378 km

r_o = circular orbit radius, typically 6748 km for an orbital altitude of 370 km (200 nmi)

$$J_2 = 0.00108263 \text{ for Earth}$$

i = parking orbit inclination, deg. Can be computed for a given launch geometry from

$$\cos i = \cos \phi_L \times \sin \Sigma_L \quad (26)$$

This correction, multiplied by the orbital stay time of N revolutions, must be considered in determining a biased launch time and, hence, the right ascension of the launch site at lift-off:

$$\alpha_{L_{EFF}} = \alpha_L + \dot{\Omega} \times N, \text{ deg} \quad (27)$$

5. Dogleg ascent. Planar ascent has been considered exclusively, thus far. Reasons for performing a gradual powered plane change maneuver during ascent may be many. Inability to launch in a required azimuth direction because of launch site constraints is the prime reason for desiring a dogleg ascent profile. Other reasons may have to do with burn strategies or intercept of an existing orbiter by the ascending spacecraft, especially if its inclination is less than the latitude of the launch site. Doglegs are usually accomplished by a sequence of out-of-plane yaw turns during first- and second-stage burn, optimized to minimize performance loss and commencing as soon as possible after the early, low-altitude, high aerodynamic pressure phase of flight is completed, or after the necessary lateral range angle offset has been achieved.

By contrast, powered plane change maneuvers out of parking orbit or during transplanetary injection are much less efficient, as a much higher velocity vector must now be rotated through the same angle, but they may on occasion be operationally preferable.

As already discussed, a special geometric situation develops whenever the departure asymptote declination magnitude exceeds the latitude of the launch site, causing a "split azimuth" daily launch window. Figure 13 shows the effects of asymptote declination and range safety constraints upon the launch problem. As the absolute value of declination increases, it eventually reaches the safety constraint on azimuth, preventing any further planar launches. The situation occurs mostly early and/or late in the mission's departure launch period, and is frequently associated with dual launches, when month-long departure periods are desired.

The Shuttle-era Space Transportation System (STS), including contemplated upper stages, is capable of executing dogleg operations as well. These would, however, effectively reduce the launch vehicle's payload (or C_3) capability, as they did on expendable launch vehicles of the past.

6. Tracking and orientation. As the spacecraft moves away from the Earth along the asymptote, it is seen at a nearly constant declination—that of the departure asymptote, δ_∞ (DLA in the plotted data). The value of DLA greatly affects tracking coverage by stations located at various latitudes; highest daily spacecraft elevations, and thus best reception, are enjoyed by stations whose latitude is closest to DLA. Orbit determination, using radio doppler data, is adversely affected by DLA's near zero degrees.

The spacecraft orientation in the first few weeks is often determined by a compromise between communication (antenna pointing) and solar heating constraints. The Sun-spacecraft-Earth (SPE) angle, defined as the angle between the outgoing V -infinity vector and the Sun-to-Earth direction, is very useful and is presented in the plots under the acronym ZALS. It was defined in the discussion of Fig. 16. This quantity has many uses:

- (1) If the spacecraft is Sun-oriented, ZALS equals the Earth cone angle (CA), depicted in Fig. 19 (the cone

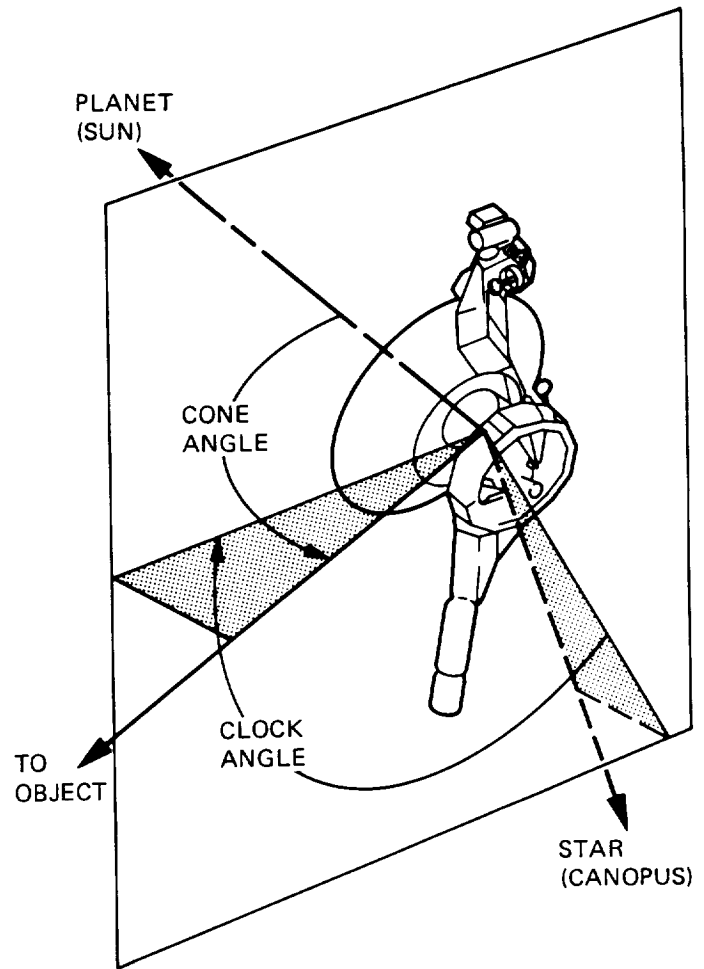


Fig. 19. Definition of cone and clock angle

angle of an object is a spacecraft-fixed coordinate, an angle between the vehicle's longitudinal -Z axis and the object direction).

- (2) The Sun-phase angle, Φ_S (phase angle is the Sun-object-spacecraft angle) describes the state of the object's disk lighting: a fully lit disk is at zero phase. For the Earth (and Moon), several days after launch, the sun-phase angle is:

$$\Phi_S = 180 - \text{ZALS} \quad (28)$$

- (3) The contour labeled $\text{ZALS} = 90^\circ$ separates two categories of transfer trajectories—those early departures that first cut inside Earth's orbit, thus starting out at negative heliocentric true anomalies for $\text{ZALS} > 90^\circ$, and those later ones that start at positive true anomalies, heading out toward Jupiter and never experiencing the increased solar heating at distances of less than 1 AU for $\text{ZALS} < 90^\circ$.

7. Post-launch spacecraft state. After the spacecraft has departed from the immediate vicinity of Earth (i.e., left the Earth's sphere of influence of about 1-2 million km), it moves on a heliocentric conic, whose initial conditions may be approximated as

$$\mathbf{V}_{S/C} = \mathbf{V}_{EARTH} + \mathbf{V}_\infty \quad (29)$$

$$\mathbf{R}_{S/C} = \mathbf{R}_{EARTH} + \mathbf{V}_{S/C} \times \Delta t \quad (30)$$

where \mathbf{R} and \mathbf{V} of Earth are evaluated from an ephemeris at time of injection and Δt represents time elapsed since then (in seconds). The \mathbf{V}_∞ vector in EME50 cartesian coordinates can be constructed using $\sqrt{C_3 L} = V_\infty$, $\text{DLA} = \delta_\infty$, and $\text{RLA} = \alpha_\infty$ in three components as follows:

$$\mathbf{V}_\infty = (V_\infty \times \cos \alpha_\infty \times \cos \delta_\infty, V_\infty \times \sin \alpha_\infty \times \cos \delta_\infty, V_\infty \times \sin \delta_\infty) \quad (31)$$

8. Orbital launch problem. Orbital launch from the Shuttle, from other elements of the STS, or from any temporary or permanent orbital space station complexes, introduces entirely new concepts into the Earth-departure problem. Some of the new constraints, already mentioned, limit our ability to launch a given interplanetary mission. The slowly regressing space station orbit (see Eq. 25) generally does not contain the V -infinity vector required at departure. Orbit lifetime or other considerations may dictate a space station's orbital altitude that may be too high for an efficient injection burn. Innovative departure strategies are beginning to emerge, attempting to alleviate these problems — a recent Science

Applications, Inc. (SAI) study (Ref. 10) points to some of the techniques available, such as passive wait for natural alignment of the continuously regressing space station orbit plane (driven by Earth's oblateness) with the required V -infinity vector, or the utilization of 2- and 3- impulse maneuvers, seeking to perform spacecraft plane changes near the apogee of a phasing orbit where velocity is lowest and thus turning the orbit is easiest. These two approaches can be combined with each other, as well as with other suitable maneuvers, such as:

- (1) Deep space propulsive burns for orbit shaping and phasing,
- (2) Gravity assist flyby, including Earth return ΔVEGA ,
- (3) Aerodynamic turns at grazing perigees or at intermediate planetary swingbys, and
- (4) Multiple revolution injection burns, requiring several low, grazing passes, combined with apogee plane change maneuvers, etc.

All of these devices can be optimized to permit satisfactory orbital launches, as well as to achieve the most desirable conditions at the final arrival body. In general, space launch advantages, such as on-orbit assembly and checkout of payloads and clustered multiple propulsion stages, or orbital construction of bulky and fragile subsystems (solar panels, sails, antennas, radiators, booms, etc.) will, it is hoped, greatly outweigh the significant deep-space mission penalties incurred because of the space station's inherent orbital orientation incompatibility with departure requirements.

D. Planetary Arrival Synthesis

The planetary arrival trajectory design problem involves satisfying the project's engineering and science objectives at the target body by shaping the arrival trajectory in a suitable manner. As these objectives may be quite diverse, only four illustrative scenarios shall be discussed in this section—flyby, orbiter, atmospheric probe, and, to a small extent, lander missions.

1. Flyby trajectory design. In this mission mode, the arrival trajectory is not modified in any deterministic way at the planet—the original aim point and arrival time are chosen to satisfy the largest number of potential objectives, long beforehand.

This process involves the choice of arrival date to ensure desirable characteristics, such as the values of the variables VHP, DAP, ZAPS, etc., presented in plotted form in the data section of this volume.

DAP, the planet-equatorial declination, δ_∞ , of the incoming asymptote, i.e., of the V -infinity vector, provides the measure of the minimum possible inclination of flyby. Its negative is also known as the latitude of vertical impact (LVI).

The magnitude of V -infinity, $VHP = |V_\infty|$, enables one to control the flyby turn angle $\Delta\psi$ between the incoming and outgoing V_∞ vectors by a suitable choice of closest approach (C/A) radius, r_p (see Fig. 20):

$$\Delta\psi = 180 - 2\rho, \text{ deg} \quad (32)$$

where ρ , the asymptote half-angle, is found from:

$$\cos \rho = \frac{1}{e} = \frac{1}{1 + \frac{V_{\infty}^2 r_p}{\mu_p}} \quad (33)$$

VHP also enables the designer to evaluate planetocentric velocity, V , at any distance, r , on the flyby hyperbola:

$$V = \sqrt{\frac{2\mu_p}{r} + V_\infty^2}, \text{ km/s} \quad (34)$$

In the above equations, μ_p (or GM_p), is the gravitational parameter of the arrival body.

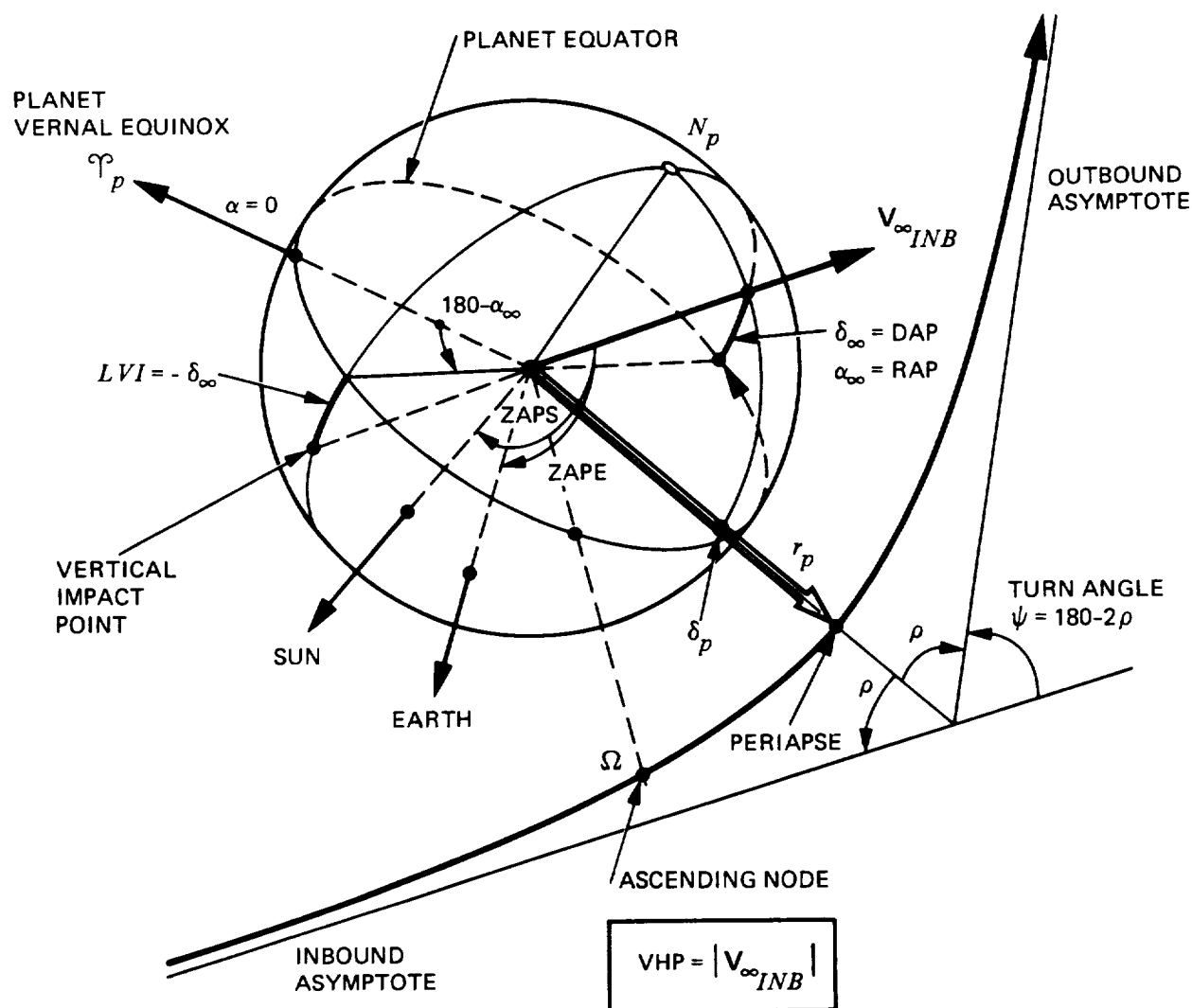


Fig. 20. Planetary flyby geometry

Another pair of significant variables on which to base arrival date selection are ZAPS and ZAPE—the angles between V_∞ and the planet-to-Sun and -Earth vectors, respectively. These two angles represent the cone angle (CA) of the planet during the far-encounter phase for a Sun- or an Earth-oriented spacecraft, in that order. ZAPS also determines the phase angle, Φ_S , of the planet's solar illumination, as seen by the spacecraft on its far-encounter approach leg to the planet:

$$\Phi_S = 180 - \text{ZAPS} \quad (35)$$

Both the cone angle and the phase angle have already been defined and discussed in the Earth departure section above.

The flyby itself is specified by the aim point chosen upon the arrival planet target plane. This plane, often referred to as the B -plane, is a highly useful aim point design tool. It is a plane passed through the center of a celestial body normal to V_∞ , the relative spacecraft incoming velocity vector at infinity. The incoming asymptote, i.e., the straight-line, zero-gravity extension of the V_∞ -vector, penetrates the B -plane at the aim point. This point, defined by the target vector B in the B -plane, is often described by its two components $B \cdot \hat{T}$ and $B \cdot \hat{R}$, where the axes \hat{T} and \hat{R} form an orthogonal set with V_∞ . The \hat{T} -axis is chosen to be parallel to a fundamental plane, usually the ecliptic (Fig. 21) or alternatively, the planet's equator. The magnitude of B equals the semi-minor axis of the flyby hyperbola, b , and can be related to the closest approach distance, also referred to as the periape radius, r_p , by

$$|B| = \frac{\mu_p}{V_\infty^2} \left(\left(1 + \frac{V_\infty^2 r_p}{\mu_p} \right)^2 - 1 \right)^{1/2}, \text{ km} \quad (36)$$

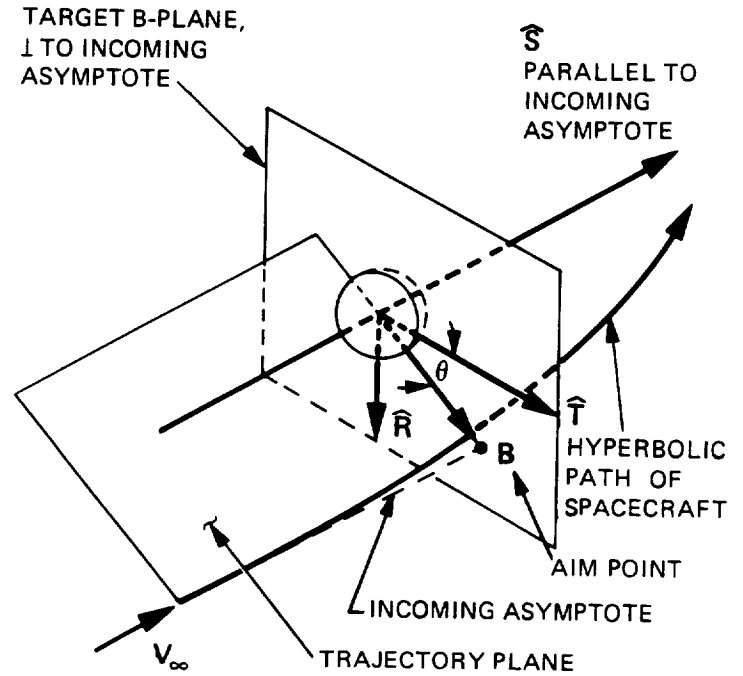
or

$$r_p = \frac{\mu_p}{V_\infty^2} + \left(\left(\frac{\mu_p}{V_\infty^2} \right)^2 + |B|^2 \right)^{1/2}, \text{ km} \quad (37)$$

The direction angle θ of the B -vector, B , measured in the target plane clockwise from the T -axis to the B -vector position can easily be related to the inclination, i , of the flyby trajectory, provided that both δ_∞ (DAP) and the T -axis, from which θ is measured clockwise, are defined with respect to the same fundamental plane to which the inclination is desired. For a system based on the planet equator (Fig. 22):

$$\cos i_{PEQ} = \cos \theta_{PEQ} \times \cos \delta_{\infty PEQ} \quad (38)$$

which assumes that θ_{PEQ} is computed with the T -axis parallel to the planet equator (i.e., $T_{PEQ} = V_\infty \times \text{POLE}_{PEQ}$), not the ecliptic, as is frequently assumed ($T_{ECL} = V_\infty \times \text{POLE}_{ECL}$). Care must be taken to use the θ angle as defined and intended.



- B MISS PARAMETER, $B\hat{S}$
(TARGET VECTOR)
- θ AIM POINT ORIENTATION
- \hat{S} PARALLEL TO INCOMING ASYMPTOTE, V_∞
- \hat{T} PARALLEL TO ECLIPTIC PLANE
AND \perp TO \hat{S}
- $\hat{R} = \hat{S} \times \hat{T}$

Fig. 21. Definition of target or arrival B -plane coordinates

The two systems of B -plane T -axis definition can be reconciled by a planar rotation, $-\Delta\theta$, between the ecliptic \hat{T} - and \hat{R} -axes and the \hat{T}' - and \hat{R}' -axis orientations of the equator based system

$$\tan \Delta\theta = \frac{\sin(\alpha_\infty - \alpha_{EP})}{\cos \delta_\infty \times \tan \delta_{EP} - \sin \delta_\infty \times \cos(\alpha_\infty - \alpha_{EP})} \quad (39)$$

where

α_{EP} and δ_{EP} are right ascension and declination of the ecliptic pole in planet equatorial coordinates. For Mars using constants in Section V:

$$\alpha_{EP} = 267.6227, \quad \delta_{EP} = 63.2838, \text{ deg}$$

α_∞ and δ_∞ are RAP and DAP, the directions of incoming V_∞ , also in planet equatorial coordinates.

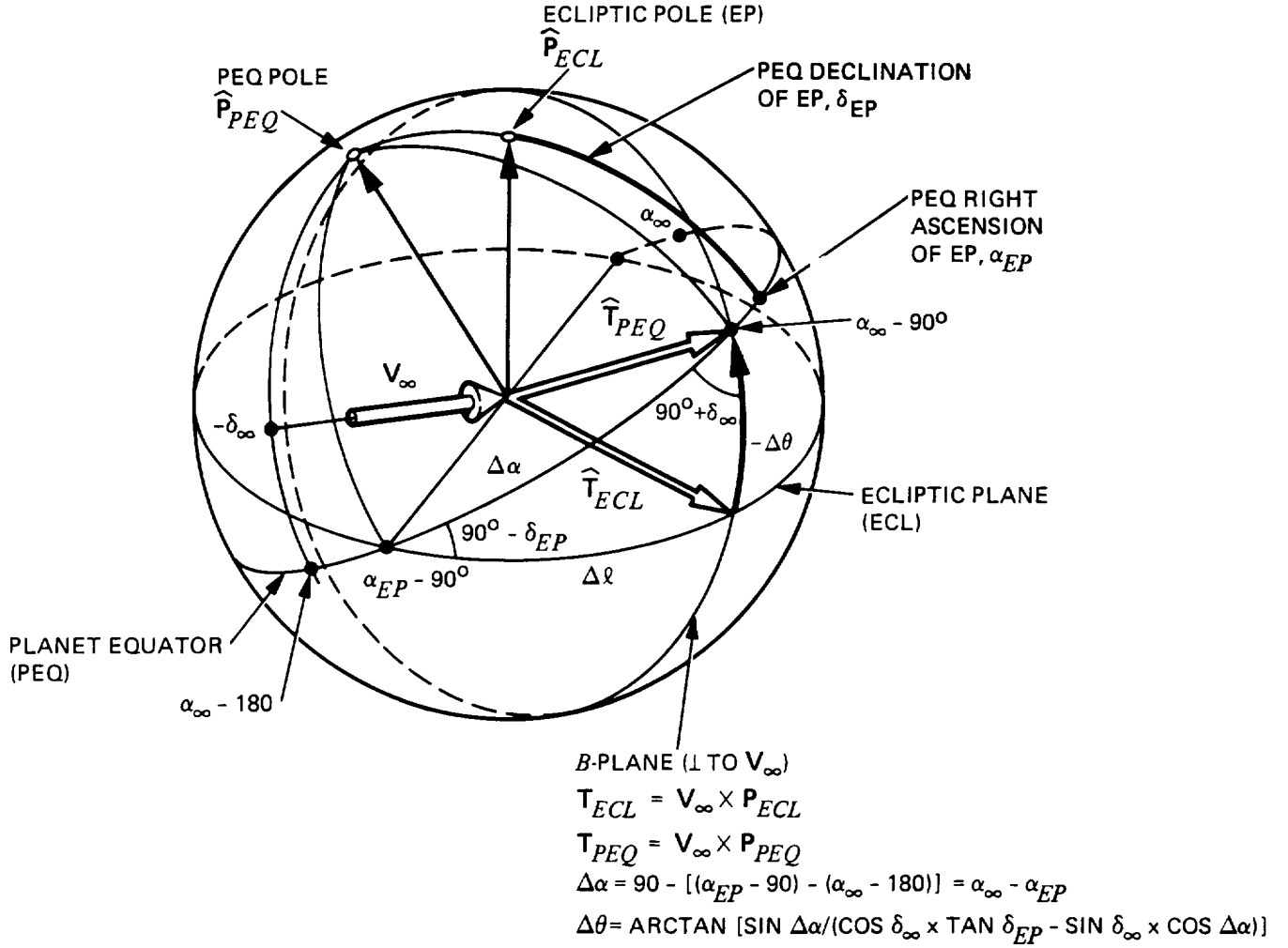


Fig. 22. Two \hat{T} -axis definitions in the arrival B -plane

The correction $\Delta\theta$ is applied to a θ angle computed in the ecliptic system as follows (Fig. 22):

$$\theta_{PEQ} = \theta_{ECL} + \Delta\theta \quad (40)$$

The ecliptic \hat{T} , \hat{R}_{ECL} axes, however, have to be rotated by $-\Delta\theta$ (clockwise direction is positive in the B -plane) to obtain planet equatorial \hat{T} , \hat{R}_{PEQ} coordinate axes. The B -magnitude of an aim point in either system is the same.

The projections of the Sun-to-planet and Earth-to-planet vectors into the B -plane represent aim point loci of diametric Sun and Earth occultations, respectively, as defined in Fig. 23. The B -plane θ -angles (with respect to \hat{T}_{ECL} axis) of these variables are presented and labeled ETSP and ETEP, respectively, in the plotted mission data. In addition to helping design or else avoid diametric occultations, these quantities allow computation of phase angles, Φ_i , of the planet at the spacecraft

periapse, at the entry point of a probe, or generally at any position r (subscript S = Sun, could be replaced by E = Earth, if desired), (see Fig. 24):

$$\begin{aligned} \cos \Phi_S = & -\cos \beta_\infty \times \cos ZAP_S - \sin \beta_\infty \times \sin ZAP_S \\ & \times \cos (ET_S P - \theta_{S/C}) \end{aligned} \quad (41)$$

where

- $\theta_{S/C}$ = the aim point angle in the B -plane, must be with respect to the same \hat{T} , as ETSP.
- β_∞ = the arrival range angle from infinity (a position far out on the incoming asymptote) to the point of interest r (Fig. 25).

The computation of the arrival range angle, β_∞ , to the position of the desired event depends on its type, as follows:

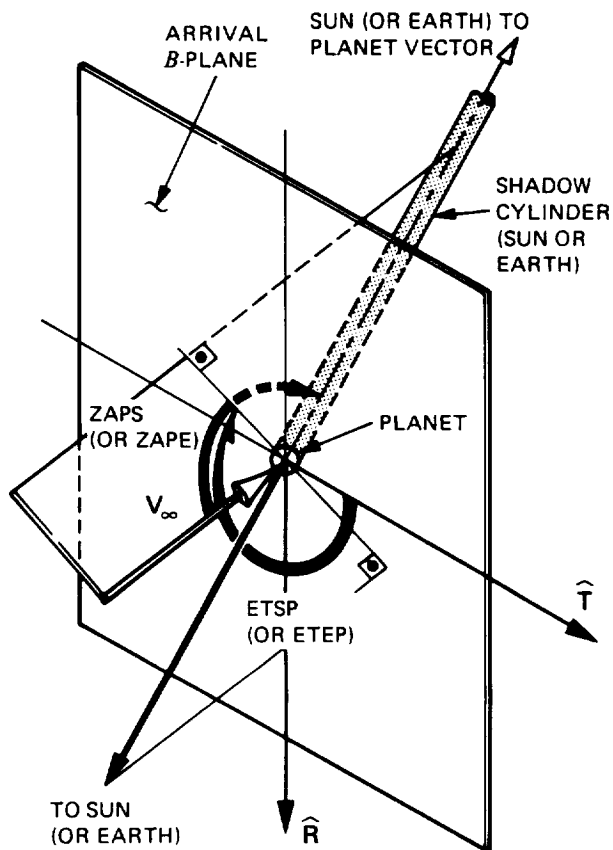


Fig. 23. Definition of approach orientational coordinates ZAPS and ETSP, ZAPE and ETEP

1. At flyby periapse, ($\beta_{\infty} \geq 90$ deg):

$$\cos \beta_{\infty} = \cos (-\nu_{\infty}) = \frac{-1}{1 + \frac{V_{\infty}^2 r_p}{\mu_p}} \quad (42)$$

(r_p is periapse radius).

2. At given radius r , anywhere on the flyby trajectory (see Fig. 25):

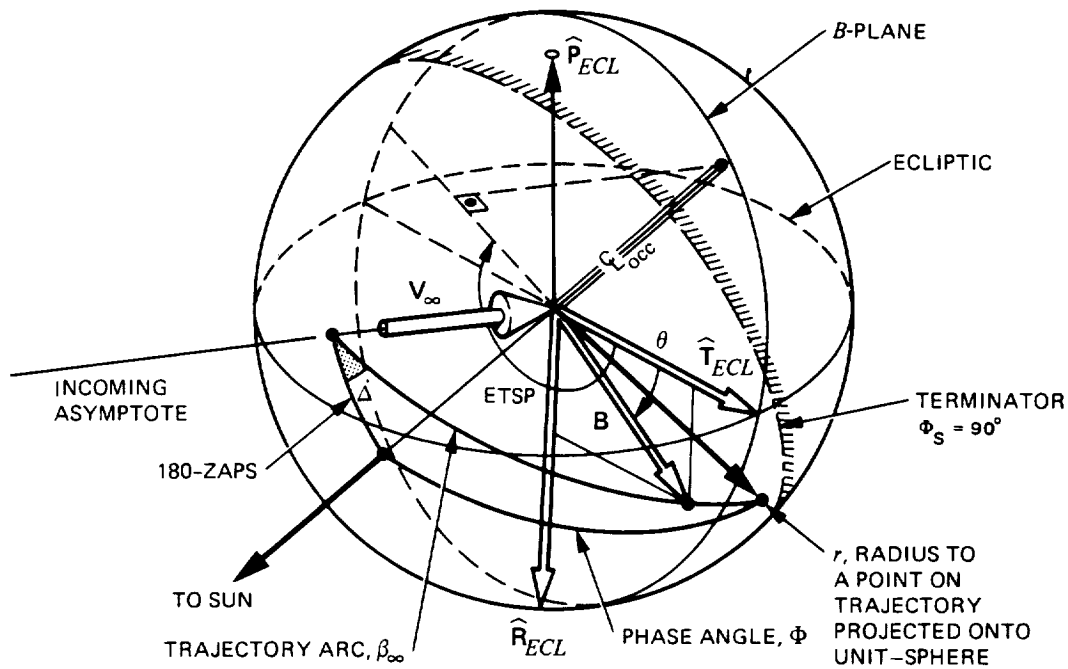
$$\beta_{\infty} = -\nu_{\infty} + \nu_r \quad (43)$$

v_∞ should be computed from periaepse equation, Eq. (42) v_r at r can be obtained from ($-v_\infty \leq v_r \leq +v_\infty$, v_r has negative values on the incoming branch):

$$\cos \nu_r = \frac{\frac{r_p}{r} \left(2 + \frac{r_p V_\infty^2}{\mu_p} \right) - 1}{\left(1 + \frac{r_p V_\infty^2}{\mu_p} \right)} \quad (44)$$

3. At the entry point having a specified flight path angle γ_E (Fig. 25):

$$\beta_{\infty} = -\nu_{\infty} + \nu_E \quad (45)$$



$$\Delta = \text{ETSP} - 180^\circ - \theta$$

Fig. 24. Phase angle geometry at arrival planet

ORIGINAL PAGE IS
OF POOR QUALITY

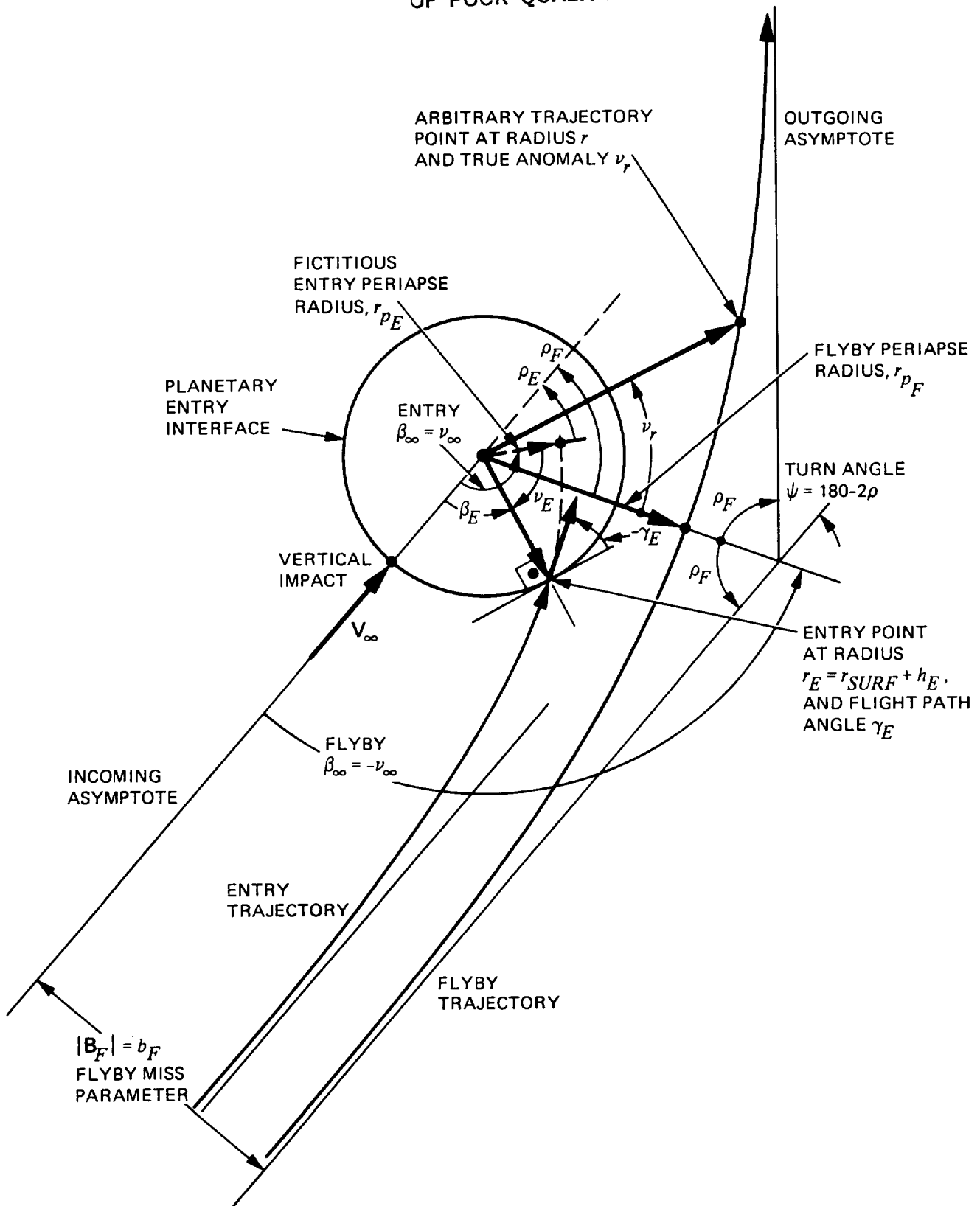


Fig. 25. Typical entry and flyby trajectory geometry

where ν_E is the true anomaly at entry, should always be negative, and can be computed if entry radius and altitude, $r_E = r_{SURF} + h_E$ and γ_E , the entry angle, are known:

$$\cos \nu_E = \frac{\frac{r_p}{r_E} \left(2 + \frac{r_p V_\infty^2}{\mu_p} \right) - 1}{\left(1 + \frac{r_p V_\infty^2}{\mu_p} \right)} \quad (46)$$

whereas the fictitious periape radius r_p for the entry, to satisfy γ_E at r_E , is equal to

$$r_p = \left(\frac{\mu_p}{V_\infty^2} \right) \left[-1 + \sqrt{1 + \left(\frac{V_\infty^2}{\mu_p} \right) r_E \cos^2 \gamma_E \left(2 + \frac{V_\infty^2}{\mu_p} r_E \right)} \right] \quad (47)$$

The B value corresponding to this entry point can be computed from Eq. (36), while the θ angle in the B -plane would depend on the desired entry latitude inclination, Eq. (38), or phase angle, Eq. (41).

The general flyby problem poses the least stringent constraints on a planetary encounter mission, thus allowing optimization choices from a large list of secondary parameters, such as satellite viewing and occultation, planetary fields and particle *in situ* measurements, special phase-angle effects, etc.

A review of the plotted handbook variables, required in the phase-angle equation (Eq. 41), shows that the greatest magnitude variations are experienced by the ZAPS angle, which is strongly flight-time dependent: the longer the trip, the smaller ZAPS. For low equatorial inclination, direct flyby orbits, this implies a steady move of the periape towards the lit side and, eventually, to nearly subsolar periapes for long missions. This also implies that on such flights the approach legs of the trajectory are facing the morning terminator or even the dark side, as trip time becomes longer, exhibiting large phase angles (recall that phase is the supplement of the ZAPS angle on the approach leg). This important variation is caused by a gradual shift of the incoming approach direction, as flight time increases, from the subsolar part of the target planet's leading hemisphere (in the sense of its orbital motion) to its antisolar part.

The arrival time choice on a very fine scale may greatly depend on the desire to observe specific atmospheric/surface features or to achieve close encounters with specific satellites of the arrival planet. Passages through special satellite event zones, e.g., flux tubes, wakes, geocentric and/or heliocentric

occultations, require close control of arrival time. The number of satellites passed at various distances also depends on the time of planet C/A. These fine adjustments do, however, demand arrival time accuracies substantially in excess of those provided by the computational algorithm used in this effort, which generated the subject data (accuracies of 1-5 min for events or 1-2 h for encounters would be required vs uncertainties of up to 1.5 days actually obtained with the rectilinear impact pseudo-state theorem). Numerically searched-in integrated trajectories, based on the information presented as a first guess input, are mandatory for such precision trajectory work.

Preliminary design considerations for penetrating, grazing, or avoiding a host of planet-centered fields and particle structures, such as magnetic fields, radiation belts, plasma tori, ring and debris structures, occultations by Sun, Earth, stars, or satellites, etc., can all be presented on specialized plots, e.g., the B -plane, and do affect the choice of suitable aim point and arrival time. All of these studies require the propagation of a number of flyby trajectories. Adequate initial conditions for such efforts can be found in the handbook as: VHP (V_∞) and DAP (δ_∞) already defined, as well as RAP (α_∞), the planet equatorial right ascension of the incoming asymptote (i.e., its east longitude from the ascending node of the planet's mean orbital plane on its mean equator, both of date). The designer's choice of the aim point vector, either as B and θ , or as cartesian $\mathbf{B} \cdot \hat{\mathbf{T}}$ and $\mathbf{B} \cdot \hat{\mathbf{R}}$, completes the input set. Suitable programs generally exist to process this information.

2. Capture orbit design. The capture problem usually involves the task of determining what kind of spacecraft orbit is most desired and the interconnected problem of how and at what cost such an orbit may be achieved. A scale of varying complexity may be associated with the effort envisioned—an elliptical long period orbit with no specific orientation at the trivial end of the scale, through orbits of controlled or optimized lines of apsides (i.e., periape location), nodes, inclination, or a safe perturbed orbital altitude. Satellite G/A-aided capture, followed by a satellite tour, involving multiple satellite G/A encounters on a number of revolutions, each designed to achieve specific goals, probably rates as the most complex capture orbit class. Some orbits are energetically very difficult to achieve, such as close circular orbits, but all require significant expenditures of fuel. As maneuvers form the background to this subject a number of useful orbit design concepts shall be presented to enable even an unprepared user to experiment with the data presented.

The simplest and most efficient mode of orbit injection is a coplanar burn at a common periape of the arrival hyperbola and the resulting capture orbit (Fig. 26). The maneuver ΔV required is:

$$\Delta V = \sqrt{V_{\infty}^2 + \frac{2\mu_p}{r_p}} - \sqrt{\frac{2\mu_p \times r_A}{r_p(r_A + r_p)}} \quad \text{km/s} \quad (48)$$

The orbital period for such an orbit, requiring knowledge of periapse and apoapse radii, r_p and r_A , is

$$P = 2\pi \sqrt{\left[\frac{r_A + r_p}{2}\right]^3 / \mu_p} \quad \text{s} \quad (49)$$

If on the other hand, a known orbit period P (in seconds) is desired, the expression for ΔV is

$$\Delta V = \sqrt{V_{\infty}^2 + \frac{2\mu_p}{r_p}} - \sqrt{\frac{2\mu_p}{r_p} - 3\sqrt{\left(\frac{2\mu_p \times \pi}{P}\right)^2}} \quad (50)$$

A plot of orbit insertion ΔV required as a function of r_p and P (using Eq. 50) is presented in Fig. 27. The apoapse radius of such an orbit of given period would be

$$r_A = \sqrt[3]{\frac{2\mu_p \times P^2}{\pi^2}} - r_p \quad \text{km} \quad (51)$$

An evaluation of Eq. (50) (and Fig. 27) shows that lowest orbit insertion ΔV is obtained for the lowest value of r_p , the longest period P , and the lowest V_{∞} of arrival.

Of some interest is injection into circular capture orbits, a special case of the coapsidal insertion problem. It can be shown (Ref. 9) that an optimal ΔV exists for insertion into capture orbits of constant eccentricity, including $e = 0$, i.e., circular orbits, which would require a specific radius:

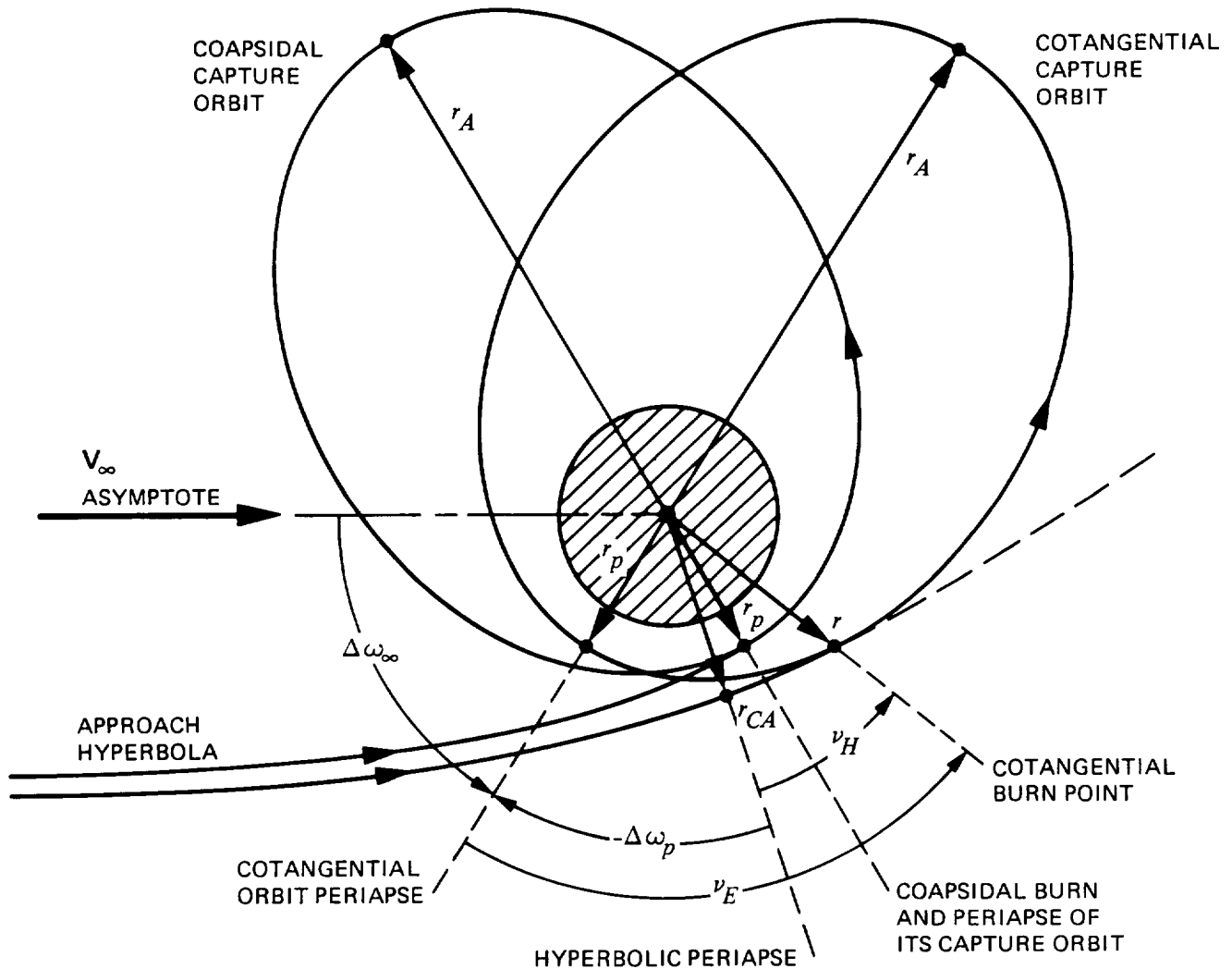


Fig. 26. Coapsidal and cotangential capture orbit insertion geometries

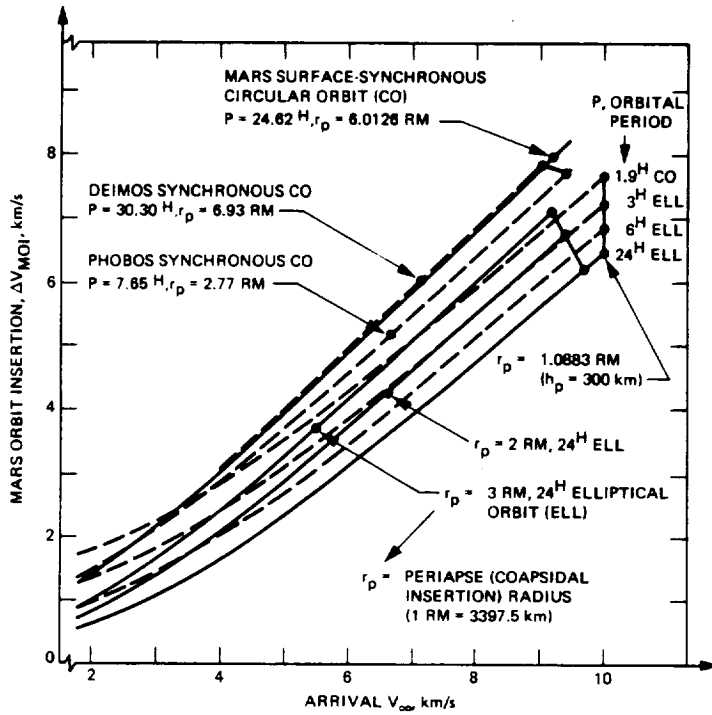


Fig. 27. Coapsidal capture orbit insertion maneuver ΔV requirements for Mars (using Eq. 50)

$$r_{CO} = \frac{2\mu_p}{V_\infty^2} \quad (52)$$

while the corresponding optimal value for ΔV would be

$$\Delta V_{CO} = \frac{V_\infty}{\sqrt{2}} \quad (53)$$

Frequently the orbital radius obtained by use of Eq. (52) is incompatible with practical injection aspects or with arrival planet science and engineering objectives.

A more general coplanar mode of capture orbit insertion, requiring only tangentiality of the two trajectories at an arbitrary maneuver point of radius r common to both orbits, Fig. 26, requires a propulsive effort of

$$\Delta V = \sqrt{V_\infty^2 + \frac{2\mu_p}{r}} - \sqrt{\frac{2\mu_p(r_A + r_p - r)}{r(r_A + r_p)}} \quad (54)$$

It can be clearly seen that by performing the burn at periastron the substitution $r = r_p$ brings us back to Eq. (48).

The cotangential maneuver mode provides nonoptimal control over the orientation of the major axis of the capture orbit. If it is desired to rotate this line of apsides clockwise by

$|\Delta\omega_p|$, one can solve for the hyperbolic periastron r_{CA} and the burn radius r using selected values of true anomaly at hyperbolic burn point ν_H and its capture orbit equivalent

$$\nu_E = \nu_H + \Delta\omega_p \quad (55)$$

utilizing the following three equations (where E and H stand for elliptic and hyperbolic, respectively):

$$\frac{\sin \nu_H}{\sin \nu_E} = \frac{r_{CA} \left(\frac{r_{CA} V_\infty^2}{\mu_p} + 2 \right) \times (r_A - r_p)}{2 r_A r_p \left(1 + \frac{r_{CA} V_\infty^2}{\mu_p} \right)} \quad (56)$$

and

$$r = \frac{r_{CA} \left(\frac{r_{CA} V_\infty^2}{\mu_p} + 2 \right)}{\left(1 + \frac{r_{CA} V_\infty^2}{\mu_p} \right) \cos \nu_H + 1} \quad (57)$$

$$= \frac{2 r_A}{\left(\frac{r_A}{r_p} + 1 \right) + \left(\frac{r_A}{r_p} - 1 \right) \cos \nu_E} \quad (58)$$

The procedure of obtaining a solution to these equations is iterative. For a set of given values for r_A , r_p , and an assumed $\Delta\omega$, a set of ν_H and ν_E , the hyperbolic and elliptical burn point true anomalies which would satisfy Eqs. (55-58) can be found. This in turn leads to r , the maneuver point radial distance, and hence, ΔV (Eq. 54). A plot of ΔV cost for a set of consecutive $\Delta\omega_p$ choices will provide the lowest ΔV value for this maneuver mode.

For an optimal insertion into an orbit of an arbitrary major axis orientation one must turn to the more general, still coplanar, but intersecting (i.e., nontangential burn point) maneuver (see Fig. 28). It provides sufficient flexibility to allow numerical optimization of ΔV with respect to apsidal rotation, $\Delta\omega_p$.

A more appropriate way to define apsidal orientation is to measure the post-maneuver capture orbit periastron position angle with respect to a fixed direction, e.g., a far encounter point on the incoming asymptote, $-V_\infty$, thus defining a capture orbit periastron range angle

ORIGINAL PAGE IS
OF POOR QUALITY

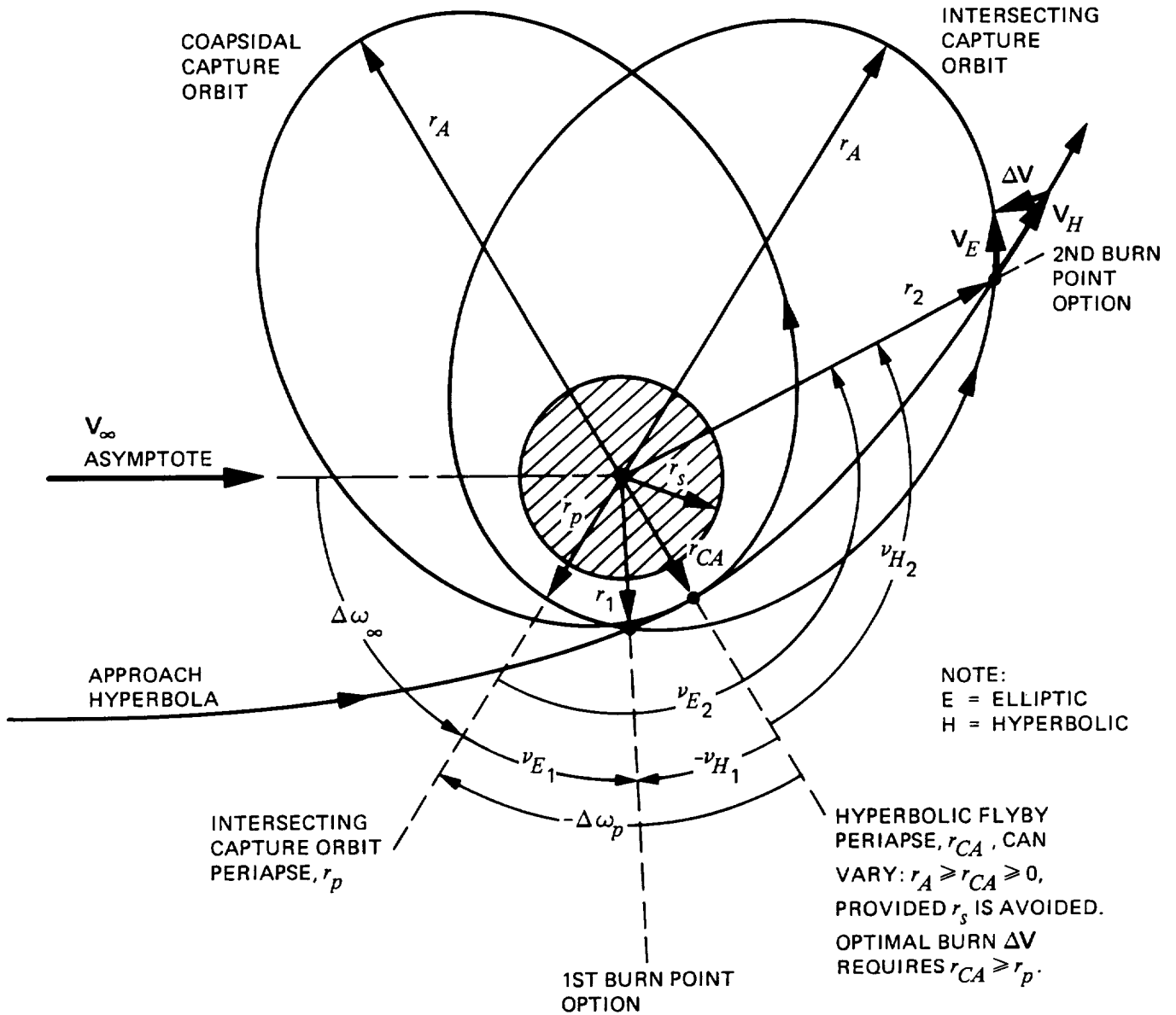


Fig. 28. Coapsidal and intersecting capture orbit insertion geometries

$$\begin{aligned}\Delta\omega_{\infty} &= \Delta\omega_p + \nu_{\infty} \\ &= \Delta\omega_p + \arccos\left(\frac{-1}{1 + \frac{V_{\infty}^2 r_p}{\mu_p}}\right)\end{aligned}\quad (59)$$

Taken from Ref. 9, the expression for the intersecting burn ΔV is:

$$\Delta V^2 = V_{\infty}^2 + 2\mu_p \left[\frac{2}{r} - \frac{1}{r_A + r_p} \right] - \frac{2}{r^2} \sqrt{\frac{2\mu_p}{r_A + r_p}} \times Q$$

where

$$Q = \left\{ \sqrt{r_A \times r_p \times r_{CA} [2\mu_p + r_{CA} V_{\infty}^2]} + \delta \sqrt{[2\mu_p (r - r_{CA}) + V_{\infty}^2 (r^2 - r_{CA}^2)] (r - r_p) (r_A - r)} \right\} \quad (60)$$

r = planet-centered radius at burn, $r_A \geq r \geq r_{CA}$, km

r_A and r_p = apoapse and periapse radii of capture ellipse

r_{CA} = closest approach radius of flyby hyperbola

δ = flag: $\delta = +1$ if injection occurs on same leg (inbound or outbound) of both hyperbola and capture ellipse, $\delta = -1$ if not.

It should be pointed out that Eq. (57) and (58) still apply in the intersecting insertion case, while Eq. (56) does not (as it assumes orbit tangency at burn point).

The evaluation of intersecting orbit insertion is more straightforward than it was for the cotangential case. By assuming V_∞ and orbit size (e.g., $V_\infty = 3$ km/s, $r_p = 1.0883$ RM, $P = 24$ hours, a typical capture orbit) and stepping through a set of values for v_E , the capture orbit burn point true anomaly, one obtains, using Eqs. (57–60), a family of curves, one for each value of R_{CA} , the hyperbolic closest approach distance. As shown in Fig. 29, the envelope of these curves provides the optimal insertion burn ΔV for any value of apsidal rotation $\Delta\omega_\infty$ desired. The plot also shows clearly that cotangential and apsidal insertion burns are energetically inferior to burns on the envelope locus. For the same assumed capture orbit, a family of optimal insertion envelopes, for a range of values of arrival V_∞ , is presented in Fig. 30.

The location of periaipse with respect to the subsolar point is of extreme importance to many mission objectives. It can be controlled by choice of departure and arrival dates, by ΔV expenditure at capture orbit insertion, by an aerodynamic maneuver during aerobraking, by depending on the planet's motion around the Sun to move the subsolar point in a manner optimizing orbital science, or by using natural perturbations and making a judicious choice of orbit size, equatorial inclination, i , and initial argument of periapsis, ω_0 , such as to cause regression of the node, $\dot{\Omega}$, and the advance of periapsis, $\dot{\omega}$, both due to oblateness to move the orbit in a desired manner or at a specific rate. Maintenance of Sun-synchronism could provide constant lighting phase angle at periaipse, etc., by some or all of these techniques. For an elliptical capture orbit (Fig. 31)

$$\dot{\Omega} = \frac{-3}{2} \times \frac{R_S^2 n J_2}{p^2} \cos i \times \frac{180}{\pi}, \text{ deg/s} \quad (61)$$

$$\dot{\omega} = \frac{3}{2} \times \frac{R_S^2 n J_2}{p^2} (2 - (5/2) \sin^2 i) \times \frac{180}{\pi}, \text{ deg/s} \quad (62)$$

where

$$n = \sqrt{\frac{\mu_P}{a^3}}, \text{ mean orbital motion, rad/s} \quad (63)$$

$$a = \frac{r_A + r_P}{2}, \text{ semi-major axis of elliptical orbit, km} \quad (64)$$

$$p = \frac{2 r_A r_P}{r_A + r_P}, \text{ semi-latus rectum of elliptical orbit, km} \quad (65)$$

R_S = Equatorial surface radius of Mars, km

J_2 = Oblateness coefficient of Mars (for values see Section V on constants).

For the example orbit (1.0883×10.733 RM) used in Figs. 29 and 30, if near equatorial, the regression of the node and advance of periaipse, computed using Eqs. (61–65), would amount to -0.272 and $+0.543$ deg/day, respectively. For contrast, for a grazing ($a = 3697.5$ km) low-inclination, near-circular orbit, the regression of the node would race along at -11.34 deg/day, while periaipse would advance at 22.68 deg/day; i.e., it would take 15.87 days for the line of apsides to do a complete turn.

It should be noted that $\dot{\Omega} = 0$ occurs for $i = 90$ deg, while $\dot{\omega} = 0$ is found for $i = 63.435$ deg. Sun-synchronism of the node is achieved by retrograde polar orbits, e.g., 1.0883 RM circular orbit should be inclined 92.649 deg.

3. Entry probe and lander trajectory design. Entry trajectory design is on one hand concerned with maintenance of acceptable probe entry angles and low relative velocity with respect to the rotating atmosphere. On the other hand, the geometric relationship of entry point, subsolar point and Earth (or relay spacecraft) is of paramount importance.

Lighting during entry and descent is often considered the primary problem to be resolved. As detailed in the flyby and orbital sections above, the choice of trip time affects the value of the ZAPS angle which in turn moves the entry point for longer missions closer to the subsolar point and even beyond, towards the morning terminator.

Landers or balloons, regardless of deceleration mode, prefer the morning terminator entry point which provides a better chance for vapor-humidity experiments, and allows a longer daylight interval for operations following arrival.

The radio-link problem, allowing data flow directly to Earth, or via another spacecraft in a relay role, is very complex. It could require studies of the Earth phase angle at the entry locations or alternately, it could require detailed parametric

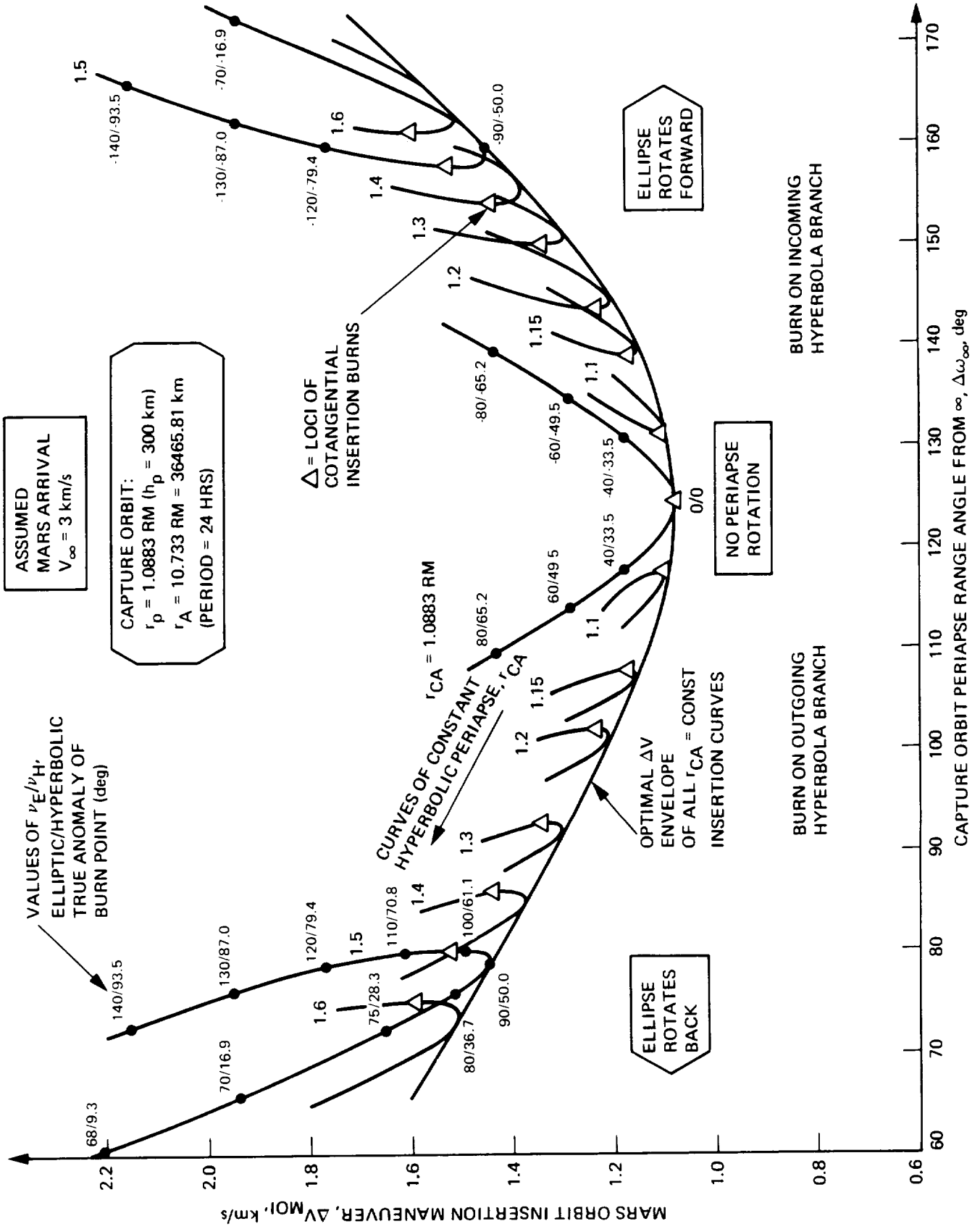


Fig. 29. Characteristics of intersecting capture orbit insertion and construction of optimal burn envelope at Mars

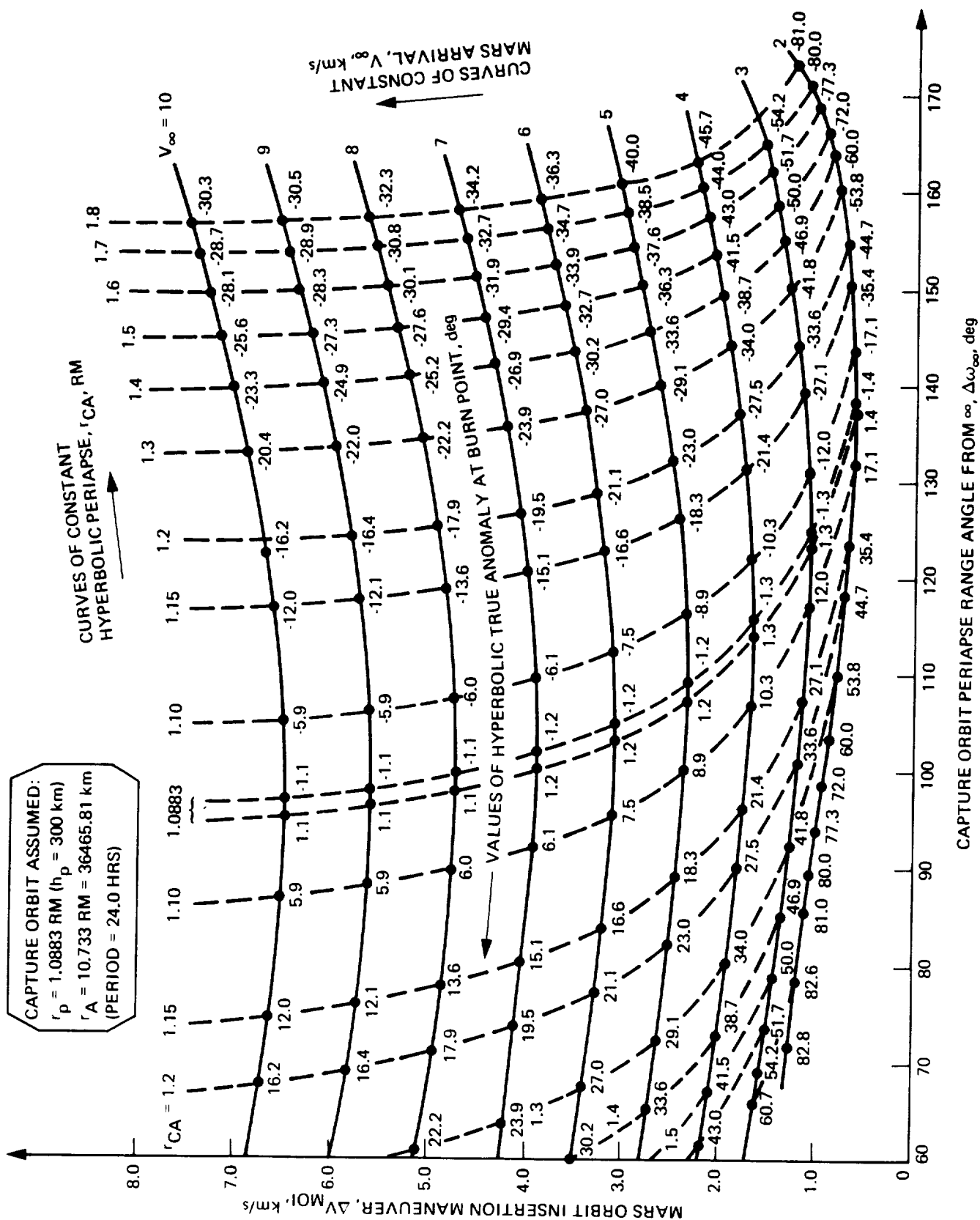


Fig. 30. Minimum ΔV required for insertion into Mars capture orbit of given apsidal orientation

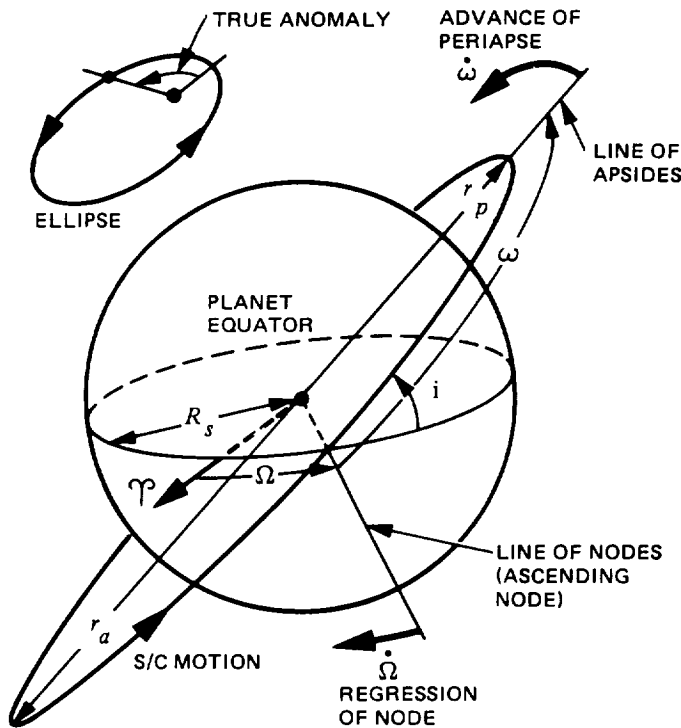


Fig. 31. General satellite orbit parameters and precessional motion due to oblateness coefficient J_2 (from Ref. 9)

studies involving relative motions of probe and relay spacecraft throughout probe entry and its following slow descent.

Balloon missions could also involve consideration of a variety of wind drift models, and thus, are even more complex as far as the communications problem with the Earth or the spacecraft is concerned.

E. Launch Strategy Construction

The constraints and desires, briefly discussed above, may be displayed on the mission space launch/arrival day plot as being limited by the contour boundaries of C_3L , the dates, DLA, VHP, ZAP, etc., thus displaying the allowable launch space.

Within this launch space a preferred day-by-day launch strategy must be specified, in accordance with prevailing objectives. The simplest launch strategy, often used to maintain a constant arrival date at the target planet, results in daily launch points on a horizontal line from leftmost to rightmost maximum allowable C_3L boundary for that arrival date. Such a strategy makes use of the fact that most arrival characteristics may stay nearly constant across the launch space. Lighting and satellite positions in this case are fixed, thus allowing a similar encounter, satellite G/A, or satellite tour.

A different choice of strategy could be to follow a contour line of some characteristic, such as DLA or ZAP. One could also follow the minimum value locus of a parameter, e.g., C_3L (i.e., the boundary between Class 1 and 2 within Type I or II) for each launch date, throughout the launch space.

Fundamentally different is a launch strategy for a dual or multiple spacecraft mission, involving more than one launch, either of which may possibly pursue divergent objectives. As an example, Fig. 32 shows the Voyagers 1 and 2 launch strategy, plotted on an Earth departure vs Saturn arrival date plot. A 14-day pad turnaround separation between launches was to be maintained, a 10-day opportunity was to be available for each launch, and the two spacecraft had substantially different objectives at Jupiter and Saturn—one was to be Io-intensive and a close Jupiter flyby, to be followed by a close Titan encounter at Saturn, and the other was Ganymede- and/or Callisto-intensive, a distant Jupiter flyby, as a safety precaution against Jovian radiation damage, aimed to continue past Saturn to Uranus and Neptune. Here, even the spacecraft departure order was reversed by the strategy within the launch space.

Launch strategies for orbital departures from a space station in a specific orbit promise to introduce new dimensions into mission planning and design. New concepts are beginning to emerge on this subject e.g., Refs. 10 and 11.

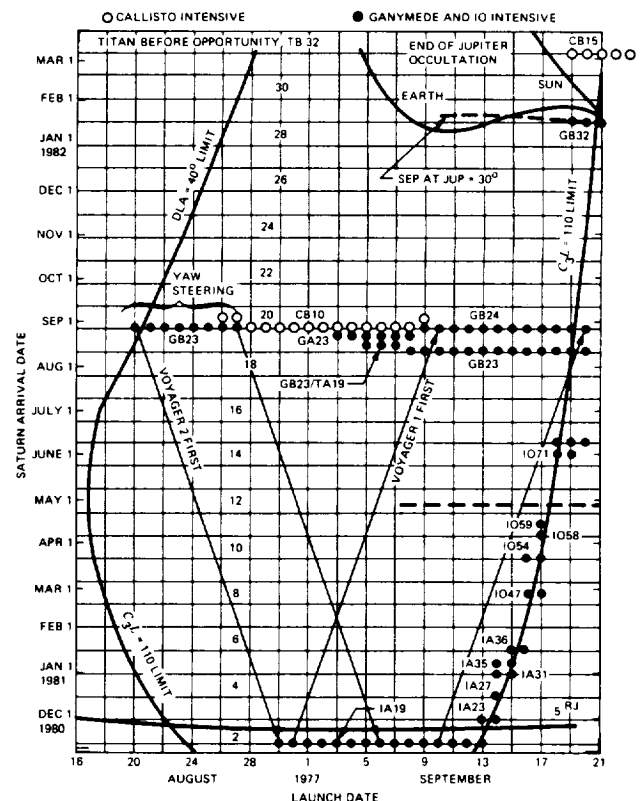


Fig. 32. Voyager (MJS77) trajectory space and launch strategy

IV. Description of Trajectory Characteristics Data

A. General

The data represent trajectory performance information plotted in the departure date vs arrival date space, thus defining all possible direct ballistic transfer trajectories between the two bodies within the time span considered for each opportunity. Twelve individual parameters are contour-plotted. The first, C_3L , is plotted bold on a Time of Flight (TFL) background; the remaining ten variables are plotted with bold contouring on a faint C_3L background. Eleven plots are presented for each of eight mission opportunities between 1990 and 2005.

The individual plots are labeled in the upper outer corner by bold logos displaying an acronym of the variable plotted, the mission's departure year, and a symbol of the target planet. These permit a quick and fail-safe location of desired information.

B. Definition of Departure Variables

C_3L : Earth departure energy (km^2/s^2); same as the square of departure hyperbolic excess velocity $V_\infty^2 = C_3L = V_I^2 - 2\mu_E/R_I$, where

V_I = conic injection velocity (km/s).

$R_I = R_S + h_I$, injection radius (km), sum of surface radius $R_{S\text{PLANET}}$ and injection altitude h_I , where R_{SEARTH} refers to Earth's surface radius. (For value, see Section V on constants.)

μ_E = gravitational constant times mass of the launch body (for values, refer to Section V on constants).

C_3L must be equal to or exceeded by the launch vehicle capabilities.

DLA: $\delta_{\infty L}$, geocentric declination (vs mean Earth equator of 1950.0) of the departure V_∞ vector. May impose launch constraints (deg).

RLA: $\alpha_{\infty L}$, geocentric right ascension (vs mean Earth equator and equinox of 1950.0) of the departure V_∞ vector. Can be used with C_3L and DLA to compute a heliocentric initial state for trajectory analysis (deg).

ZALS: Angle between departure V_∞ vector and Sun-Earth vector. Equivalent to Earth-probe-Sun angle several days out (deg).

C. Definition of Arrival Variables

VHP. $V_{\infty A}$, planetocentric arrival hyperbolic excess velocity or V -infinity (km/s), the magnitude of the

vector obtained by vectorial subtraction of the heliocentric planetary orbital velocity from the spacecraft arrival heliocentric velocity. It represents planet-relative velocity at great distance from target planet, at beginning of far encounter. Can be used to compute spacecraft velocity at any point r of flyby, including C/A (periapse) distance r_p :

$$V = \sqrt{V_\infty^2 + \frac{2\mu_p}{r}}, \text{ km/s}$$

where

$\mu_{P(MARS\text{ SYSTEM})}$ = gravitational parameter GM of the arrival planet system – Mars plus all satellites. (For values, refer to Section V on constants.)

DAP: $\delta_{\infty A}$, planetocentric declination (vs mean planet equator of date) of arrival V_∞ vector. Defines lowest possible flyby/orbiter equatorial inclination (deg).

RAP: $\alpha_{\infty A}$, planetocentric right ascension (vs mean planet equator and equinox of date, i.e., RAP is measured in the planet equator plane from ascending node of the planet's mean orbit plane on the planetary equator, both of date). Can be used together with VHP and DAP to compute an initial flyby trajectory state, but requires B -plane aim point information, e.g., B and θ (deg).

ZAPS: Angle between arrival V_∞ vector and the arrival planet-to-Sun vector. Equivalent to planet-probe-Sun angle at far encounter; for subsolar impact would be equal to 180 deg. Can be used with ETSP, VHP, DAP, and θ to determine solar phase angle at periapse, entry, etc. (deg).

ZAPE: Angle between arrival V_∞ vector and the planet-to-Earth vector. Equivalent to planet-probe-Earth angle at far encounter (deg).

ETSP: Angle in arrival B -plane, measured from T -axis*, clockwise to projection of Sun-to-planet vector. Equivalent to solar occultation region centerline direction in B -plane (deg).

ETEP: Angle in arrival B -plane, measured from T -axis*, clockwise, to projection of Earth-to-planet vector. Equivalent to Earth occultation region centerline direction in B -plane (deg).

*ETSP and ETEP plots are based on T -axis defined as being parallel to ecliptic plane (see text for explanation).

V. Table of Constants

Constants used to generate the information presented are summarized in this section.

A. Sun

$$GM = 132,712,439,935. \text{ km}^3/\text{s}^2$$

$$R_{\text{SURFACE}} = 696,000. \text{ km}$$

B. Earth/Moon System

$$GM_{\text{SYSTEM}} = 403,503.253 \text{ km}^3/\text{s}^2$$

$$GM_{\text{EARTH}} = 398,600.448 \text{ km}^3/\text{s}^2$$

$$J_2 = 0.00108263$$

$$R_{\text{EARTH SURFACE}} = 6378.140 \text{ km}$$

C. Mars System

$$GM_{\text{SYSTEM}} = 42.828.287 \text{ km}^3/\text{s}^2$$

$$J_2_{\text{MARS}} = 0.001965$$

Direction of the Martian planetary equatorial north pole (in Earth Mean Equator of 1950.0 coordinates):

$$\alpha_p = 317.342 \text{ deg}, \quad \delta_p = 52.711 \text{ deg}$$

Planet and Satellites	GM , km^3/s^2	Surface Radius, km	Mean Orbit Radius,* km	Period, hours
Mars (alone)	42,828.286	3397.5	–	24.6229621
Phobos	0.00066	$13.5 \times 10.7 \times 9.6$	9374	7.6538444
Deimos	0.00013	$7.5 \times 6.0 \times 5.5$	23457	30.2985774

*Computed from period and Mars GM , rounded.

D. Sources

The constants represent the DE-118 planetary ephemeris (Ref. 12) and Mariner 9/Viking trajectory reconstruction data. Definition of the Earth's equator (EME50.0) is consistent with Refs. 13–14, but would require minor adjustments for the new equator and equinox, epoch of J2000.0 (Ref. 15).

Acknowledgments

The contributions, reviews, and suggestions by members of the Handbook Advisory Committee, especially those of K. T. Nock, P. A. Penzo, W. I. McLaughlin, W. E. Bollman, R. A. Wallace, D. F. Bender, D. V. Byrnes, L. A. D'Amario, T. H. Sweetser, and R. E. Diehl, graphic assistance by Nanette Yin, as well as the computational and plotting algorithm development effort by R. S. Schlaifer are acknowledged and greatly appreciated. The authors would like to thank Mary Fran Buehler, Paulette Cali, Douglas Maple, and Michael Farquhar for their editorial contribution.

References

1. Sergeyevsky, A. B., "Mission Design Data for Venus, Mars, and Jupiter Through 1990," *Technical Memorandum 33-736*, Vols. I, II, III, Jet Propulsion Laboratory, Pasadena, Calif., Sept. 1, 1975.
2. Clarke, V. C., Jr., Bollman, W. E., Feitis, P. H., Roth, R. Y., "Design Parameters for Ballistic Interplanetary Trajectories, Part II: One-way Transfers to Mercury and Jupiter," *Technical Report 32-77*, Jet Propulsion Laboratory, Pasadena, Calif., Jan. 1966.

3. Snyder, G. C., Sergeyevsky, A. B., Paulson, B. L., "Planetary Geometry Handbook," *JPL Publication 82-44*, (in preparation).
4. Ross, S., *Planetary Flight Handbook*, NASA SP-35, Vol. III, Parts 1, 5, and 7, Aug. 1963 - Jan. 1969.
5. Wilson, S. W., "A Pseudostate Theory for the Approximation of Three-Body Trajectories," AIAA Paper 70-1061, presented at the AIAA Astrodynamics Conference, Santa Barbara, Calif., Aug. 1970.
6. Byrnes, D. V., "Application of the Pseudostate Theory to the Three-Body Lambert Problem," AAS Paper 79-163, presented at the AAS/AIAA Astrodynamics Conference, Provincetown, Mass., June 1979.
7. Sergeyevsky, A. B., Byrnes, D. V., D'Amario, L. A., "Application of the Rectilinear Impact Pseudostate Method to Modeling of Third-Body Effects on Interplanetary Trajectories," AIAA Paper 83-0015, presented at the AIAA 21st Aerospace Sciences Meeting, Reno, Nev., Jan. 1983.
8. Clarke, V. C., Jr., "Design of Lunar and Interplanetary Ascent Trajectories," *Technical Report 32-30*, Jet Propulsion Laboratory, Pasadena, Calif., March 15, 1962.
9. Kohlhasse, C. E., Bollman, W. E., "Trajectory Selection Considerations for Voyager Missions to Mars During the 1971-1977 Time Period," JPL Internal Document EPD-281, Jet Propulsion Laboratory, Pasadena, Calif., Sept. 1965.
10. Anonymous, "Assessment of Planetary Mission Performance as Launched From a Space Operations Center," Presented by Science Applications, Inc. to NASA Headquarters, Feb. 1, 1982.
11. Beerer, J. G., "Orbit Change Requirements and Evaluation," JPL Internal Document 725-74, Jet Propulsion Laboratory, Pasadena, Calif., March 9, 1982.
12. Newhall, XX, Standish, E. M., and Williams, J. G., "DE-102: A Numerically Integrated Ephemeris of the Moon and Planets, Spanning 44 Centuries," *Astronomy and Astrophysics*, 1983 (in press).
13. *Explanatory Supplement to the Ephemeris*, Her Majesty's Stationery Office, London, 1961.
14. Sturms, F. M., *Polynomial Expressions for Planetary Equators and Orbit Elements With Respect to the Mean 1950.0 Coordinate System*, Technical Report 32-1508, pp. 6-9, Jet Propulsion Laboratory, Pasadena, Calif., Jan. 15, 1971.
15. Davies, M. E., et al., "Report of the IAU Working Group on Cartographic Coordinates and Rotational Elements of the Planets and Satellites: 1982," *Celestial Mechanics*, Vol. 29, No. 4, pp. 309-321, April 1983.

Mission Design Data Contour Plots

**Earth to Mars Ballistic
Mission Opportunities 1990–2005**

Earth to Mars

1990

Opportunity

ENERGY MINIMA

	VALUE	TYPE	DEPARTURE (YEAR/MONTH/DAY)	ARRIVAL (YEAR/MONTH/DAY)
C ₃ L	17.780	I	90/08/29	91/03/18
C ₃ L	14.389	II	90/09/10	91/10/05
VHP	2.3281	I	90/08/27	91/05/24
VHP	2.3958	II	90/07/13	91/05/17

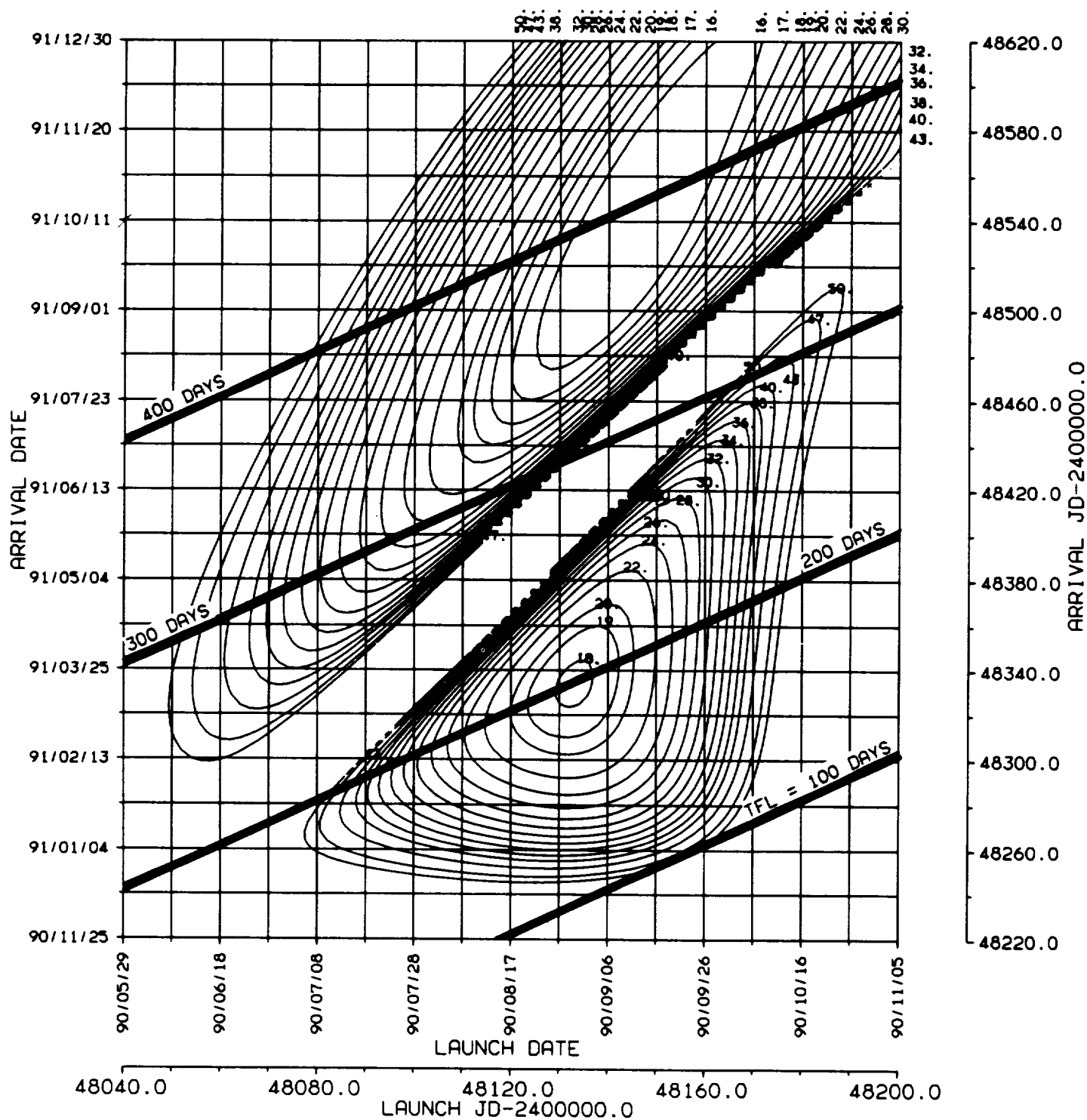
PRECEDING PAGE BLANK NOT FILMED

1.
C3L
♂
1990

ORIGINAL PAGE IS
OF POOR QUALITY

EARTH - MARS 1990 , C3L , TFL

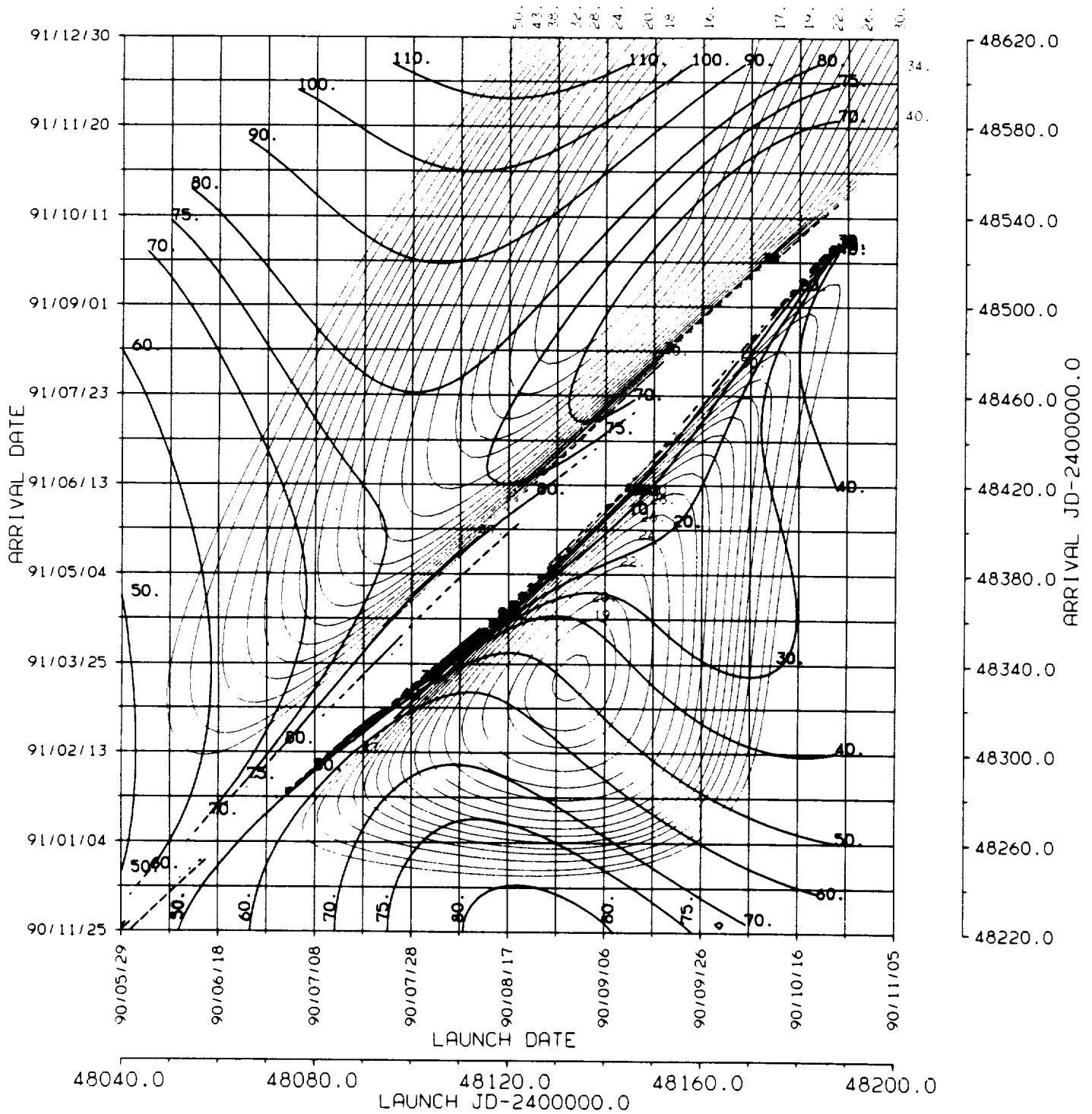
* BALLISTIC TRANSFER TRAJECTORY



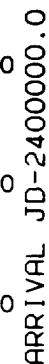
*



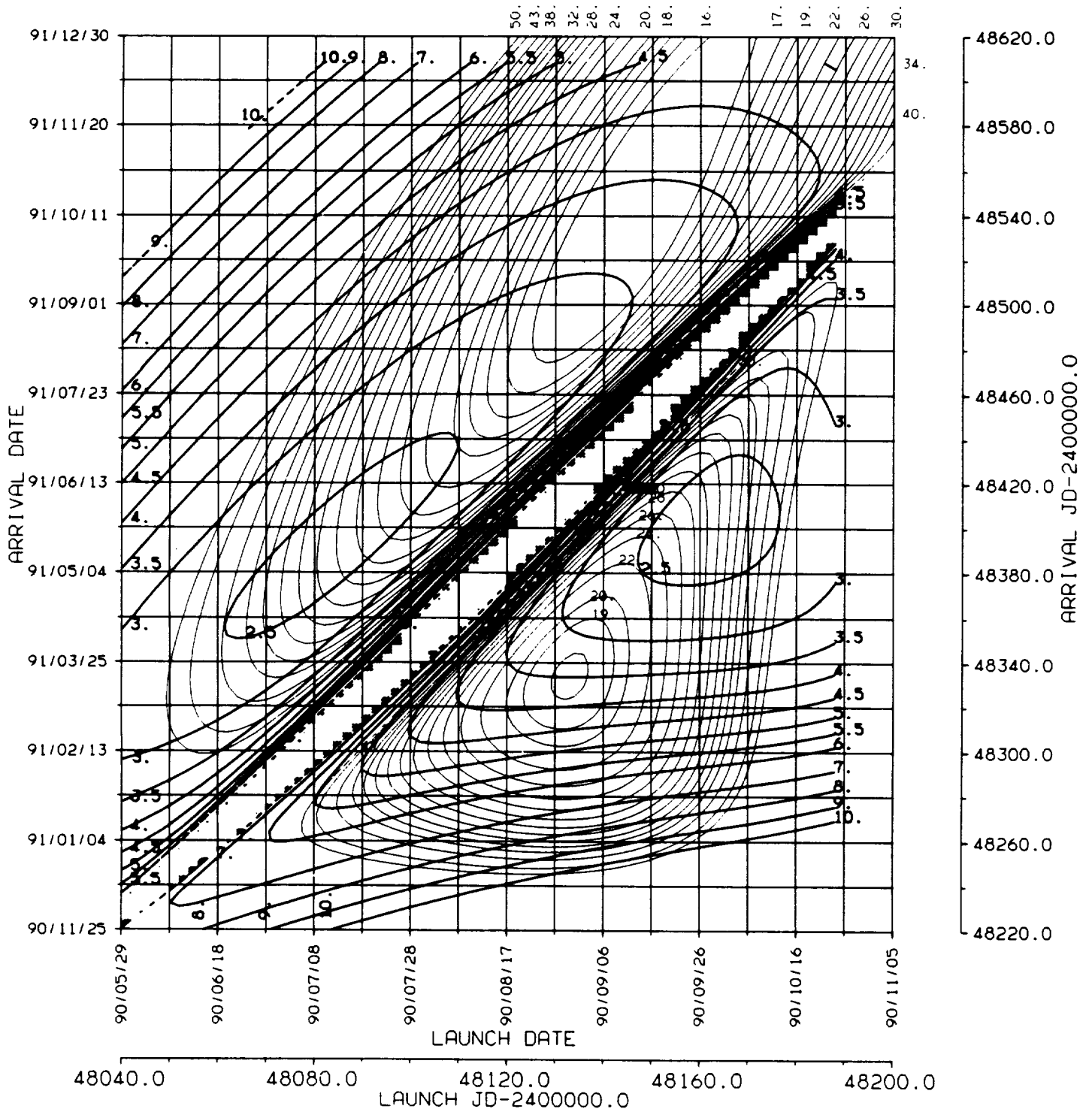
EARTH - MARS 1990 . C3L , RLA
BALLISTIC TRANSFER TRAJECTORY



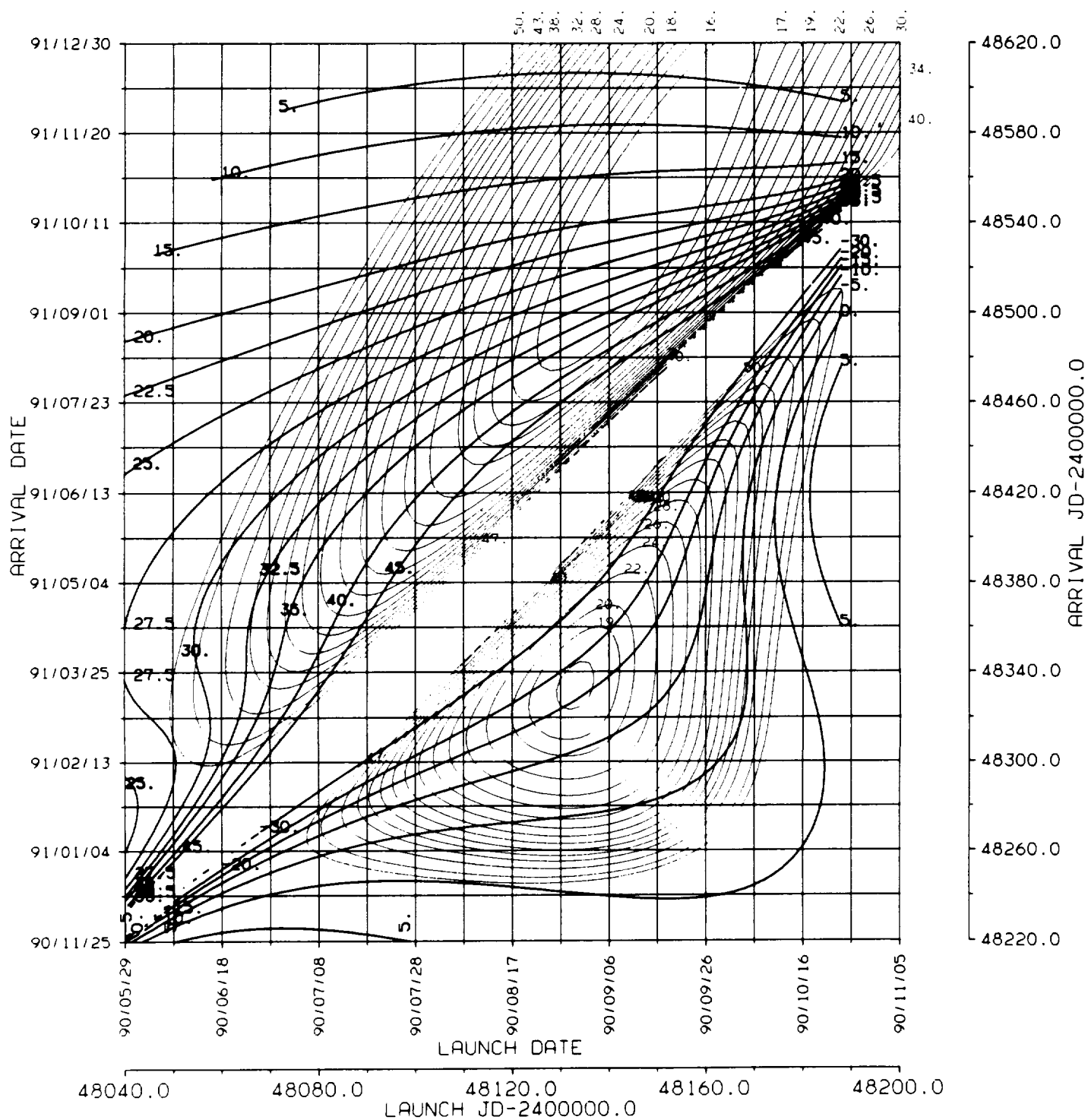
BALLISTIC TRANSFER TRAJECTORY



EARTH - MARS 1990 , C3L , VHP
* BALLISTIC TRANSFER TRAJECTORY



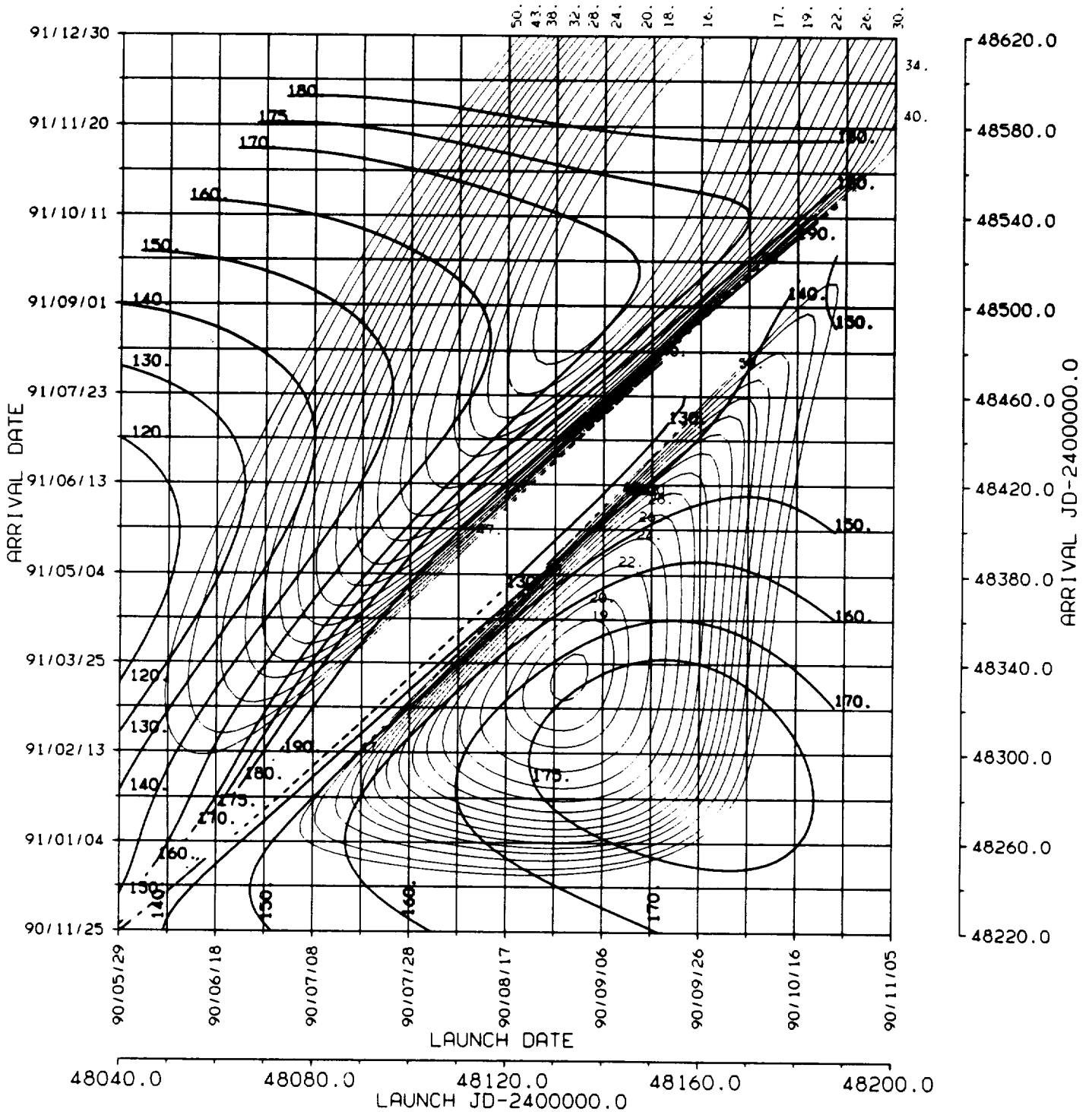
EARTH - MARS 1990 , C3L , DAP
BALLISTIC TRANSFER TRAJECTORY



7.
RAP
♂
1990

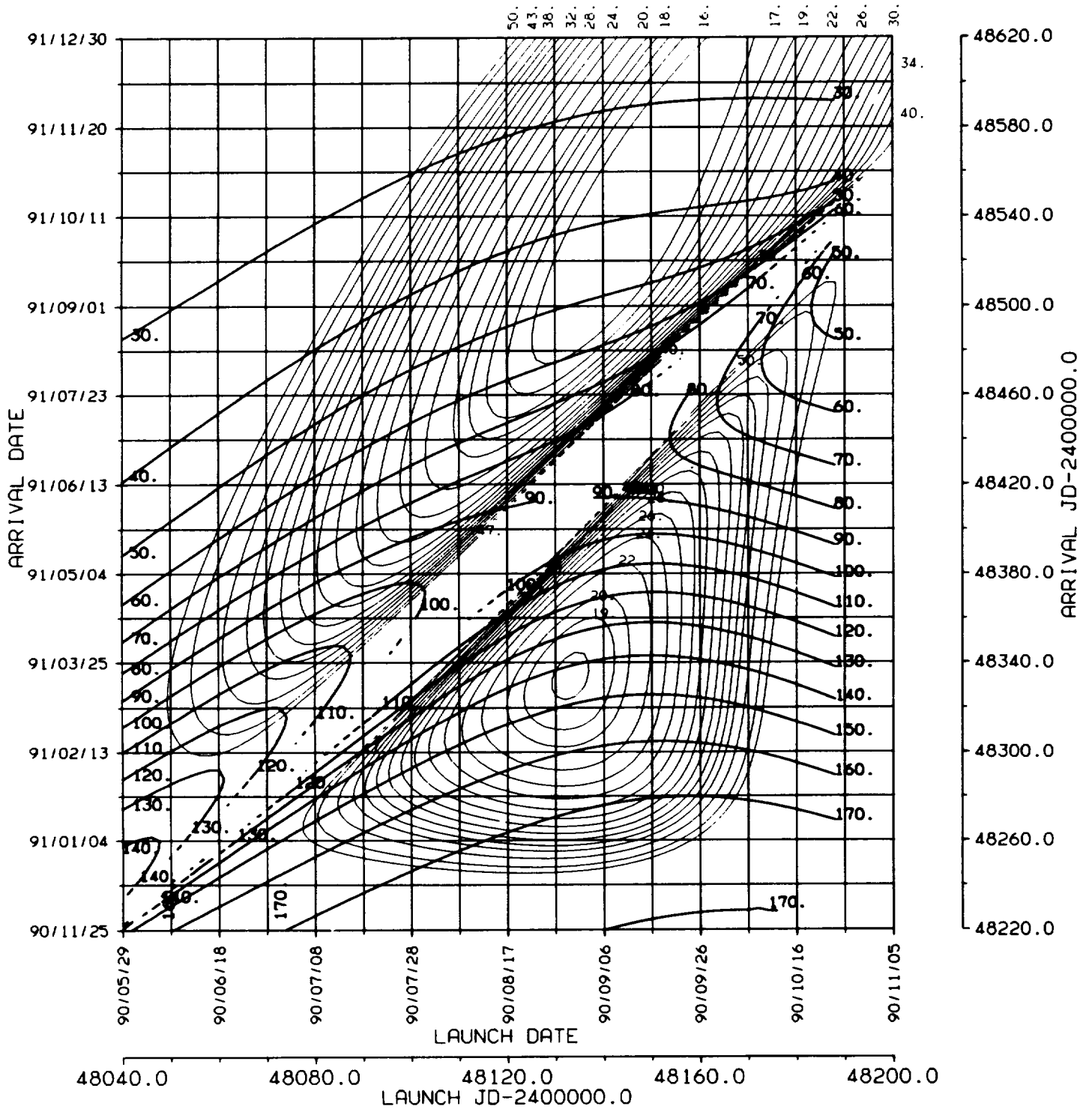
ORIGINAL PAGE IS
OF POOR QUALITY

EARTH - MARS 1990 , C3L , RAP
BALLISTIC TRANSFER TRAJECTORY

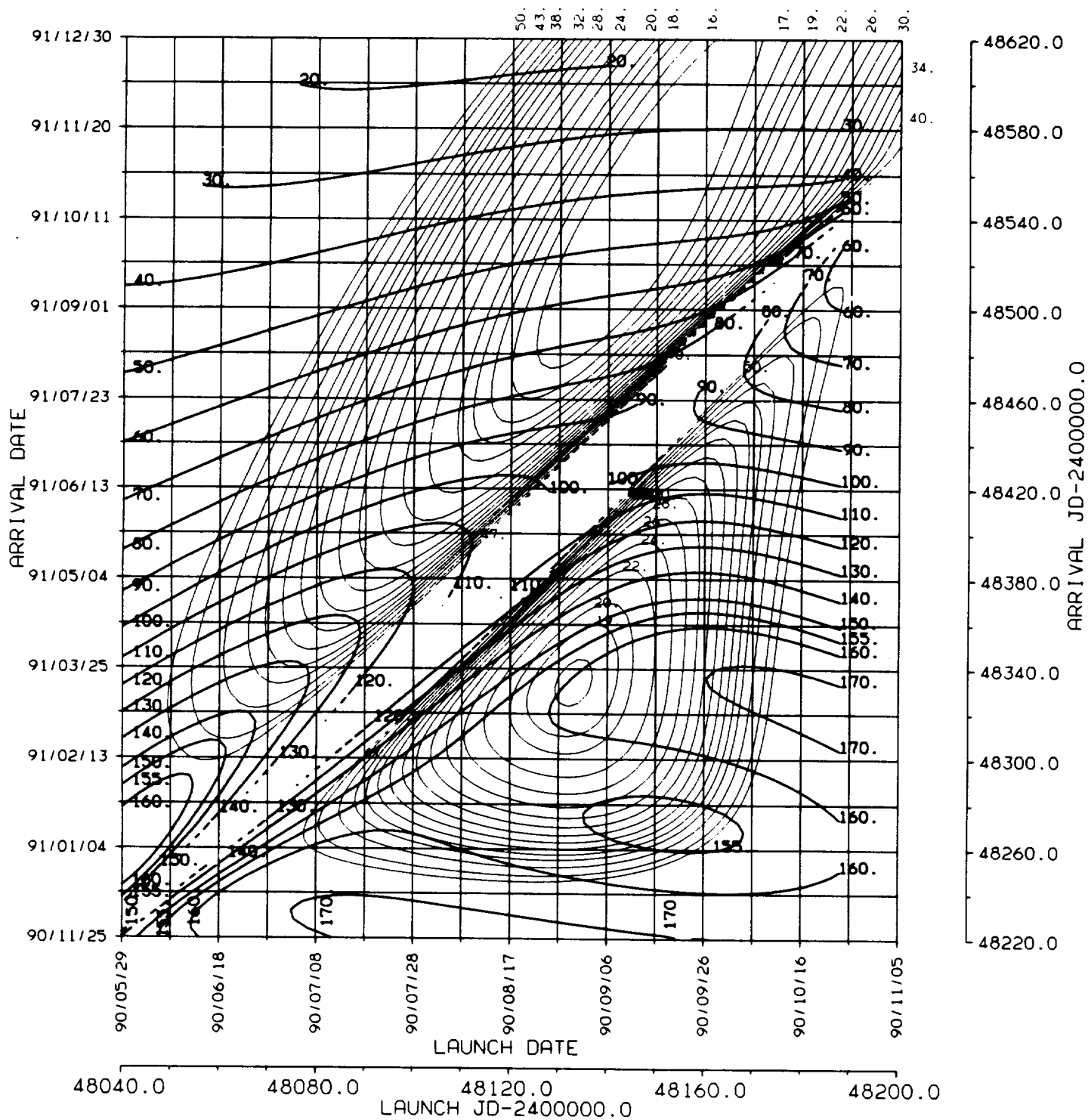


ORIGINAL PAGE 13
OF POOR QUALITY

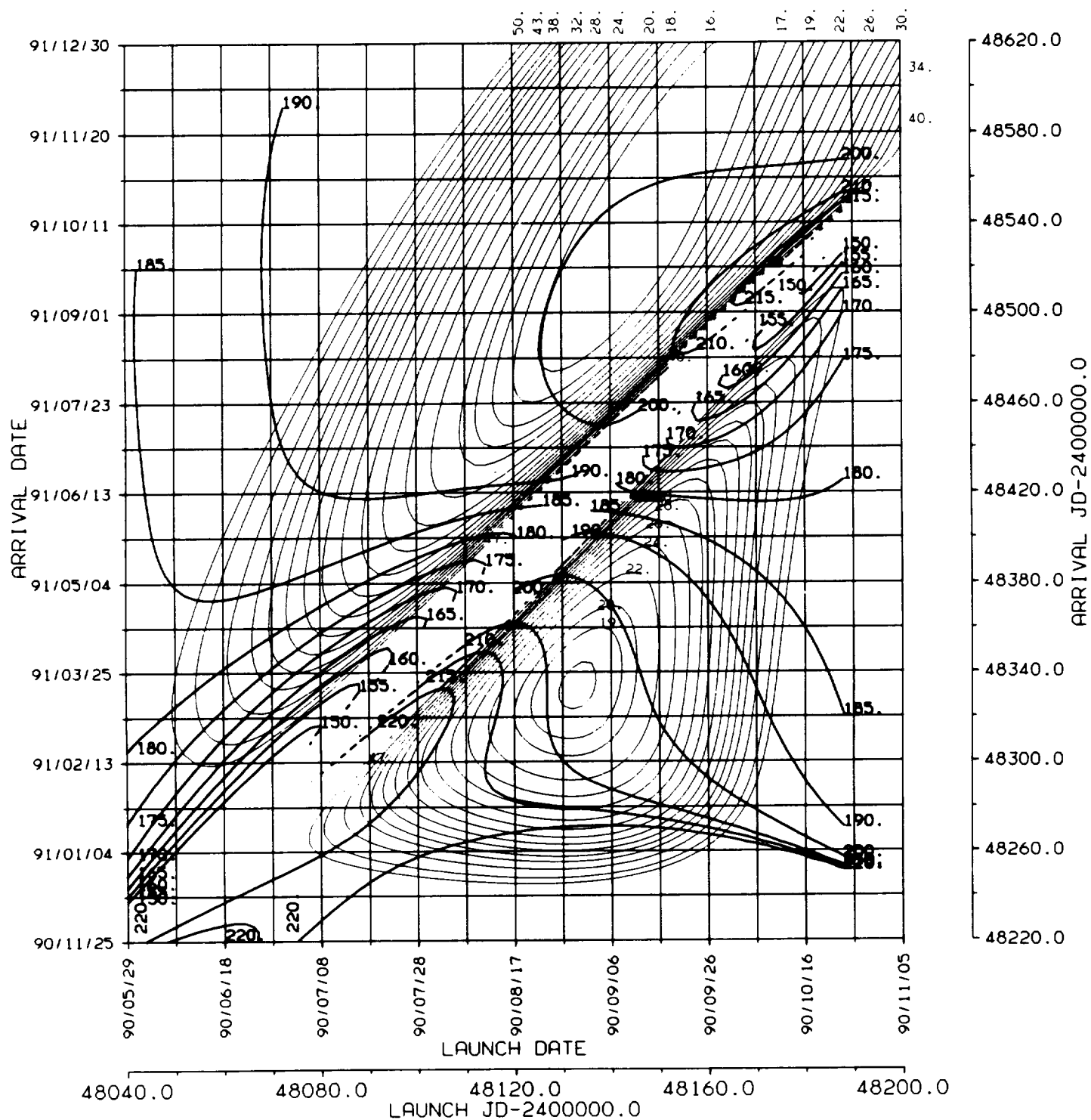
EARTH - MARS 1990 , C3L , ZAPS
BALLISTIC TRANSFER TRAJECTORY



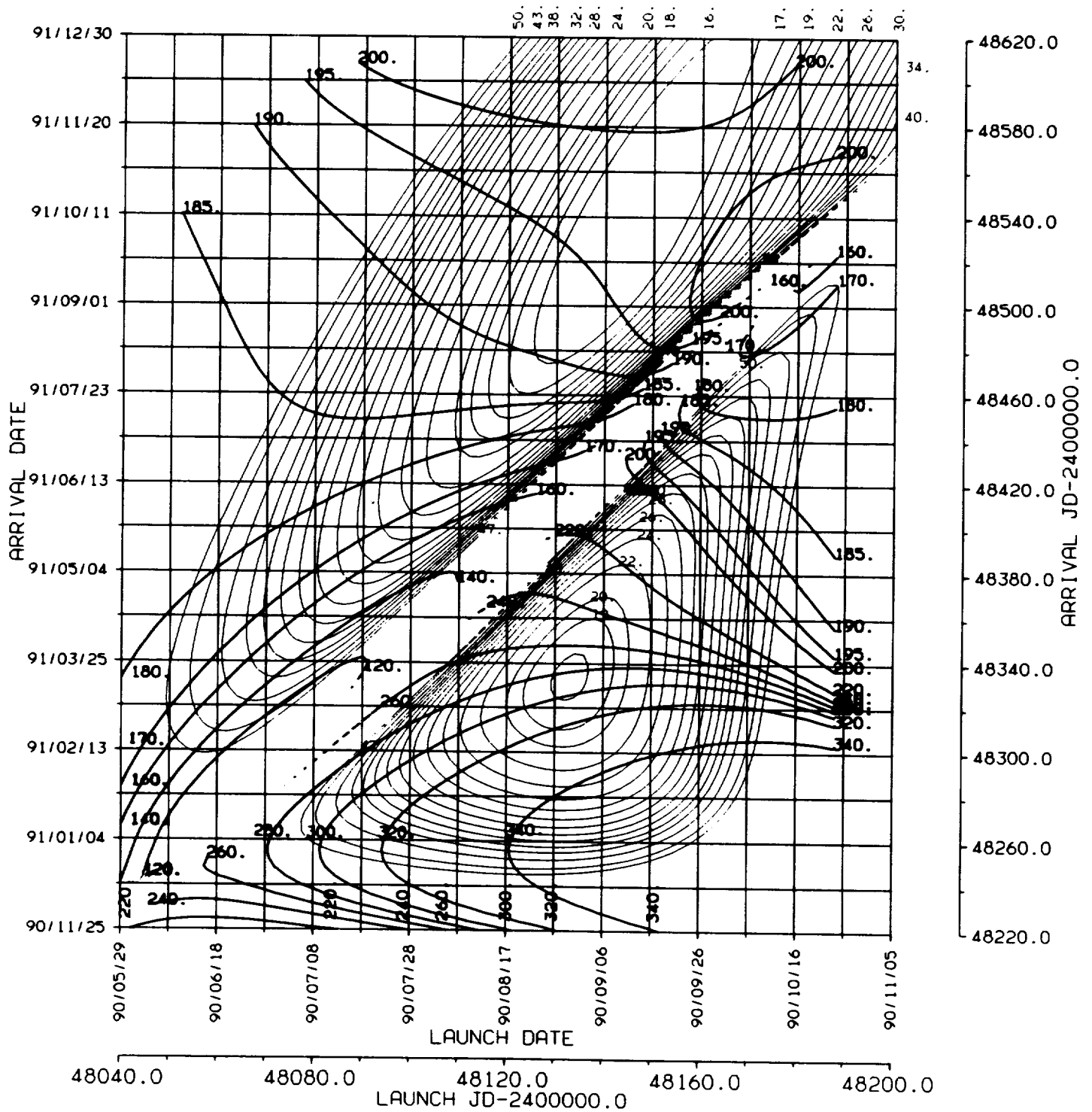
EARTH - MARS 1990 , C3L , ZAPE
* BALLISTIC TRANSFER TRAJECTORY



EARTH - MARS 1990 , C3L , ETSP
* BALLISTIC TRANSFER TRAJECTORY



EARTH - MARS 1990 , C3L , ETEP
* BALLISTIC TRANSFER TRAJECTORY



ORIGINAL PAGE IS
OF POOR QUALITY

Earth to Mars

1992

Opportunity

ENERGY MINIMA

	VALUE	TYPE	DEPARTURE (YEAR/MONTH/DAY)	ARRIVAL (YEAR/MONTH/DAY)
C ₃ L	18.341	I	92/10/06	93/05/09
C ₃ L	11.732	II	92/09/30	93/09/19
VHP	2.3844	I	92/10/29	93/07/25
VHP	2.3987	II	92/09/04	93/08/04

1.
C3L

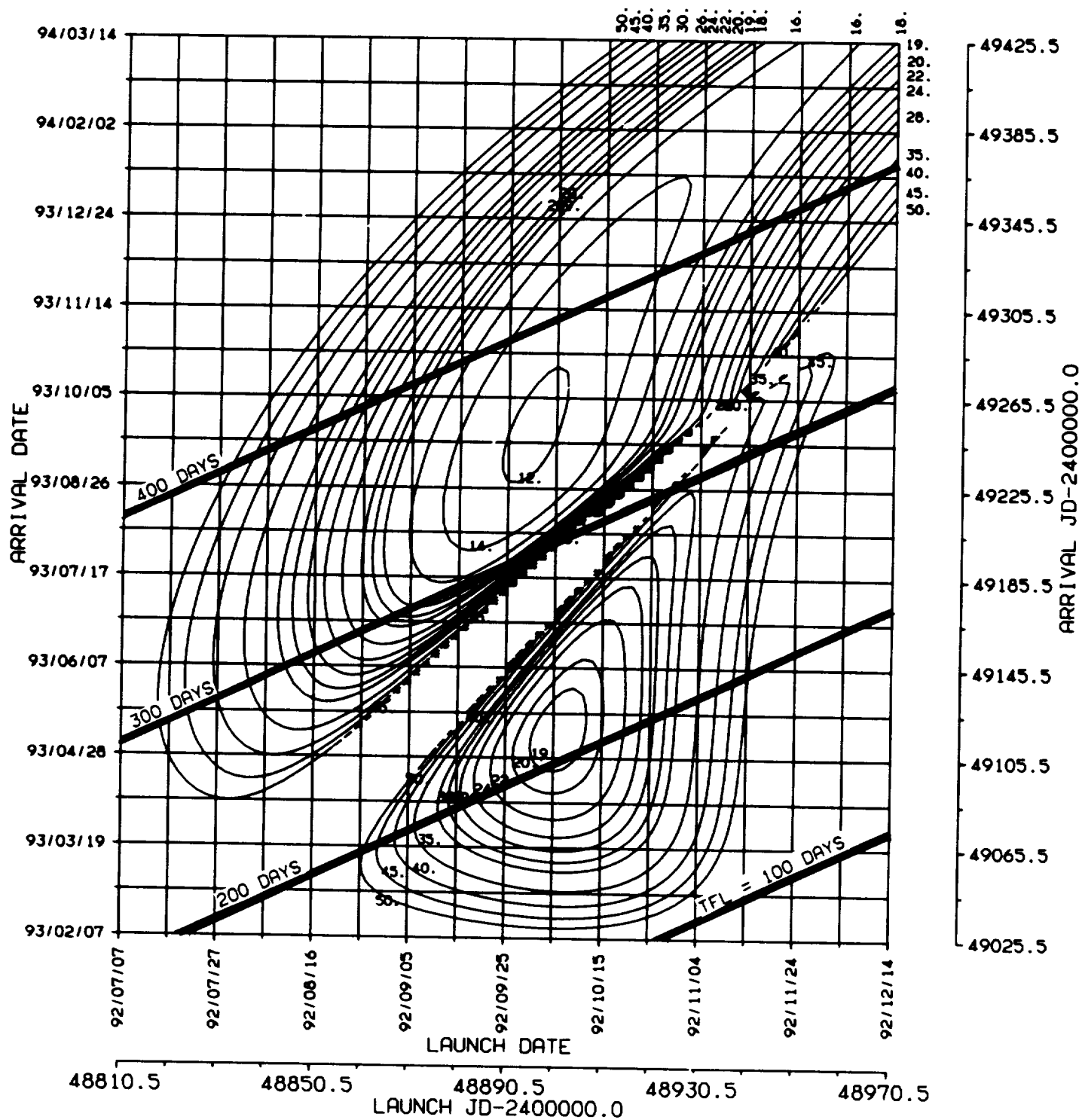


1992

ORIGINAL PAGE IS
OF POOR QUALITY

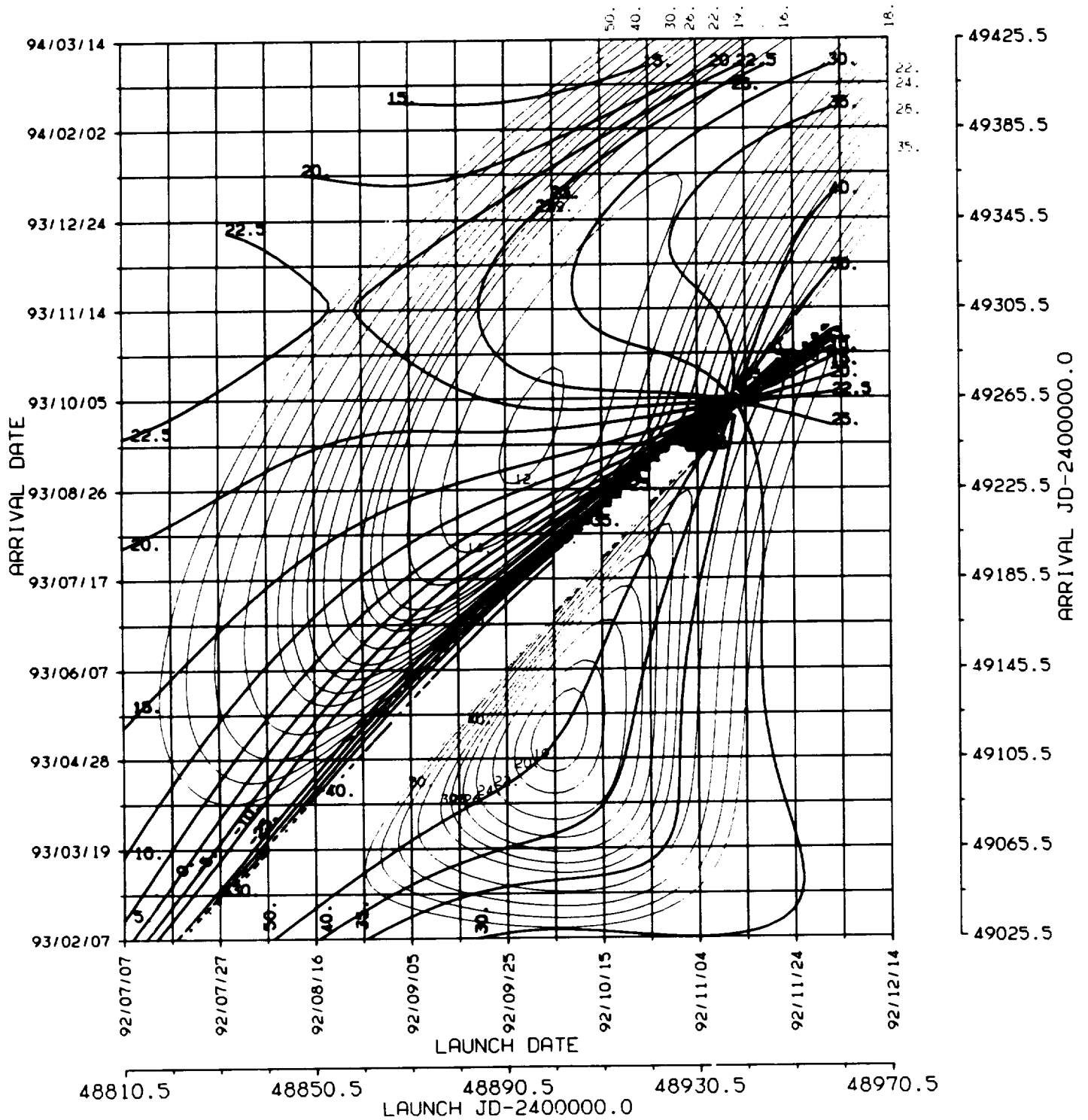
EARTH - MARS 1992 , C3L . TFL

* BALLISTIC TRANSFER TRAJECTORY



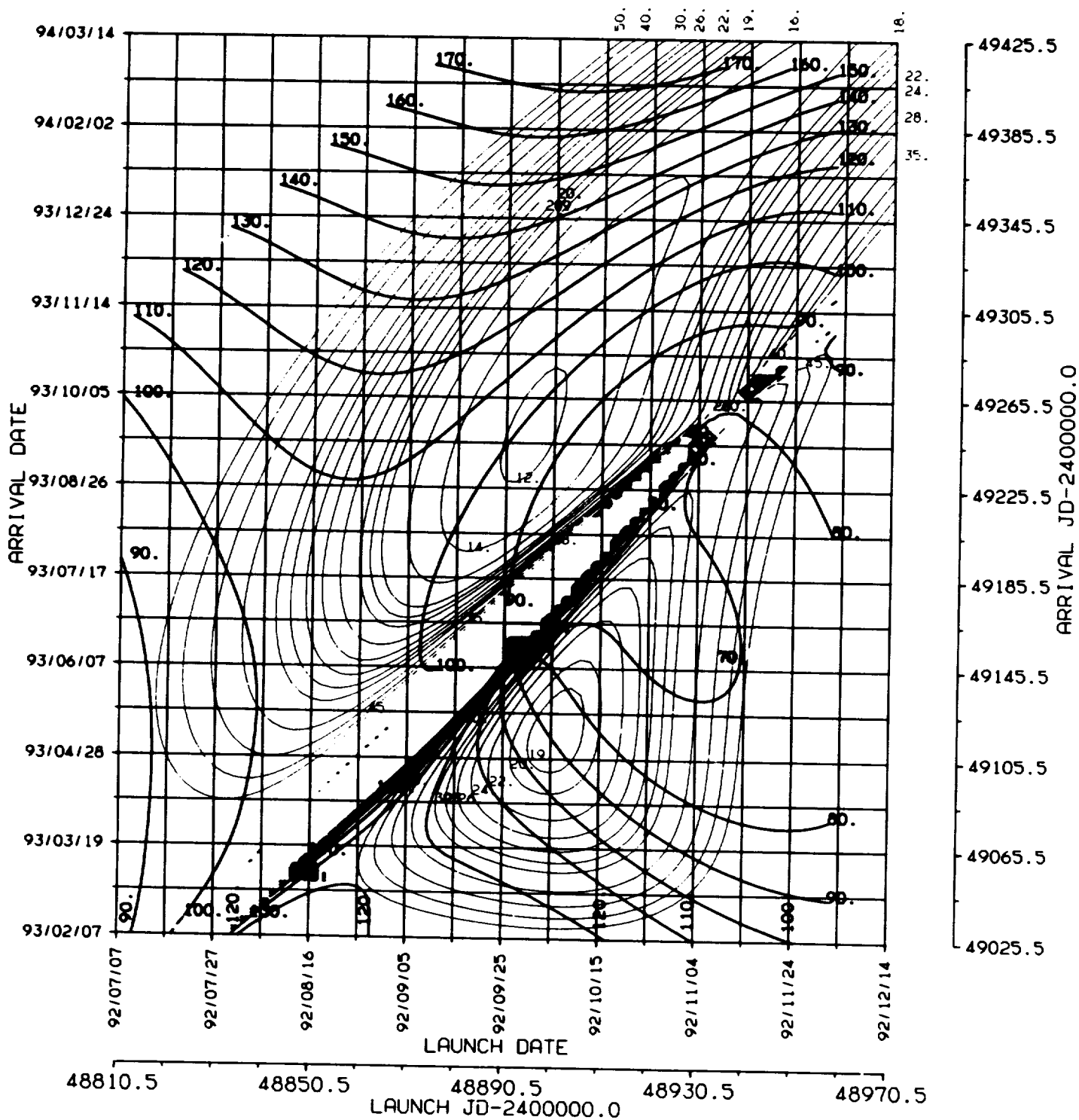
ORIGINAL PAGE 11
OF POOR QUALITY

EARTH - MARS 1992 , C3L , DLA
BALLISTIC TRANSFER TRAJECTORY



ORIGINAL PAGE IS
OF POOR QUALITY

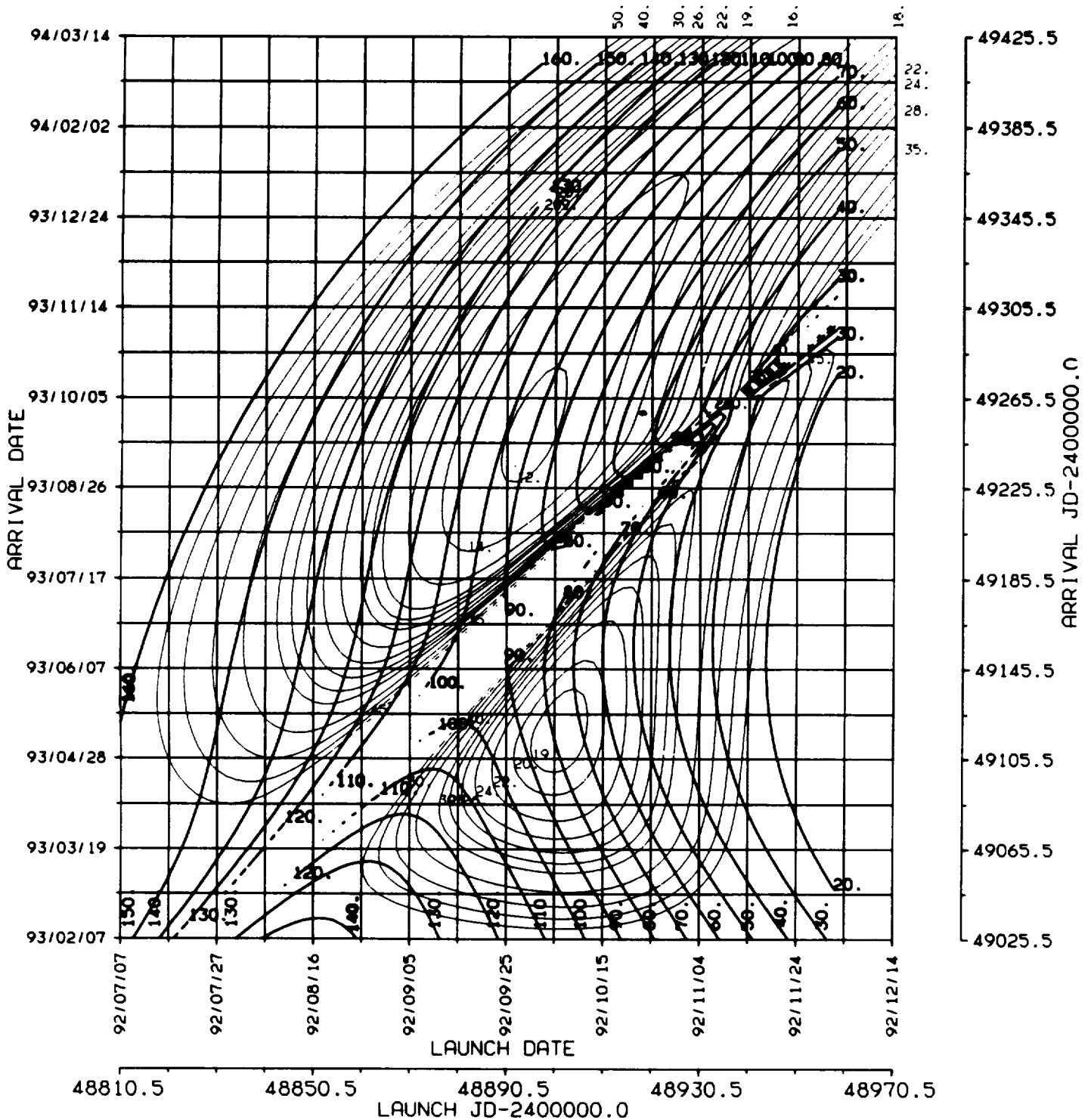
EARTH - MARS 1992, C3L, RLA
BALLISTIC TRANSFER TRAJECTORY



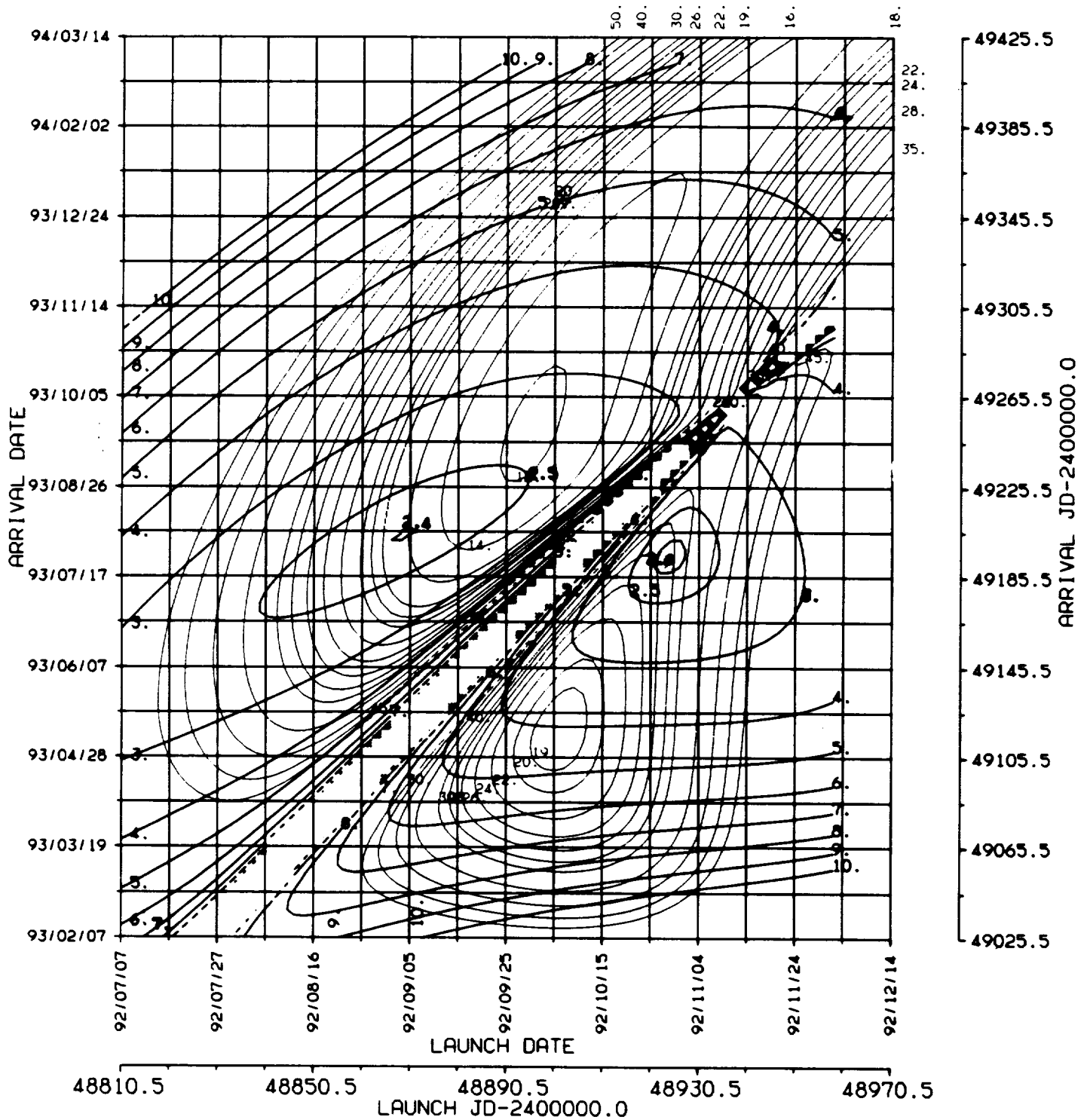
ORIGINAL PAGE IS
OF POOR QUALITY

4.
ZALS
♂
1992

EARTH - MARS 1992 , C3L , ZALS
BALLISTIC TRANSFER TRAJECTORY



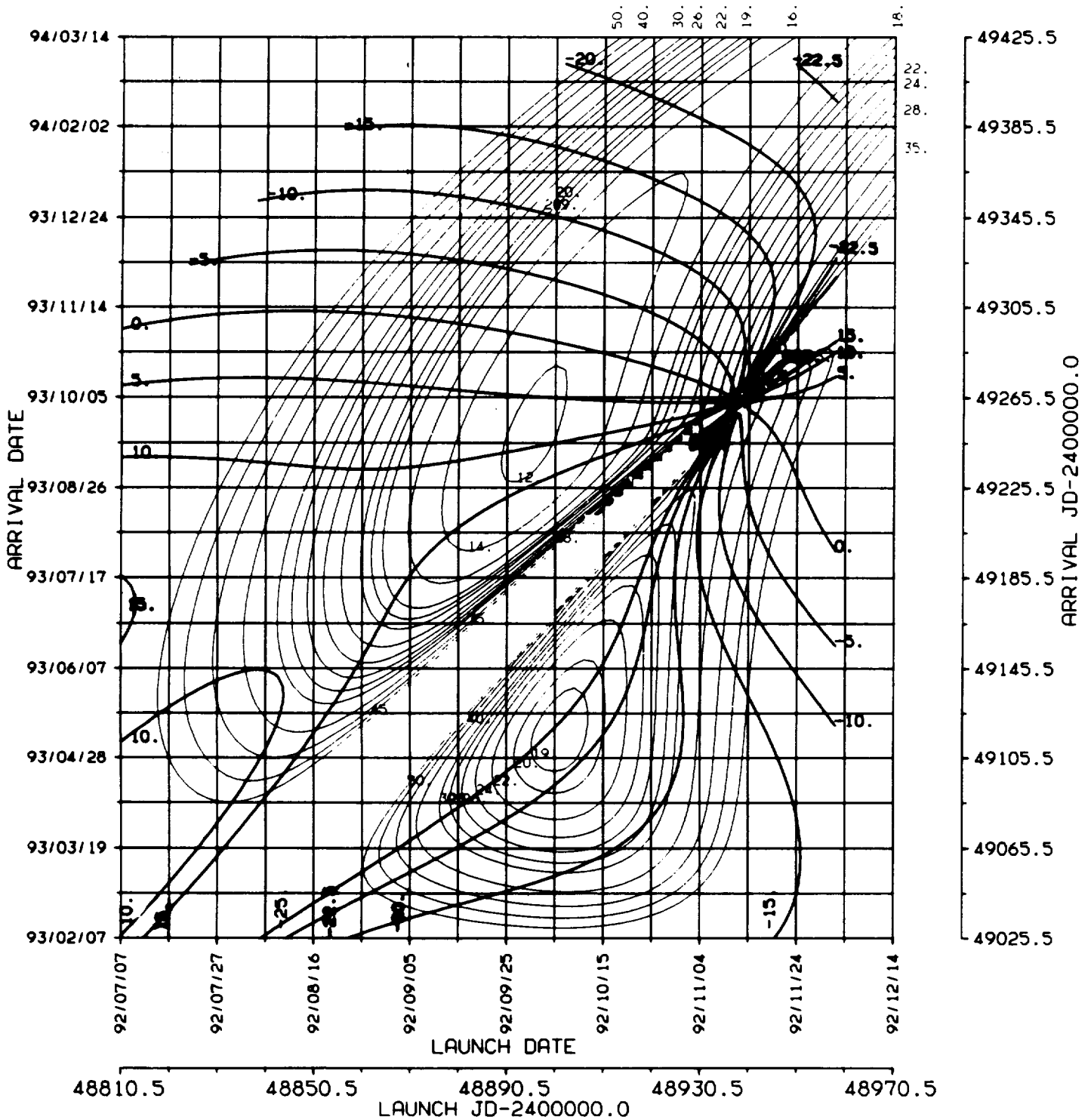
EARTH - MARS 1992 , C3L , VHP
BALLISTIC TRANSFER TRAJECTORY



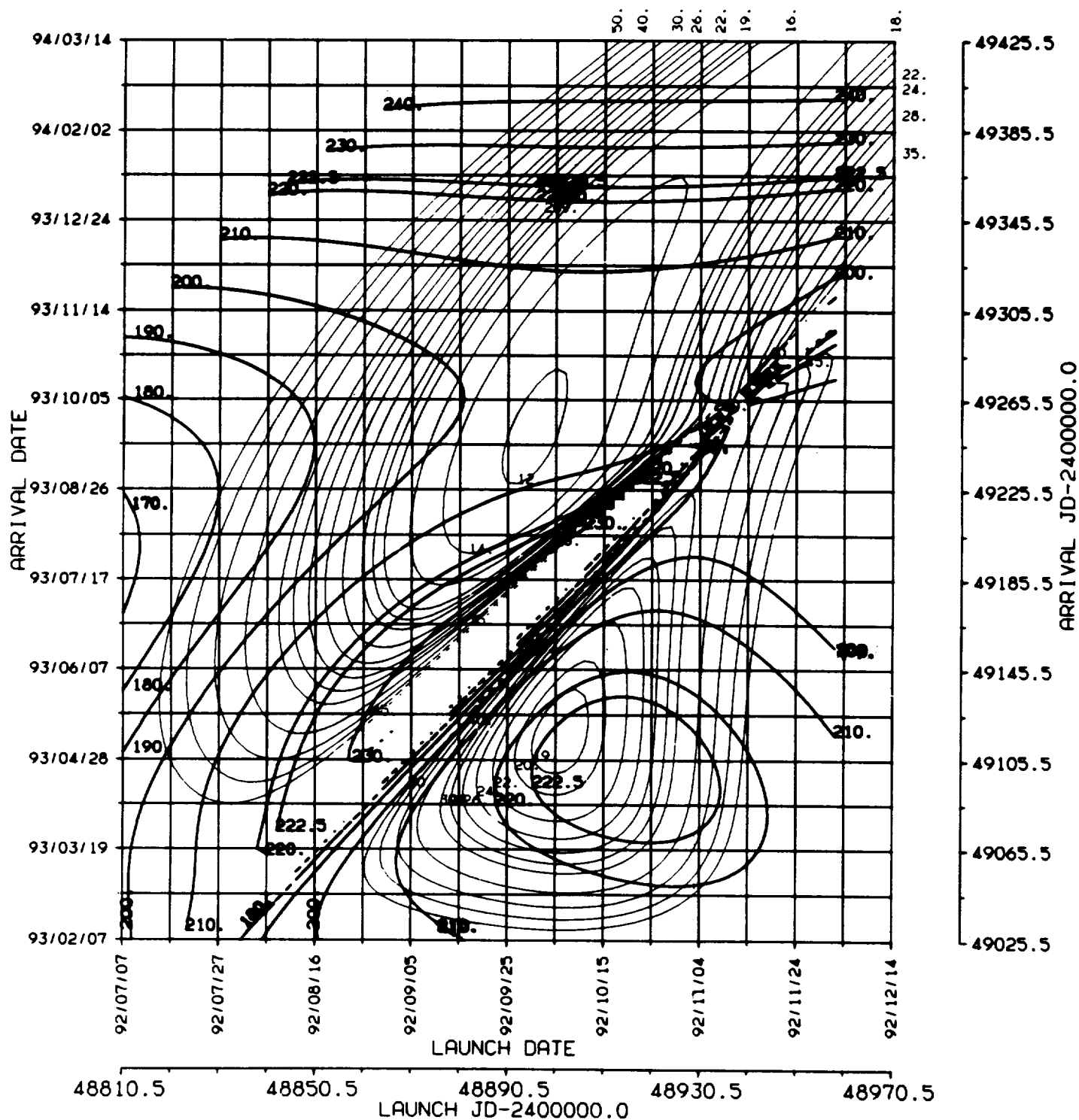
ORIGINAL PAGE IS
OF POOR QUALITY

6.
DAP
♂
1992

EARTH - MARS 1992 , C3L , DAP
* BALLISTIC TRANSFER TRAJECTORY

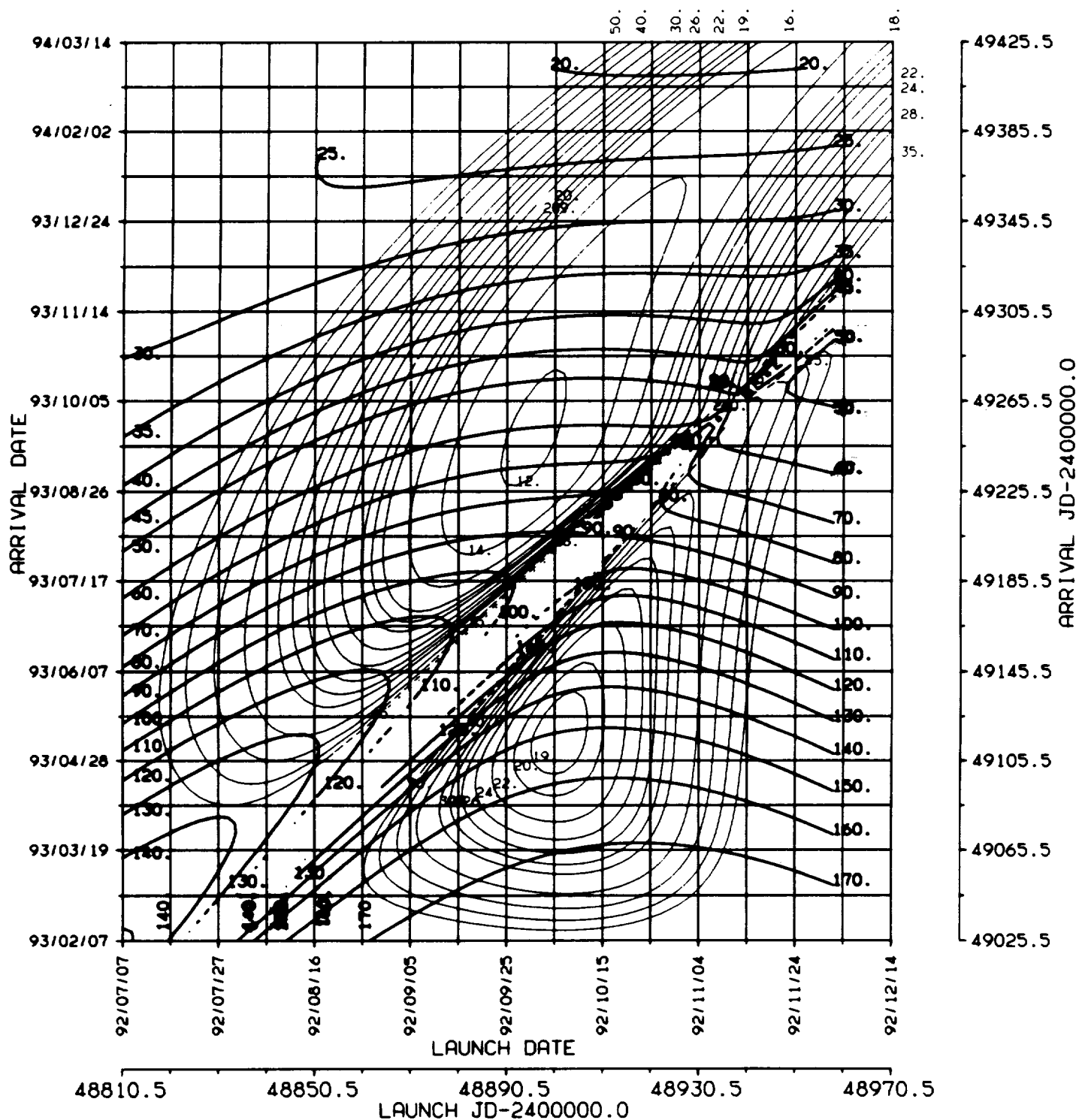


EARTH - MARS 1992 , C3L , RAP
* BALLISTIC TRANSFER TRAJECTORY



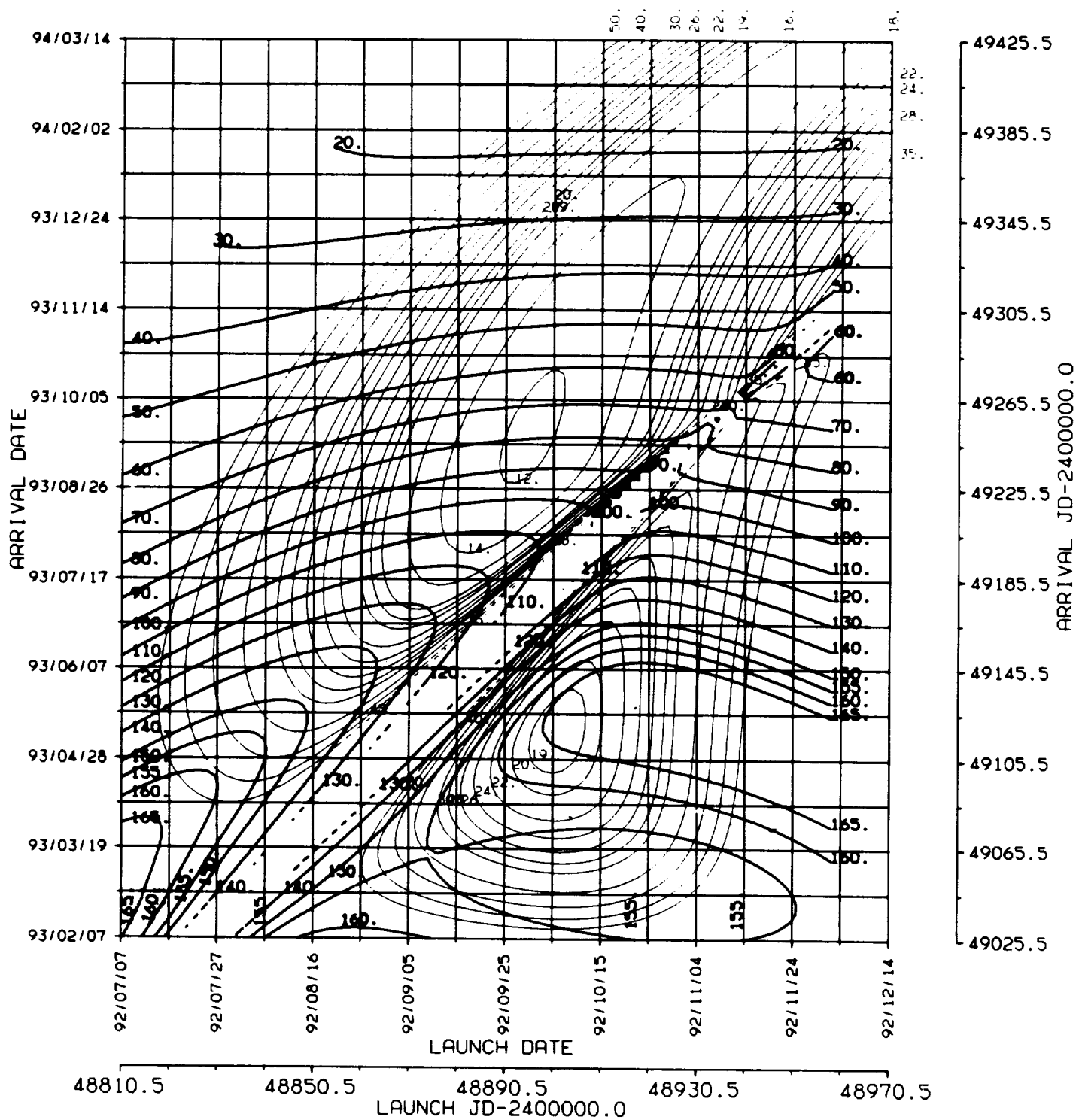
ORIGINAL PAGE 19
OF POOR QUALITY

EARTH - MARS 1992 , C3L , ZAPS
* BALLISTIC TRANSFER TRAJECTORY

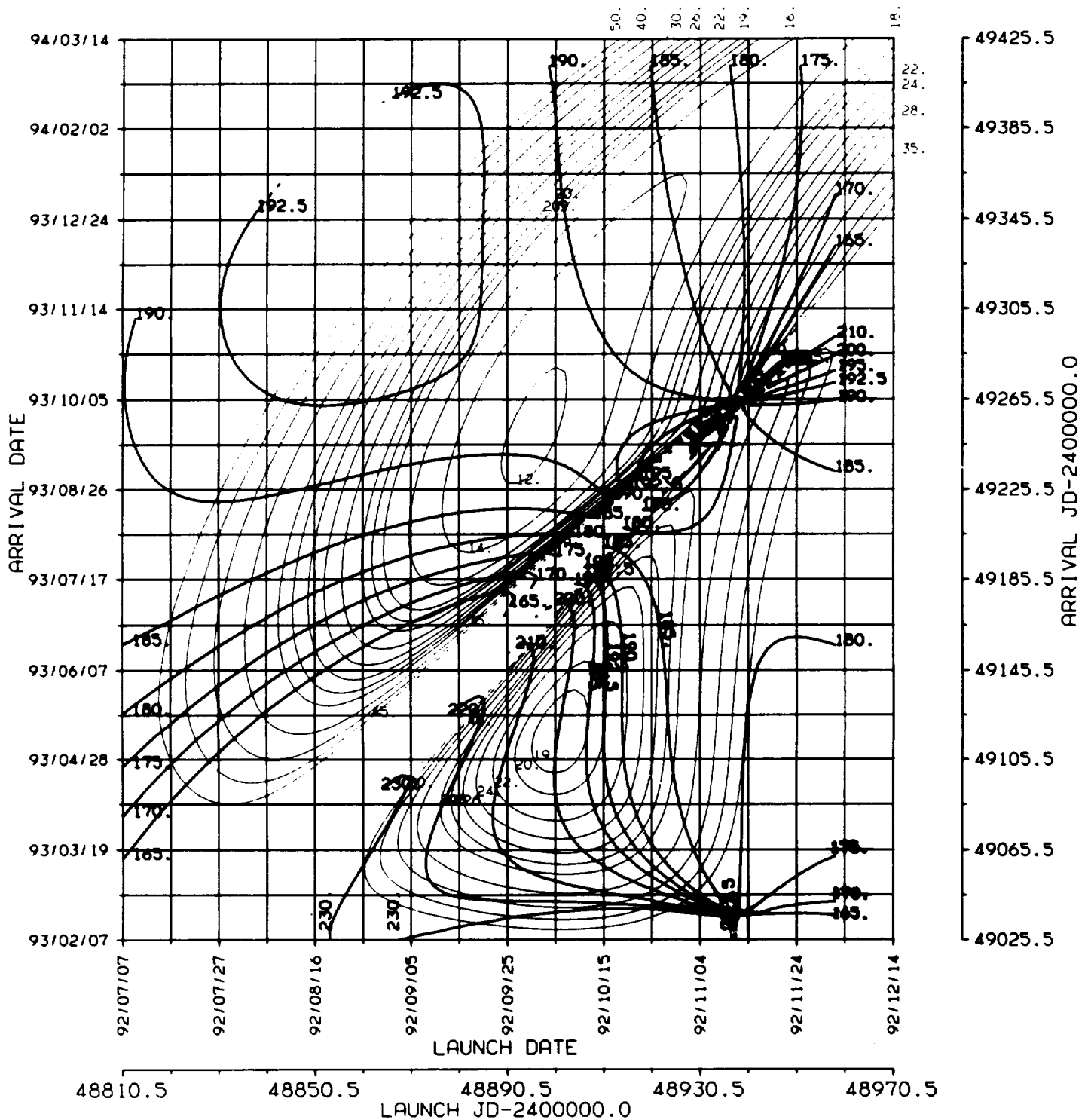


ORIGINAL PAGE IS
OF POOR QUALITY

EARTH - MARS 1992 . C3L . ZAPE
BALLISTIC TRANSFER TRAJECTORY



EARTH - MARS 1992 . C3L , ETSP
BALLISTIC TRANSFER TRAJECTORY

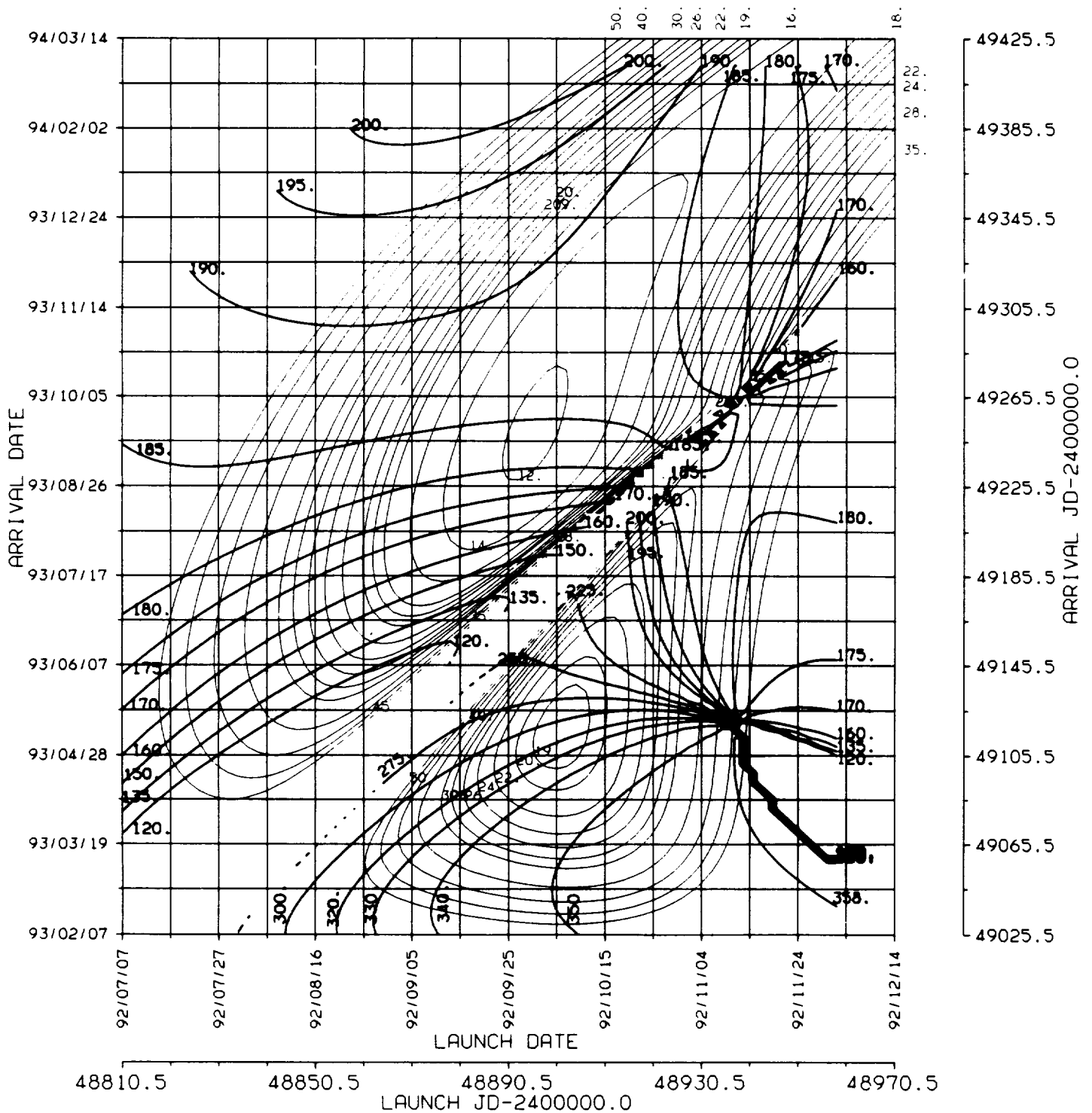




1992

ORIGINAL PAGE IS
OF POOR QUALITY

EARTH - MARS 1992 , C3L , ETEP
* BALLISTIC TRANSFER TRAJECTORY



ORIGINAL PAGE IS
OF POOR QUALITY

Earth to Mars

1994

Opportunity

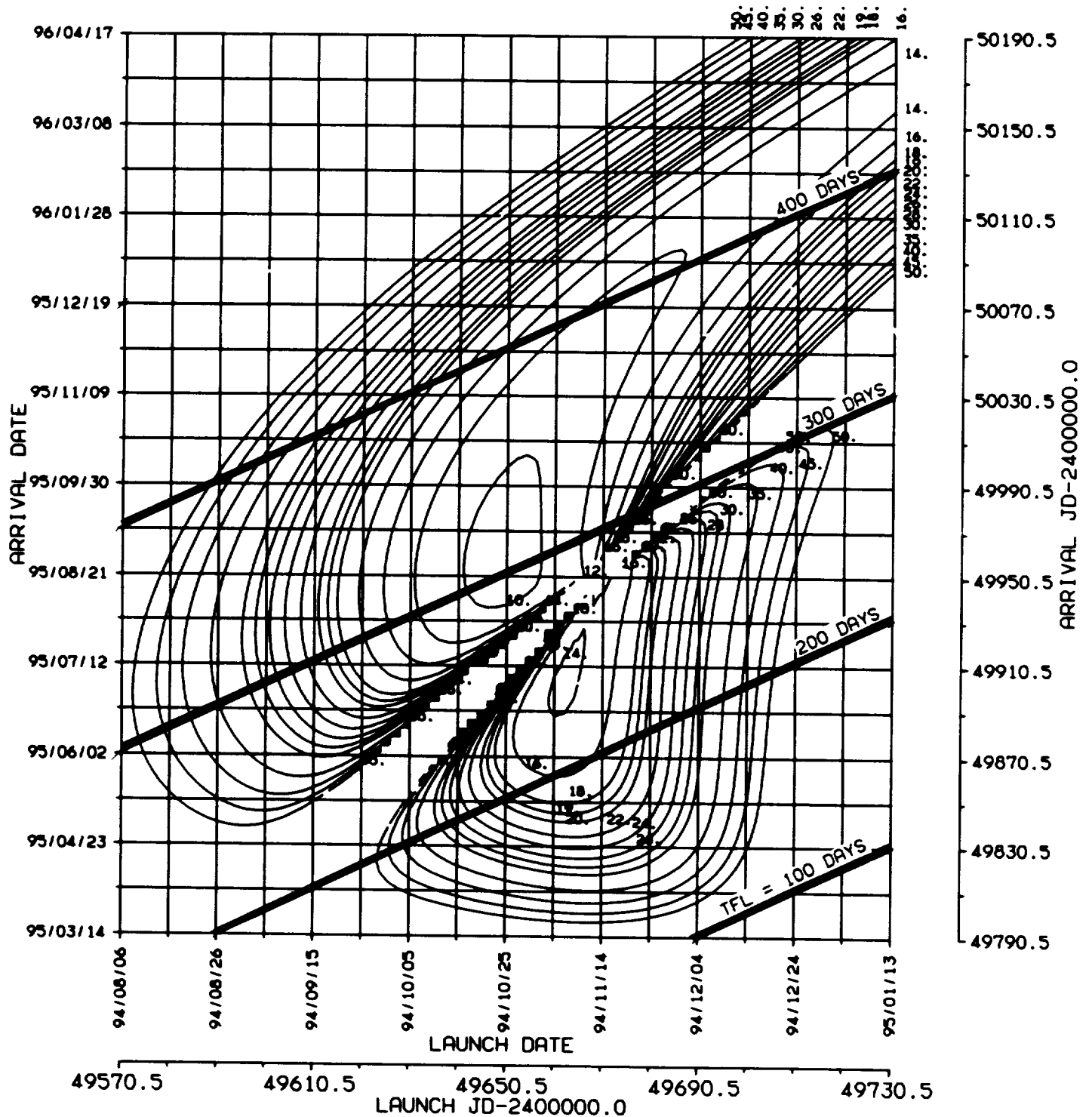
ENERGY MINIMA

	VALUE	TYPE	DEPARTURE (YEAR/MONTH/DAY)	ARRIVAL (YEAR/MONTH/DAY)
C ₃ L	13.766	I	94/11/06	95/07/05
C ₃ L	9.4674	II	94/10/24	95/08/27
VHP	2.5727	I	94/11/12	95/08/21
VHP	2.5142	II	94/11/03	95/09/06

1.
C3L
♂
1994

ORIGINAL PAGE 19
OF POOR QUALITY

EARTH - MARS 1994 , C3L . TFL
* BALLISTIC TRANSFER TRAJECTORY



1994



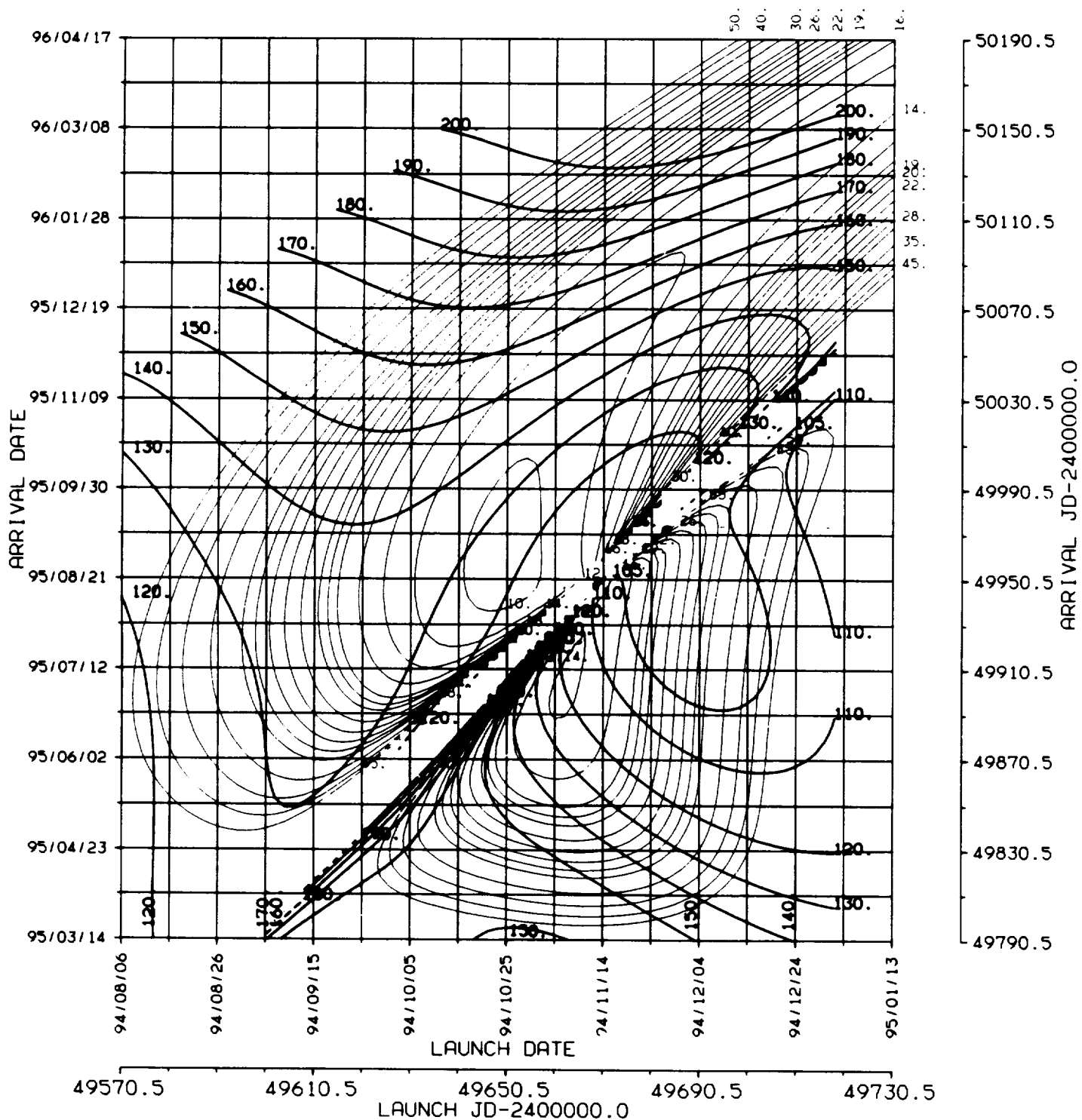
3.
RLA



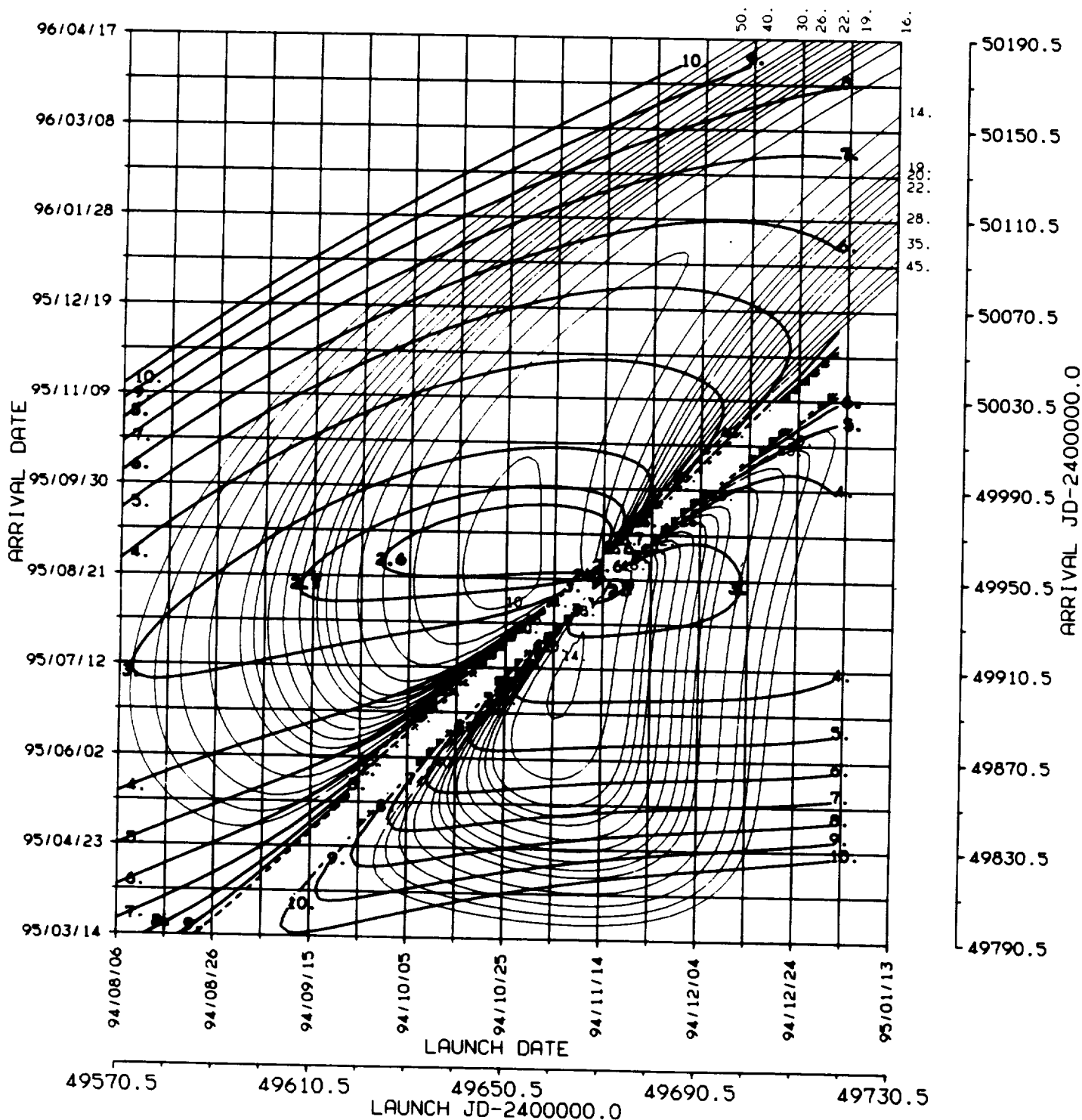
1994

ORIGINAL PAGE 19
OF POOR QUALITY

EARTH - MARS 1994 , C3L , RLA
BALLISTIC TRANSFER TRAJECTORY



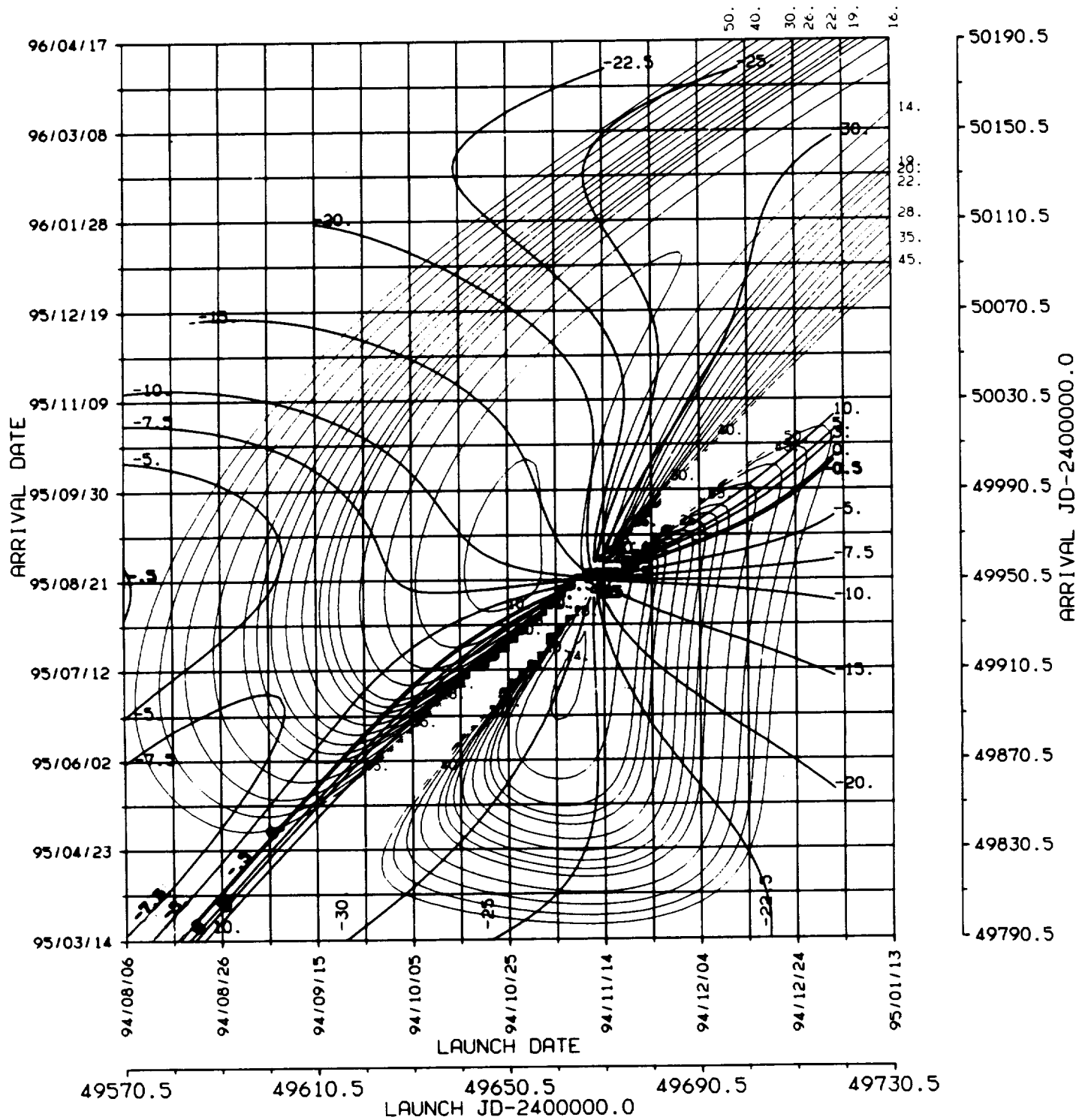
EARTH - MARS 1994 , C3L , VHP
BALLISTIC TRANSFER TRAJECTORY



ORIGINAL PAGE IS
OF POOR QUALITY

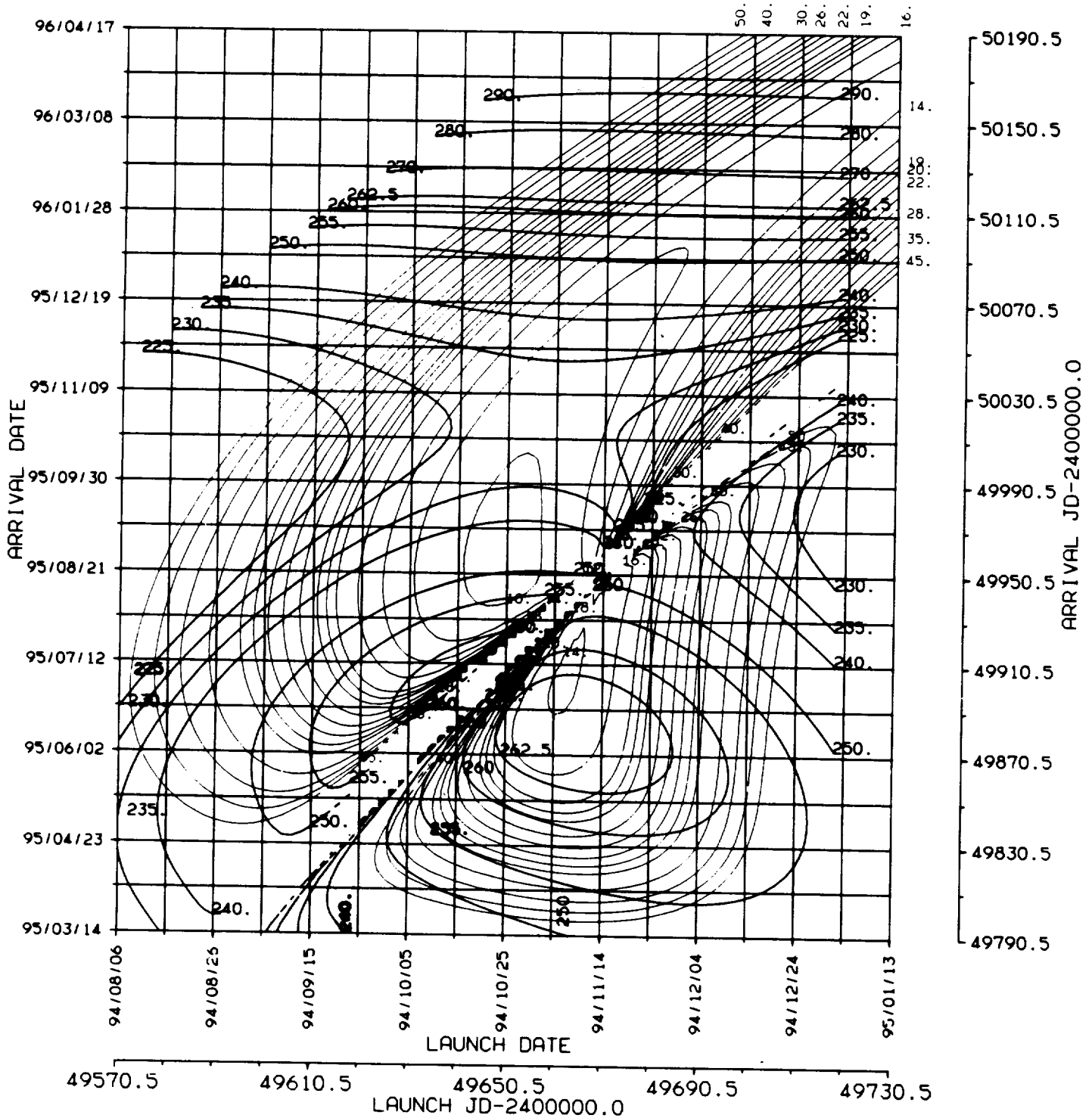
6.
DAP
♂
1994

EARTH - MARS 1994 , C3L , DAP
* BALLISTIC TRANSFER TRAJECTORY

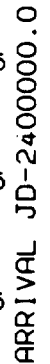


ORIGINAL PAGE IS
OF POOR QUALITY

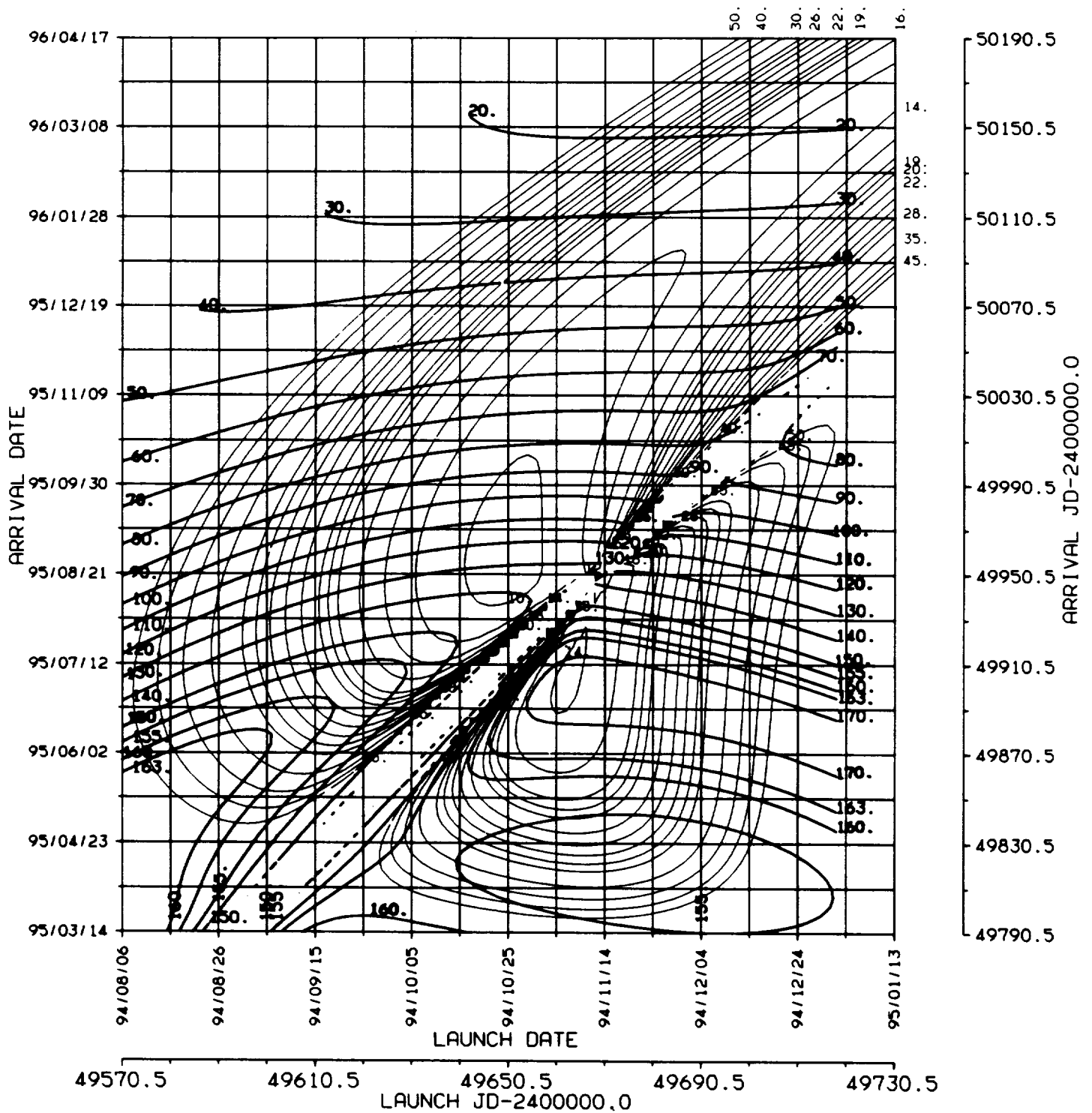
EARTH - MARS 1994 , C3L , RAP
BALLISTIC TRANSFER TRAJECTORY



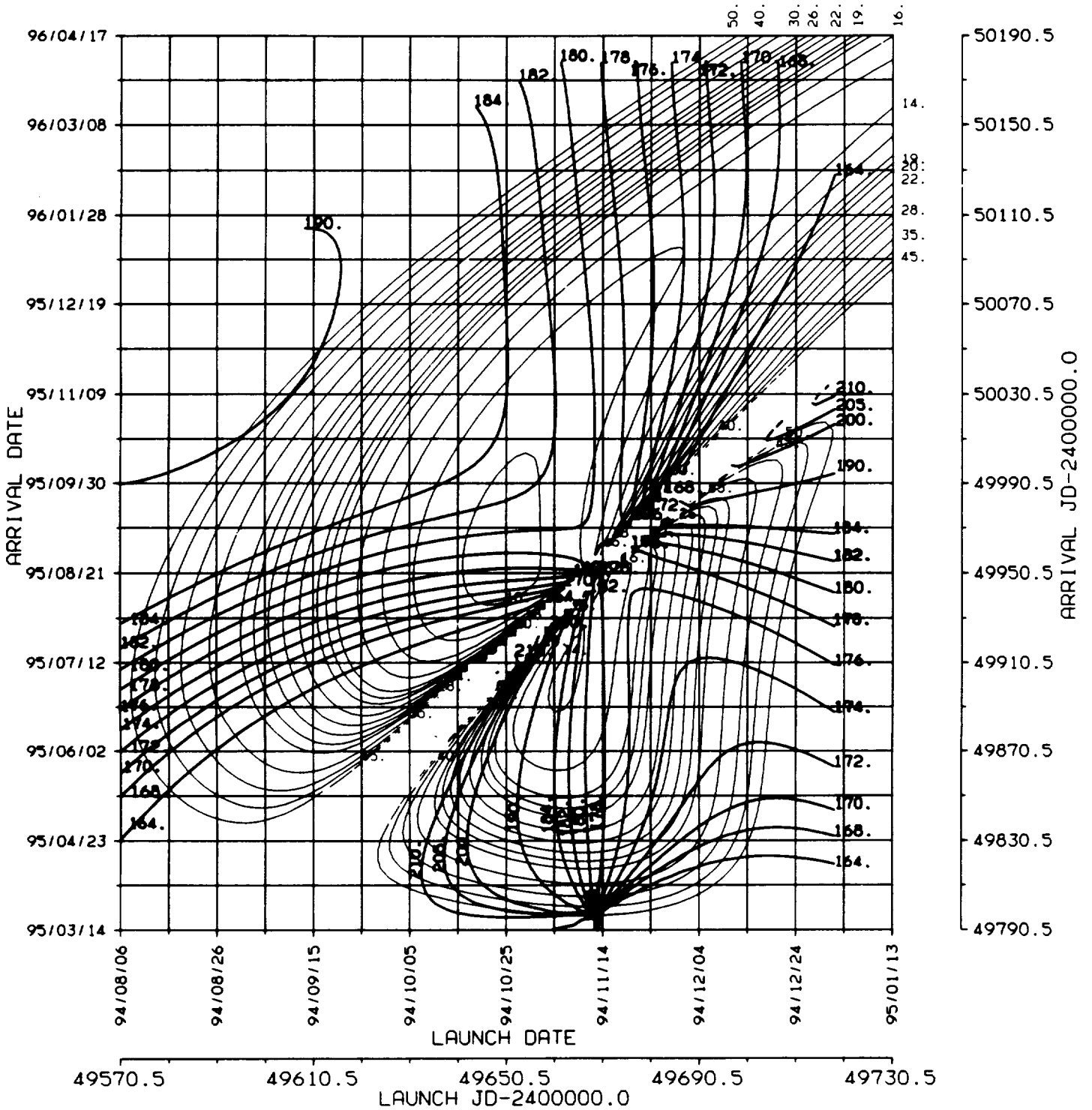
✱



EARTH - MARS 1994 , C3L , ZAPE
* BALLISTIC TRANSFER TRAJECTORY



EARTH - MARS 1994 , C3L , ETSP
* BALLISTIC TRANSFER TRAJECTORY

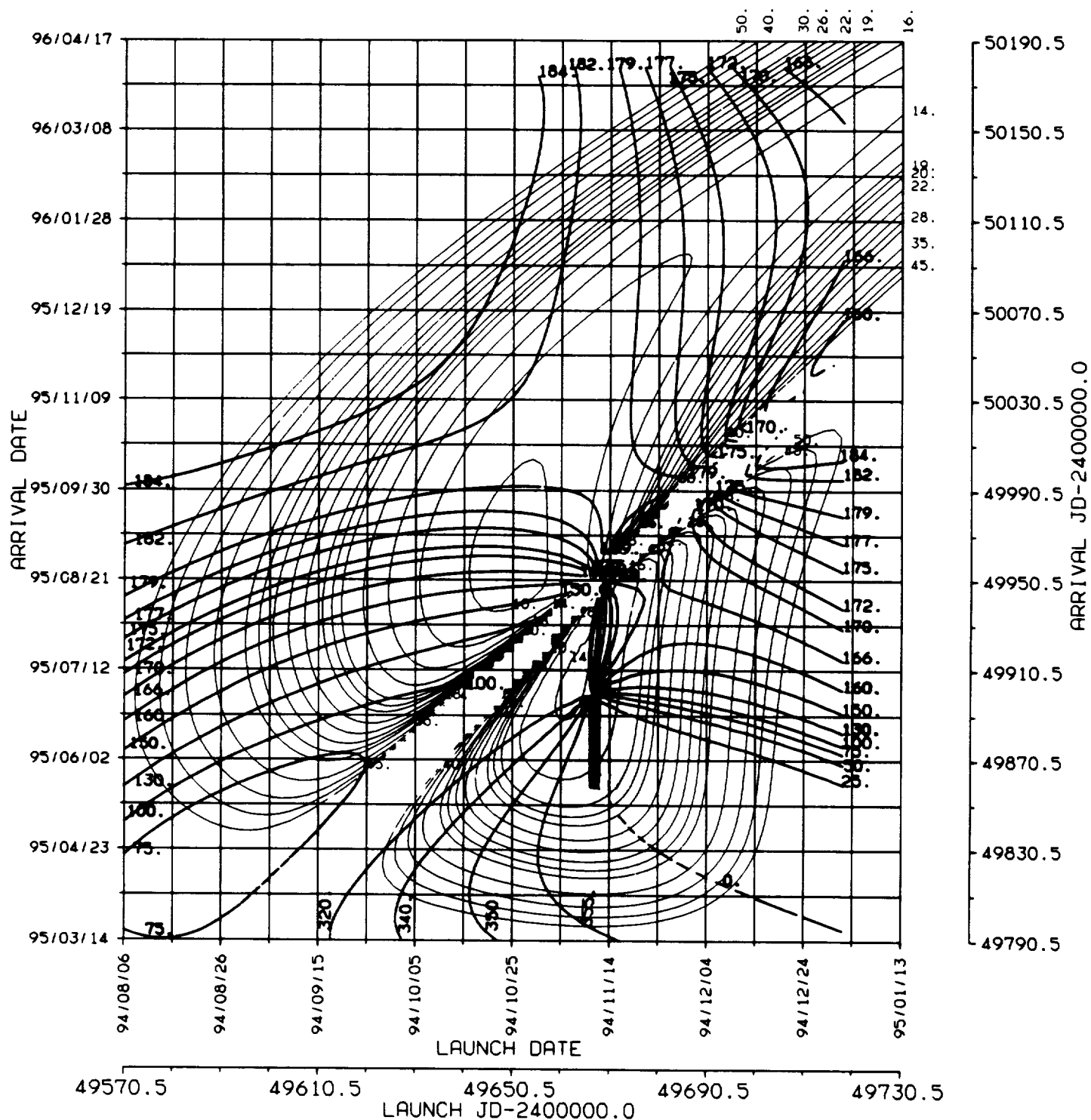




1994

ORIGINAL PAGE IS
OF POOR QUALITY

EARTH - MARS 1994 , C3L , ETEP
* BALLISTIC TRANSFER TRAJECTORY



ORIGINAL PAGE IS
OF POOR QUALITY

Earth to Mars

1996/7

Opportunity

ENERGY MINIMA

	VALUE	TYPE	DEPARTURE (YEAR/MONTH/DAY)	ARRIVAL (YEAR/MONTH/DAY)
C ₃ L	9.0071	I	96/11/30	97/07/19
C ₃ L	8.9323	II	96/11/21	97/09/29
VHP	3.4813	I	97/01/06	97/08/31
VHP	2.8683	II	96/11/16	97/09/15

1.
C3L

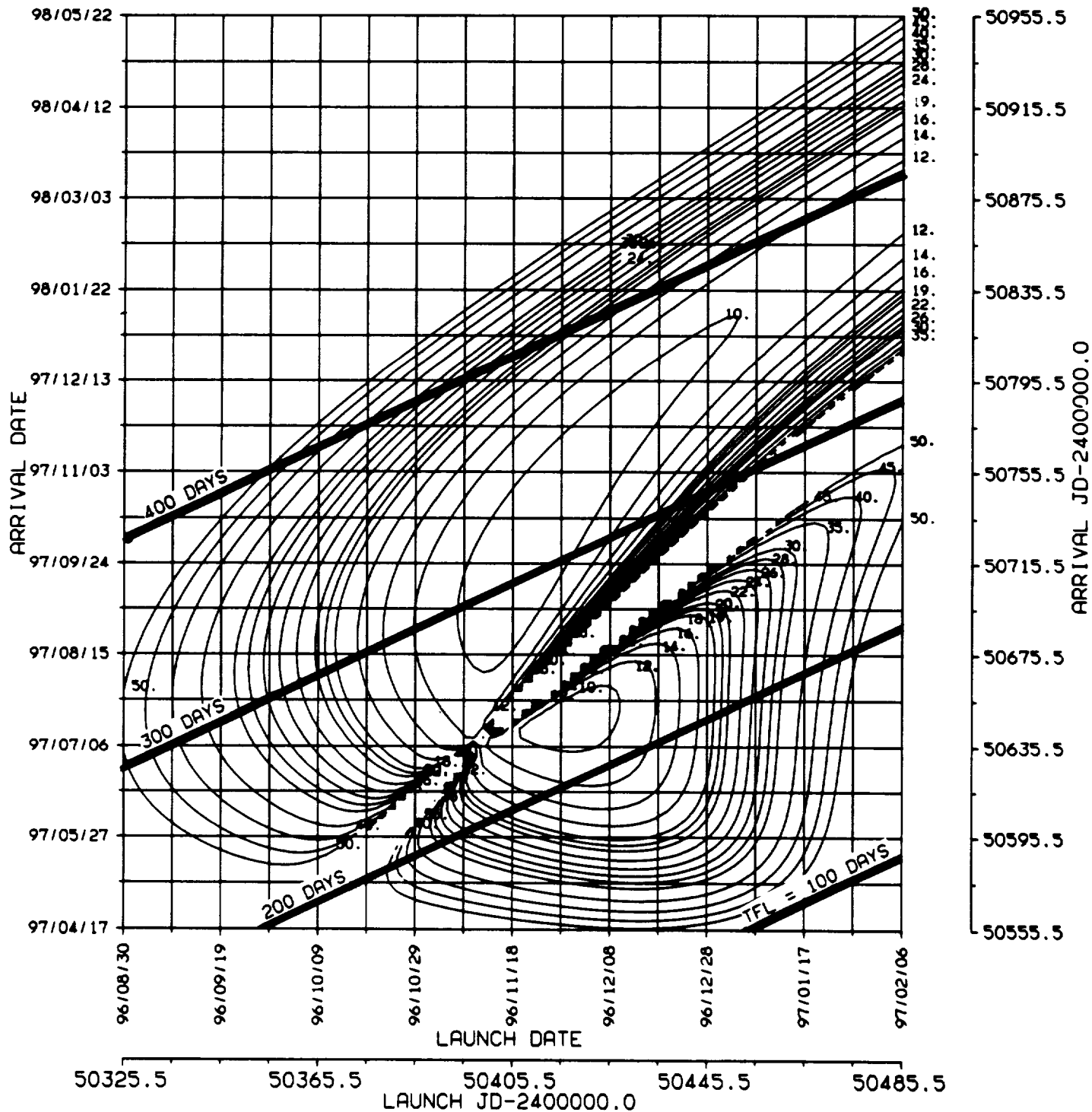


ORIGINAL PAGE IS
OF POOR QUALITY

1996/7

EARTH - MARS 1996/7 , C3L . TFL

* BALLISTIC TRANSFER TRAJECTORY

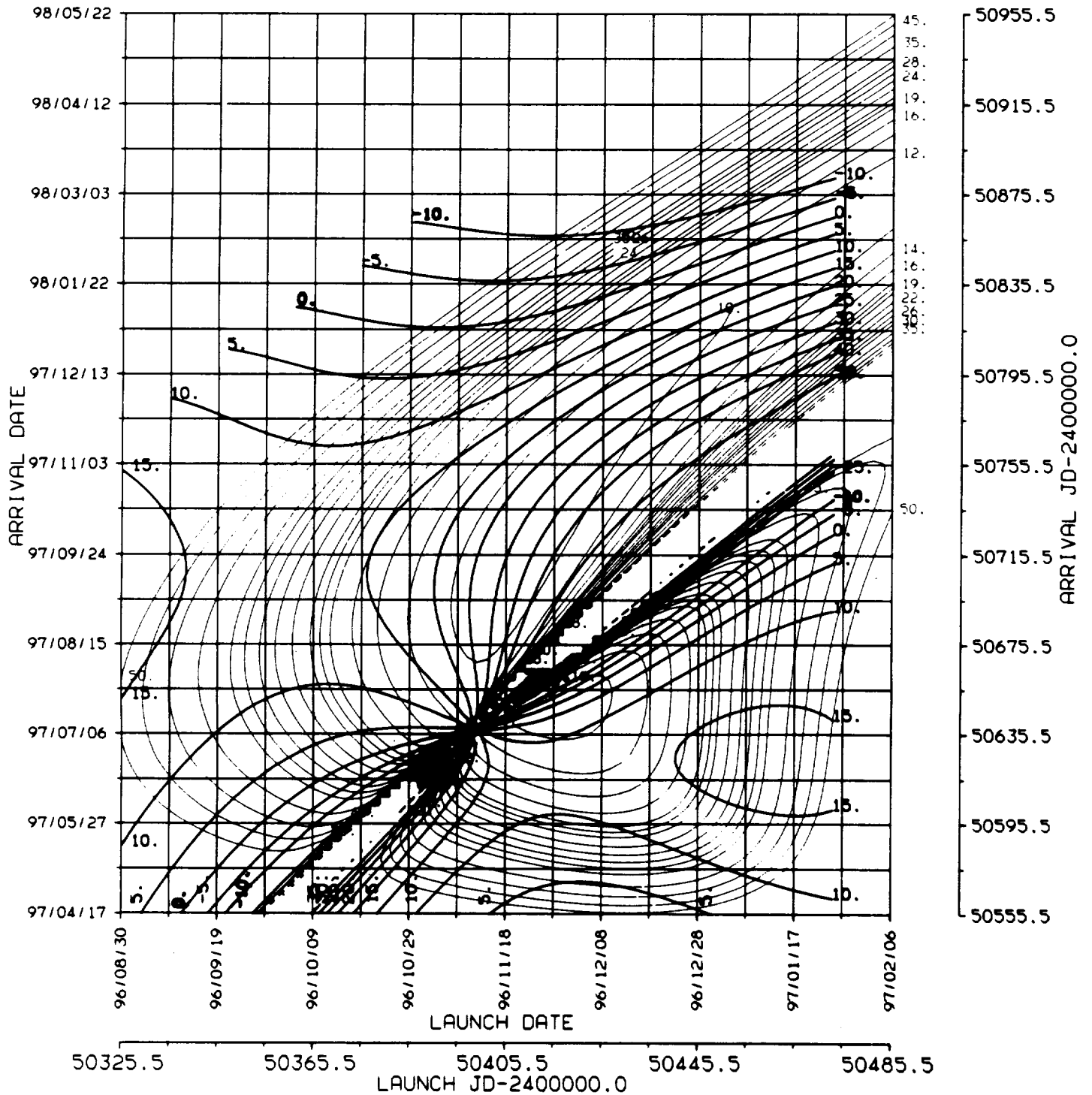


ORIGINAL PAGE IS
OF POOR QUALITY

2.
DLA
♂

1996/7

EARTH - MARS 1996/7 , C3L , DLA
BALLISTIC TRANSFER TRAJECTORY



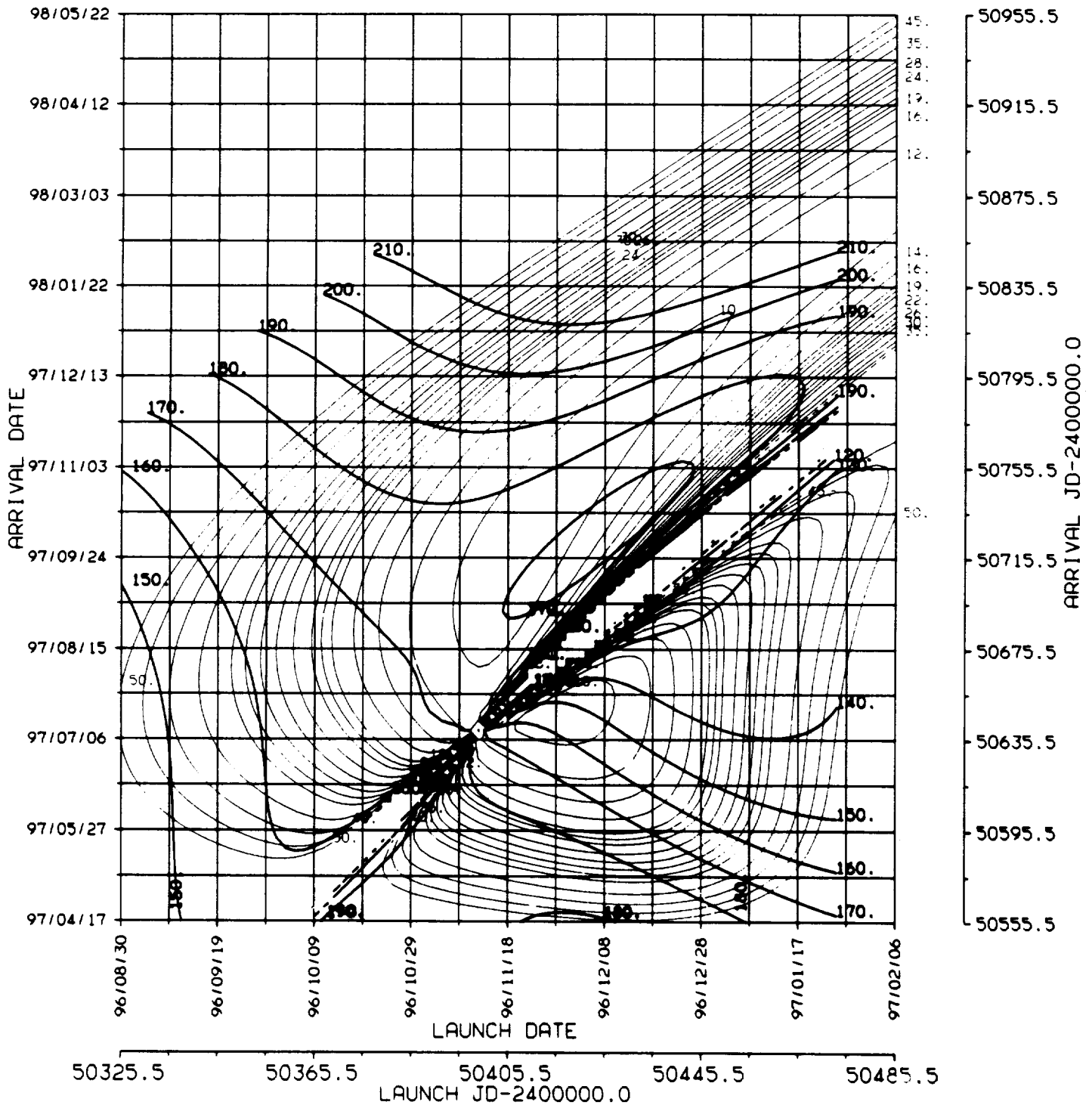
3.
RLA



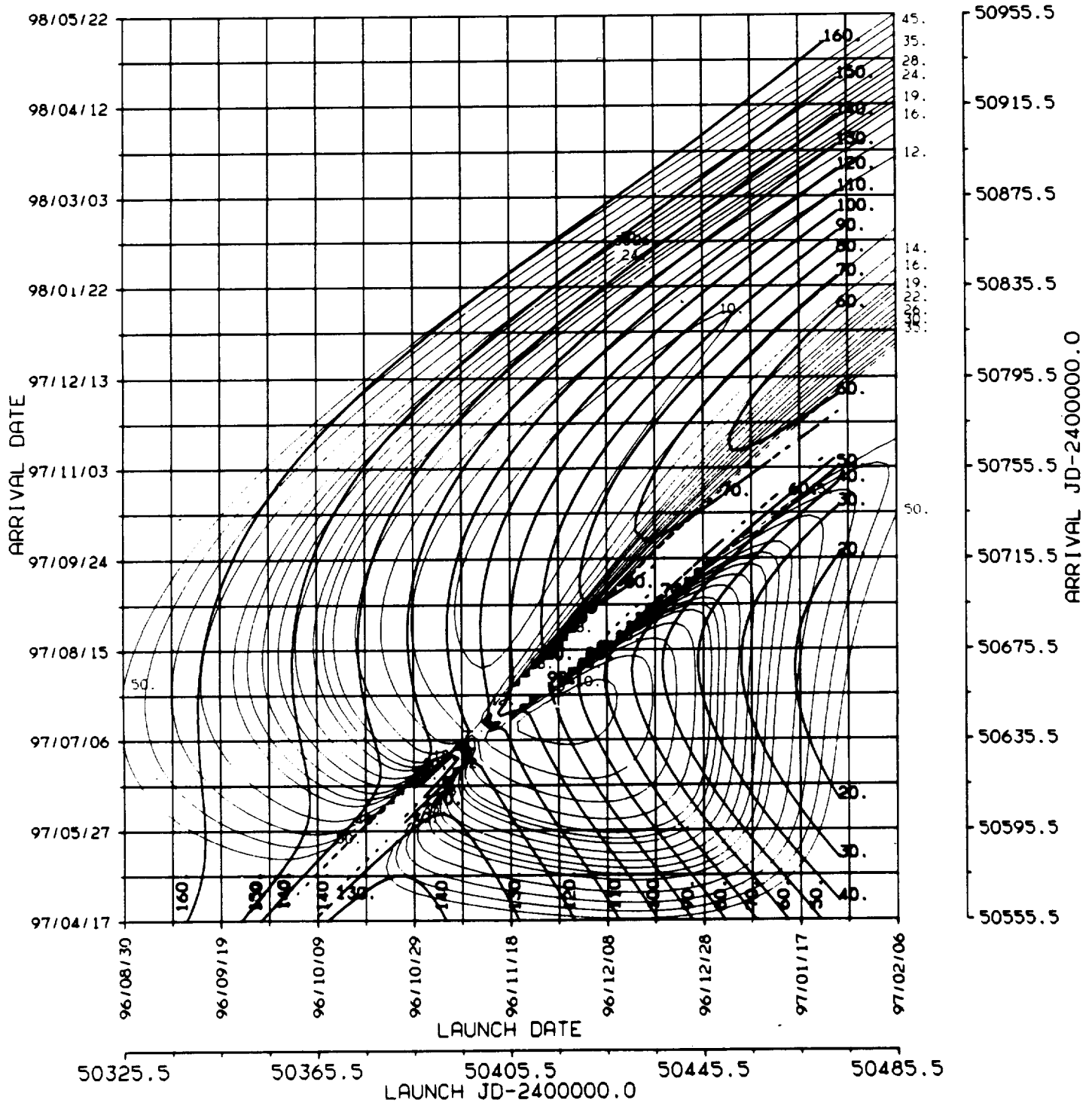
ORIGINAL PAGE IS
OF POOR QUALITY

1996/7

EARTH - MARS 1996/7 , C3L , RLA
BALLISTIC TRANSFER TRAJECTORY

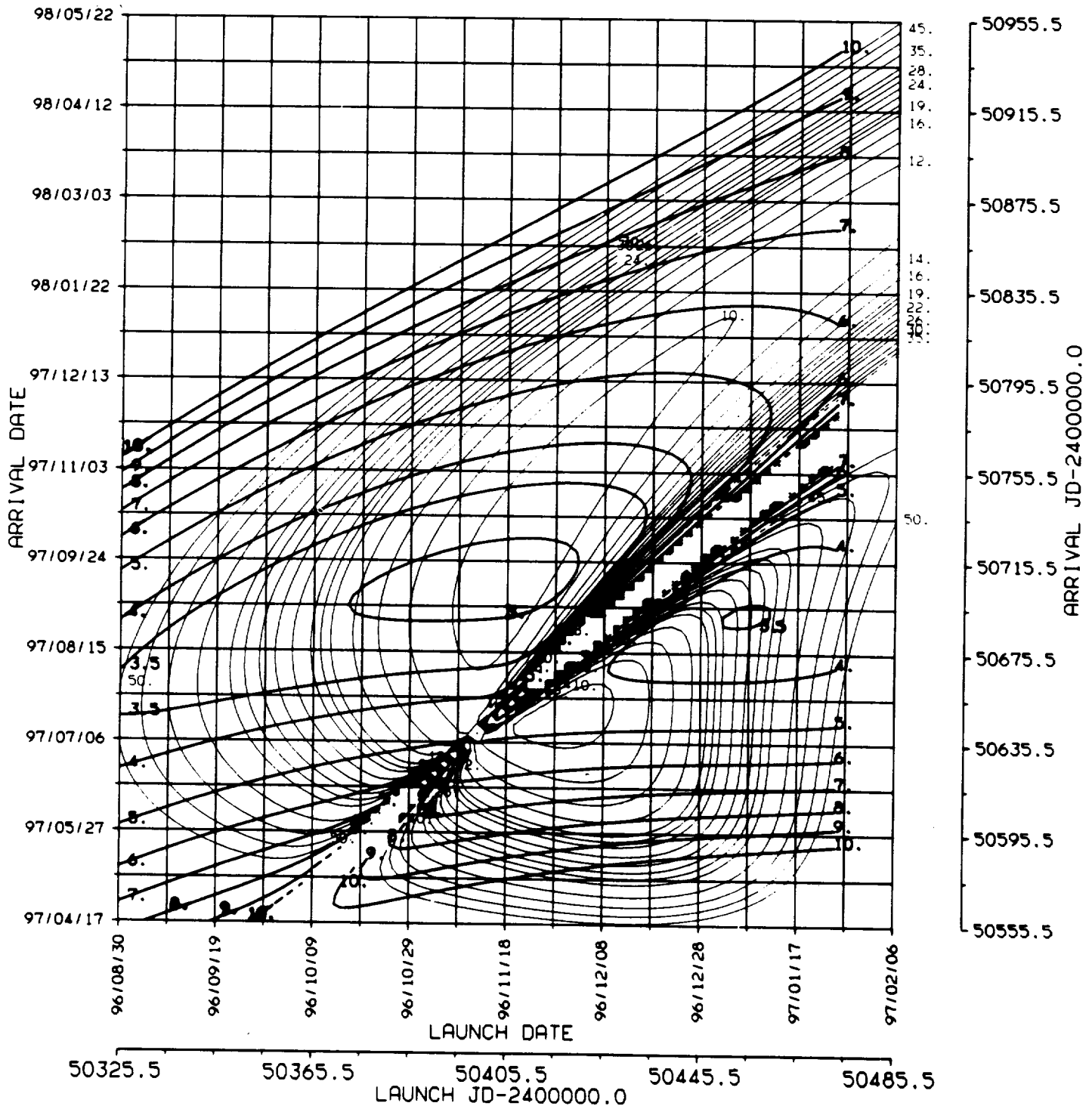


EARTH - MARS 1996/7 , C3L , ZALS
BALLISTIC TRANSFER TRAJECTORY



1996/7

EARTH - MARS 1996/7 , C3L , VHP
* BALLISTIC TRANSFER TRAJECTORY

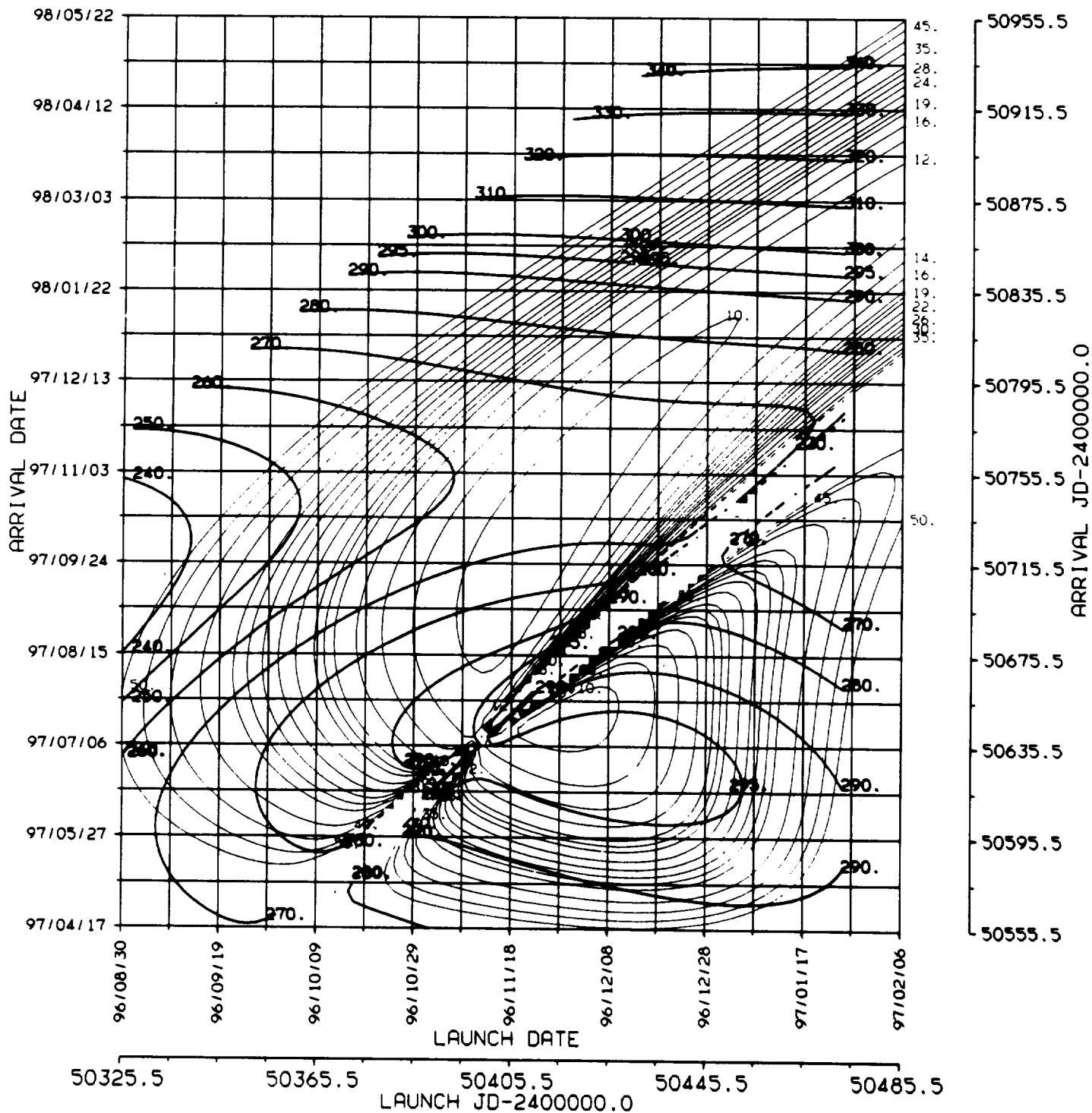


7.
RAP



ORIGINAL PAGE IS
OF POOR QUALITY

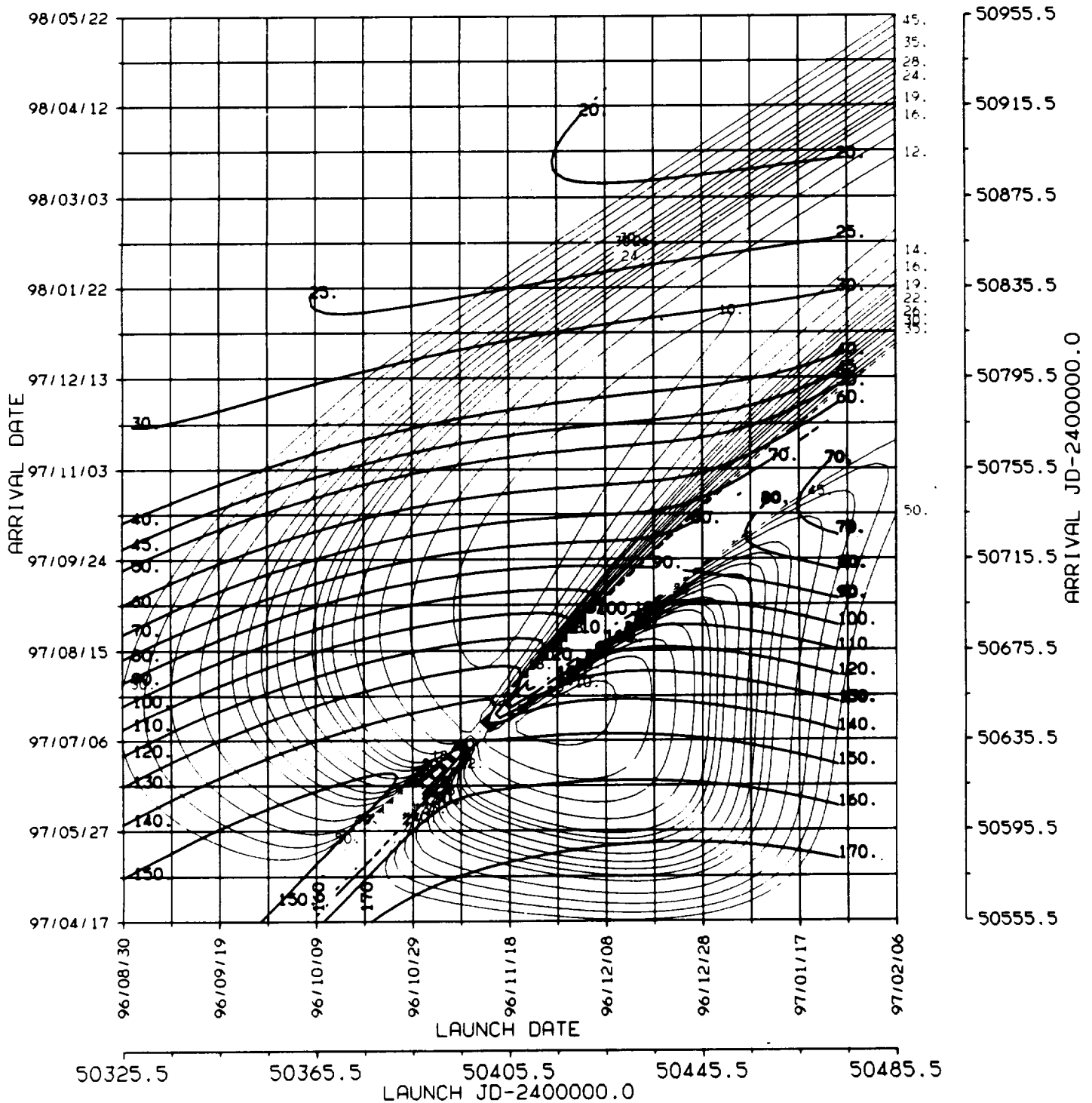
1996/7 EARTH - MARS 1996/7 , C3L , RAP
* BALLISTIC TRANSFER TRAJECTORY



ORIGINAL PAGE IS
OF POOR QUALITY

8.
ZAPS
♂
1996/7

EARTH - MARS 1996/7 , C3L , ZAPS
BALLISTIC TRANSFER TRAJECTORY



1996/7 EARTH - MARS 1996/7 . C3L , ZAPE
BALLISTIC TRANSFER TRAJECTORY



EARTH - MARS 1996/7 , C3L , ETSP
* BALLISTIC TRANSFER TRAJECTORY

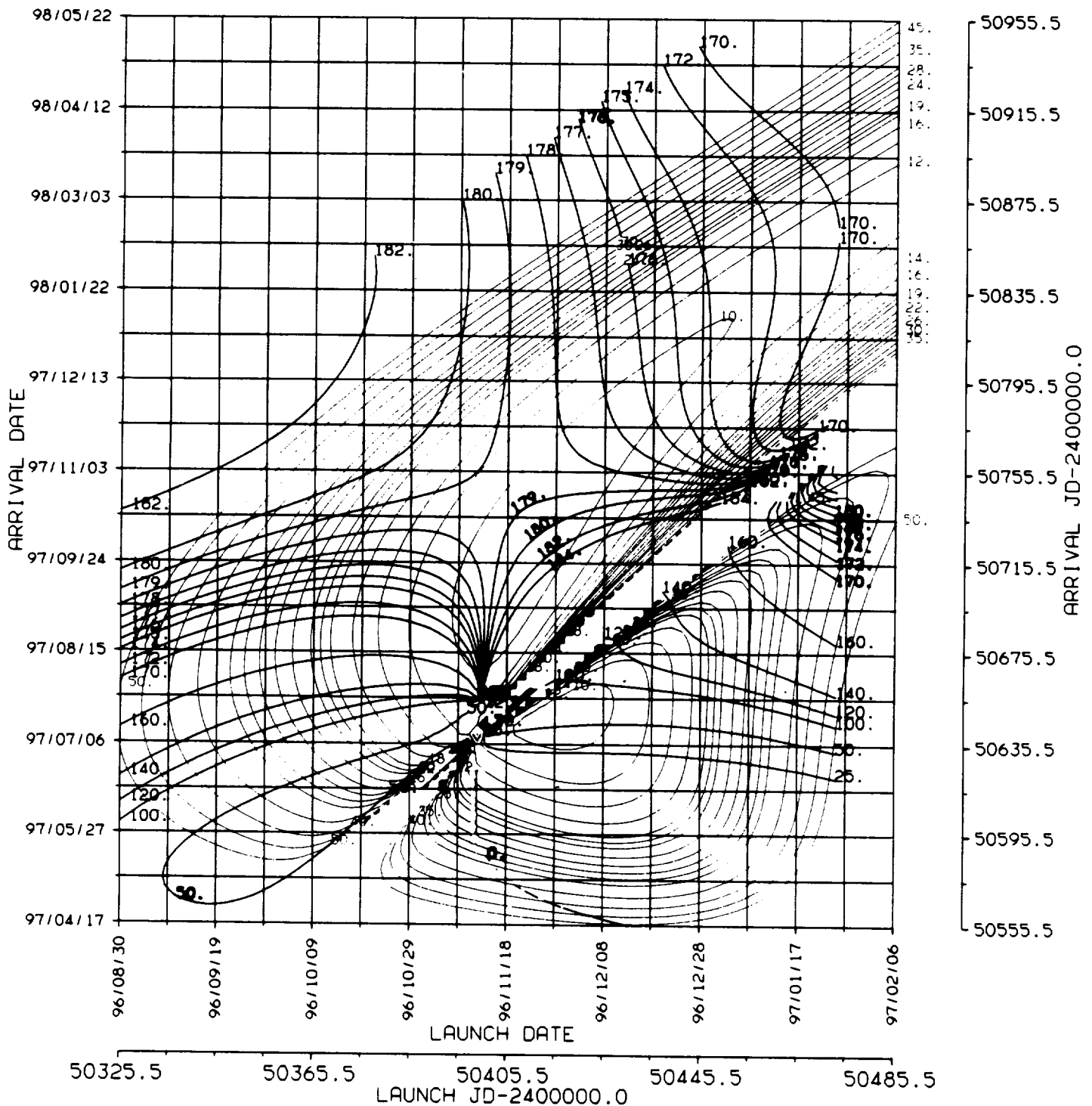




1996/7

EARTH - MARS 1996/7 , C3L , ETEP
BALLISTIC TRANSFER TRAJECTORY

ORIGINAL PAGE IS
OF POOR QUALITY



Earth to Mars

1998/9

Opportunity

ENERGY MINIMA

	VALUE	TYPE	DEPARTURE (YEAR/MONTH/DAY)	ARRIVAL (YEAR/MONTH/DAY)
C ₃ L	9.0164	I	99/01/16	99/07/30
C ₃ L	8.4403	II	99/02/07	99/12/31
VHP	3.7826	I	99/02/19	99/09/20
VHP	3.3391	II	98/12/08	99/09/23

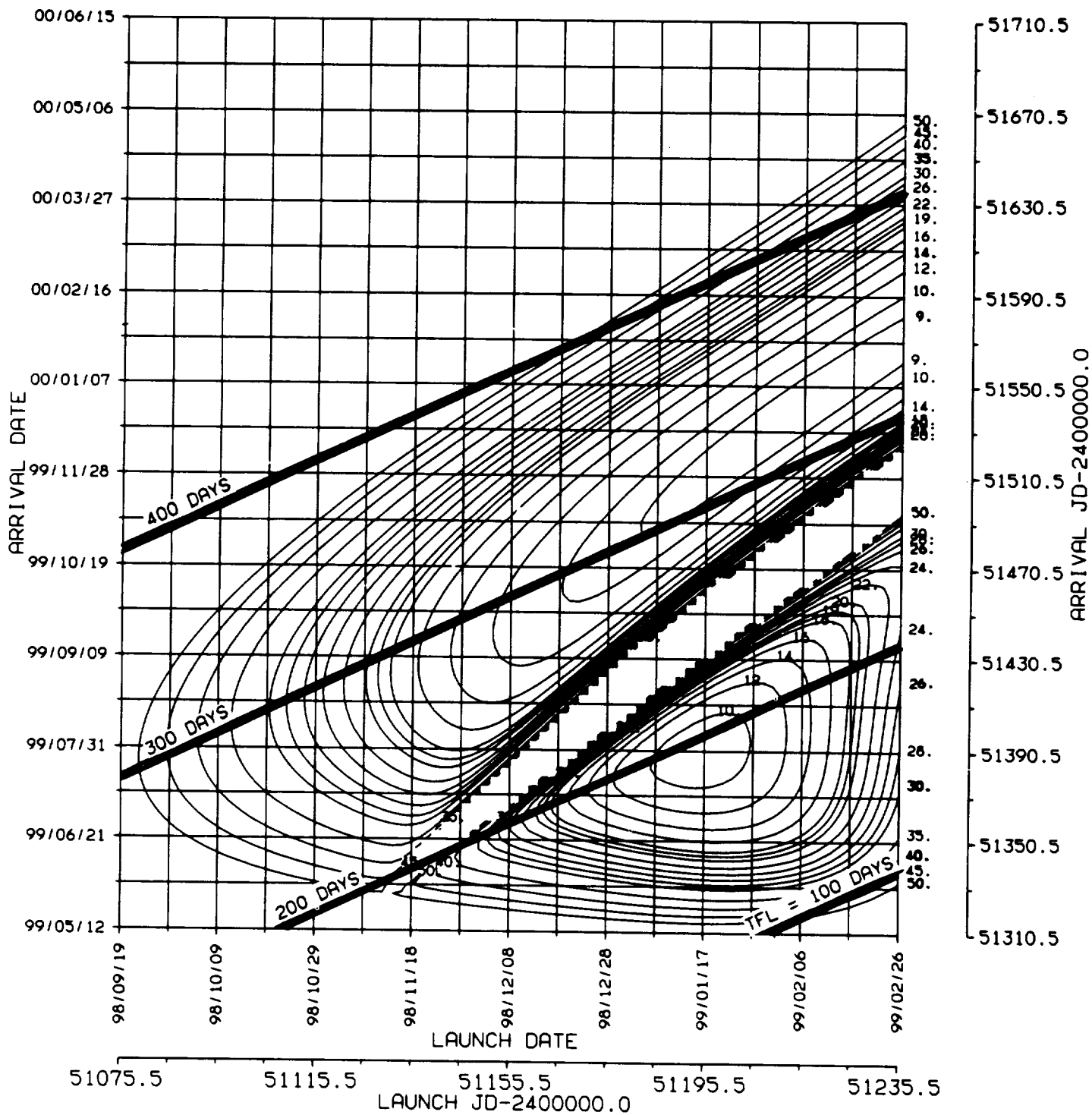


ORIGINAL PAGE 19
OF POOR QUALITY

1998/9

EARTH - MARS 1998/9 , C3L TFL

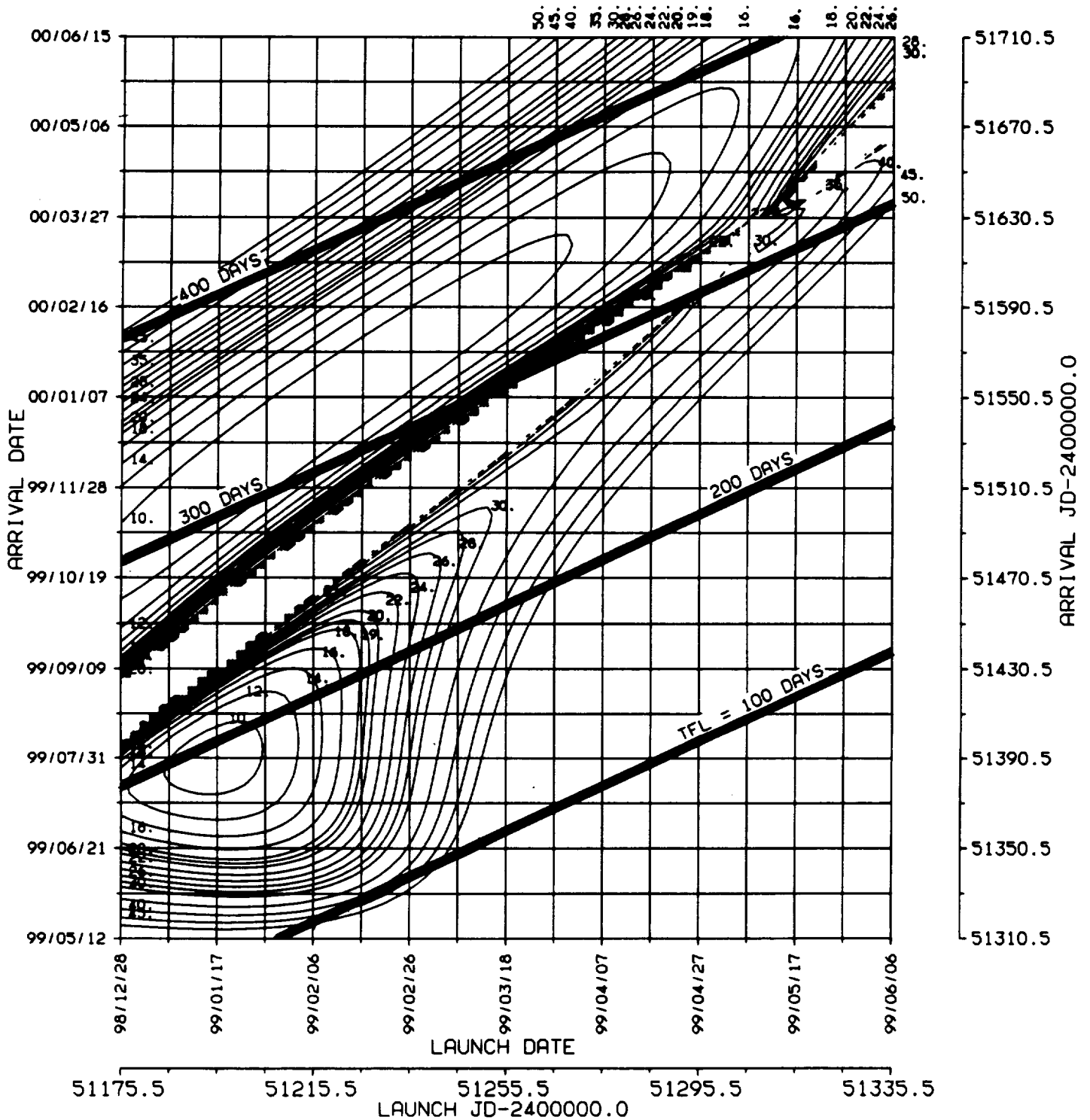
* BALLISTIC TRANSFER TRAJECTORY



ORIGINAL PAGE 19
OF POOR QUALITY

EARTH - MARS 1998/9 , C3L . TFL

* BALLISTIC TRANSFER TRAJECTORY



2.
DLA

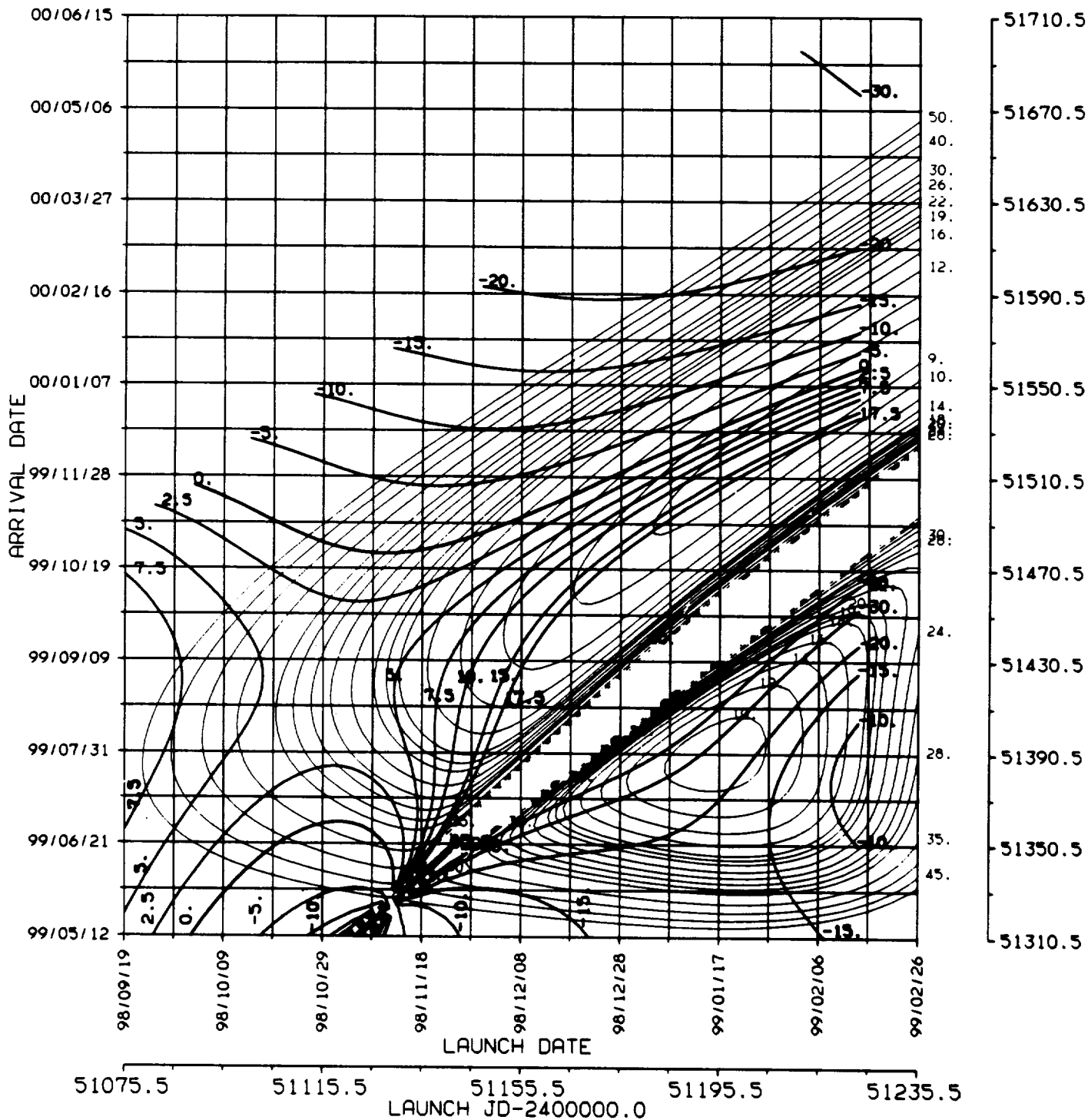


1998/9

ORIGINAL PAGE IS
OF POOR QUALITY

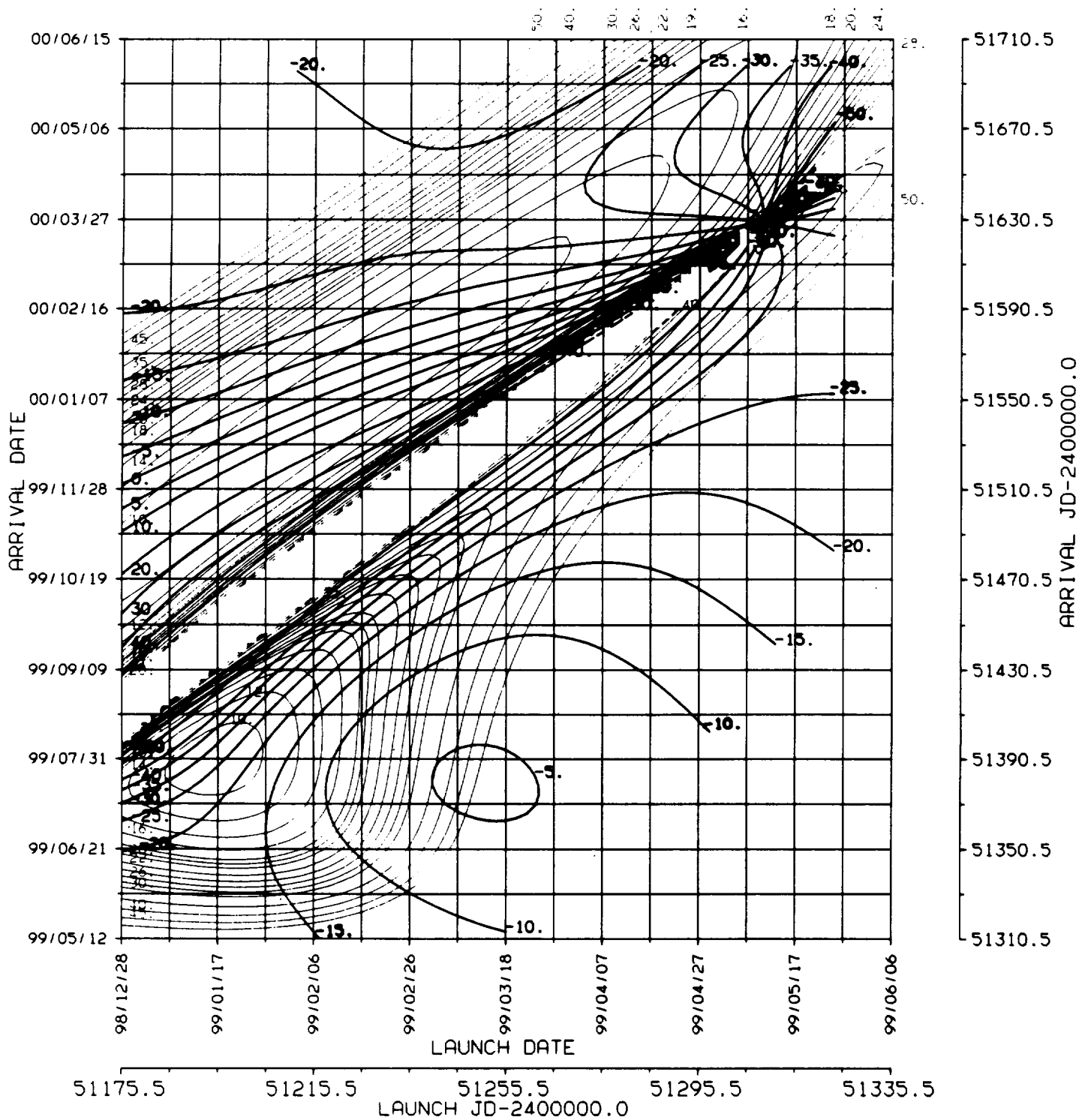
EARTH - MARS 1998/9 , C3L , DLA

* BALLISTIC TRANSFER TRAJECTORY

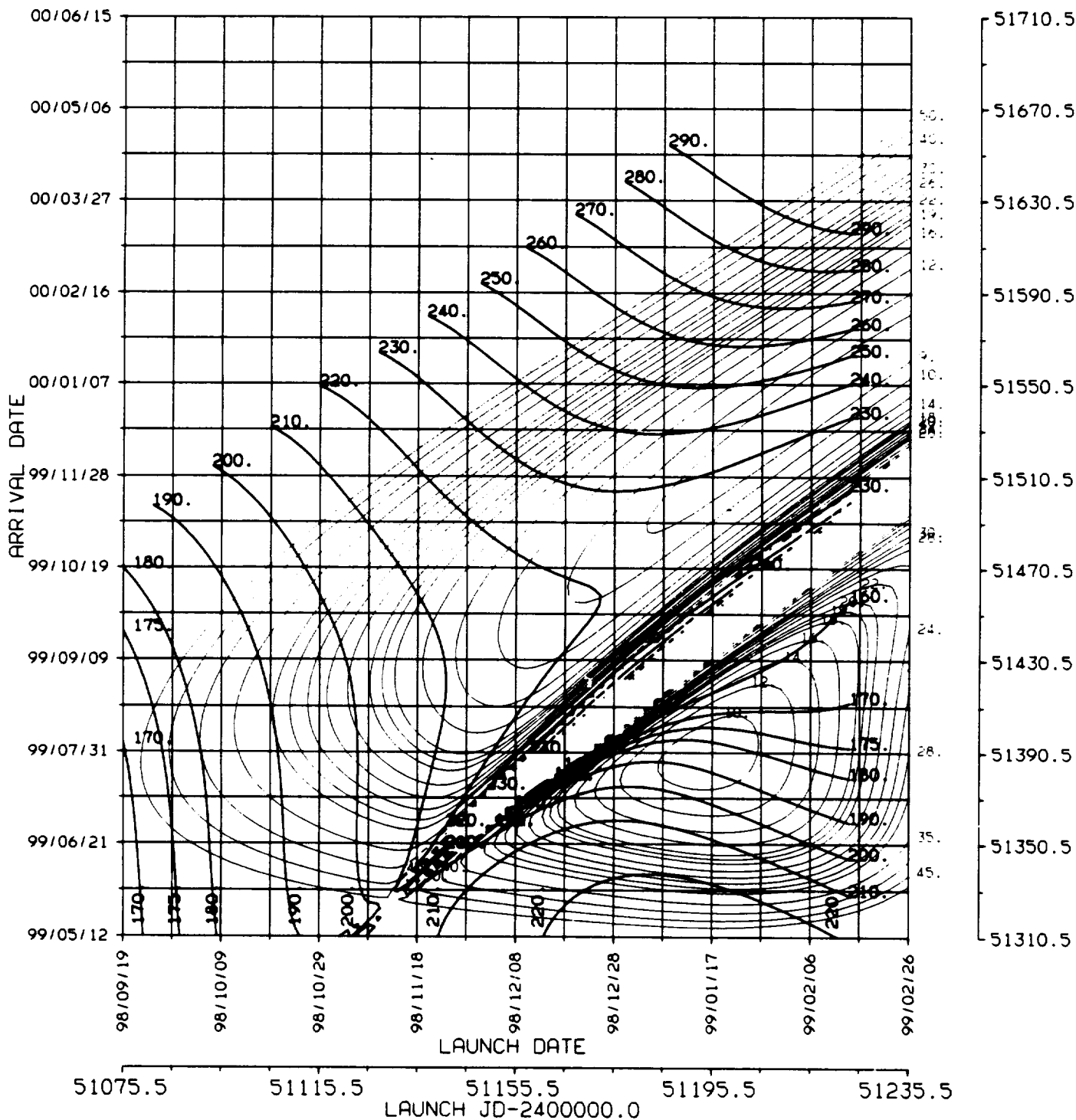


ORIGINAL PAGE IS
OF POOR QUALITY

EARTH - MARS 1998/9 , C3L , DLA
BALLISTIC TRANSFER TRAJECTORY

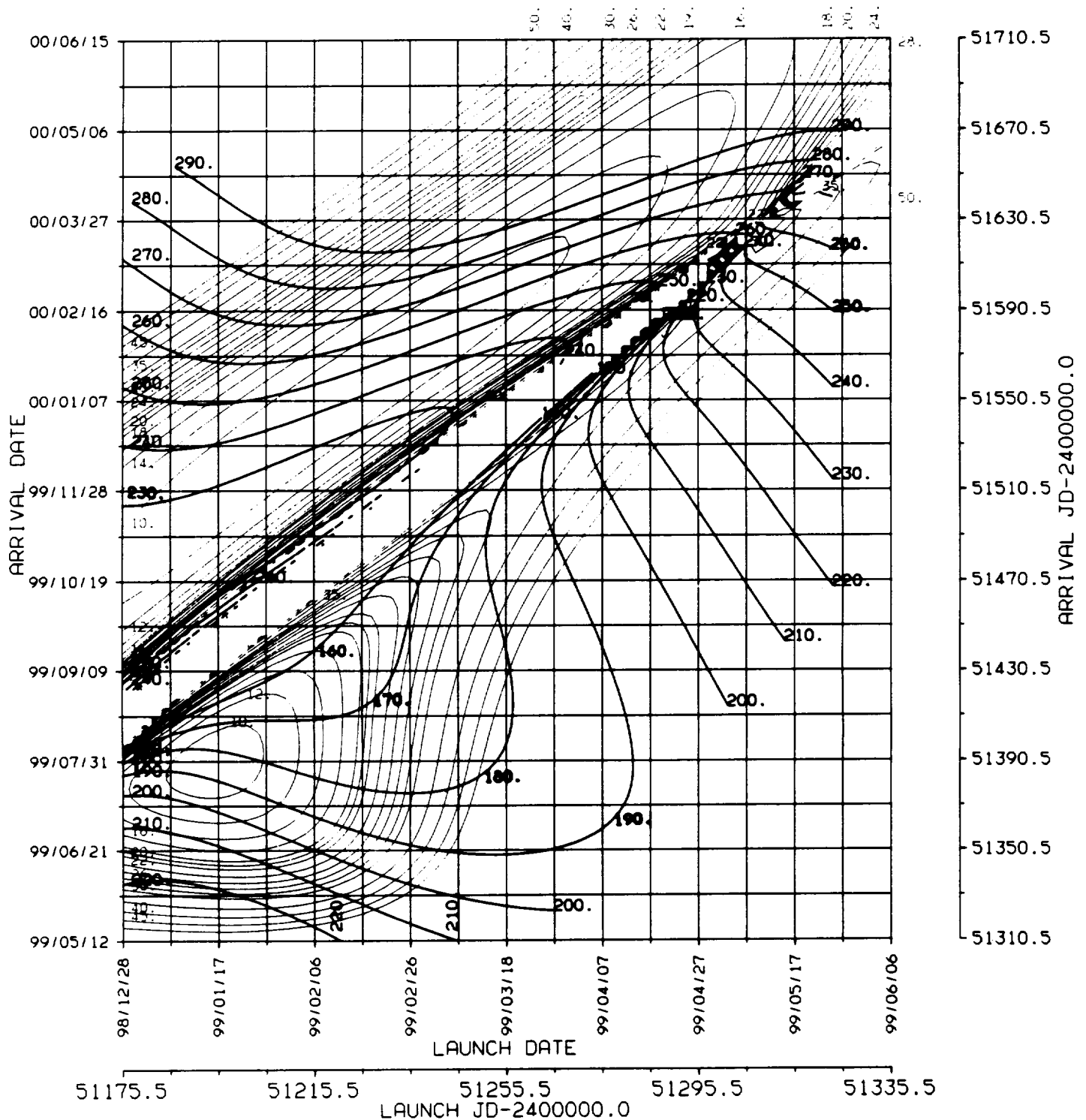


EARTH - MARS 1998/9 . C3L . RLA
BALLISTIC TRANSFER TRAJECTORY



ORIGINAL PAGE 13
OF POOR QUALITY

EARTH - MARS 1998/9 , C3L , RLA
BALLISTIC TRANSFER TRAJECTORY

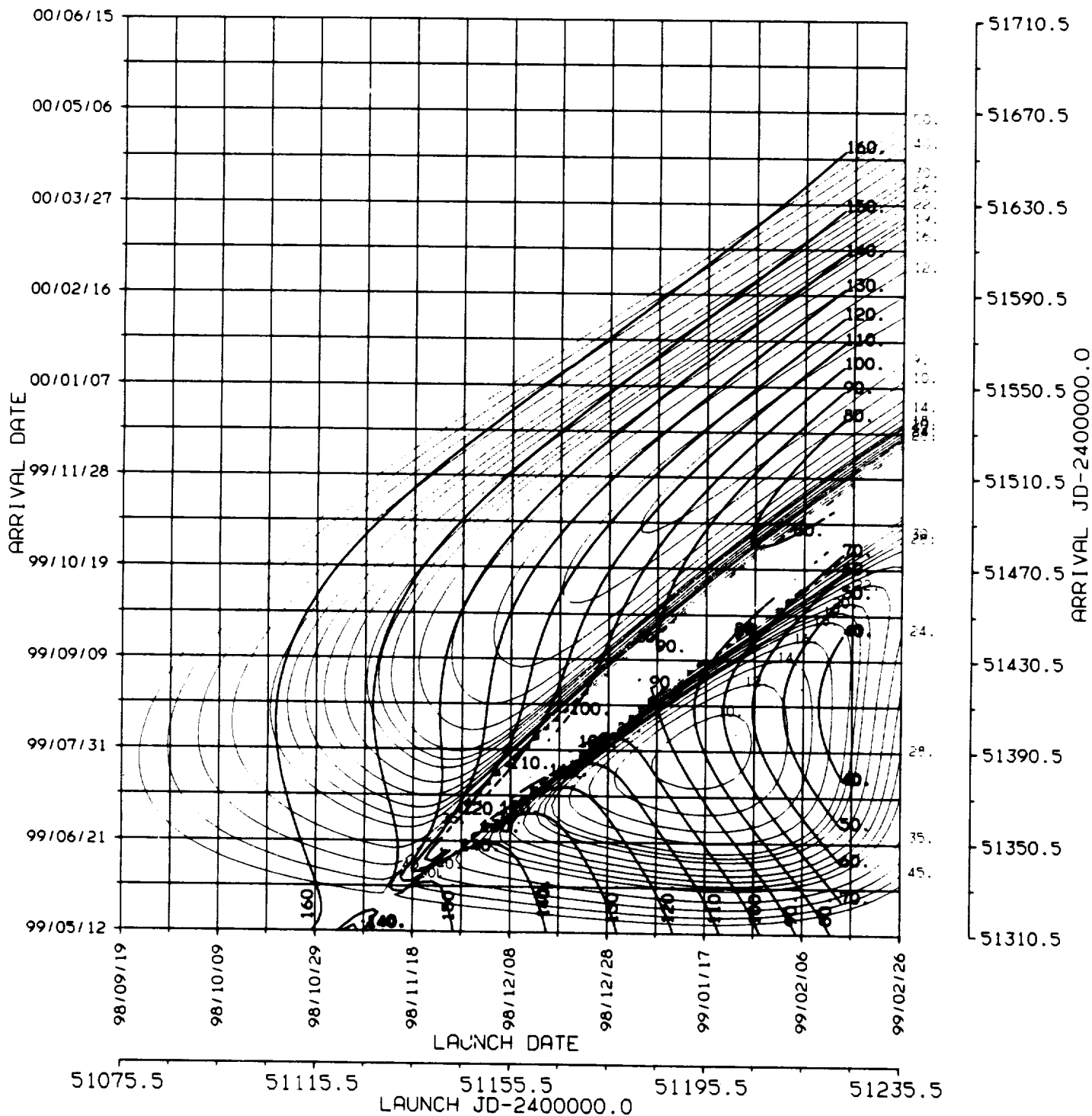


C-2

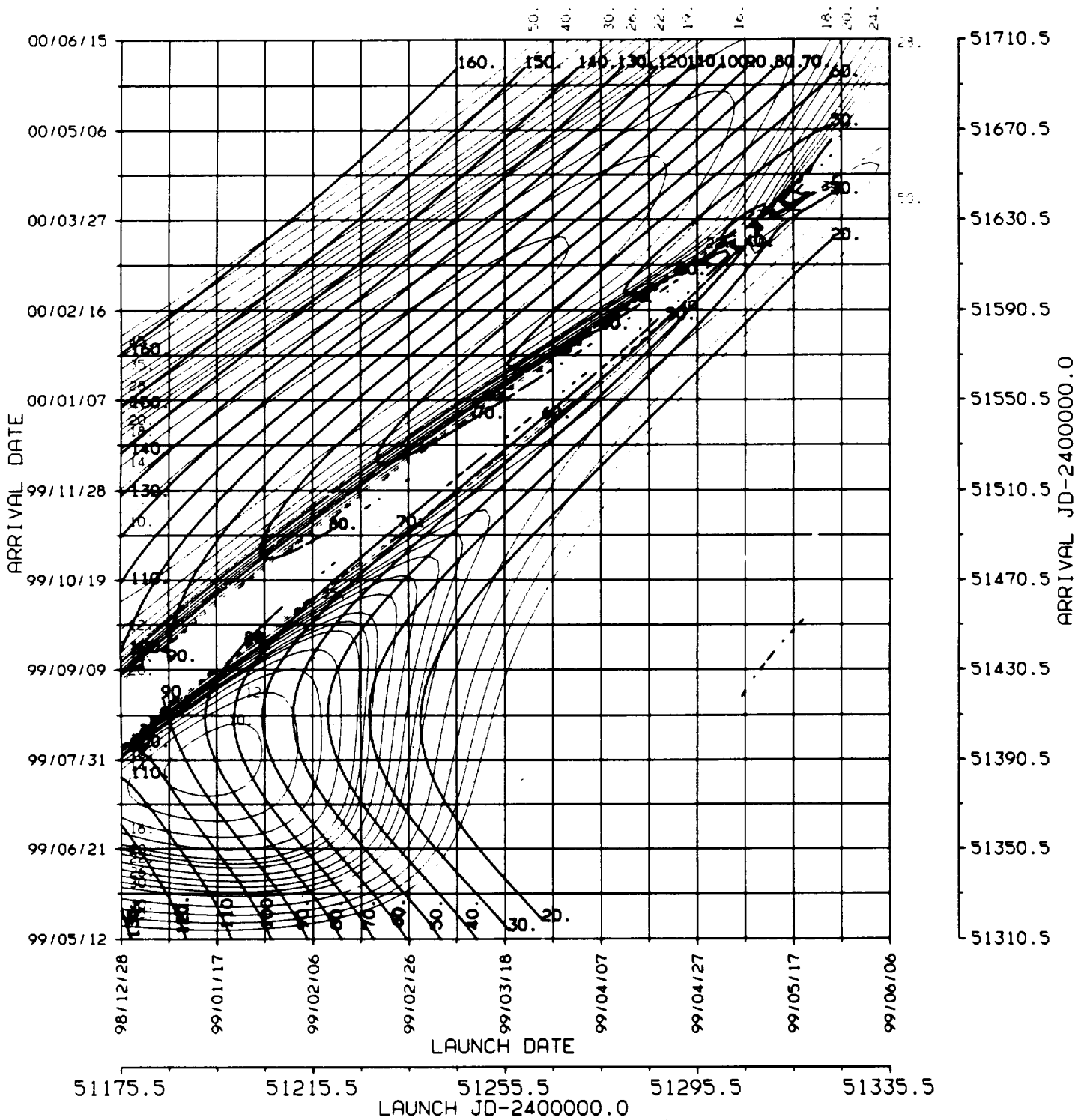
4.
ZALS
♂
1998/9

ORIGINAL PAGE IS
OF POOR QUALITY

EARTH - MARS 1998/9 . C3L . ZALS
BALLISTIC TRANSFER TRAJECTORY



EARTH - MARS 1998/9 , C3L , ZALS BALLISTIC TRANSFER TRAJECTORY



5.
VHP



1998/9

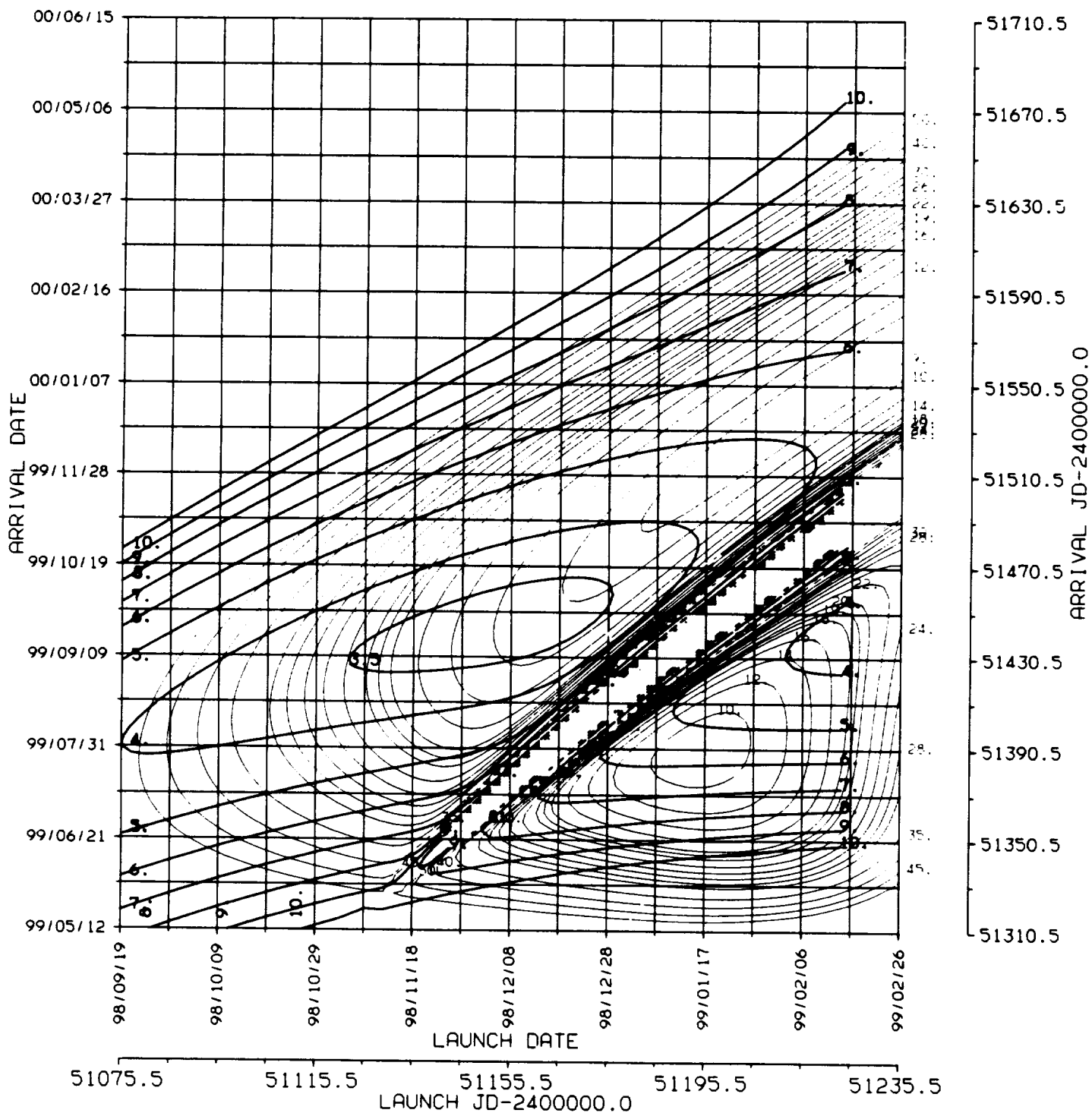
EARTH - MARS 1998/9

C3L

VHP

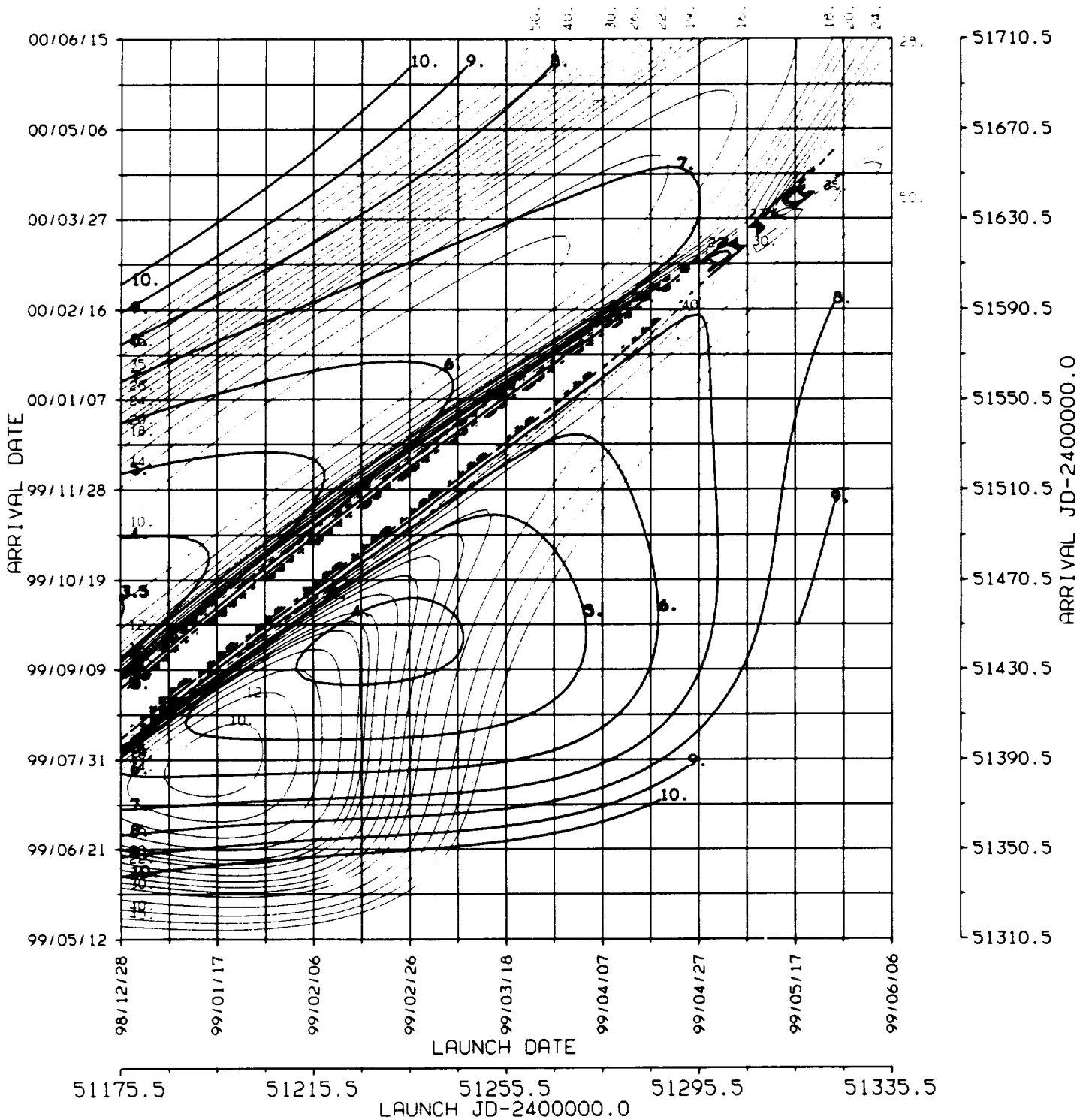
BALLISTIC TRANSFER TRAJECTORY

ORIGINAL PAGE IS
OF POOR QUALITY



ORIGINAL PAGE IS
OF POOR QUALITY

EARTH - MARS 1998/9 C3L VHP
BALLISTIC TRANSFER TRAJECTORY



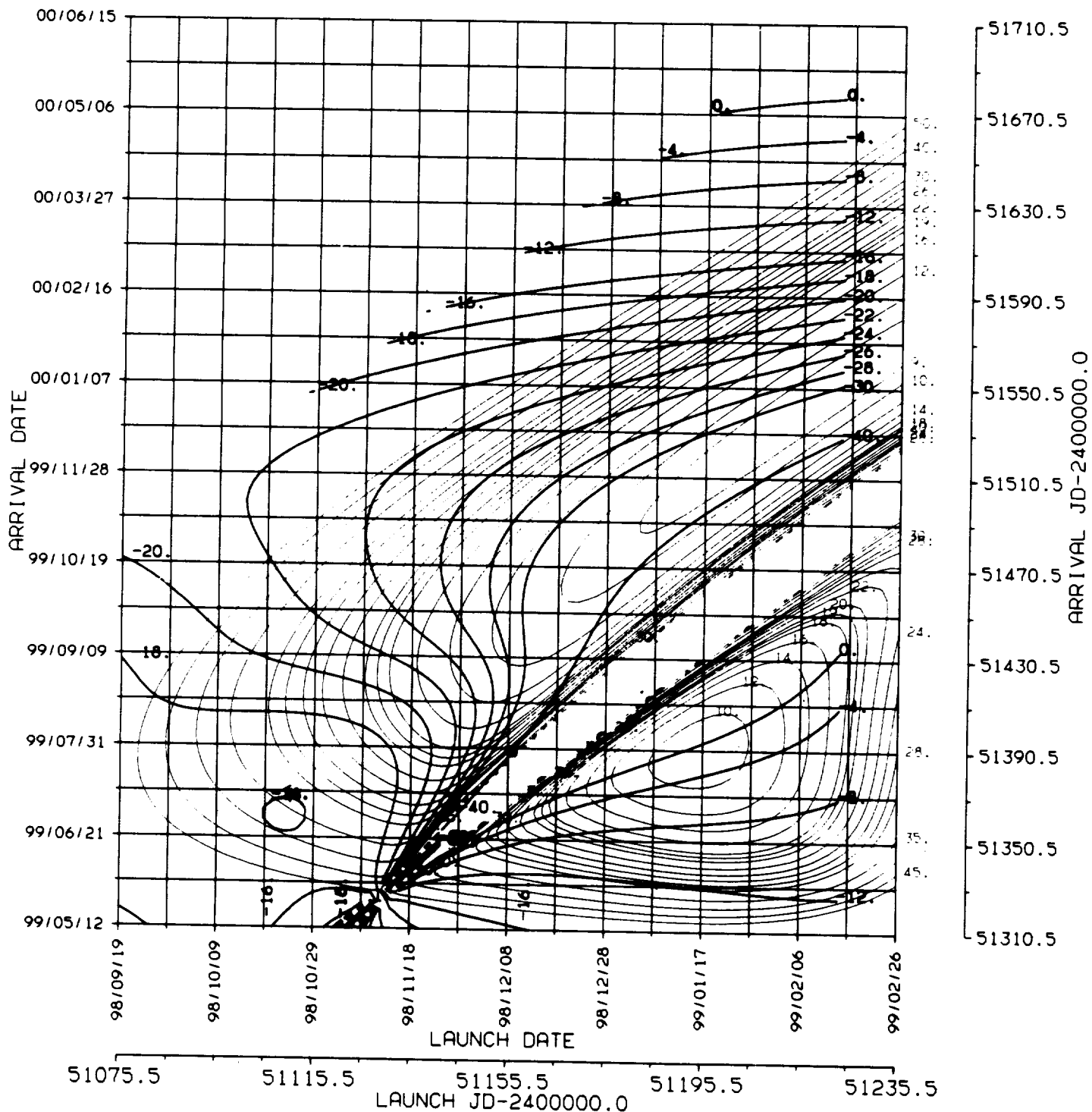
6.
DAP



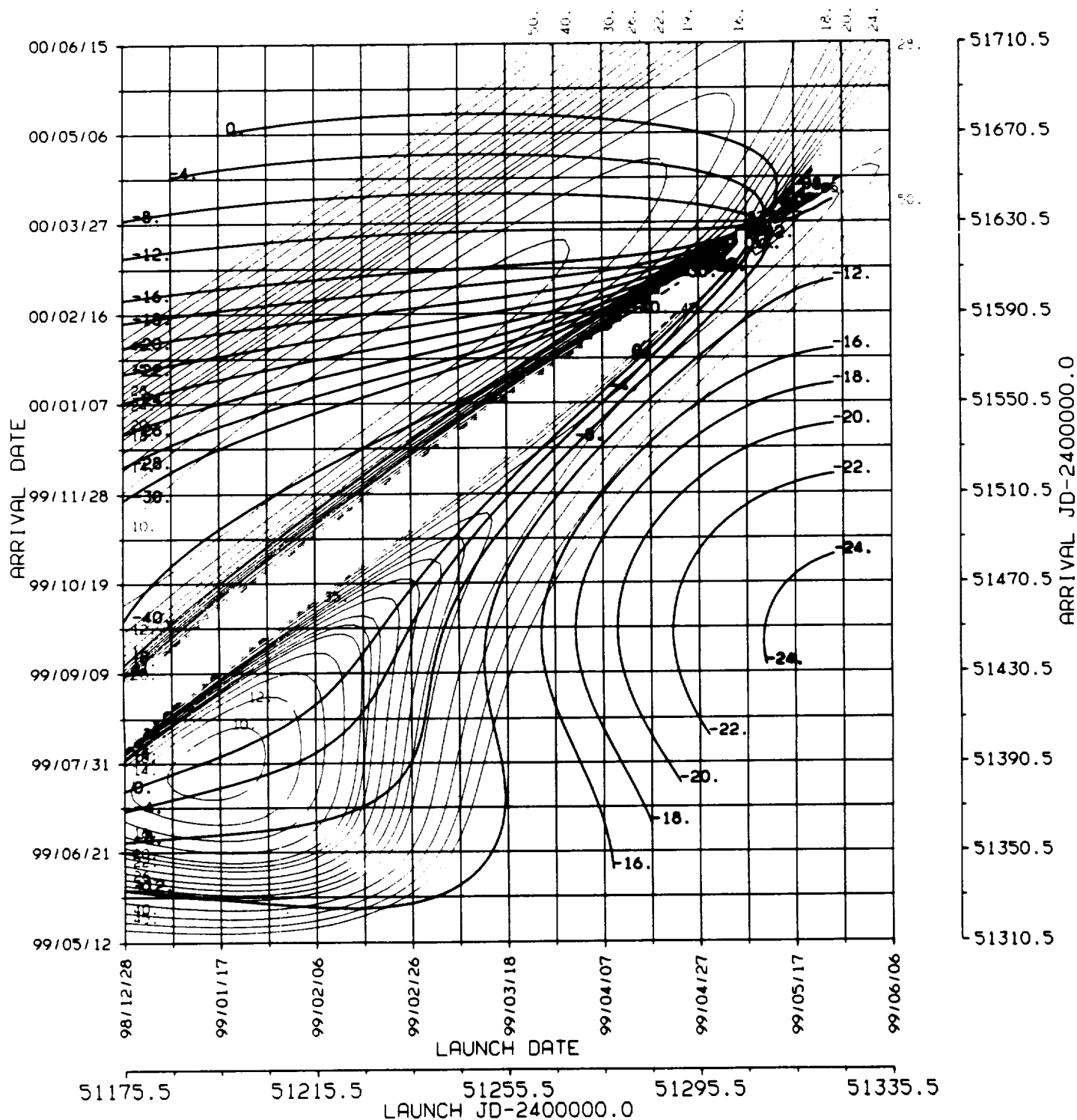
1998/9

ORIGINAL PAGE IS
OF POOR QUALITY

EARTH - MARS 1998/9 . C3L . DAP
BALLISTIC TRANSFER TRAJECTORY

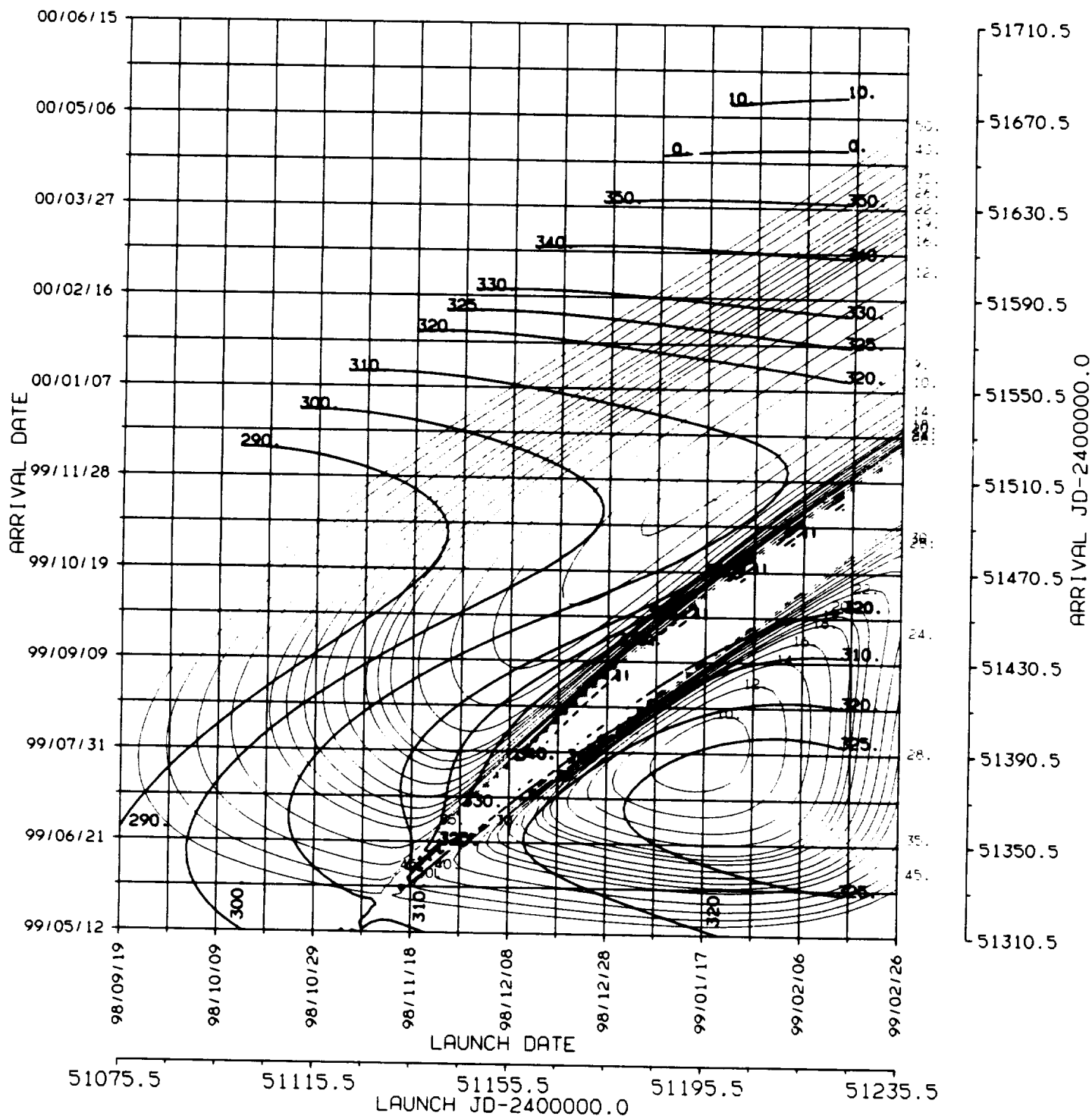


EARTH - MARS 1998/9 , C3L , DAP BALLISTIC TRANSFER TRAJECTORY

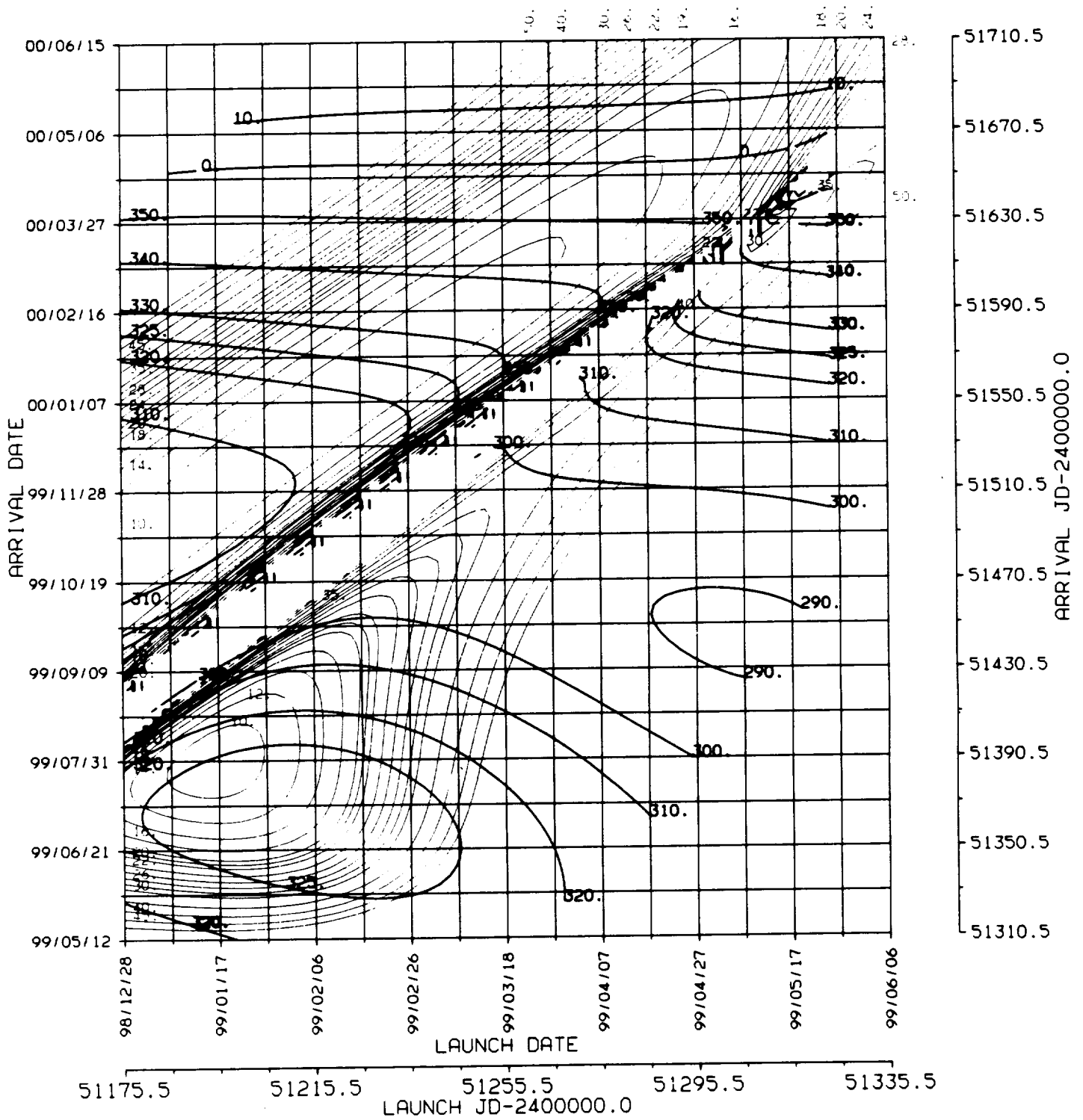


1998/9

EARTH - MARS 1998/9 . C3L . RAP
BALLISTIC TRANSFER TRAJECTORY



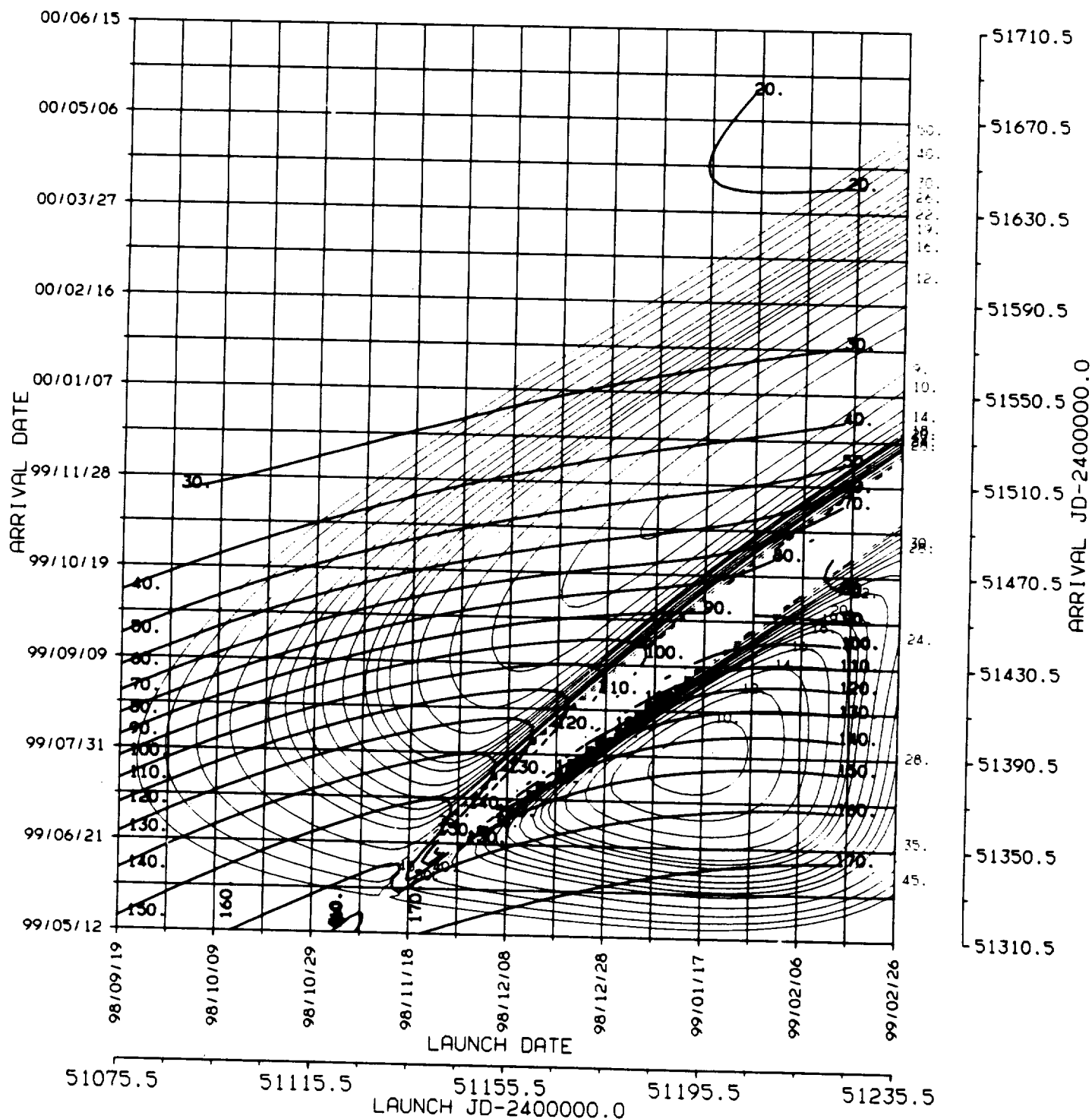
EARTH - MARS 1998/9 , C3L , RAP BALLISTIC TRANSFER TRAJECTORY



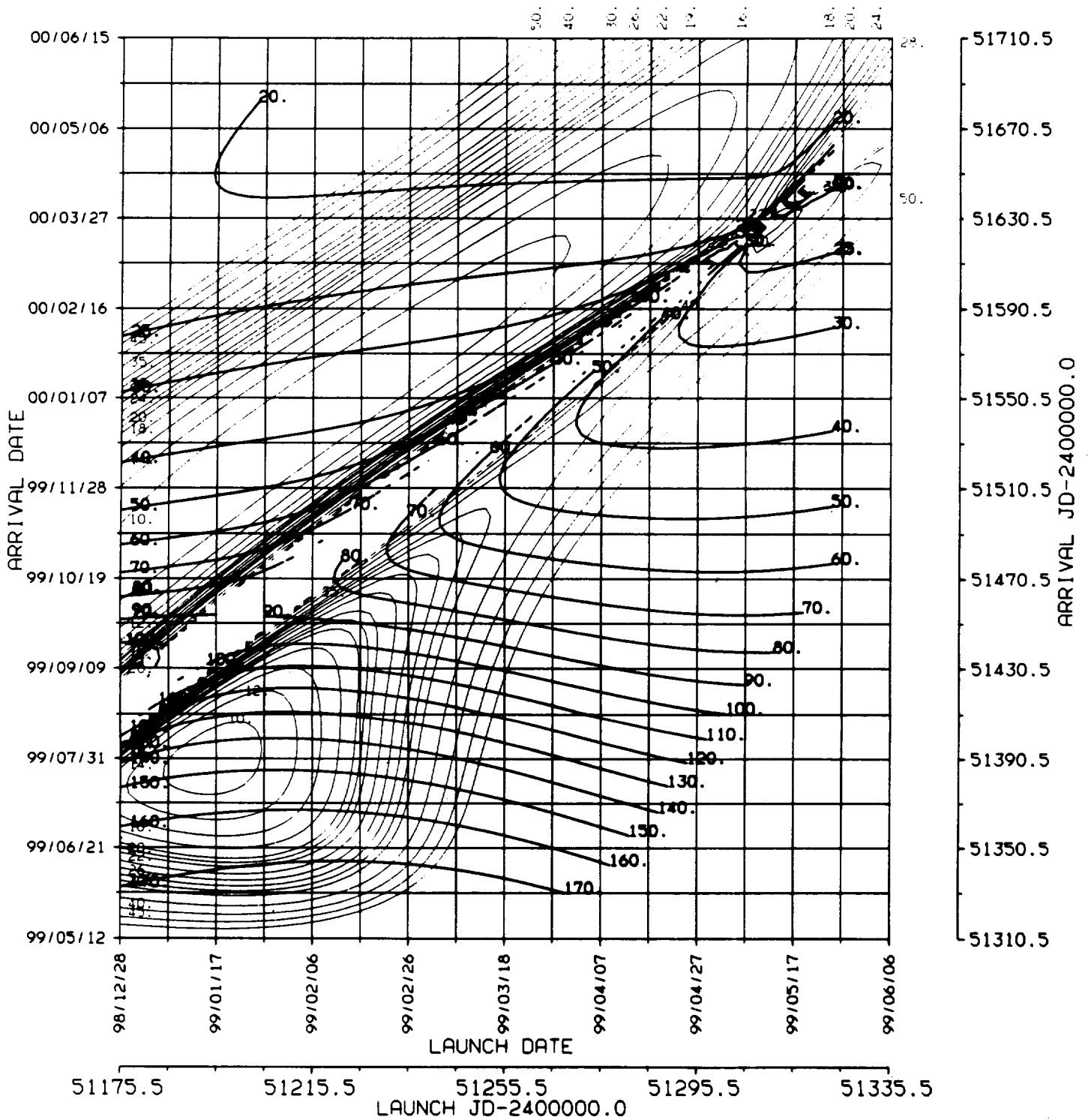


1998/9

EARTH - MARS 1998/9 . C3L . ZAPS
BALLISTIC TRANSFER TRAJECTORY



EARTH - MARS 1998/9 , C3L , ZAPS BALLISTIC TRANSFER TRAJECTORY



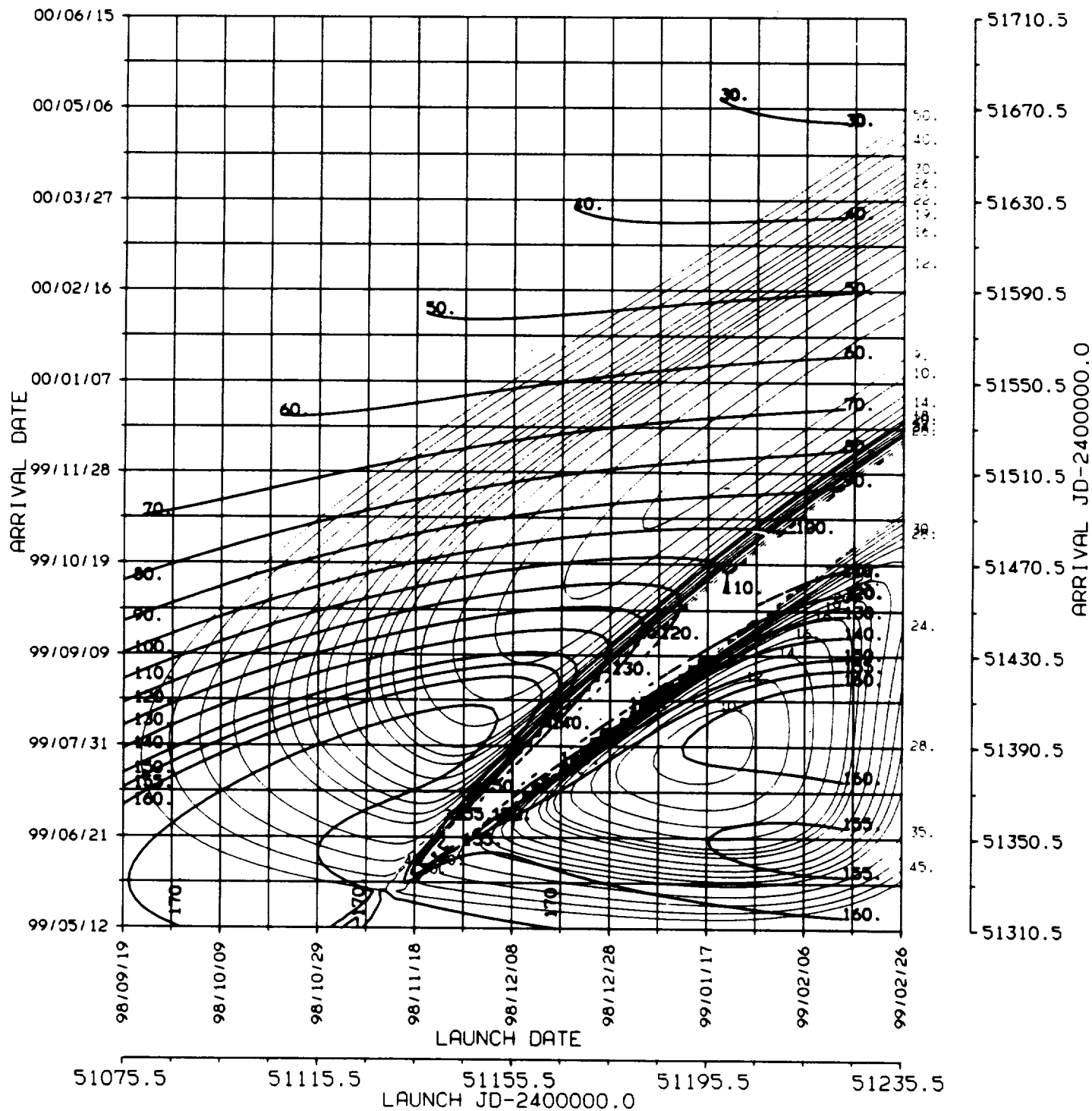
9.
ZAPE



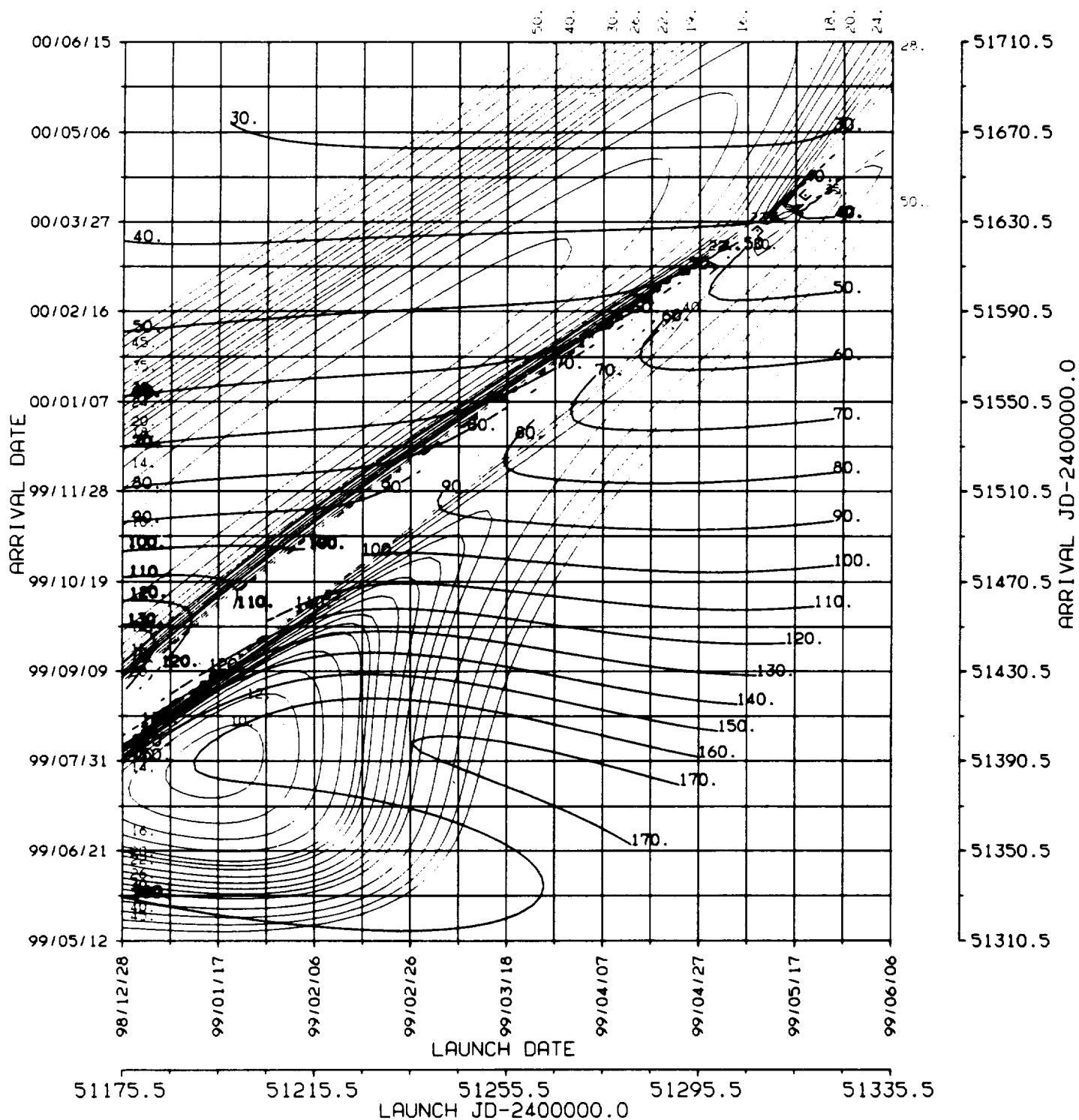
1998/9

ORIGINAL PAGE IS
OF POOR QUALITY

EARTH - MARS 1998/9 , C3L , ZAPE
BALLISTIC TRANSFER TRAJECTORY

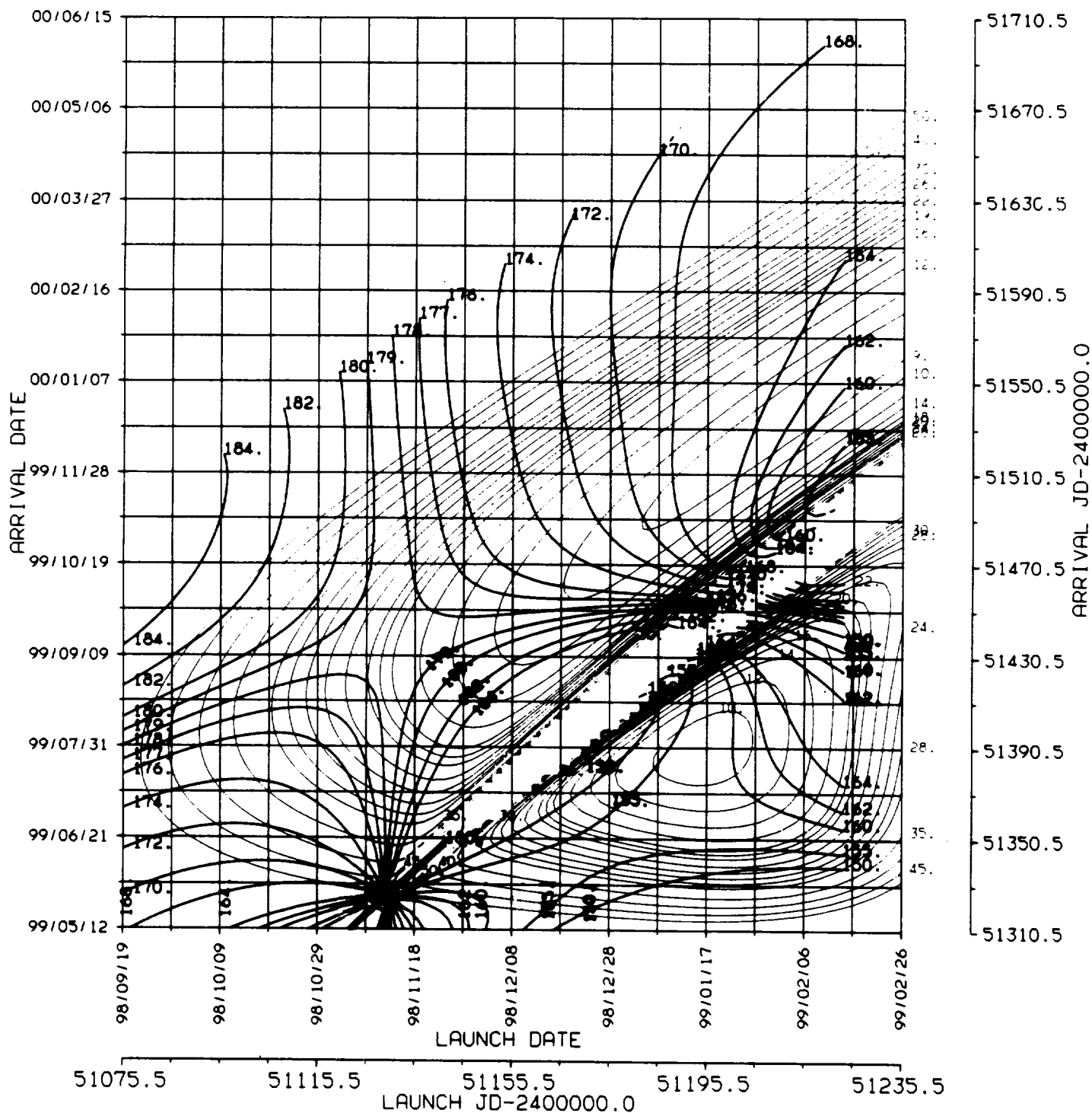


EARTH - MARS 1998/9 , C3L , ZAPE BALLISTIC TRANSFER TRAJECTORY

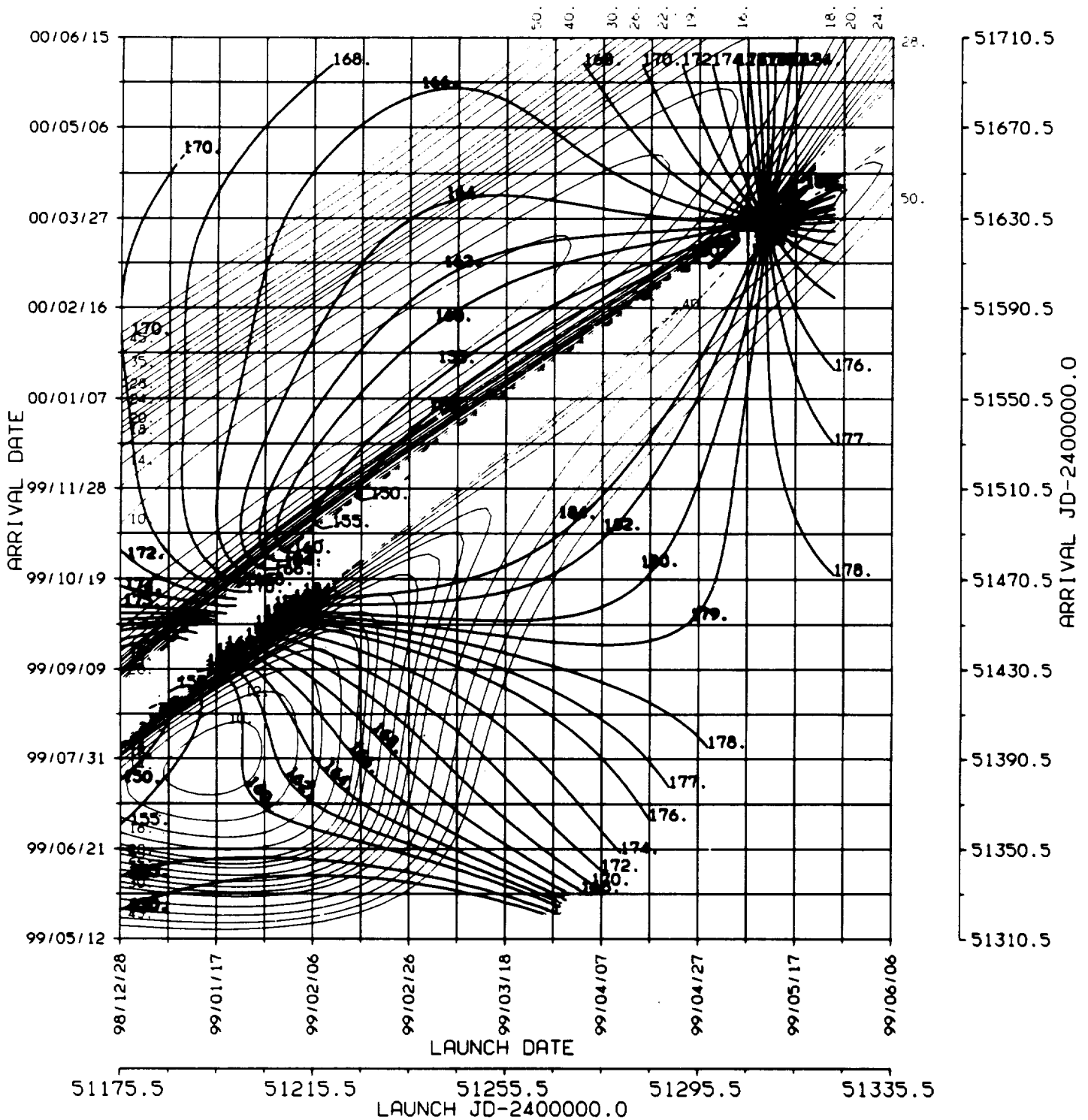


1998/9

EARTH - MARS 1998/9 , C3L , ETSP
BALLISTIC TRANSFER TRAJECTORY



EARTH - MARS 1998/9 , C3L , ETSP BALLISTIC TRANSFER TRAJECTORY



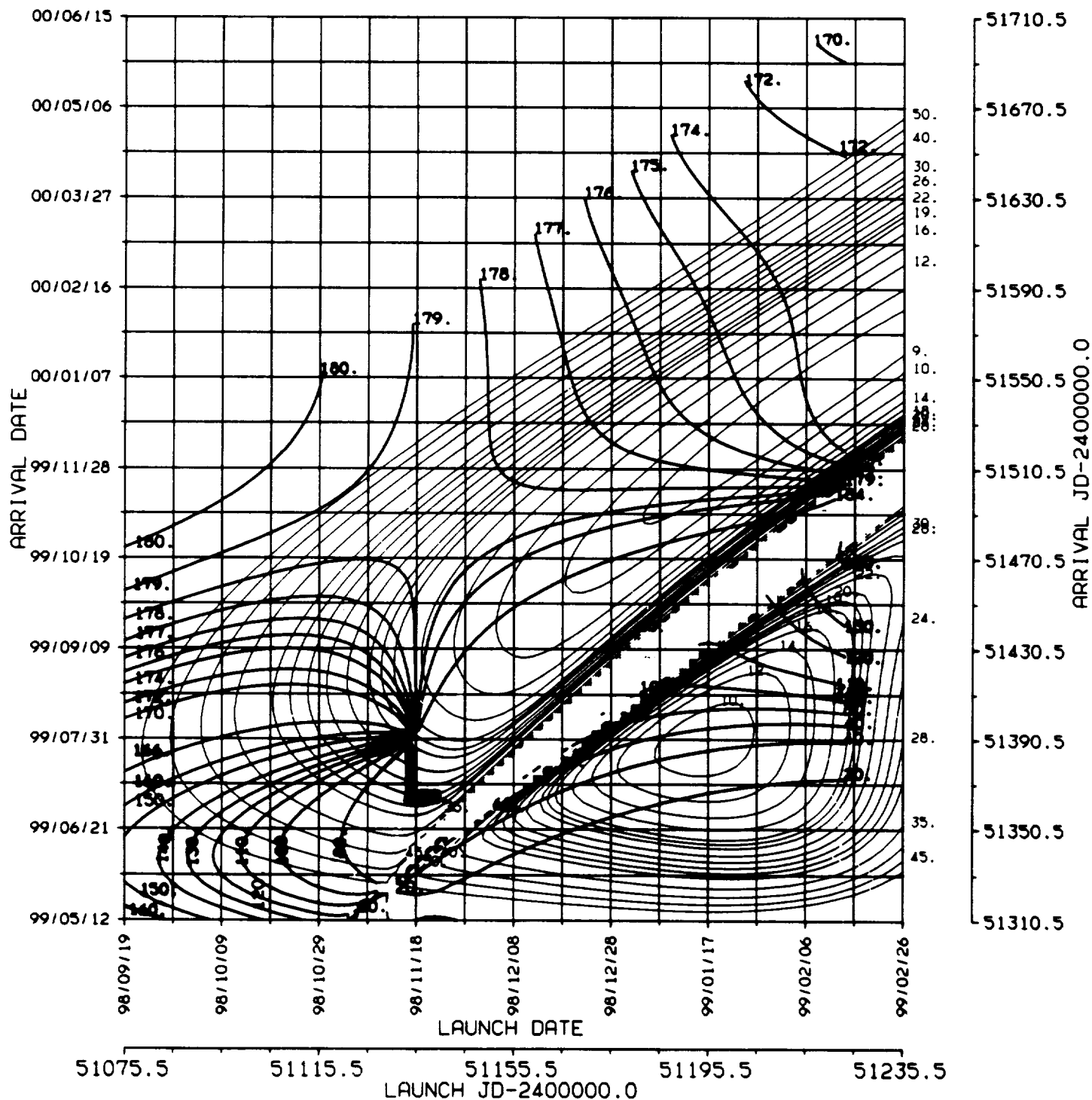


1998/9

EARTH - MARS 1998/9 , C3L , ETEP

*

BALLISTIC TRANSFER TRAJECTORY



Earth to Mars

2000/1

Opportunity

ENERGY MINIMA

	VALUE	TYPE	DEPARTURE (YEAR/MONTH/DAY)	ARRIVAL (YEAR/MONTH/DAY)
C ₃ L	8.6342	I	2001/03/19	2001/09/10
C ₃ L	7.8538	II	2001/04/16	2002/01/27
VHP	3.4757	I	2001/04/08	2001/10/24
VHP	3.7766	II	2001/01/13	2001/10/08

PRECEDING PAGE BLANK NOT FILMED

1.
C3L

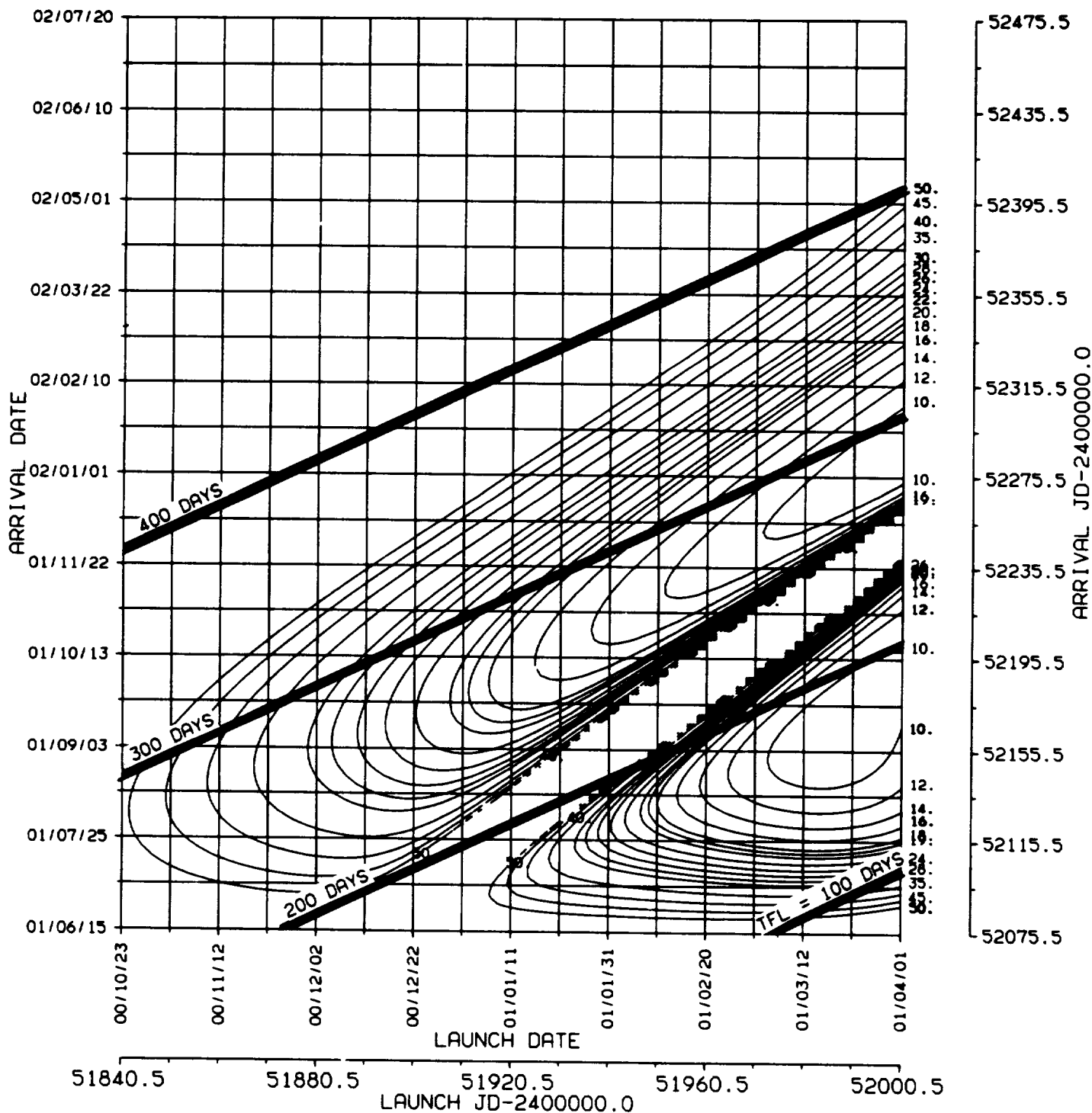


2000/1

ORIGINAL PAGE 19
OF POOR QUALITY

EARTH - MARS 2000/1 , C3L . TFL

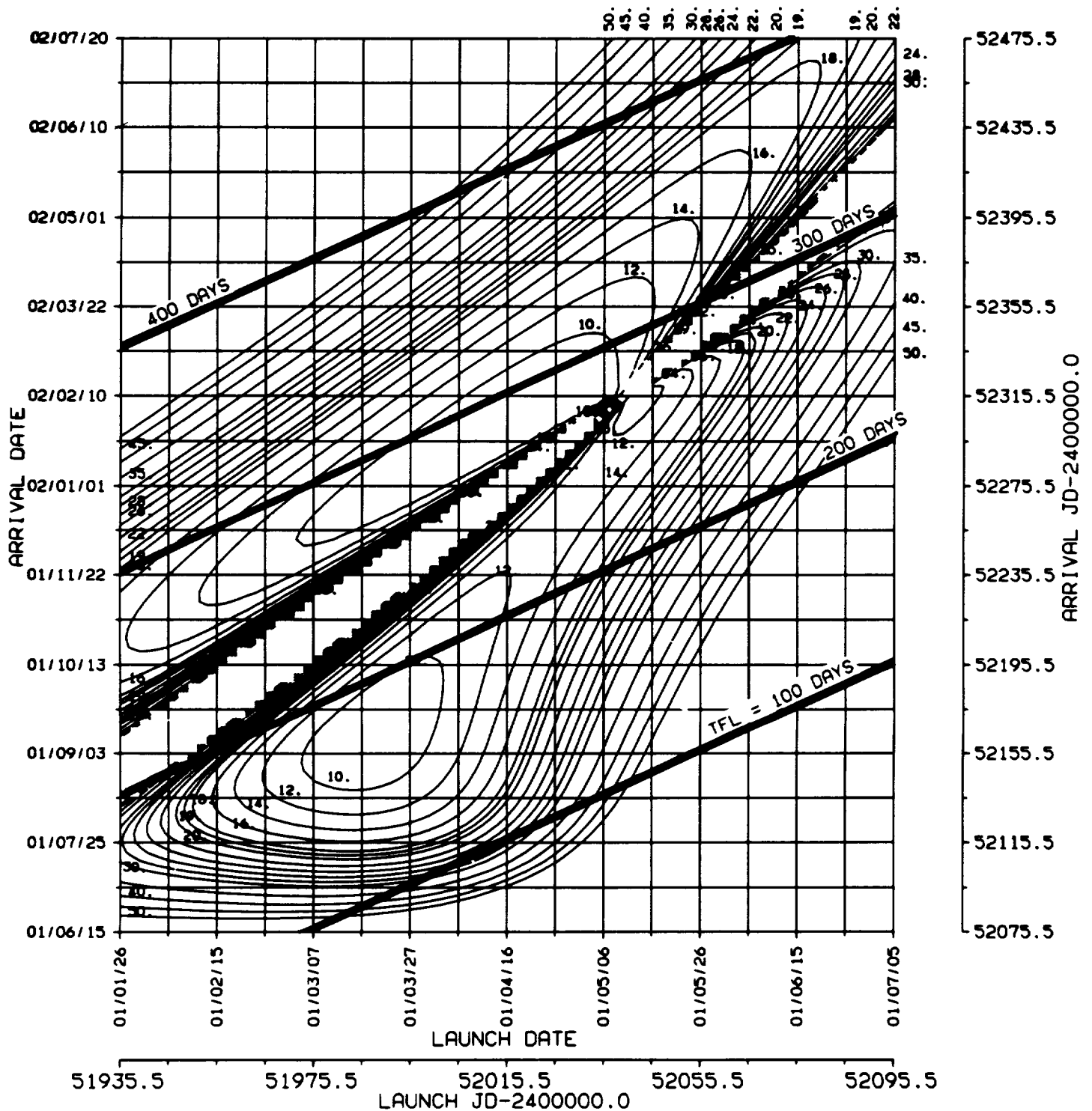
* BALLISTIC TRANSFER TRAJECTORY



ORIGINAL PAGE IS
OF POOR QUALITY

EARTH - MARS 2000/1 , C3L , TFL

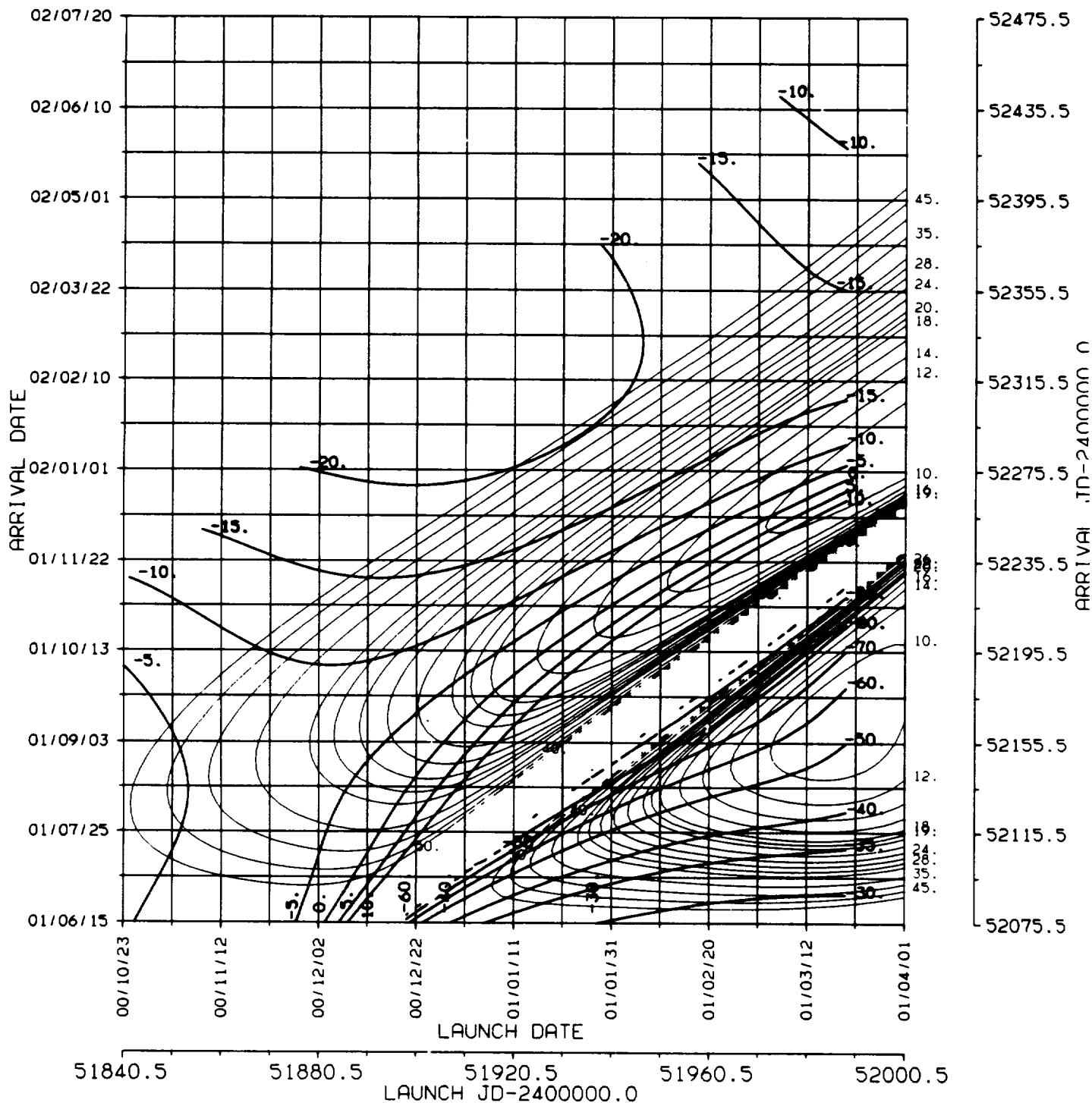
* BALLISTIC TRANSFER TRAJECTORY



2.
DLA
♂
2000/1

ORIGINAL PAGE IS
OF POOR QUALITY

EARTH - MARS 2000/1 , C3L , DLA
* BALLISTIC TRANSFER TRAJECTORY





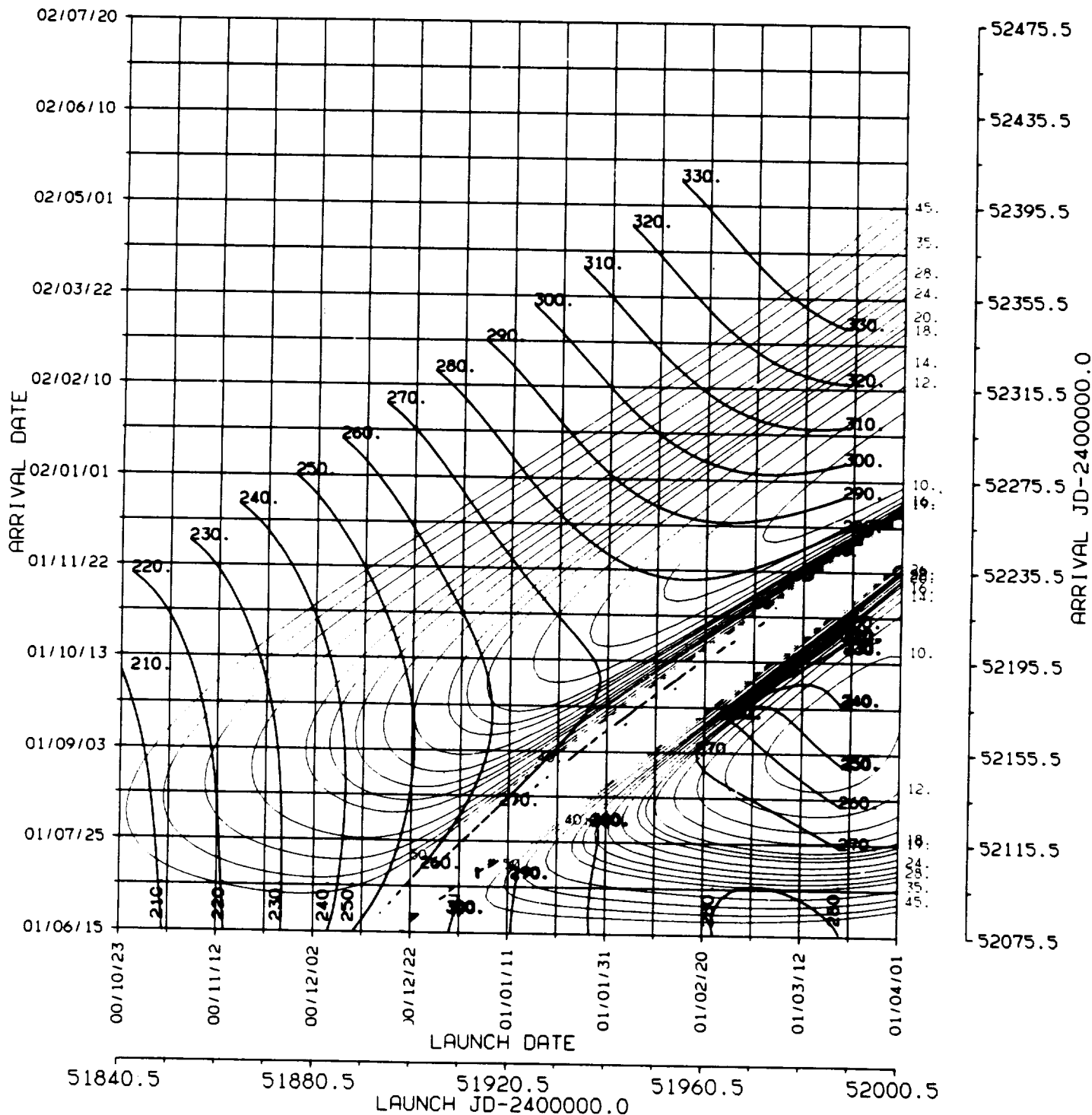
3.
RLA



2000/1

EARTH - MARS 2000/1, C3L, RLA
BALLISTIC TRANSFER TRAJECTORY

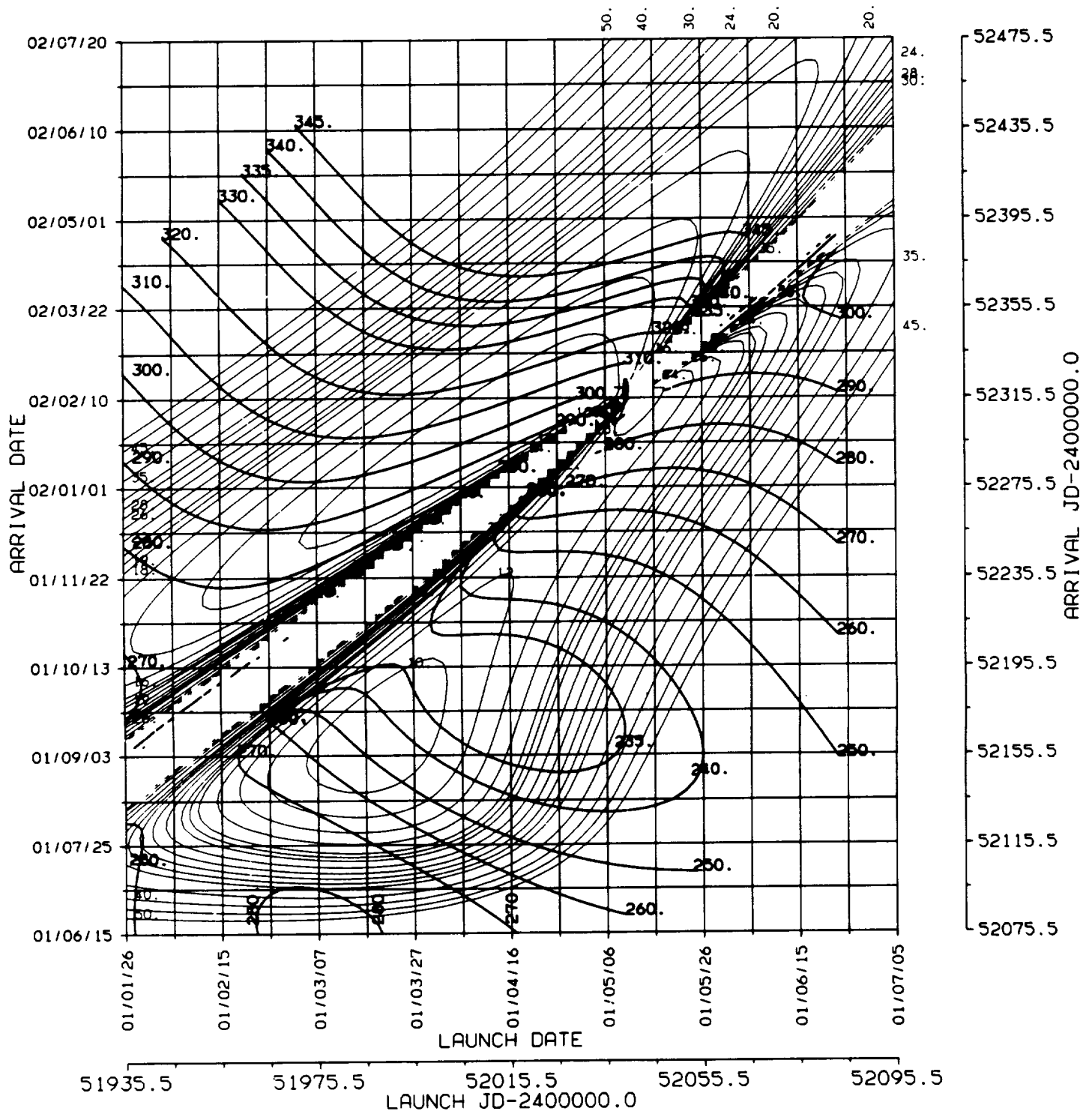
ORIGINAL PAGE 19
OF POOR QUALITY



EARTH - MARS 2000/1 , C3L , RLA

*

BALLISTIC TRANSFER TRAJECTORY



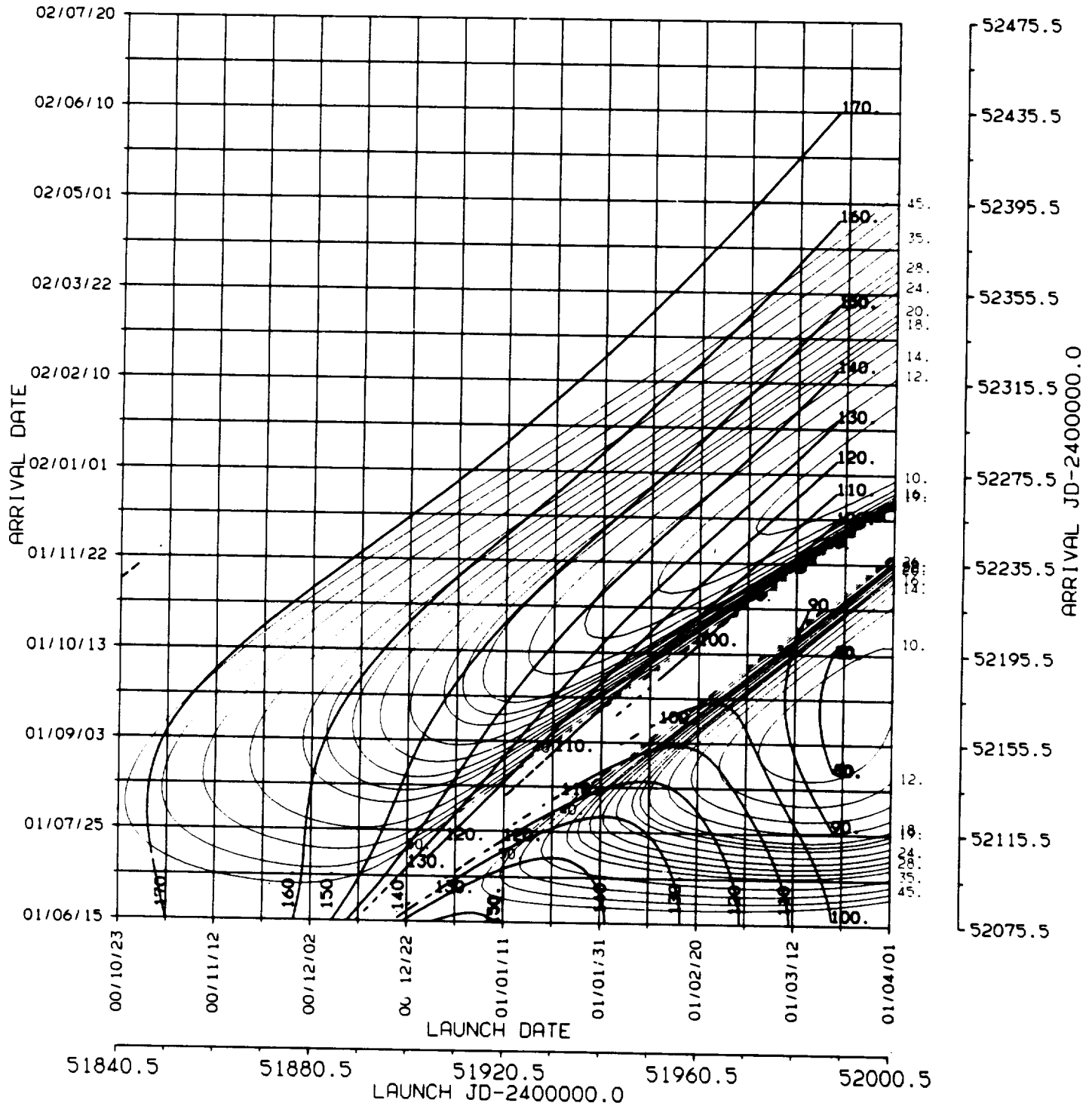
4.
ZALS



2000/1

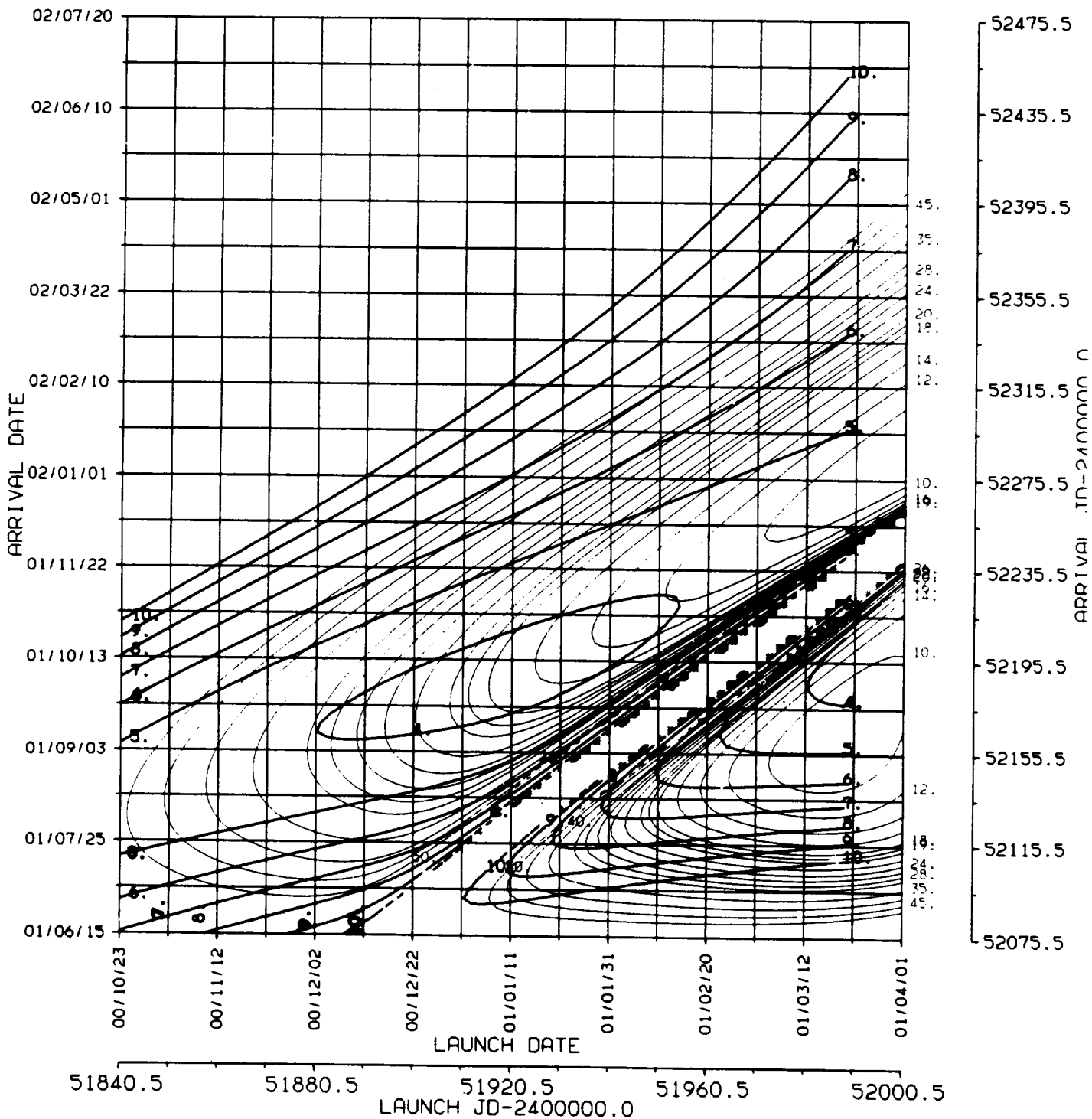
ORIGINAL PAGE IS
OF POOR QUALITY

EARTH - MARS 2000/1 , C3L , ZALS
BALLISTIC TRANSFER TRAJECTORY



2000/1

EARTH - MARS 2000/1 . C3L . VHP
BALLISTIC TRANSFER TRAJECTORY

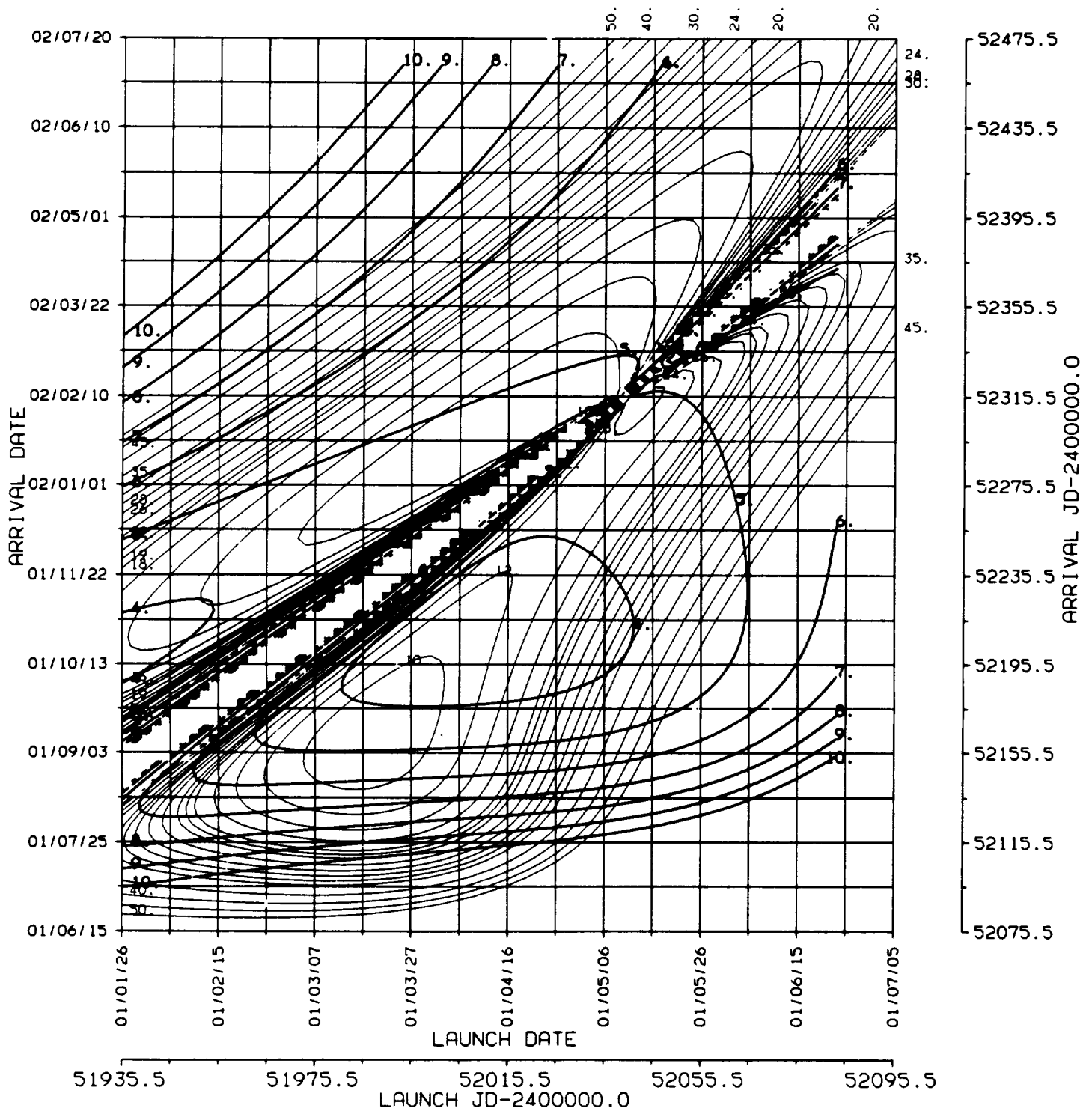


ORIGINAL PAGE IS
OF POOR QUALITY

EARTH - MARS 2000/1 , C3L , VHP

*

BALLISTIC TRANSFER TRAJECTORY



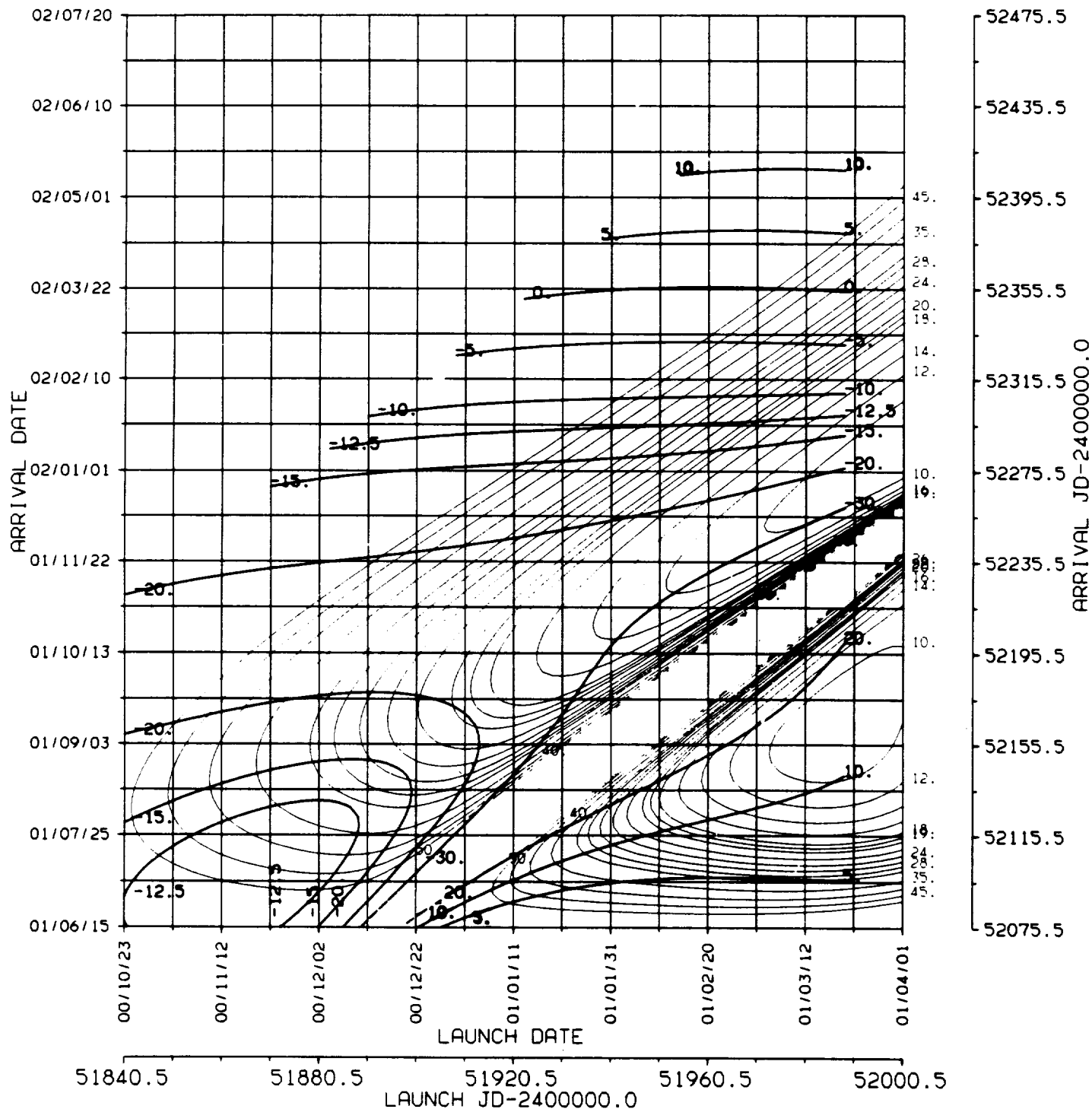
6.
DAP



2000/1

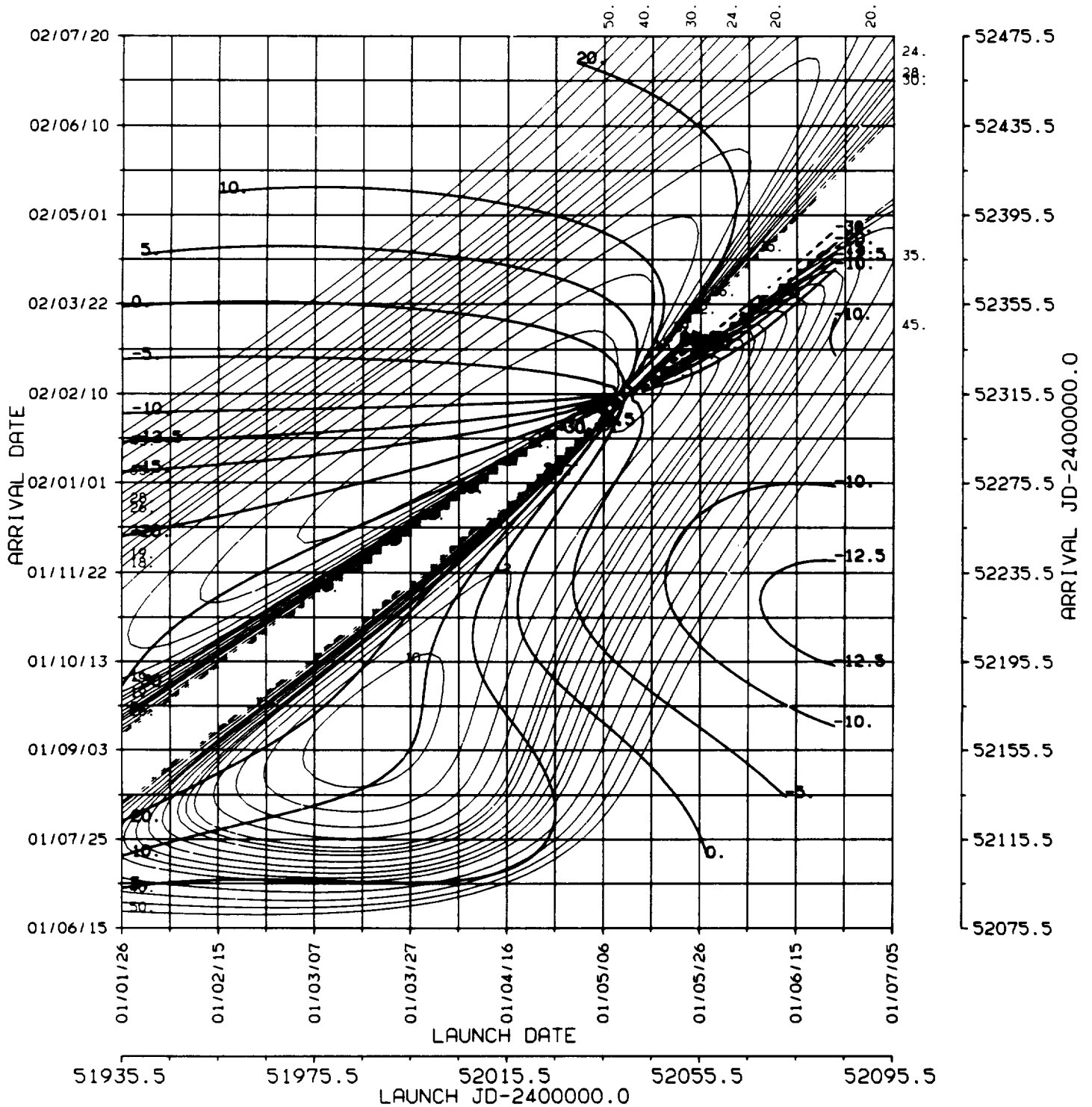
EARTH - MARS 2000/1 , C3L , DAP
BALLISTIC TRANSFER TRAJECTORY

ORIGINAL PAGE IS
OF POOR QUALITY



ORIGINAL PAGE IS
OF POOR QUALITY

EARTH - MARS 2000/1 , C3L , DAP
* BALLISTIC TRANSFER TRAJECTORY



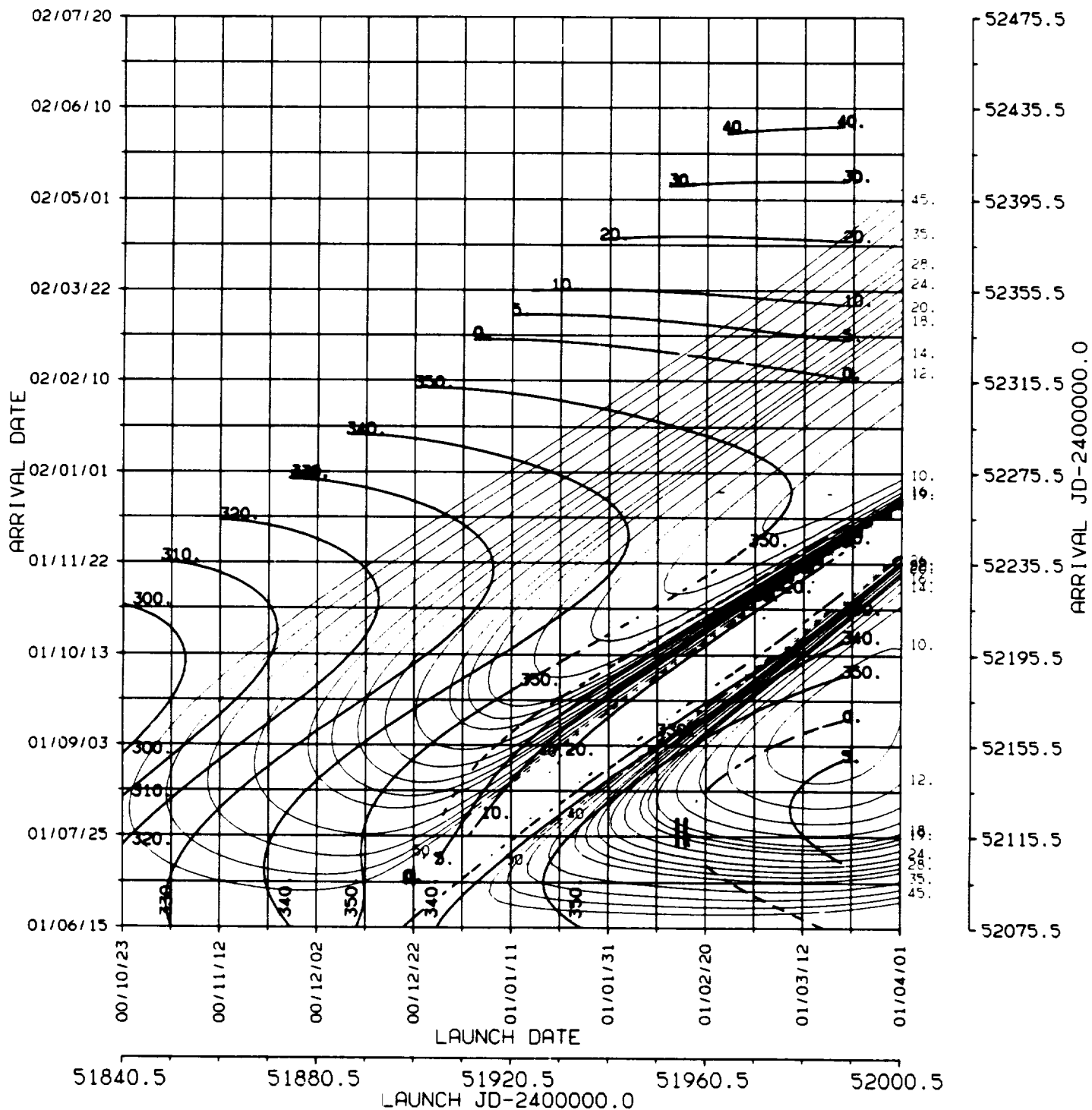
7.
RAP



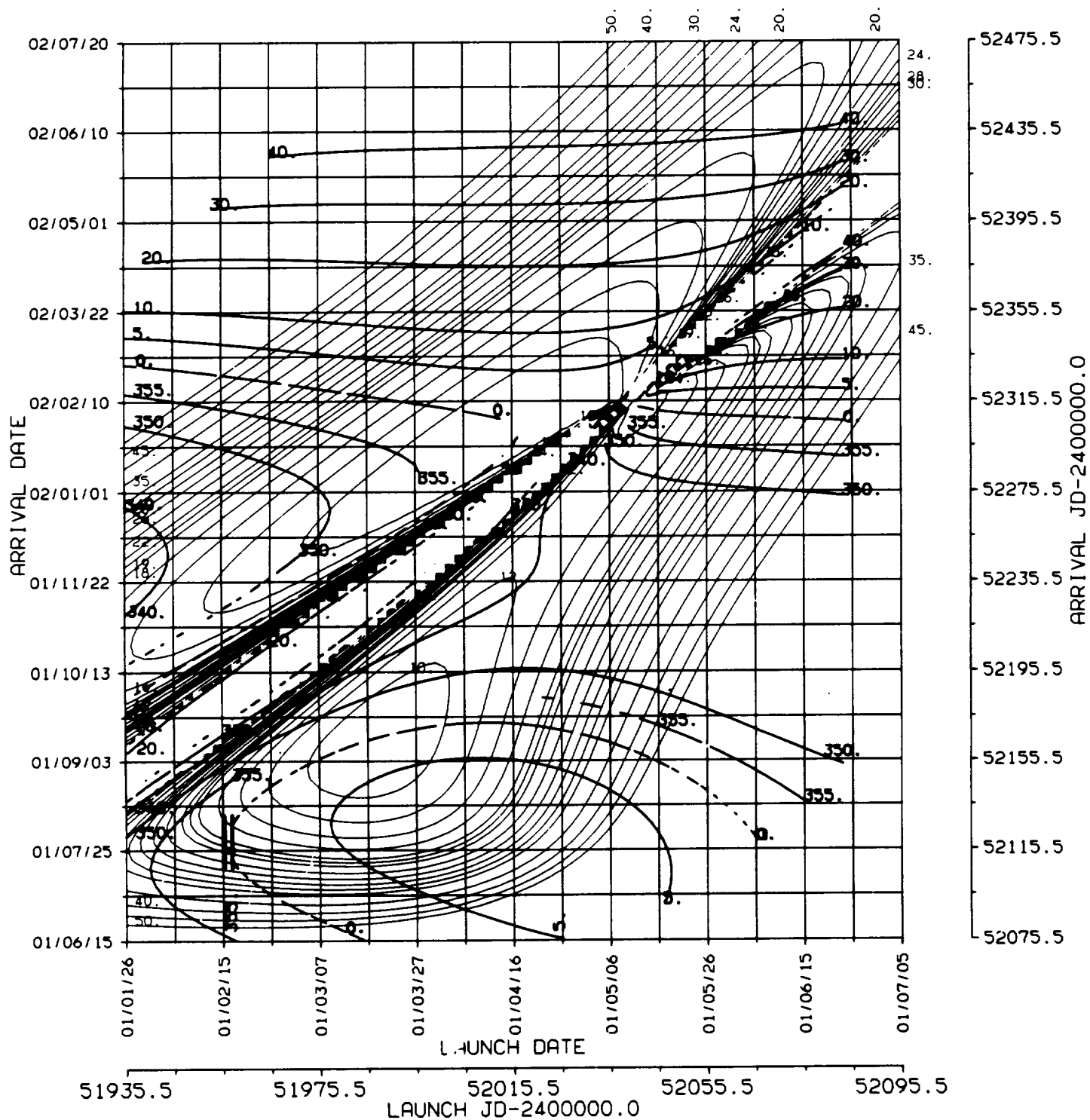
2000/1

EARTH - MARS 2000/1 , C3L , RAP
BALLISTIC TRANSFER TRAJECTORY

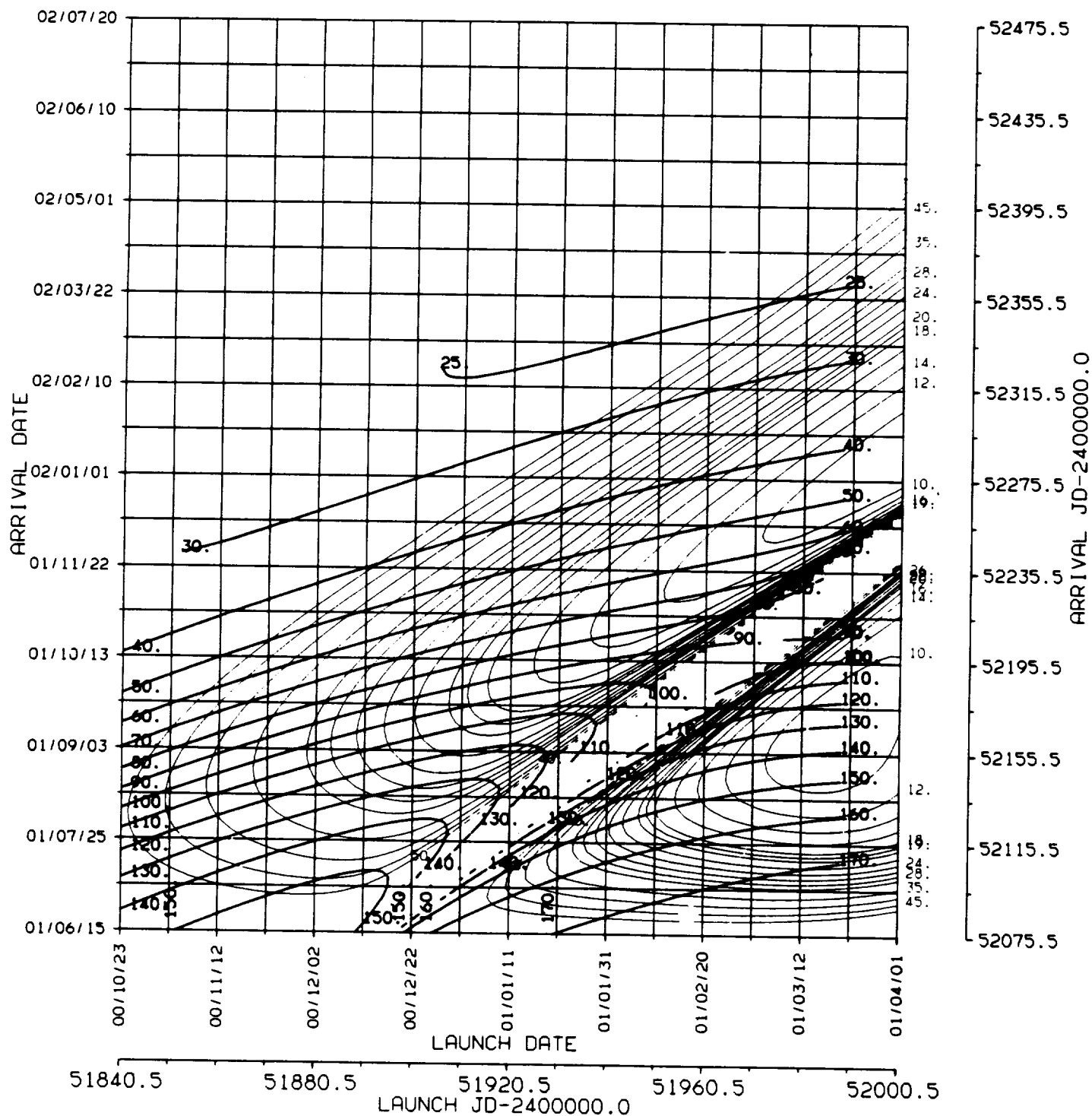
ORIGINAL PAGE IS
OF POOR QUALITY



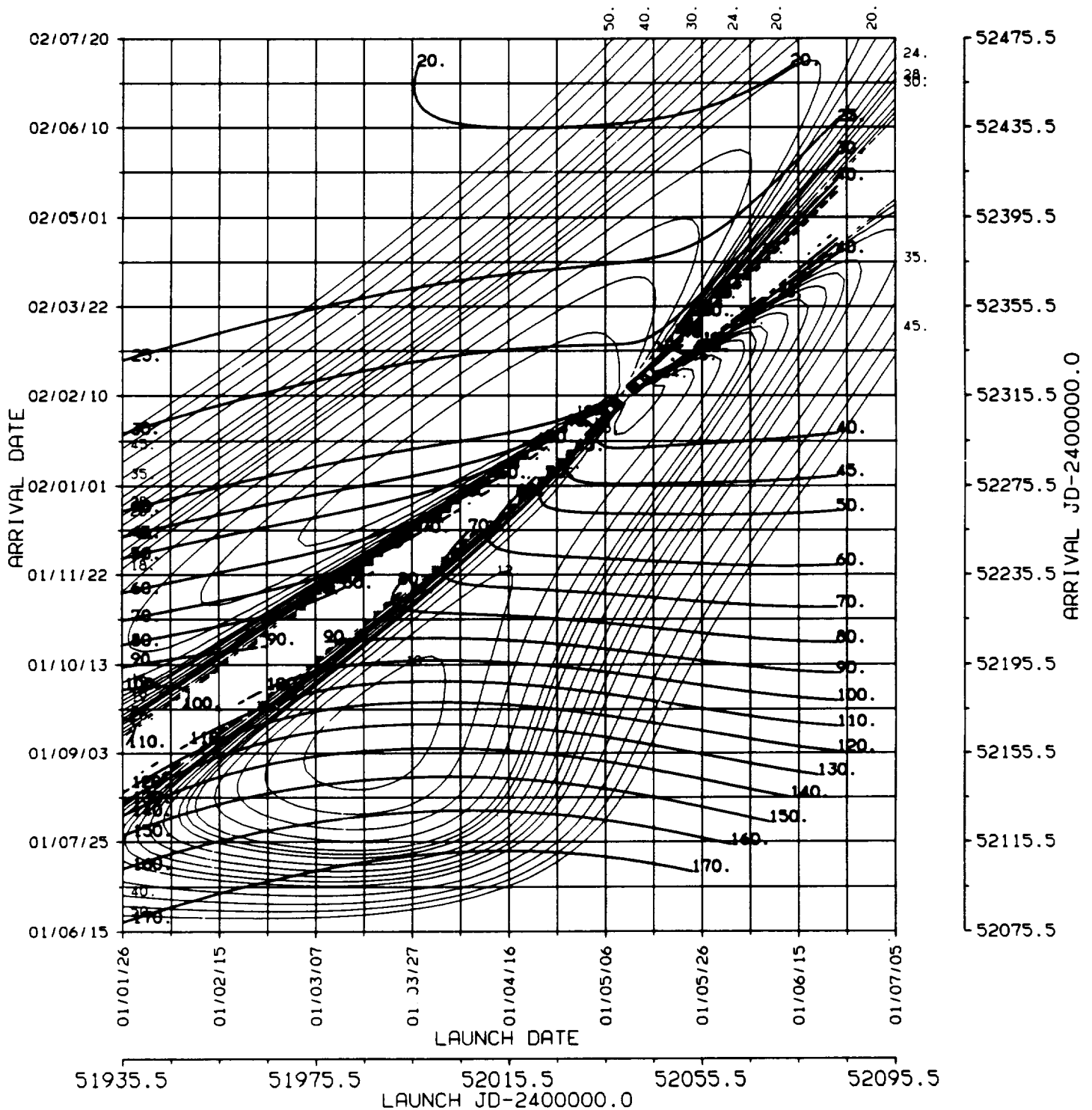
EARTH - MARS 2000/1 , C3L , RAP
* BALLISTIC TRANSFER TRAJECTORY



EARTH - MARS 2000/1 , C3L , ZAPS
BALLISTIC TRANSFER TRAJECTORY



EARTH - MARS 2000/1 , C3L , ZAPS
* BALLISTIC TRANSFER TRAJECTORY



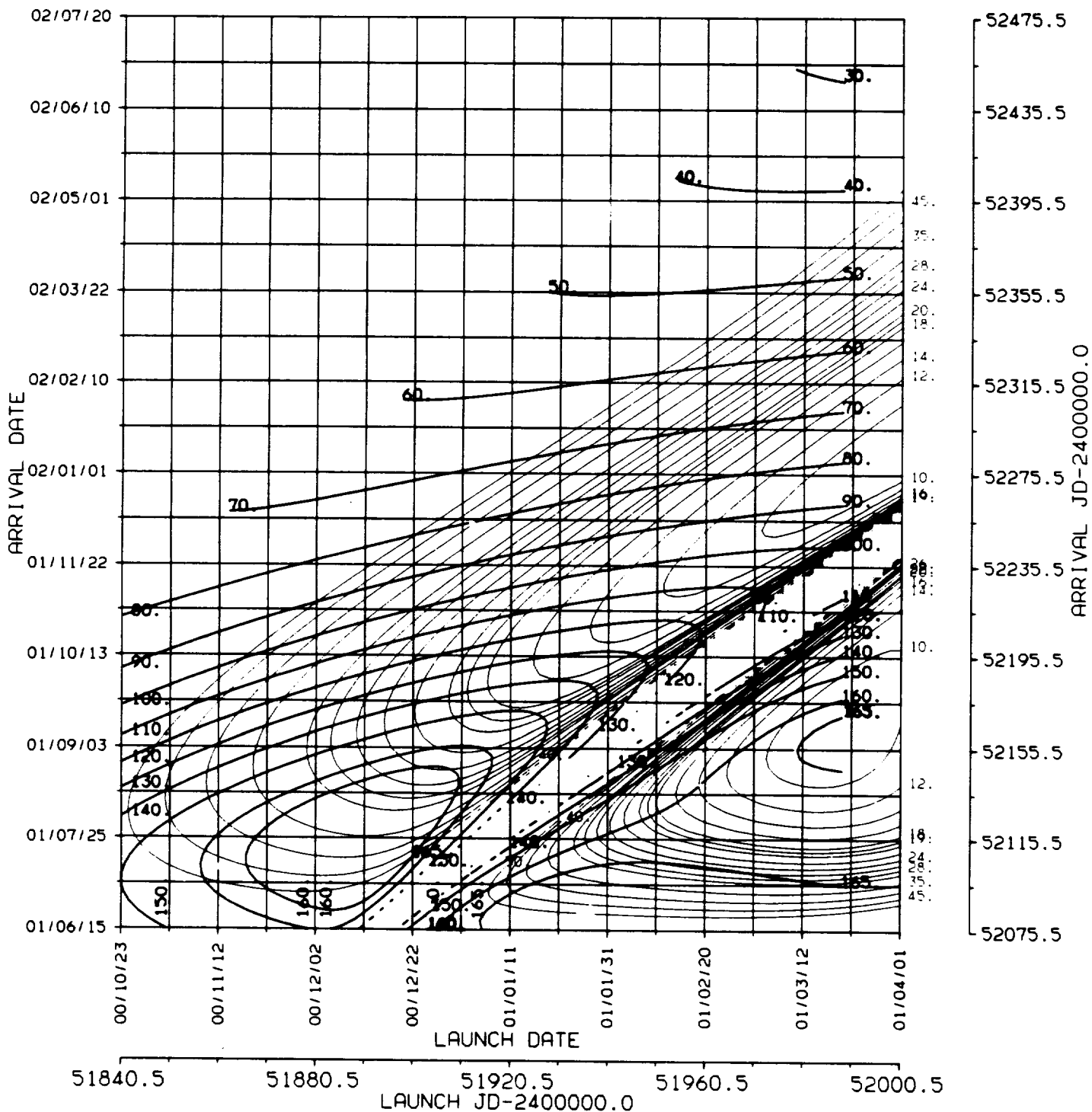
9.
ZAPE



2000/1

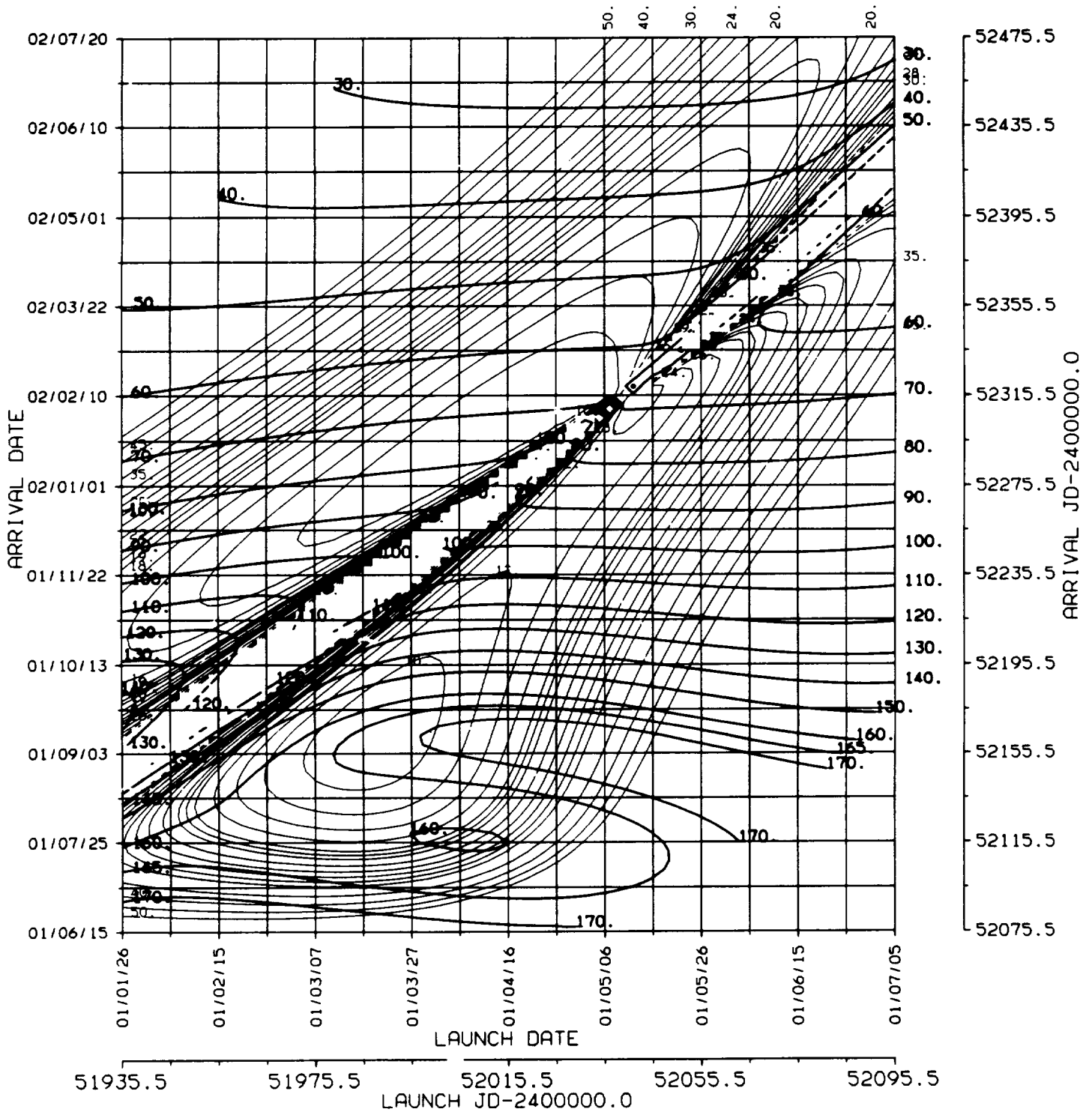
ORIGINAL PAGE IS
OF POOR QUALITY

EARTH - MARS 2000/1 , C3L , ZAPE
BALLISTIC TRANSFER TRAJECTORY



ORIGINAL PAGE IS
OF POOR QUALITY

EARTH - MARS 2000/1 , C3L , ZAPE
* BALLISTIC TRANSFER TRAJECTORY

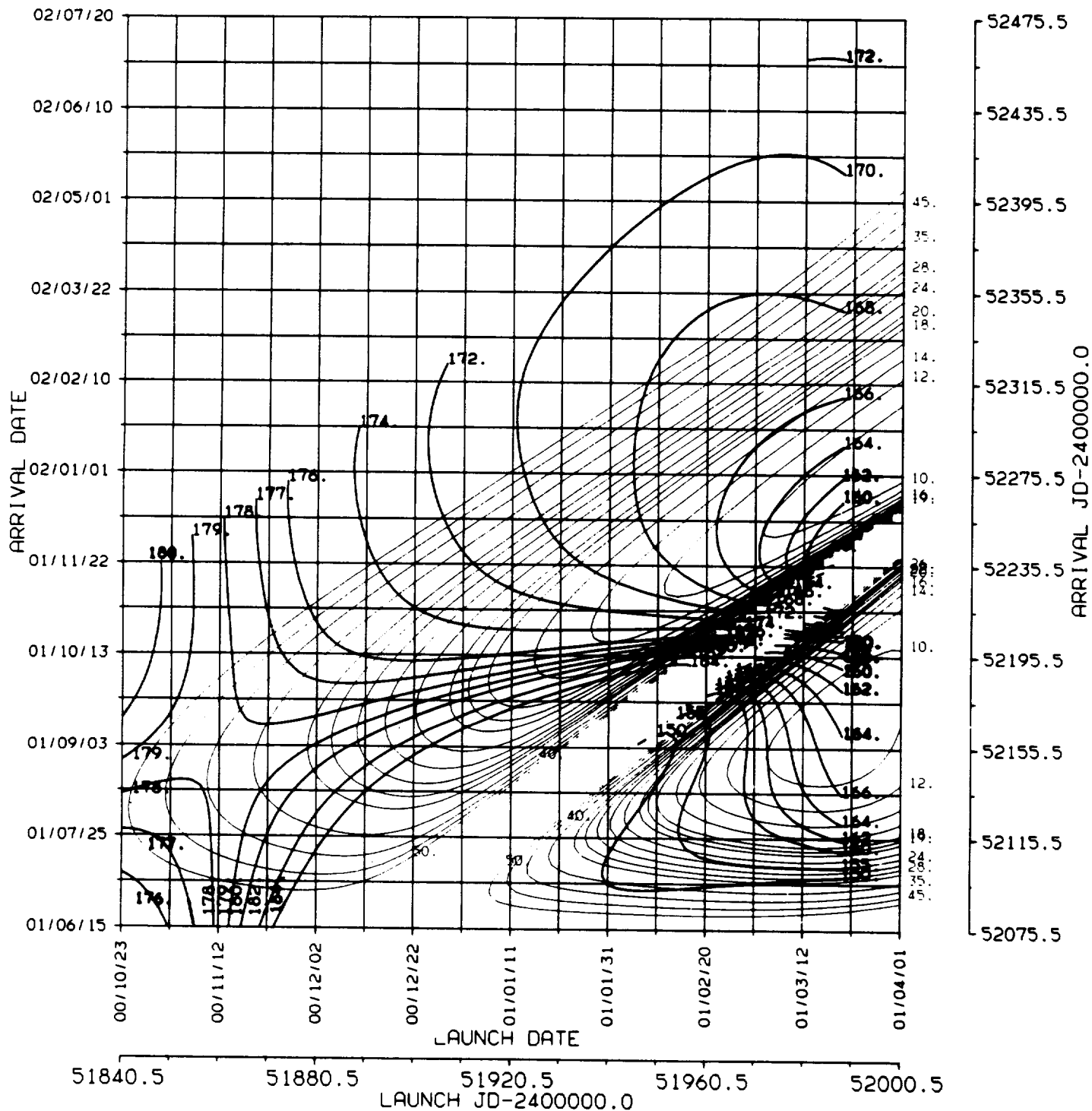




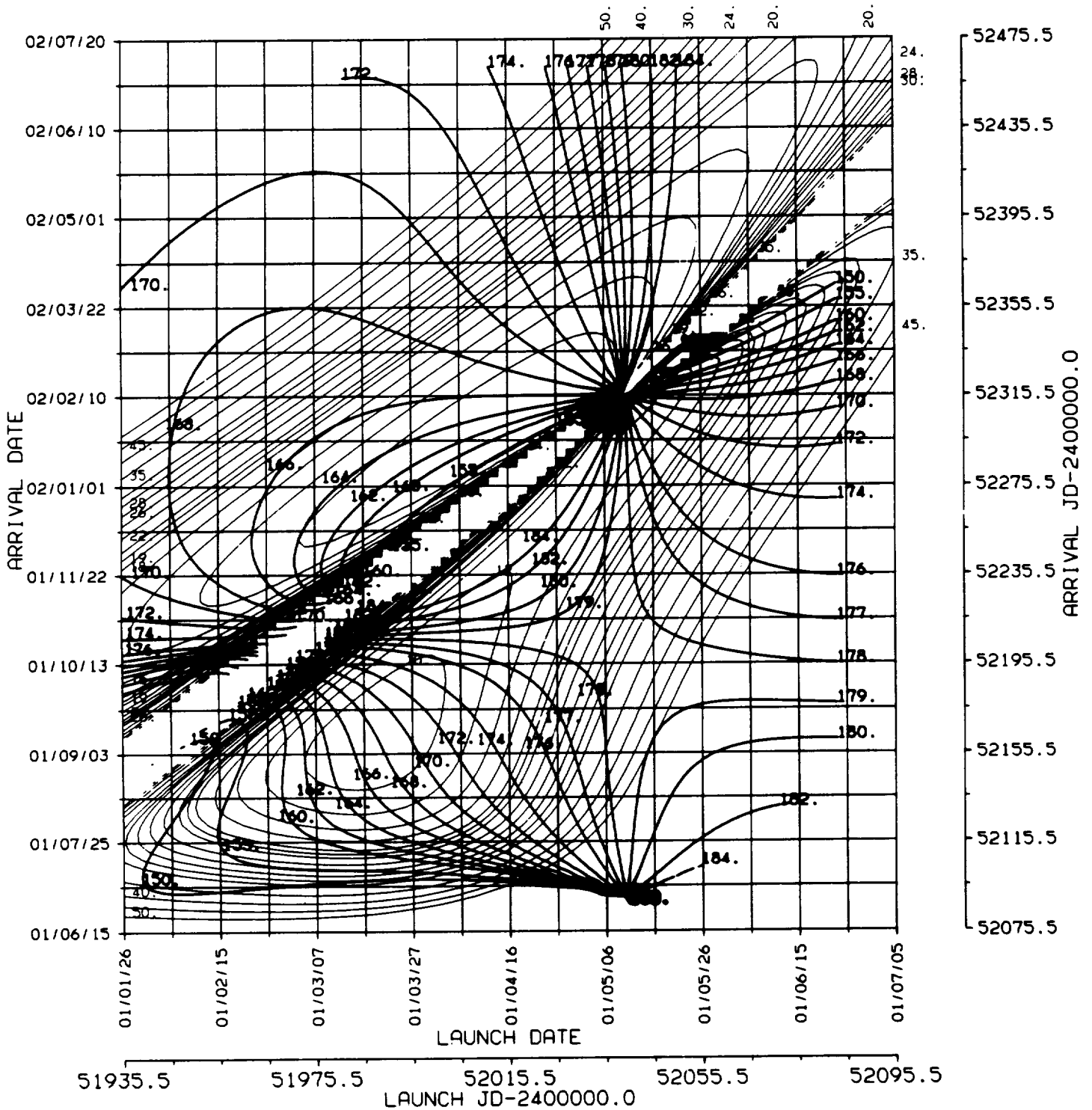
2000/1

ORIGINAL PAGE 19
OF POOR QUALITY

EARTH - MARS 2000/1, C3L, ETSP
BALLISTIC TRANSFER TRAJECTORY



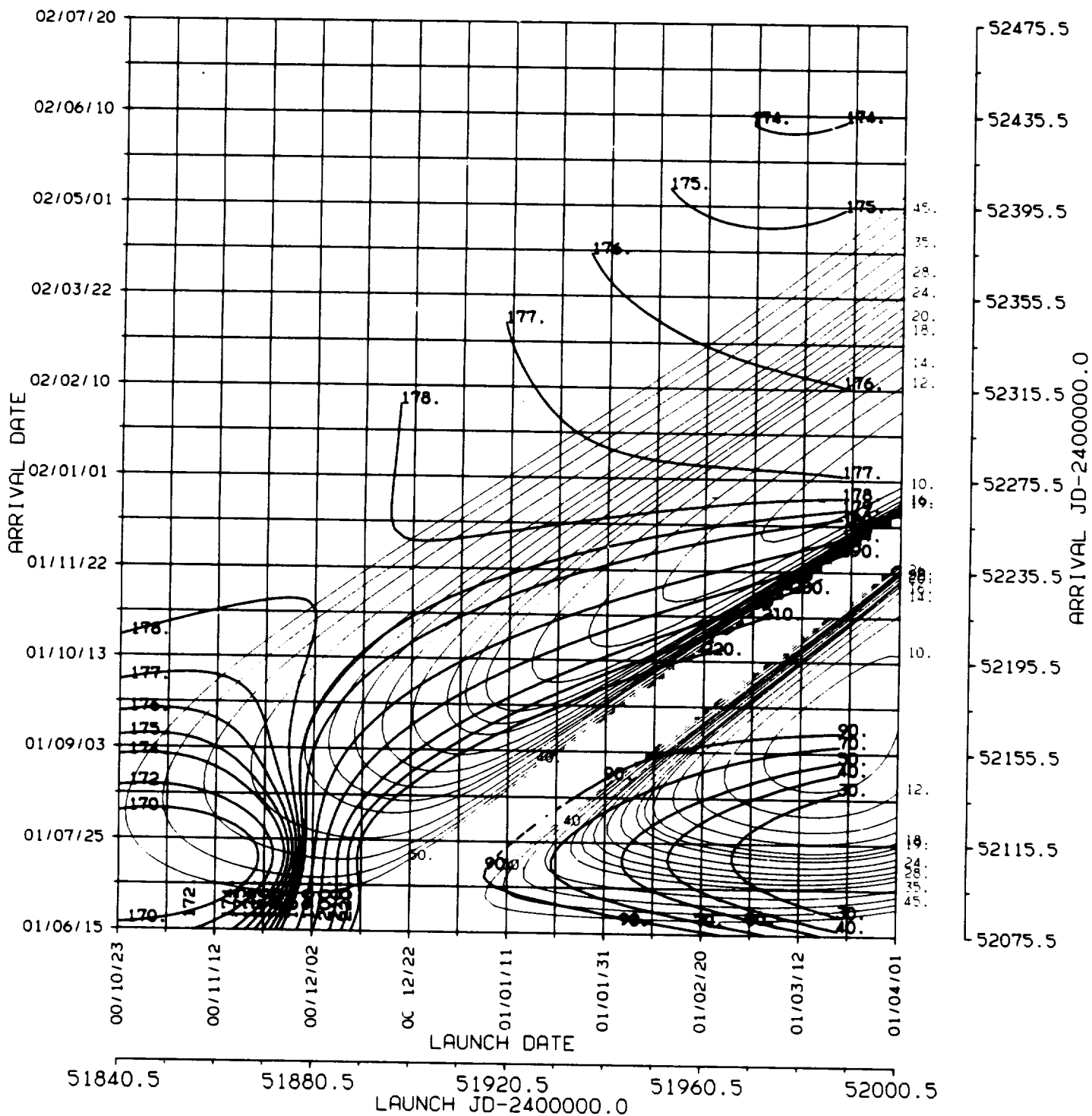
EARTH - MARS 2000/1 , C3L , ETSP
* BALLISTIC TRANSFER TRAJECTORY





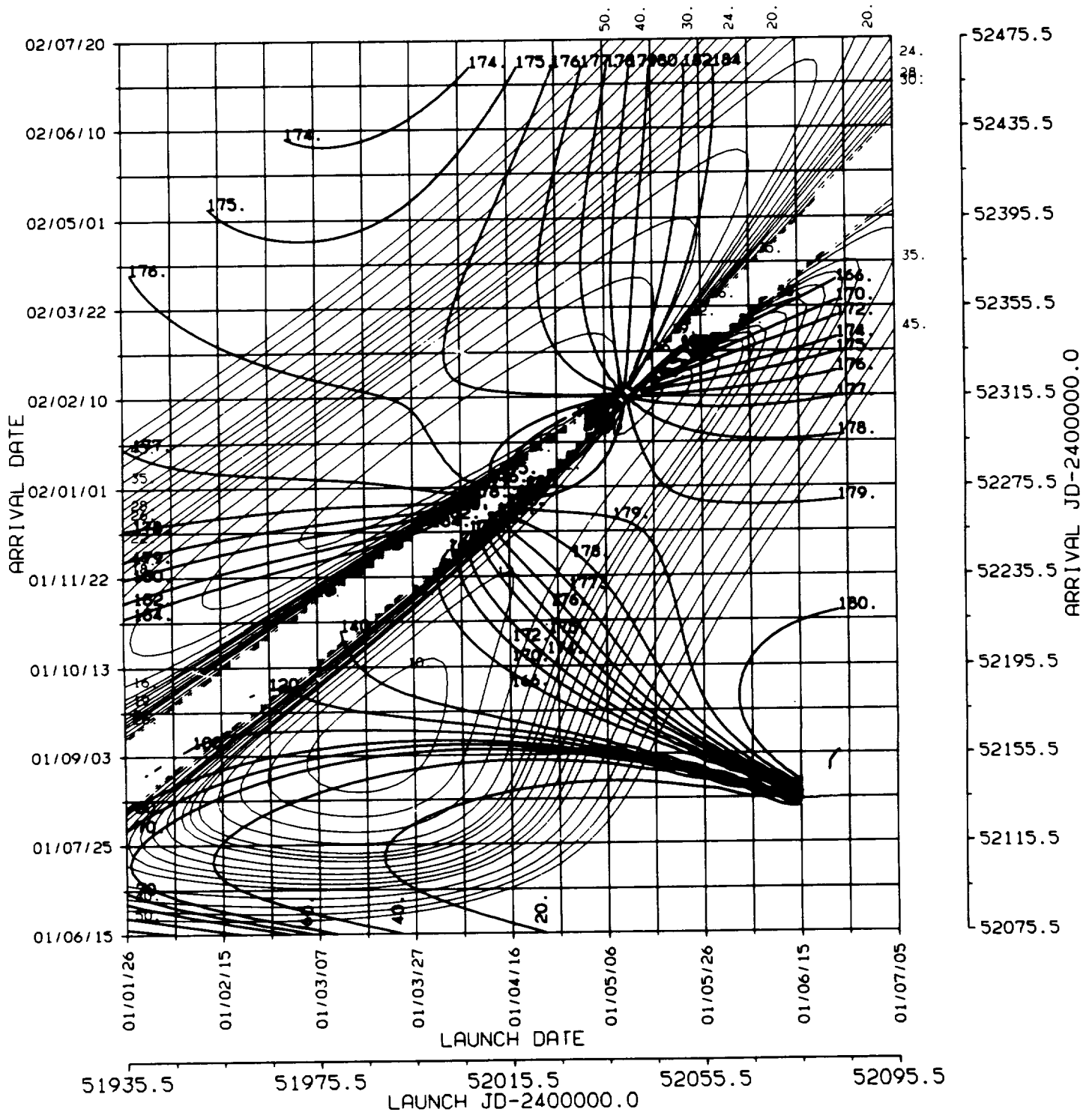
2000/1

EARTH - MARS 2000/1 , C3L , ETEP
BALLISTIC TRANSFER TRAJECTORY



ORIGINAL PAGE IS
OF POOR QUALITY

EARTH - MARS 2000/1 , C3L , ETEP
* BALLISTIC TRANSFER TRAJECTORY



Earth to Mars

2002/3

Opportunity

ENERGY MINIMA

	VALUE	TYPE	DEPARTURE (YEAR/MONTH/DAY)	ARRIVAL (YEAR/MONTH/DAY)
C ₃ L	8.8102	I	2003/06/07	2003/12/25
C ₃ L	12.564	II	2003/05/10	2003/12/29
VHP	2.6975	I	2003/06/13	2003/12/31
VHP	2.7652	II	2003/05/10	2003/12/30

PRECEDING PAGE BLANK NOT FILMED

1.
C3L



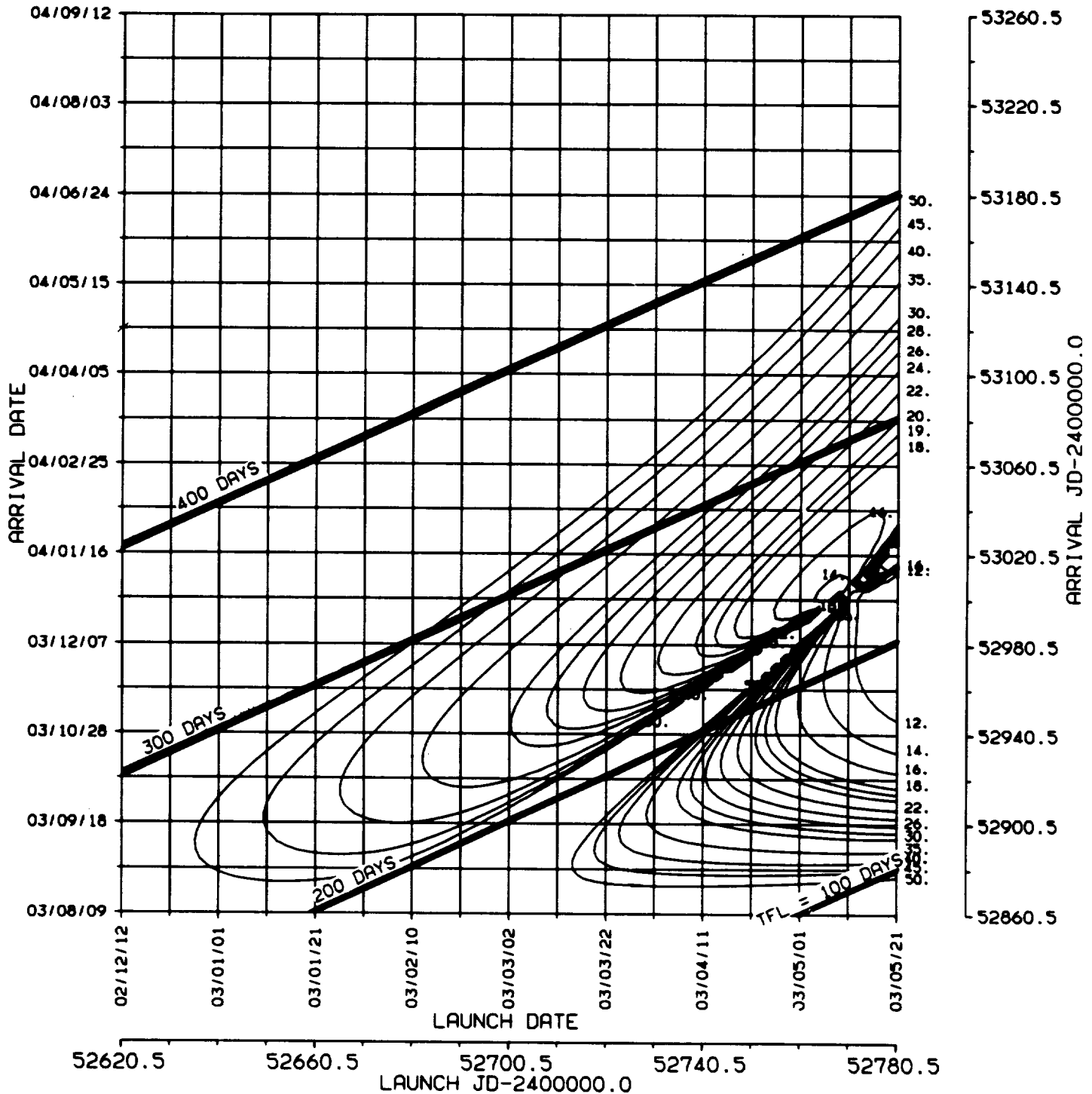
2002/3

EARTH - MARS 2002/3 , C3L , TFL

*

BALLISTIC TRANSFER TRAJECTORY

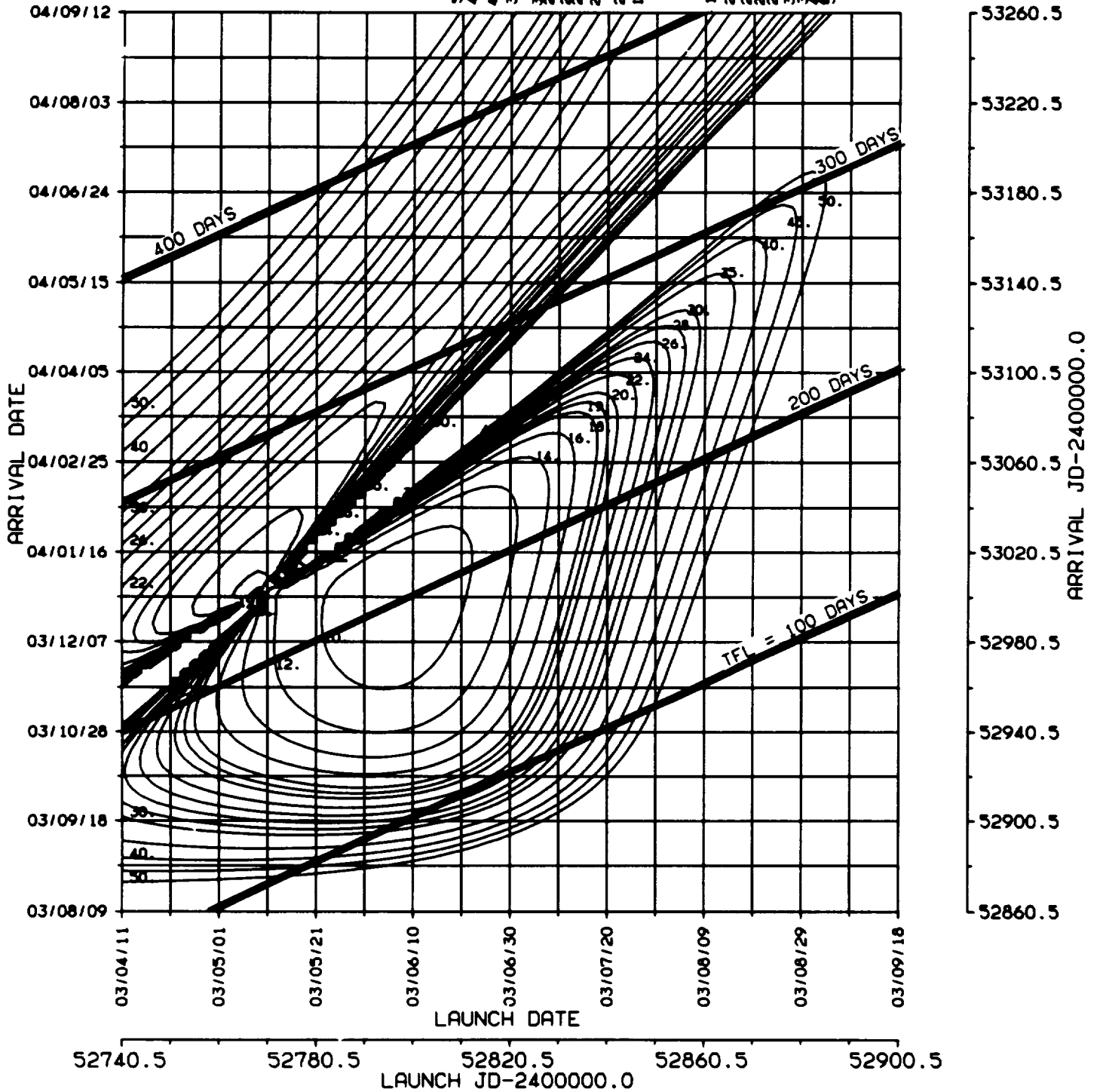
ORIGINAL PAGE 19
OF POOR QUALITY



ORIGINAL PAGE IS
OF POOR QUALITY

EARTH - MARS 2002/3 , C3L , TFL * BALLISTIC TRANSFER TRAJECTORY

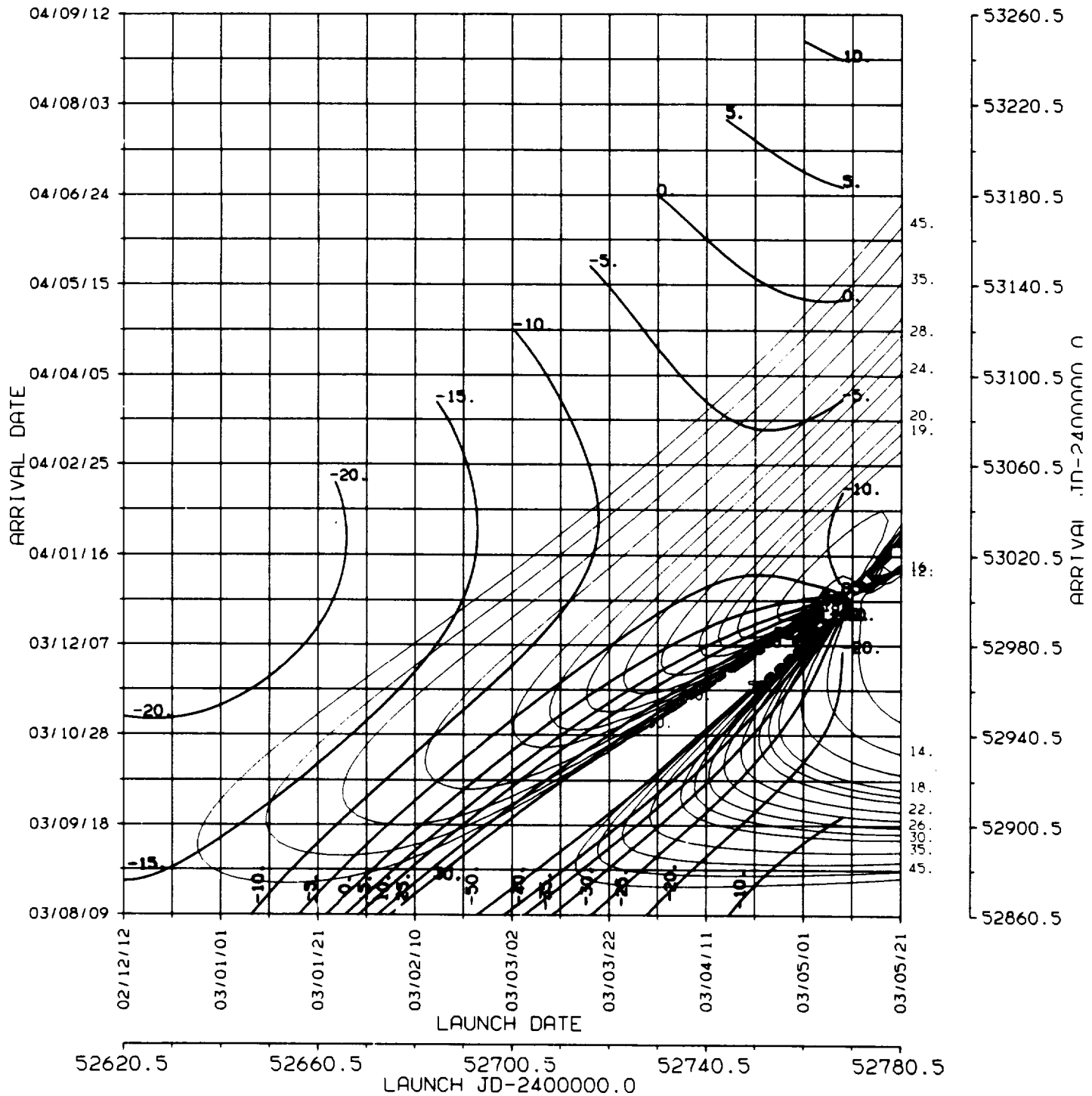
ಗ್ರಹ ಭೇದಿ ಇಂಜಿನ್‌ನ ಸ್ಥಿತಿ ಒಂದು ಇಂಜಿನ್‌ನ ಸ್ಥಿತಿ



2002/3

EARTH - MARS 2002/3 , C3L , DLA

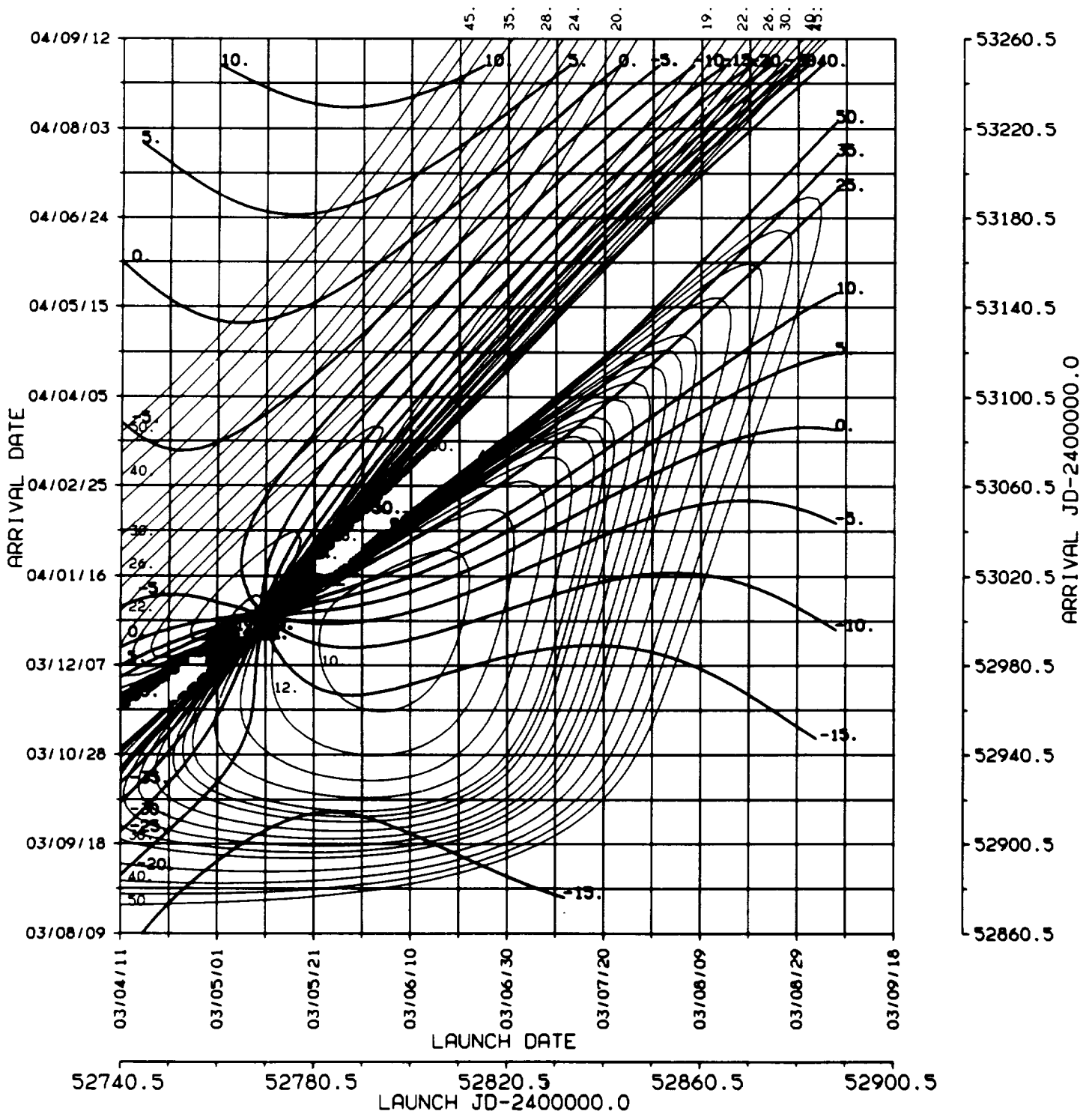
* BALLISTIC TRANSFER TRAJECTORY



EARTH - MARS 2002/3 , C3L , DLA

*

BALLISTIC TRANSFER TRAJECTORY



3.
RLA



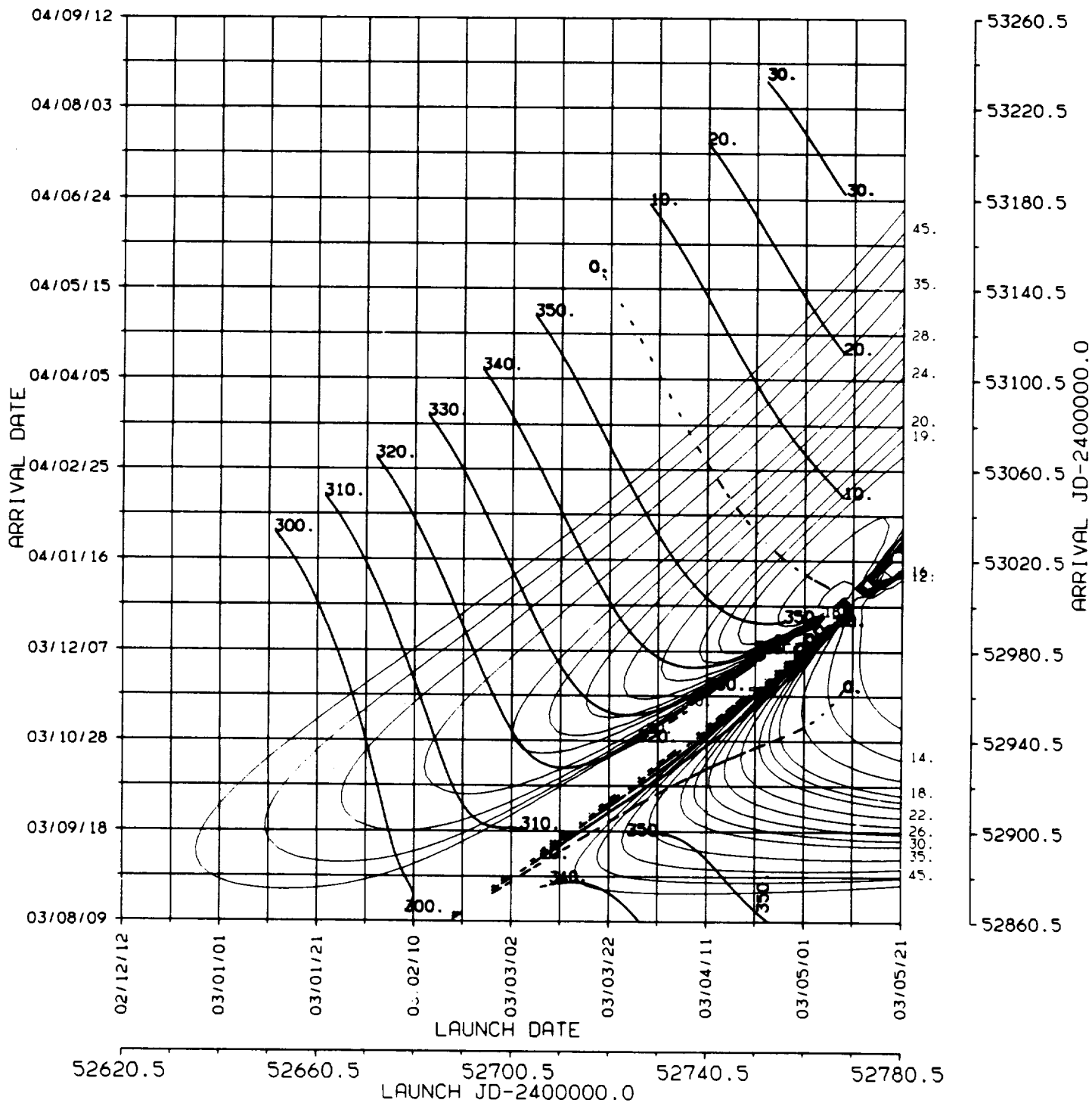
2002/3

EARTH - MARS 2002/3 , C3L , RLA

*

BALLISTIC TRANSFER TRAJECTORY

ORIGINAL PAGE IS
OF POOR QUALITY



4.
ZALS



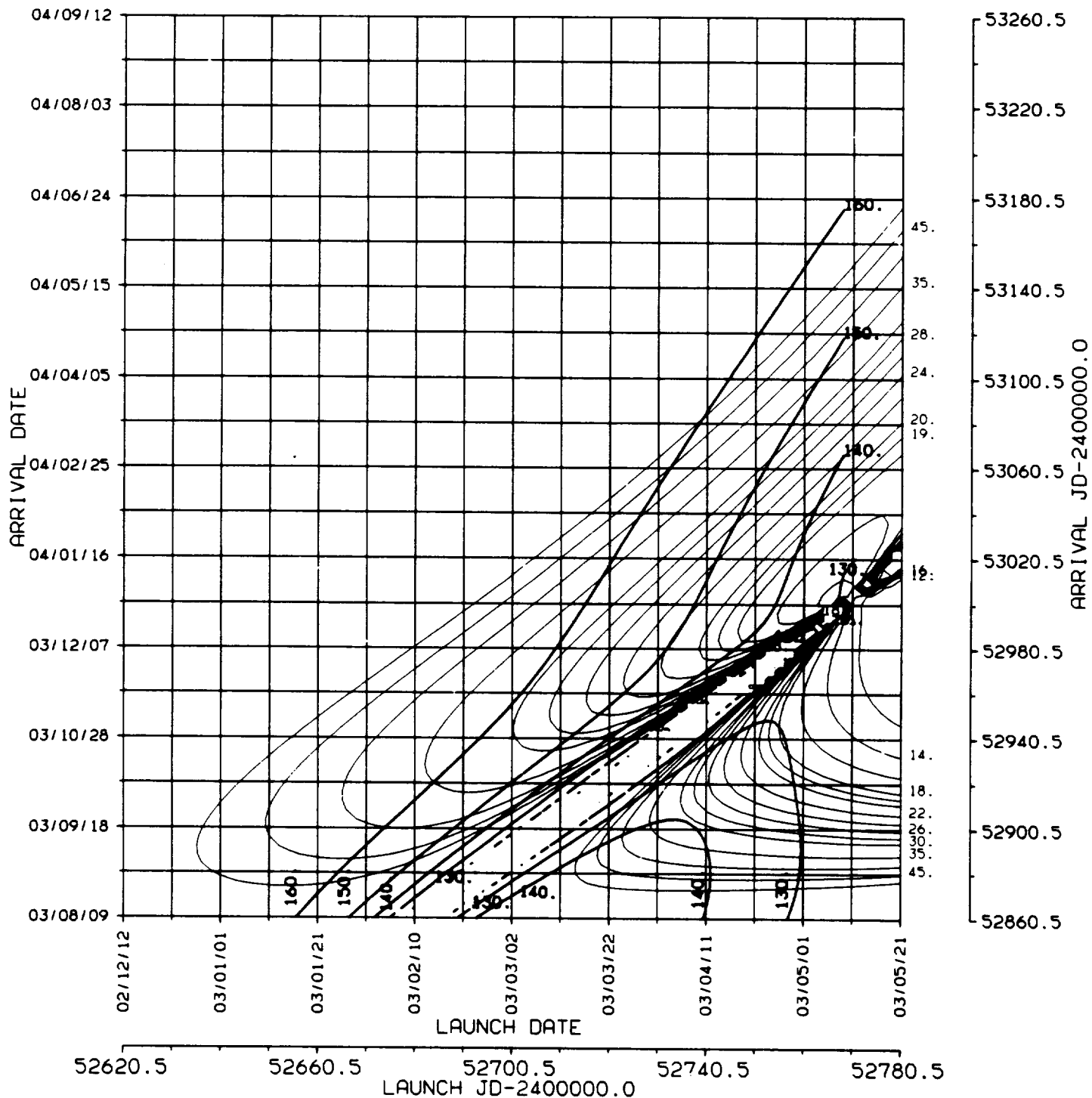
2002/3

EARTH - MARS 2002/3 , C3L , ZALS

*

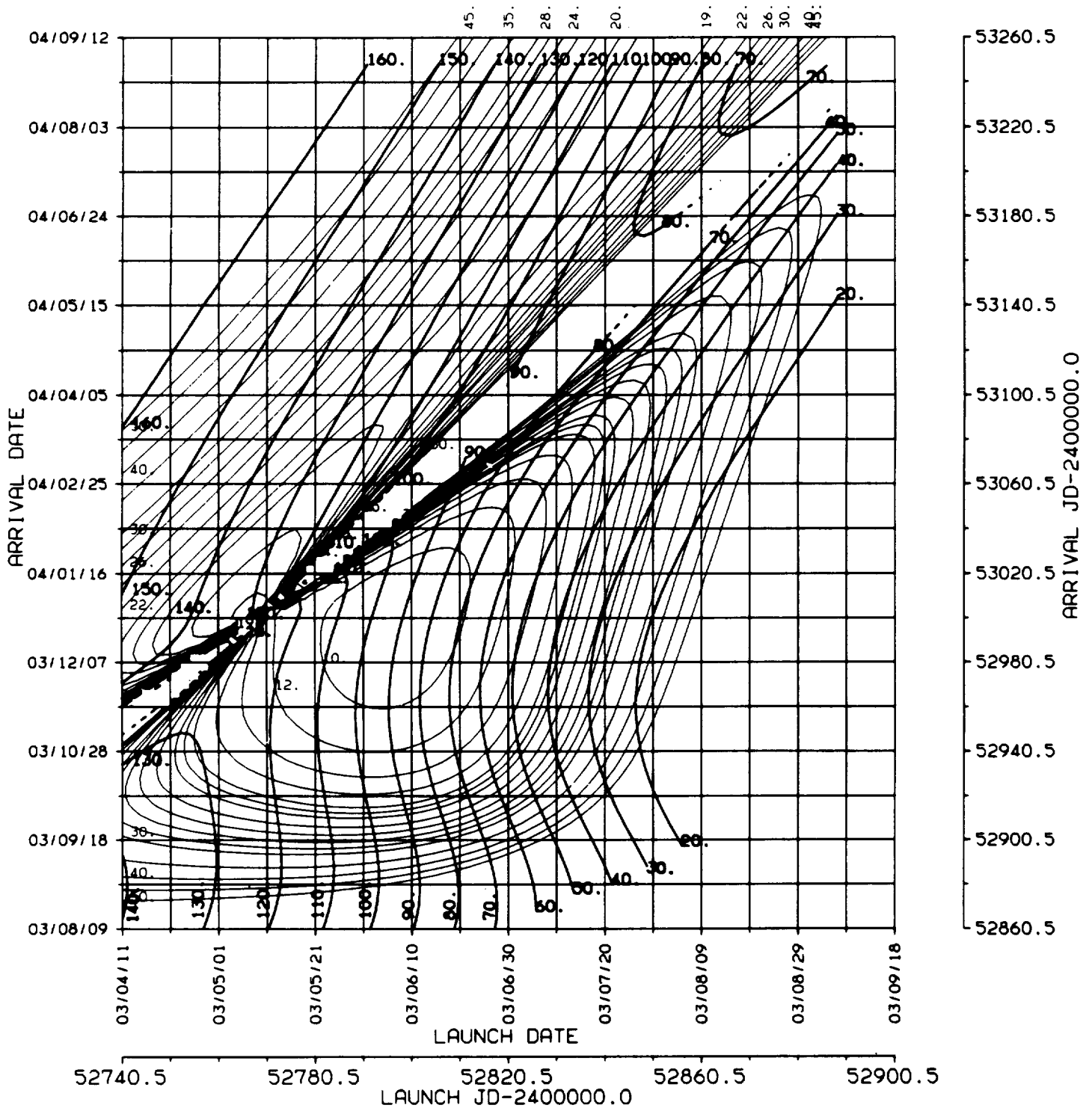
BALLISTIC TRANSFER TRAJECTORY

ORIGINAL PAGE IS
OF POOR QUALITY



ORIGINAL PAGE IS
OF POOR QUALITY

EARTH - MARS 2002/3 , C3L , ZALS
* BALLISTIC TRANSFER TRAJECTORY



5.
VHP



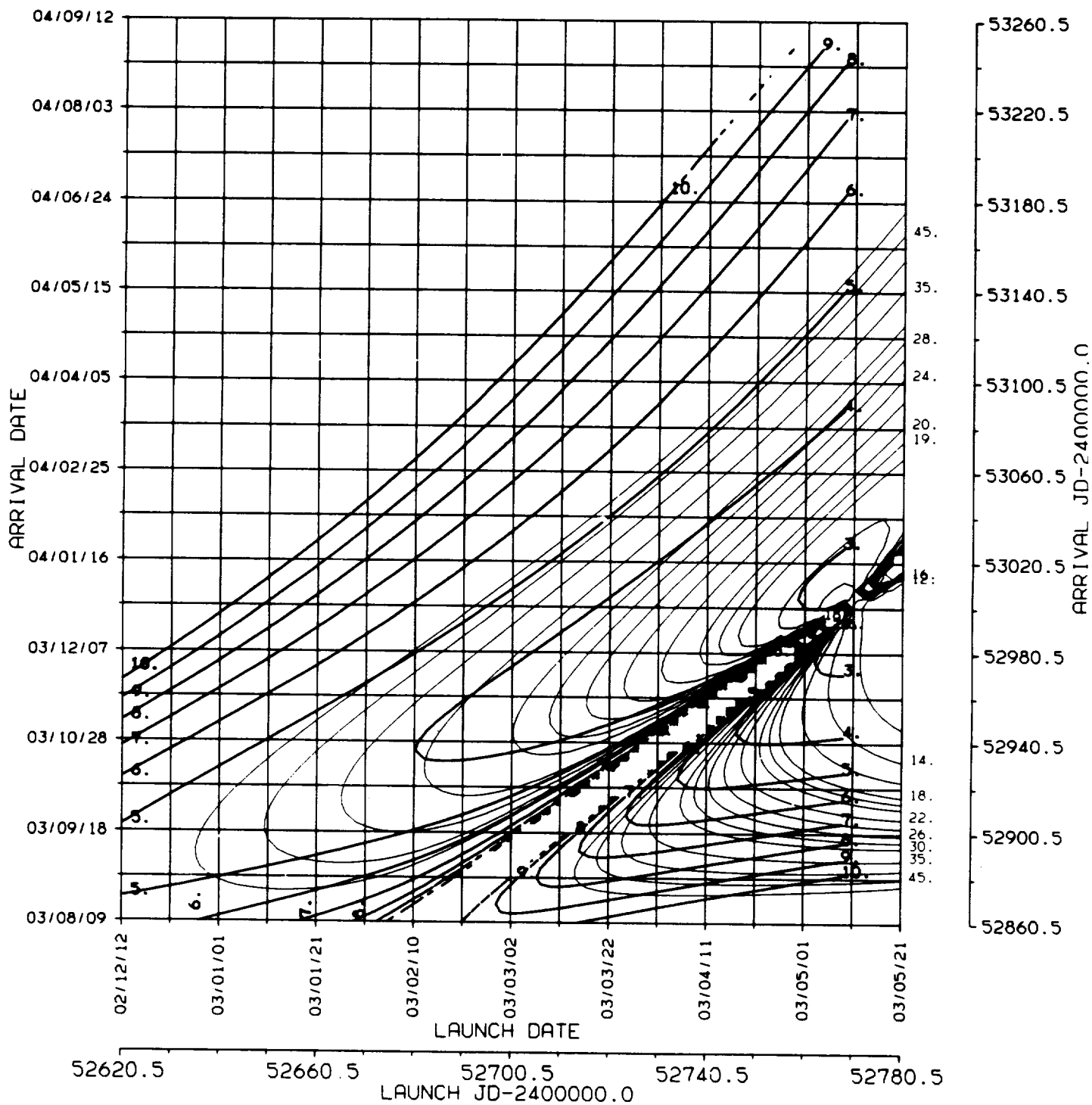
2002/3

EARTH - MARS 2002/3 , C3L , VHP

*

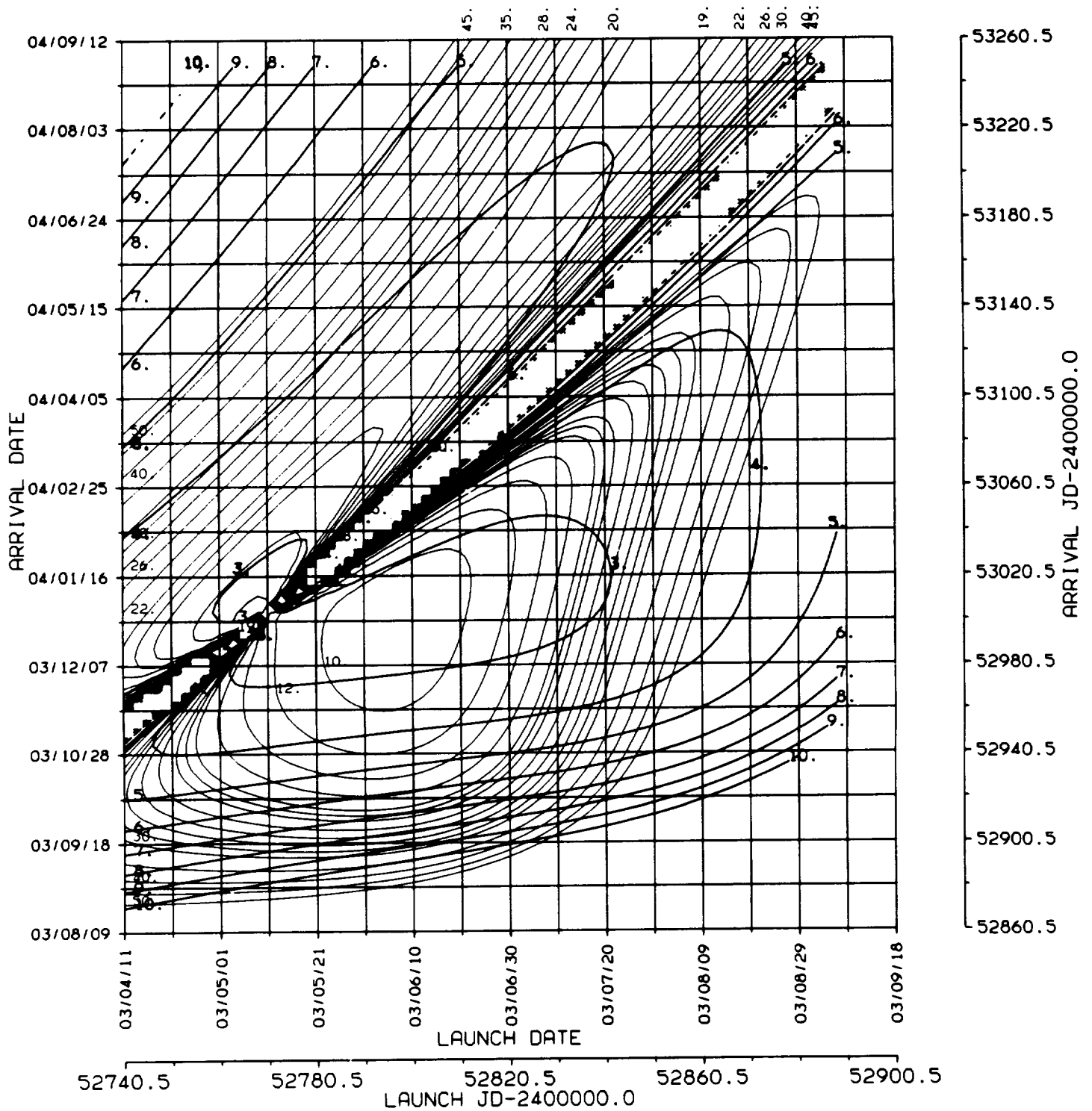
BALLISTIC TRANSFER TRAJECTORY

ORIGINAL PAGE 19
OF POOR QUALITY



ORIGINAL PAGE IS
OF POOR QUALITY

EARTH - MARS 2002/3 , C3L , VHP
* BALLISTIC TRANSFER TRAJECTORY



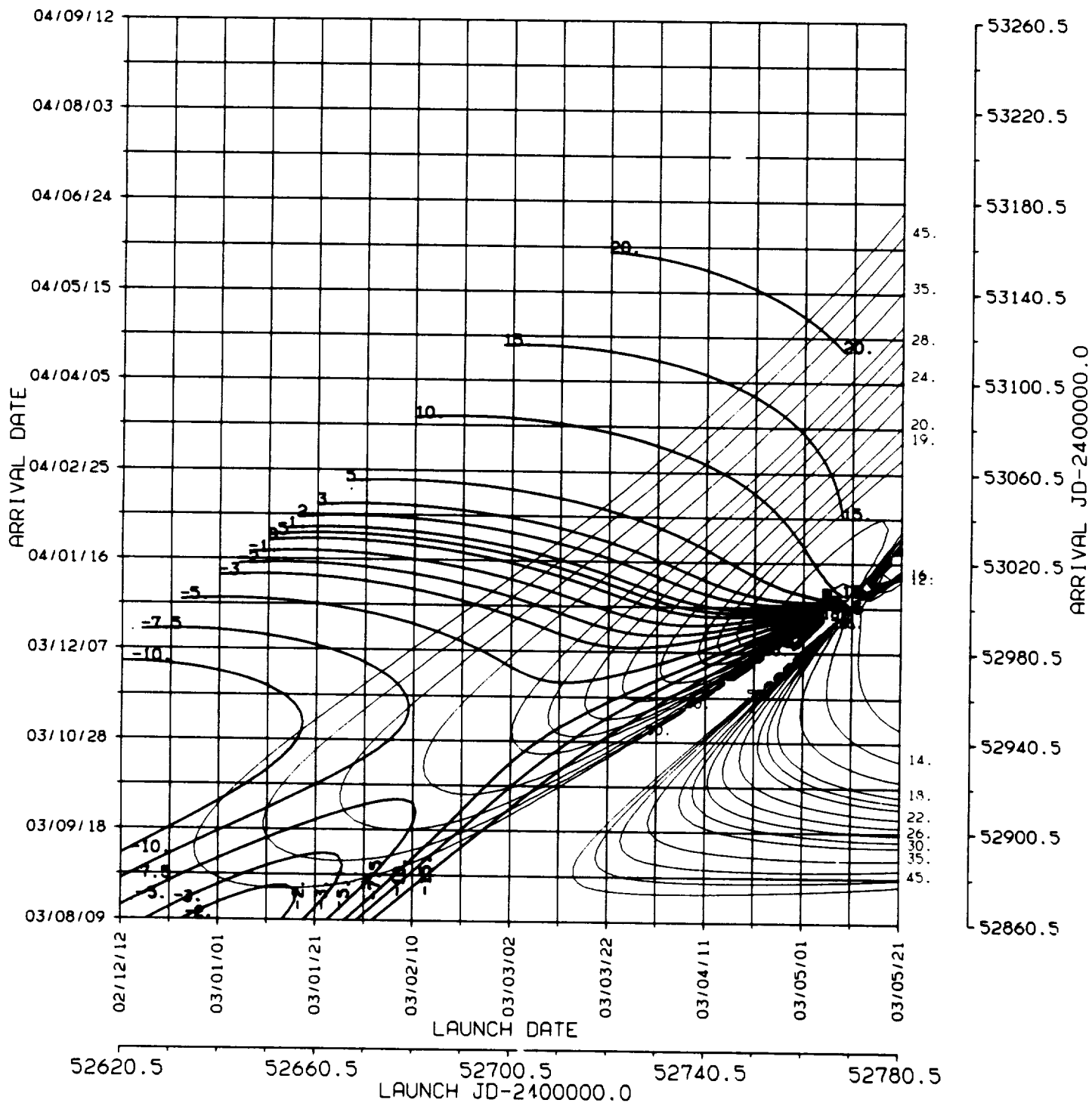
6.
DAP



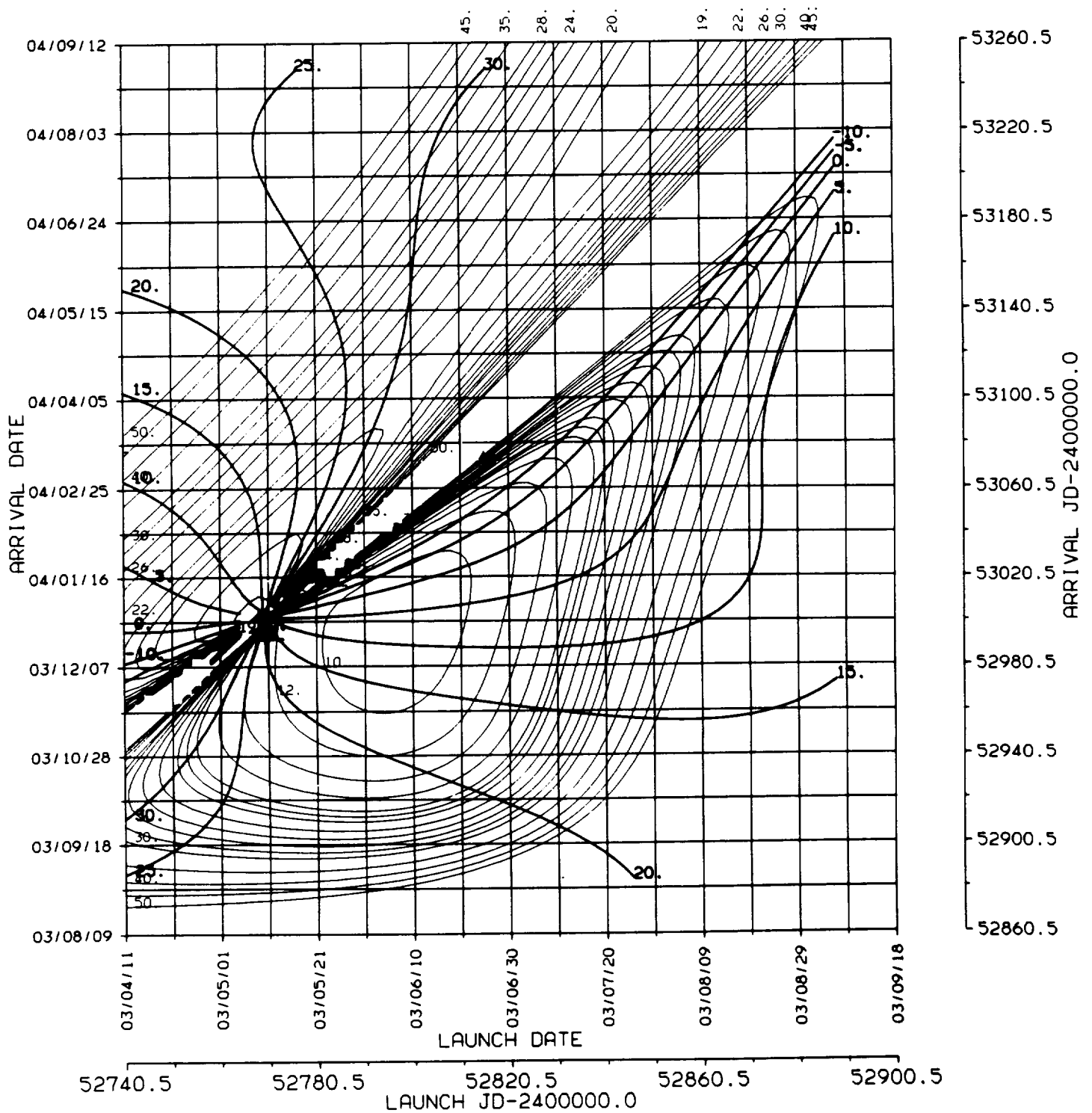
2002/3

EARTH - MARS 2002/3 , C3L , DAP

* BALLISTIC TRANSFER TRAJECTORY



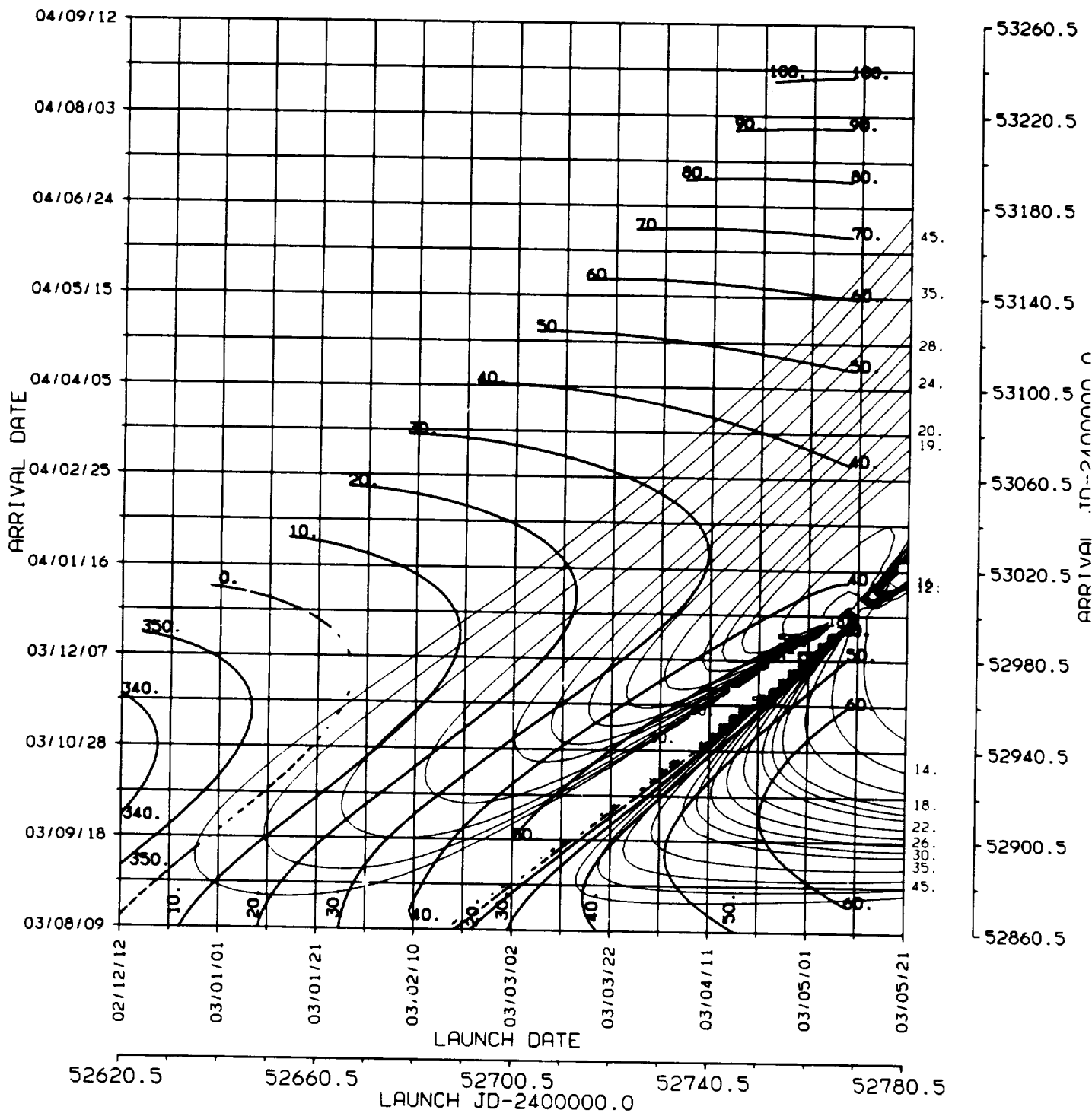
EARTH - MARS 2002/3 , C3L , DAP
* BALLISTIC TRANSFER TRAJECTORY



2002/3

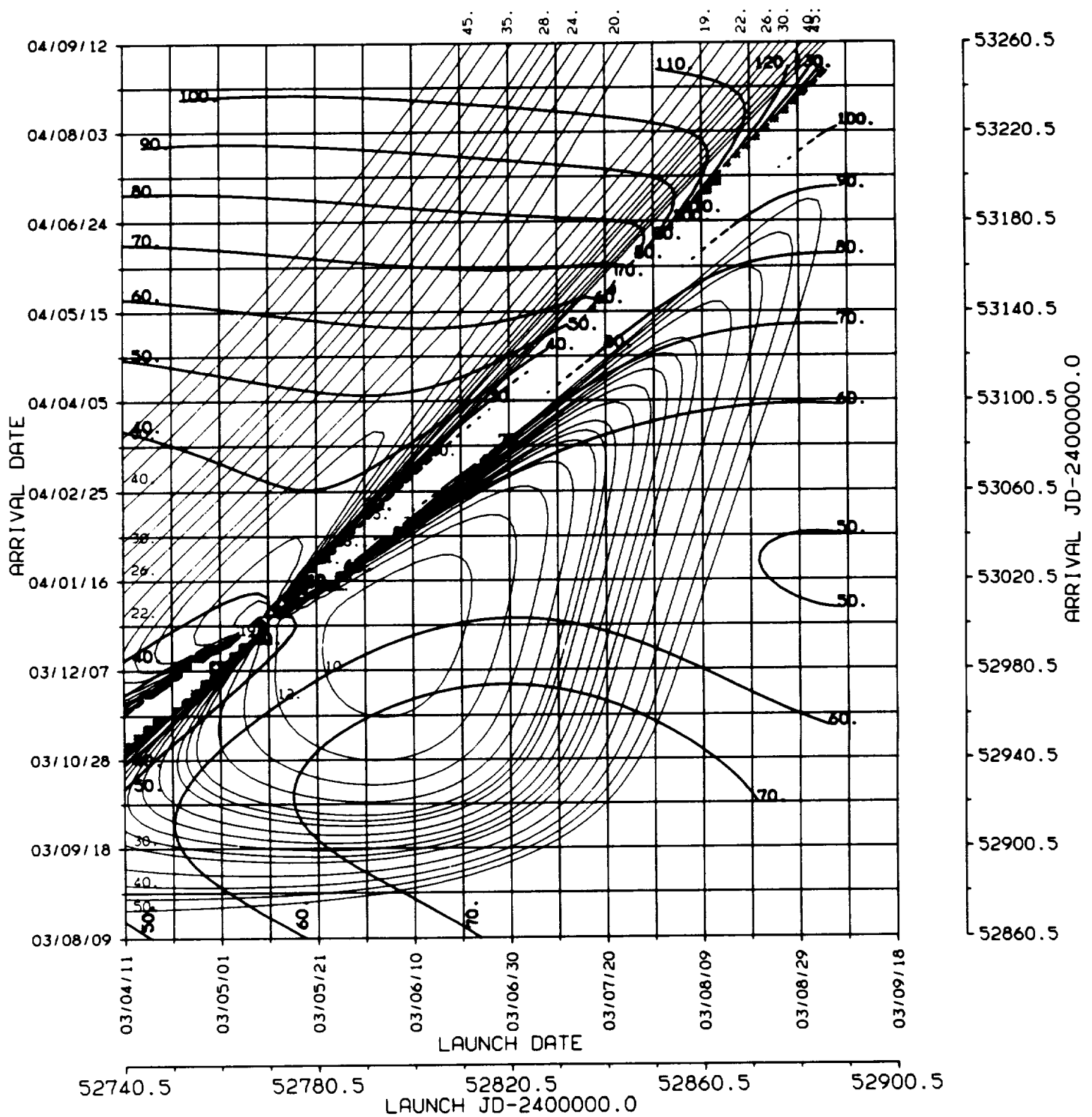
EARTH - MARS 2002/3 , C3L , RAP

* BALLISTIC TRANSFER TRAJECTORY



ORIGINAL PAGE IS
OF POOR QUALITY

EARTH - MARS 2002/3 , C3L , RAP
* BALLISTIC TRANSFER TRAJECTORY





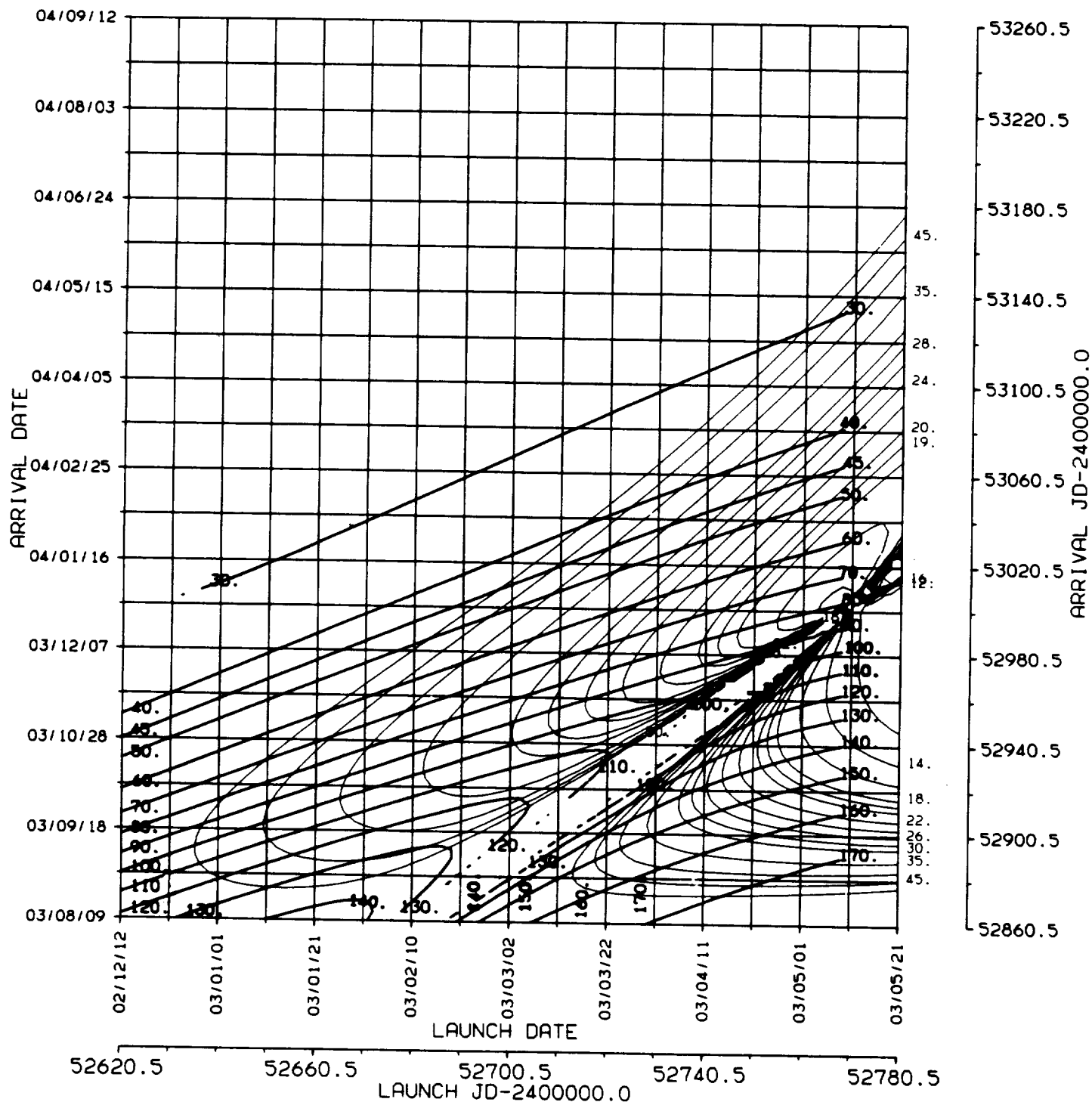
2002/3

EARTH - MARS 2002/3 , C3L , ZAPS

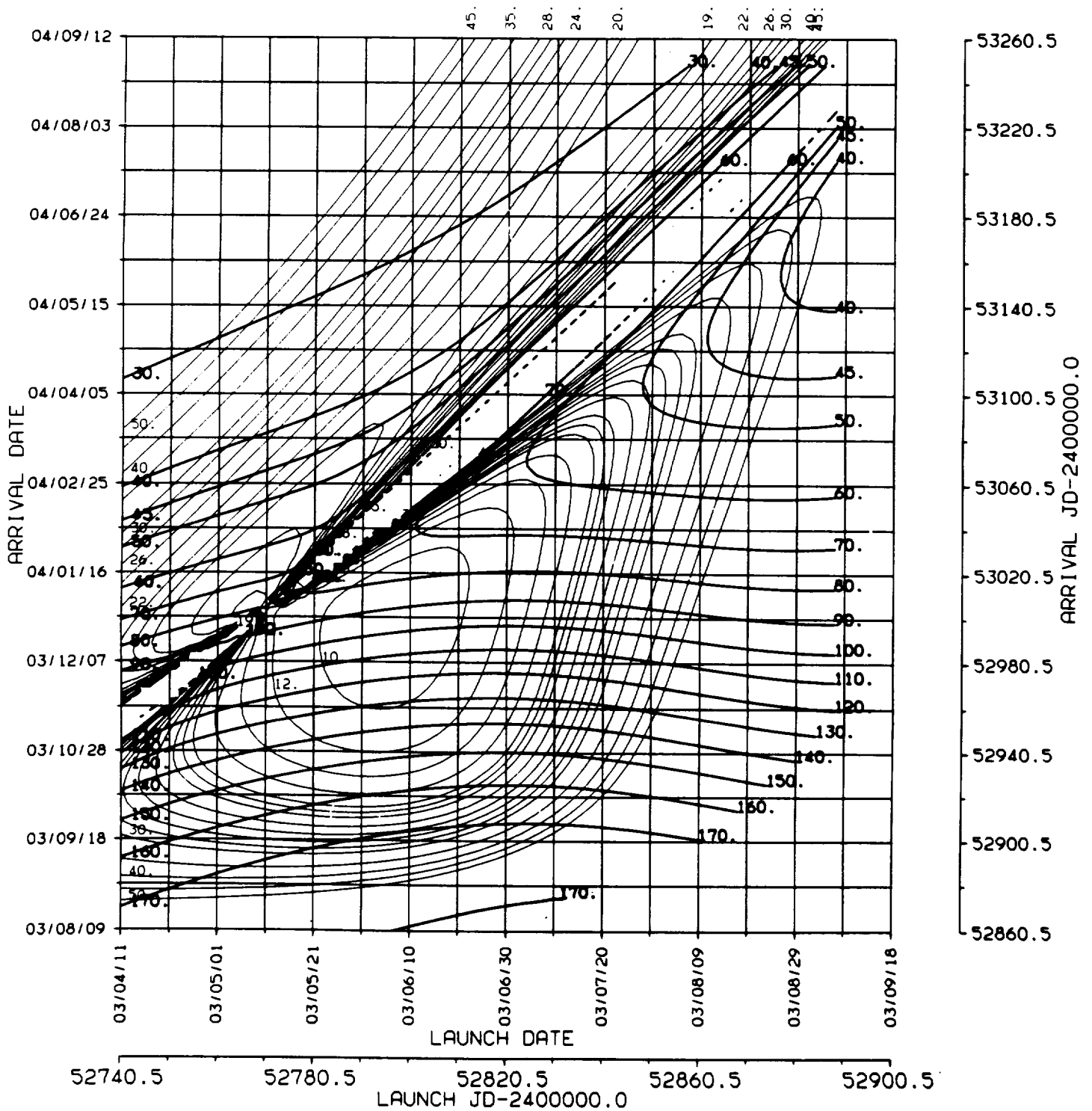
*

BALLISTIC TRANSFER TRAJECTORY

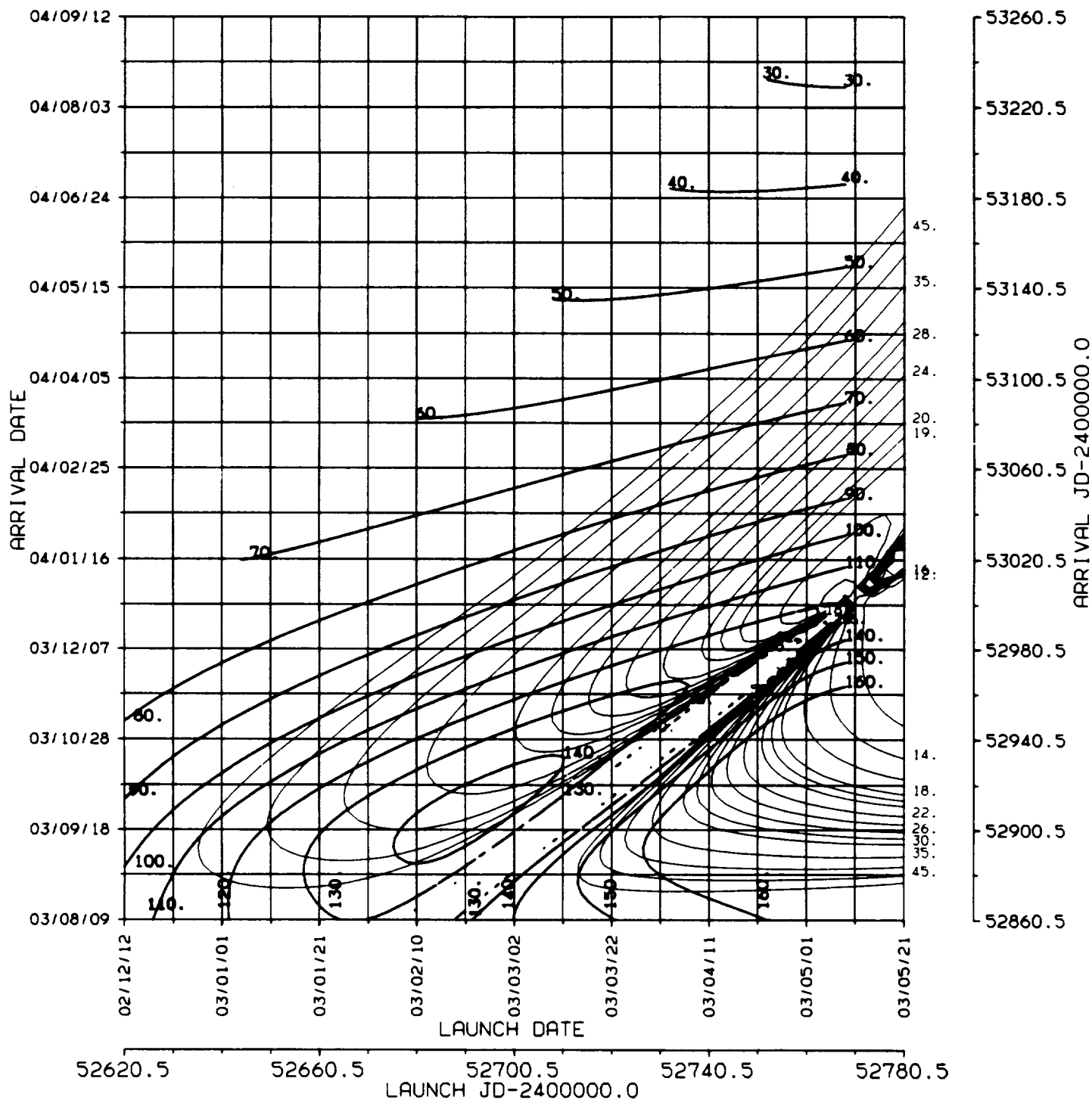
ORIGINAL PAGE 19
OF POOR QUALITY



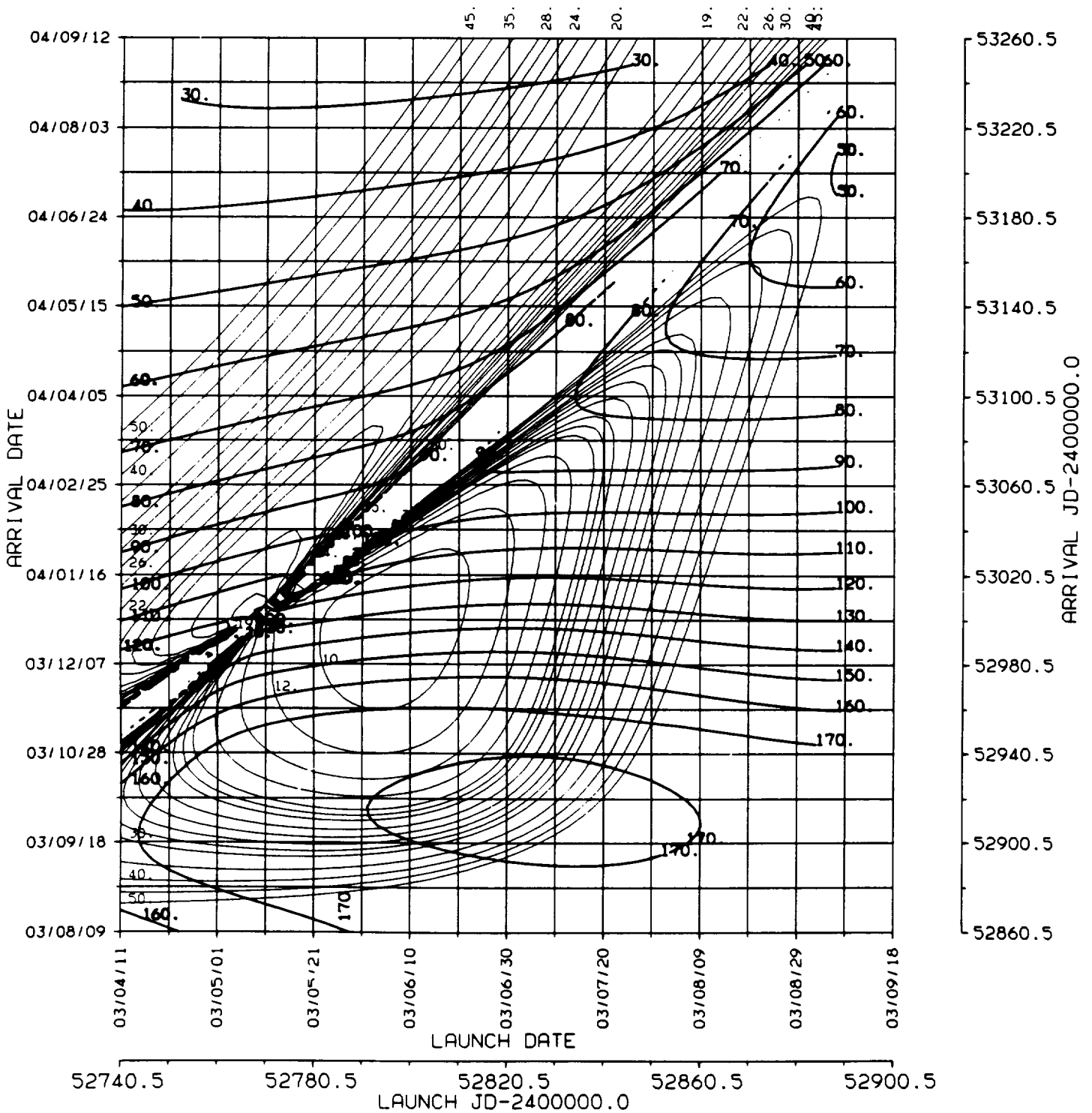
EARTH - MARS 2002/3 , C3L , ZAPS
* BALLISTIC TRANSFER TRAJECTORY



2002/3 EARTH - MARS 2002/3 , C3L , ZAPE
* BALLISTIC TRANSFER TRAJECTORY



EARTH - MARS 2002/3 , C3L , ZAPE
* BALLISTIC TRANSFER TRAJECTORY





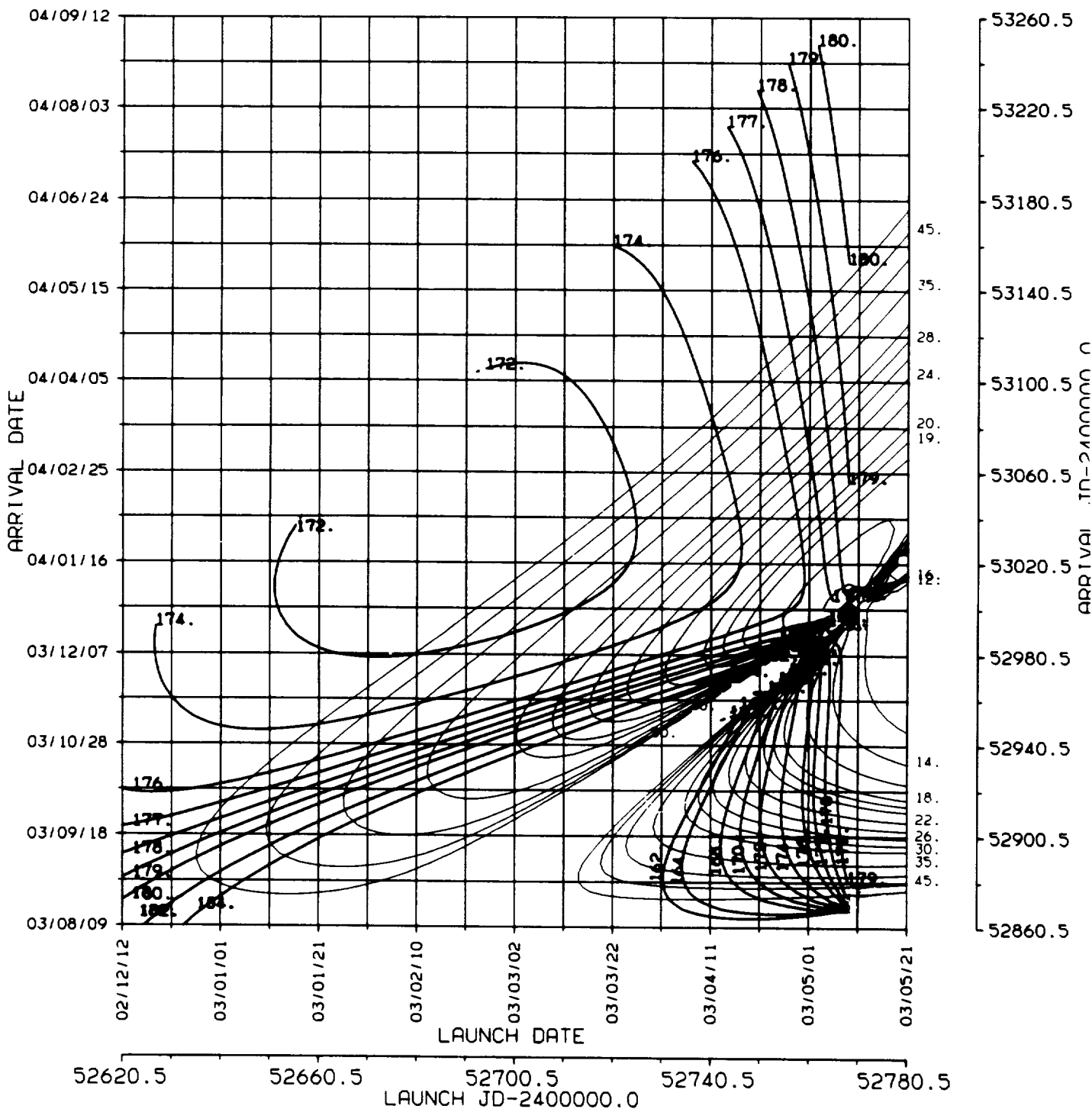
2002/3

EARTH - MARS 2002/3 , C3L , ETSP

*

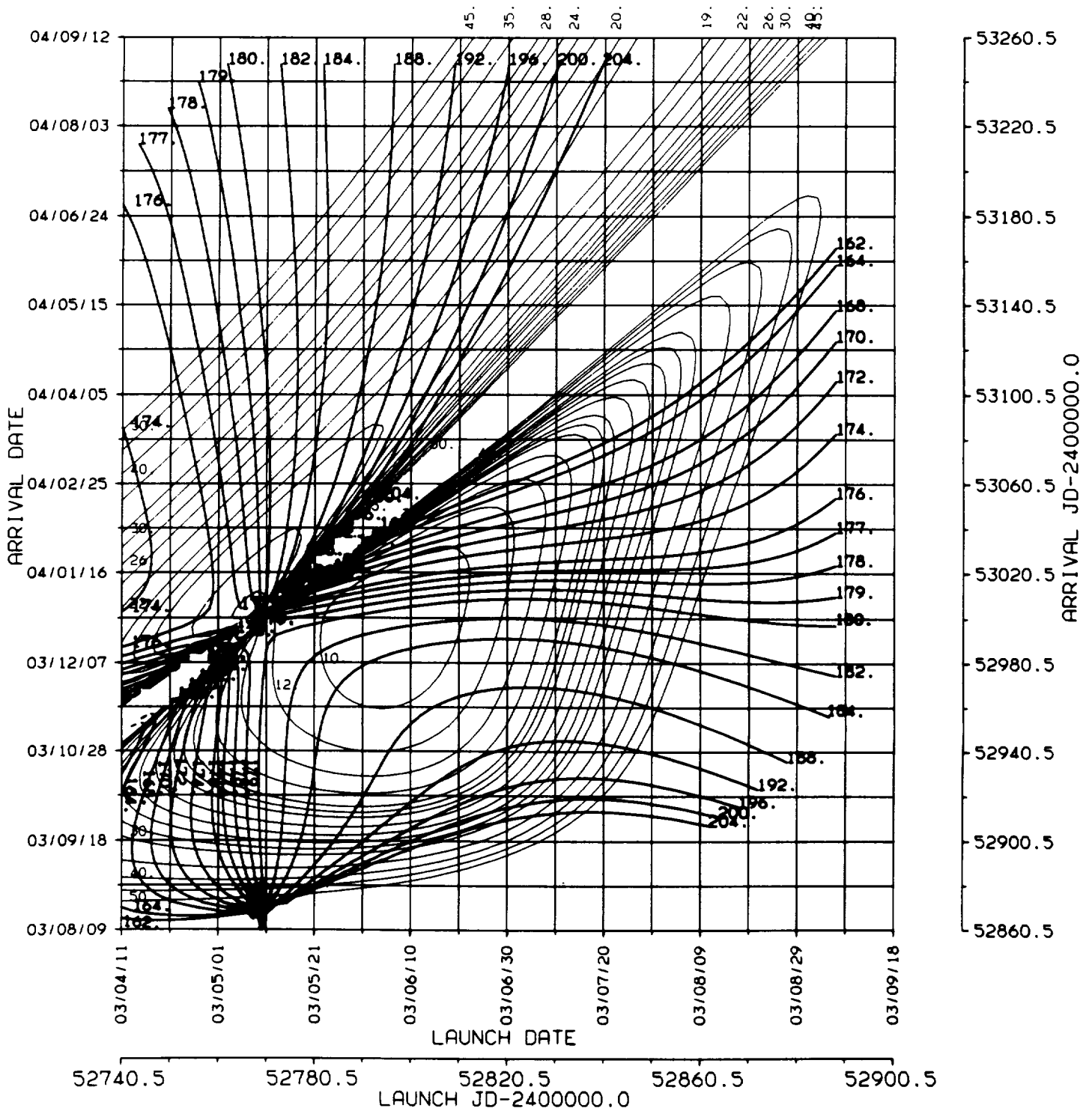
BALLISTIC TRANSFER TRAJECTORY

ORIGINAL PAGE IS
OF POOR QUALITY



ORIGINAL PAGE IS
OF POOR QUALITY

EARTH - MARS 2002/3 , C3L , ETSP
* BALLISTIC TRANSFER TRAJECTORY





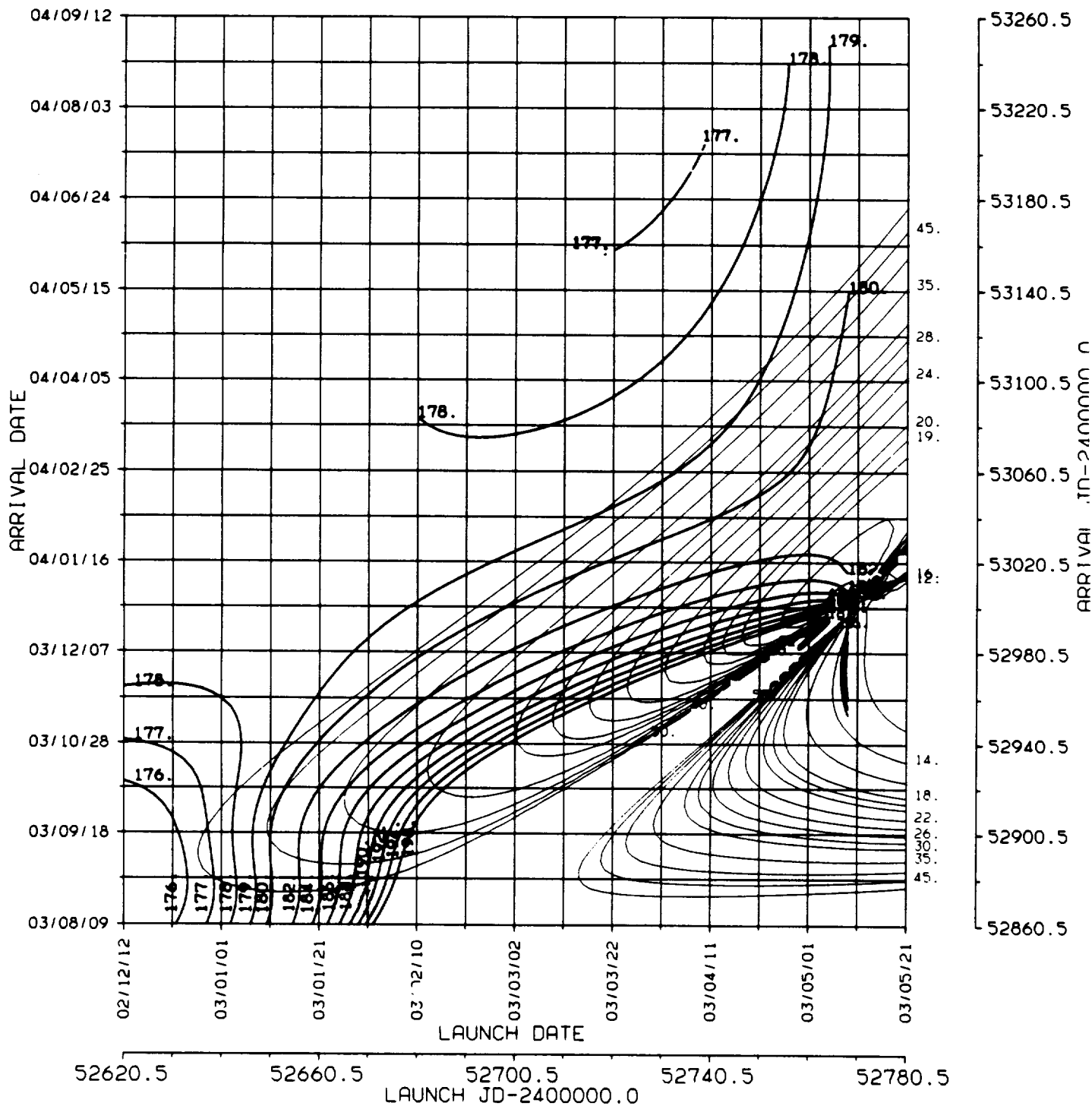
2002/3

EARTH - MARS 2002/3 , C3L , ETEP

*

BALLISTIC TRANSFER TRAJECTORY

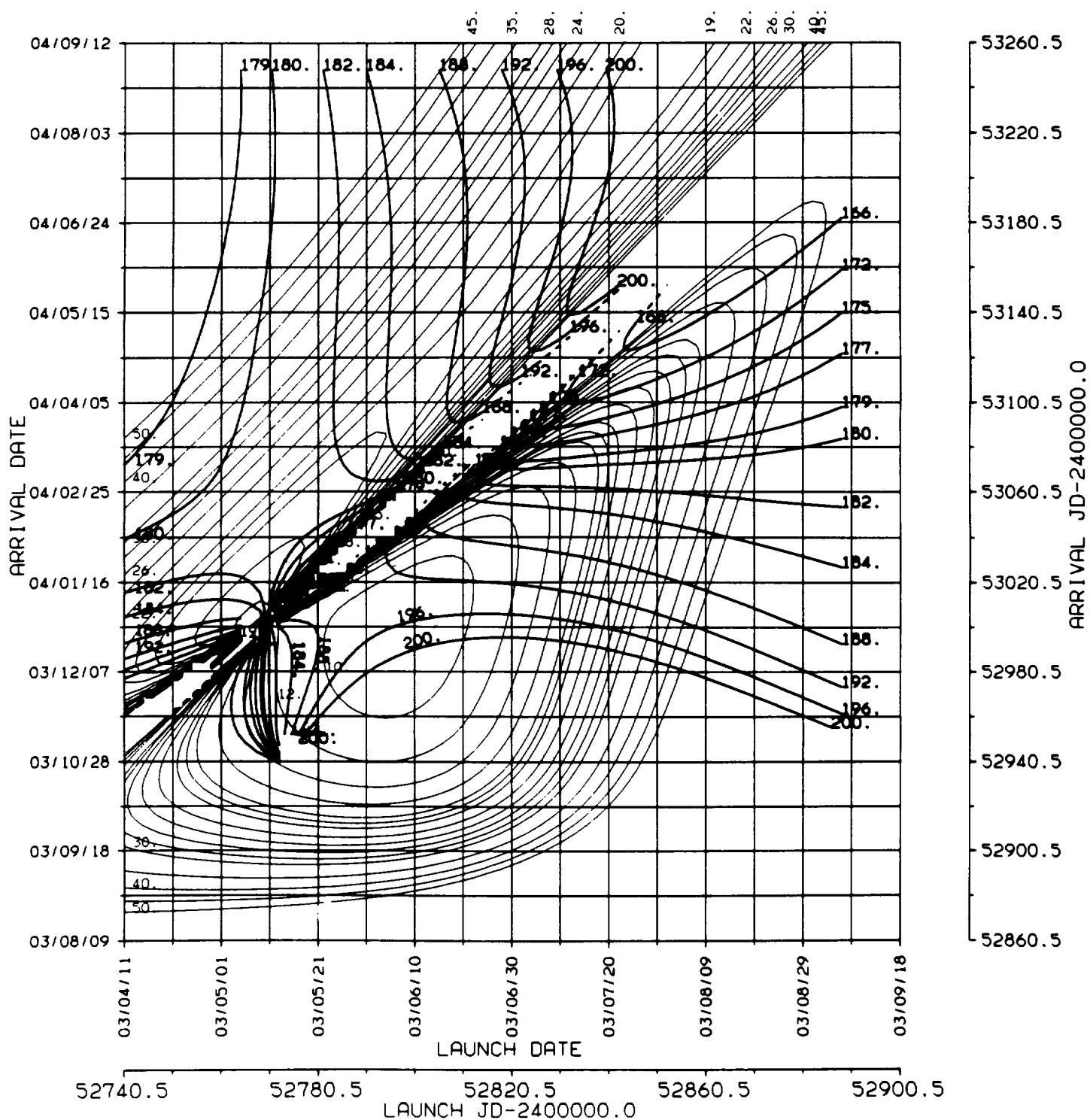
ORIGINAL PAGE IS
OF POOR QUALITY



ORIGINAL PAGE IS
OF POOR QUALITY

EARTH - MARS 2002/3 , C3L , ETEP

* BALLISTIC TRANSFER TRAJECTORY



Earth to Mars

2005

Opportunity

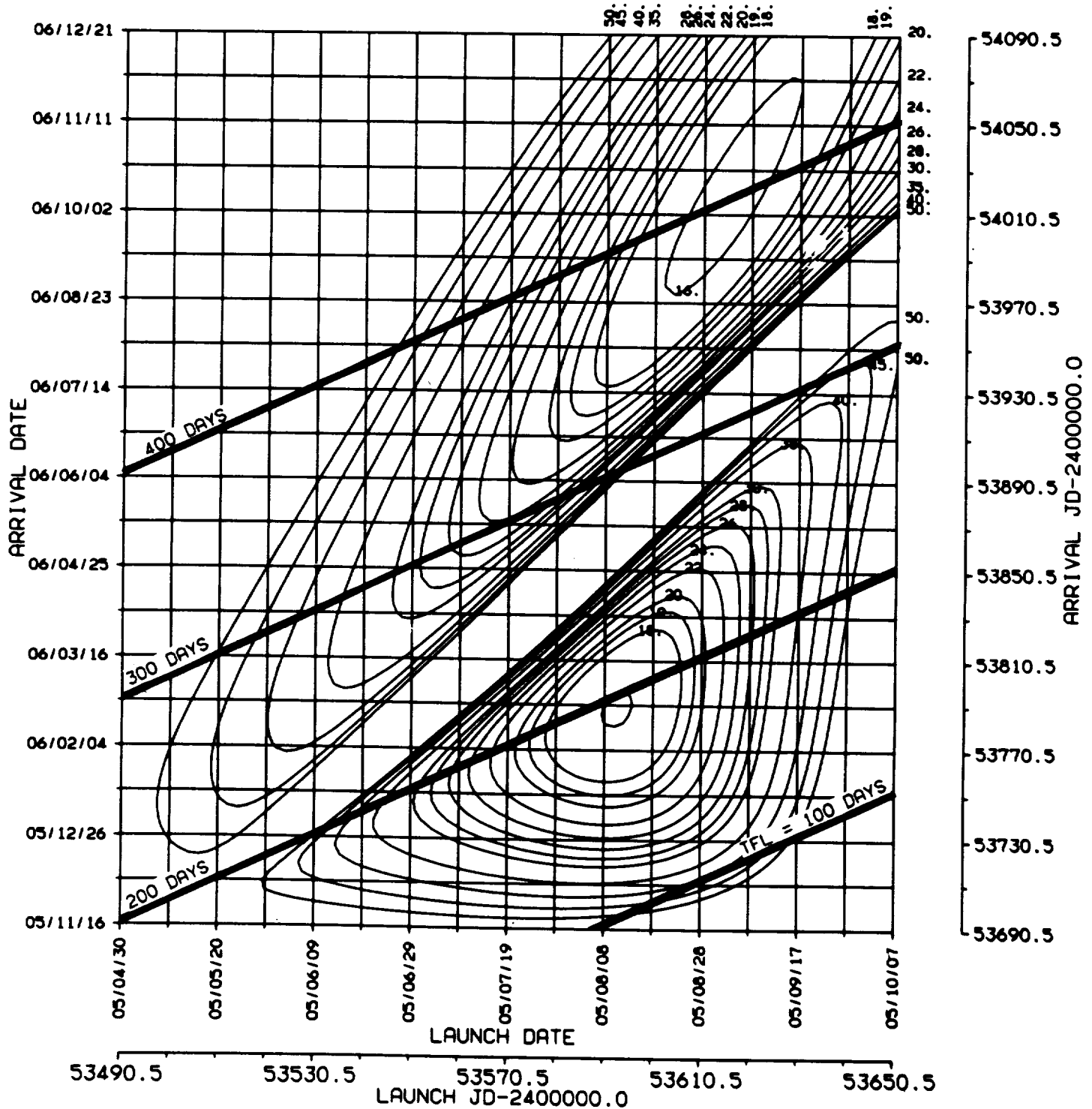
ENERGY MINIMA

	VALUE	TYPE	DEPARTURE (YEAR/MONTH/DAY)	ARRIVAL (YEAR/MONTH/DAY)
C ₃ L	15.883	I	2005/08/10	2006/02/22
C ₃ L	15.445	II	2005/09/02	2006/10/08
VHP	2.3602	I	2005/09/08	2006/04/20
VHP	2.4668	II	2005/06/21	2006/04/04

1.
C3L
♂
2005

ORIGINAL PAGE IS
OF POOR QUALITY

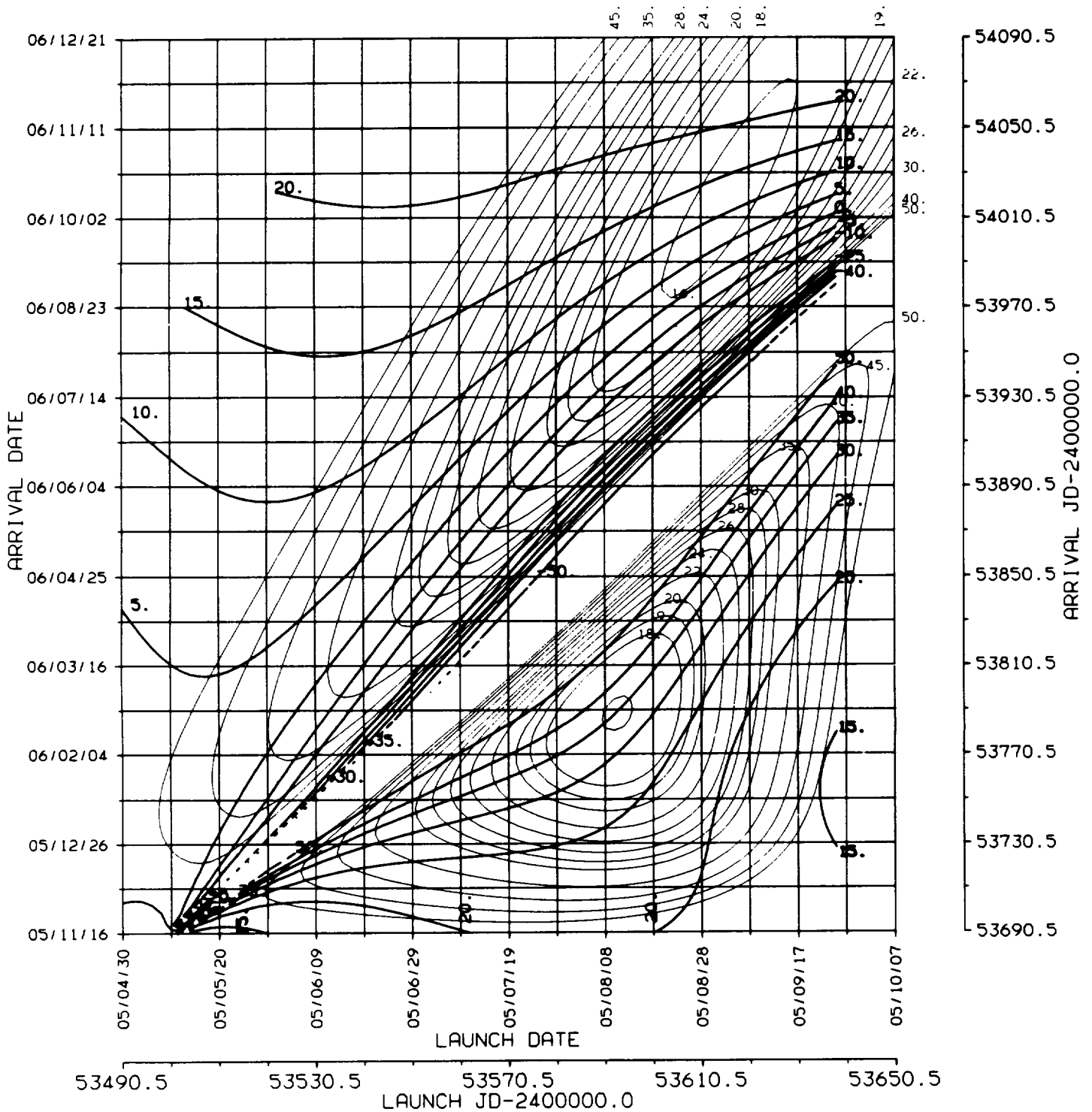
EARTH - MARS 2005 , C3L , TFL
* BALLISTIC TRANSFER TRAJECTORY



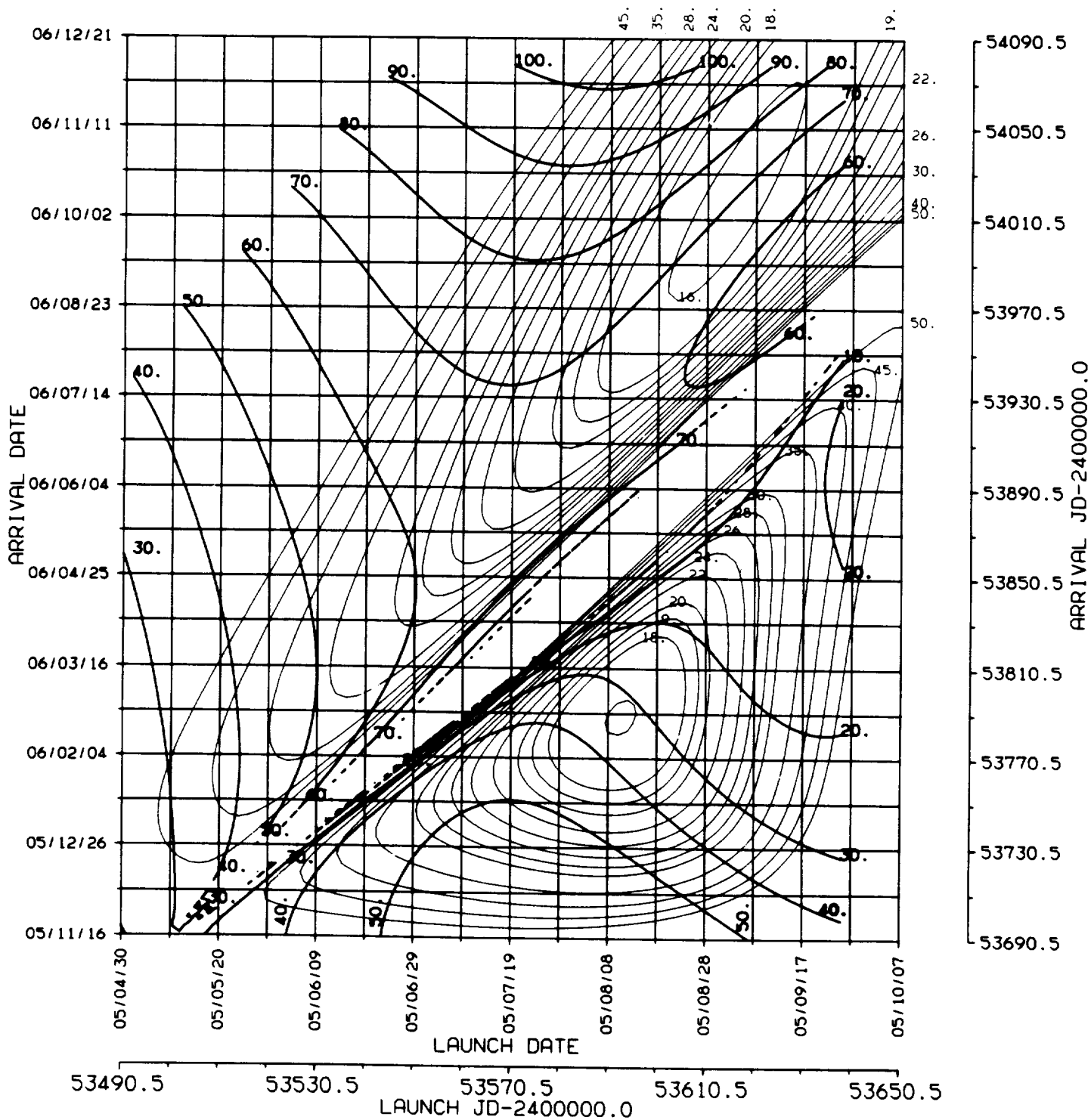
ORIGINAL PAGE IS
OF POOR QUALITY

2.
DLA
♂
2005

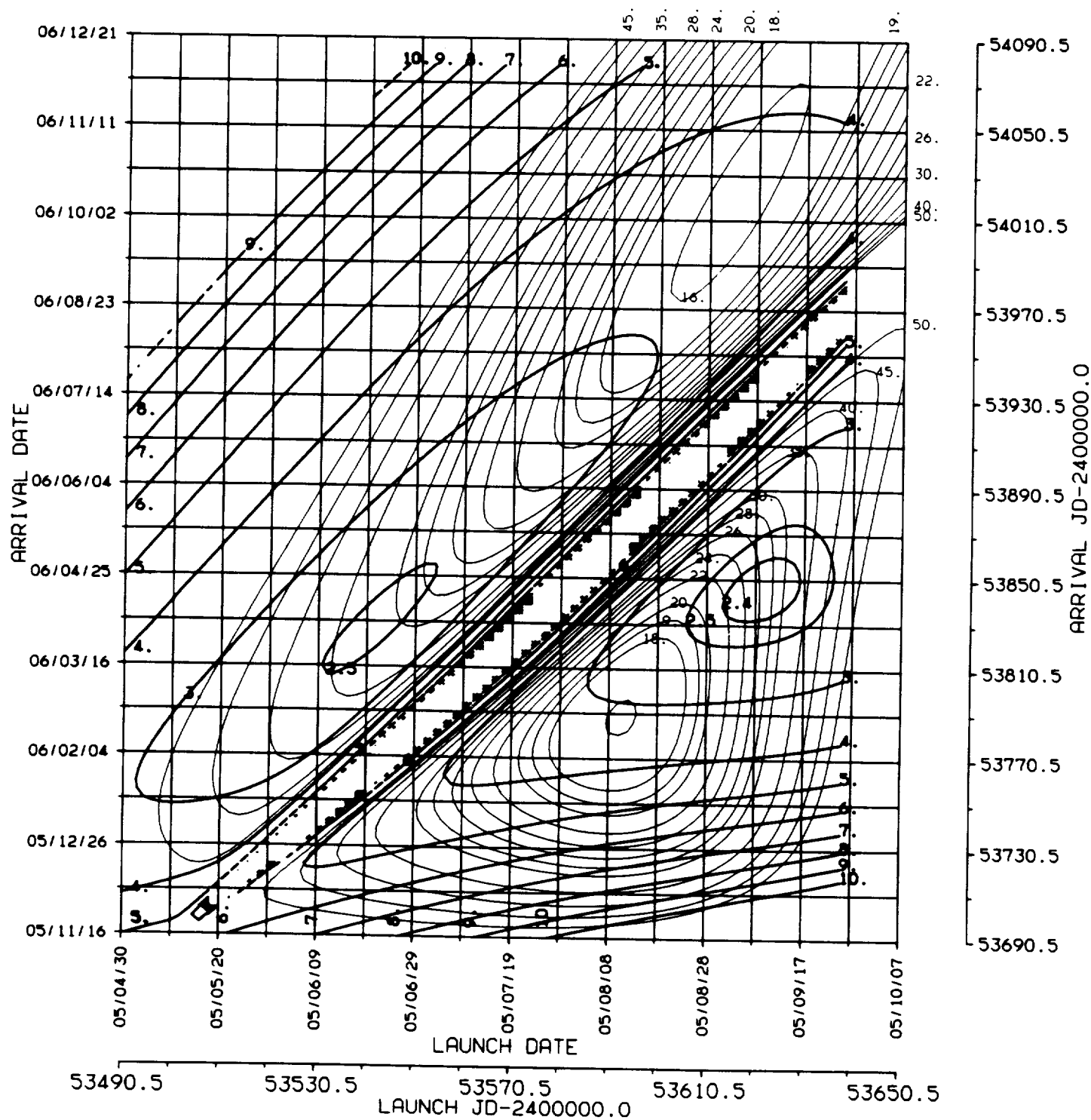
EARTH - MARS 2005 , C3L , DLA
BALLISTIC TRANSFER TRAJECTORY



EARTH - MARS 2005 , C3L , RLA
* BALLISTIC TRANSFER TRAJECTORY



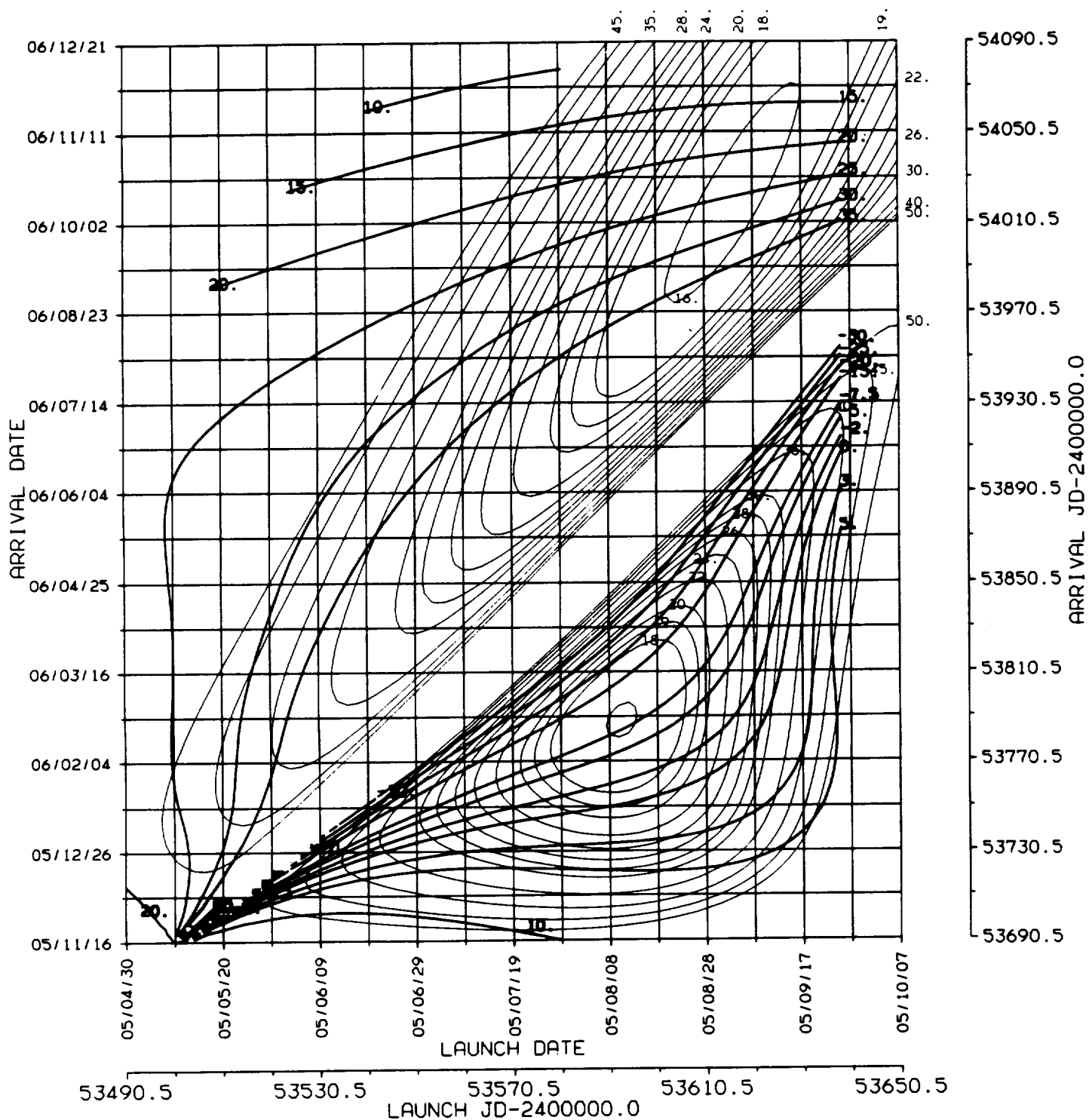
EARTH - MARS 2005 , C3L , VHP
* BALLISTIC TRANSFER TRAJECTORY



ORIGINAL PAGE 19
OF POOR QUALITY

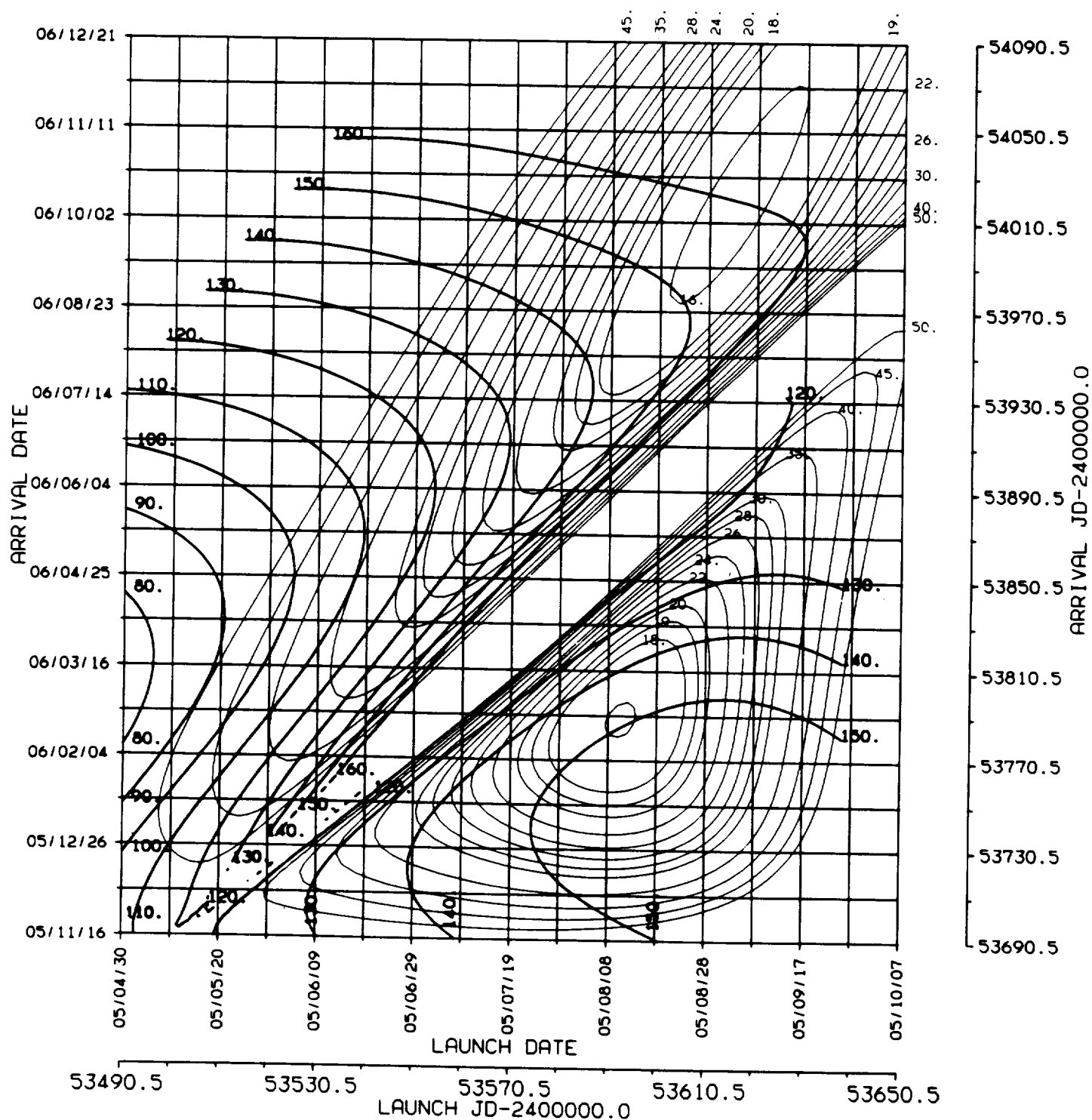
6.
DAP
♂
2005

EARTH - MARS 2005 , C3L , DAP
* BALLISTIC TRANSFER TRAJECTORY



ORIGINAL PAGE IS
OF POOR QUALITY

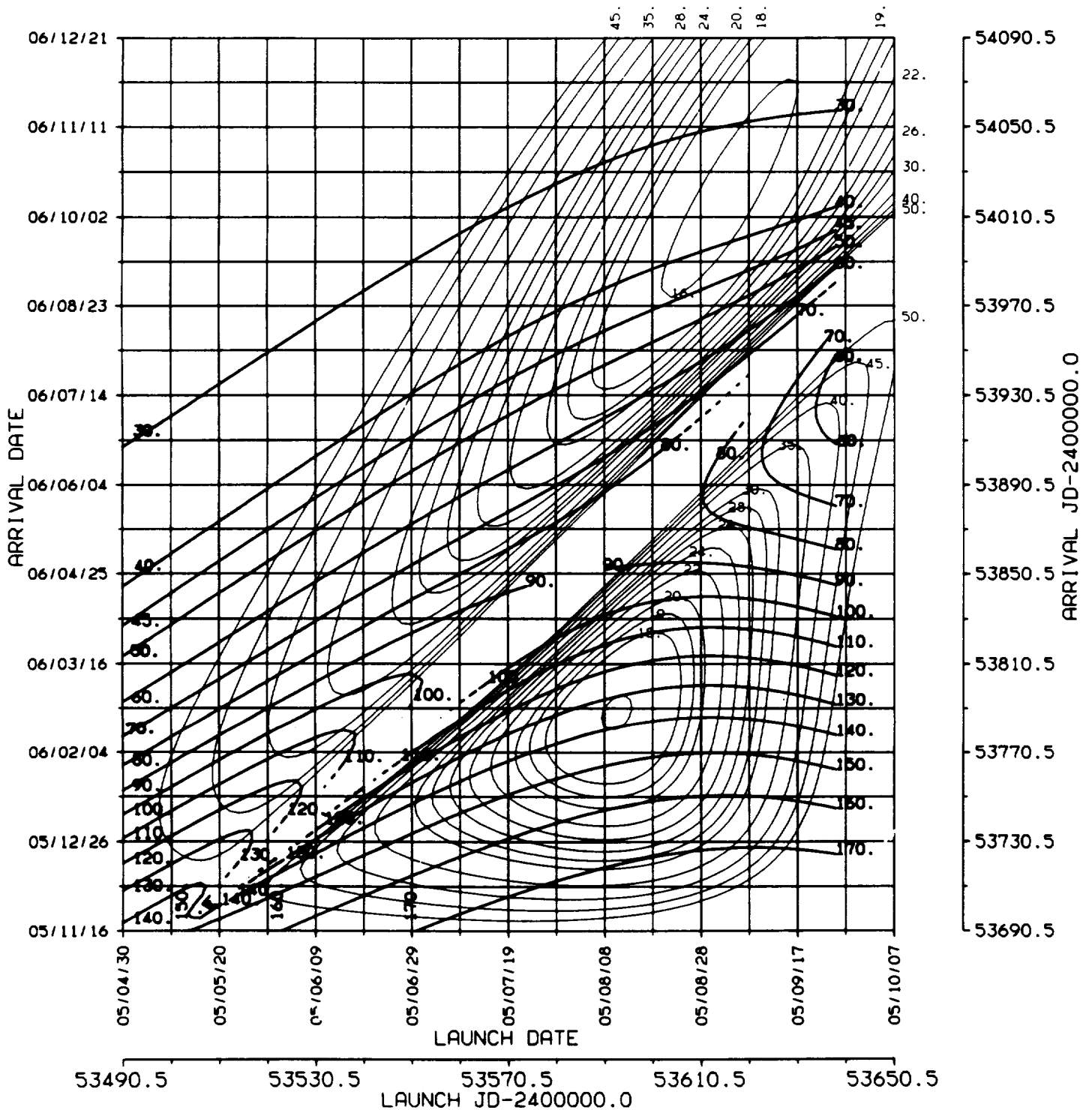
EARTH - MARS 2005 , C3L , RAP
* BALLISTIC TRANSFER TRAJECTORY



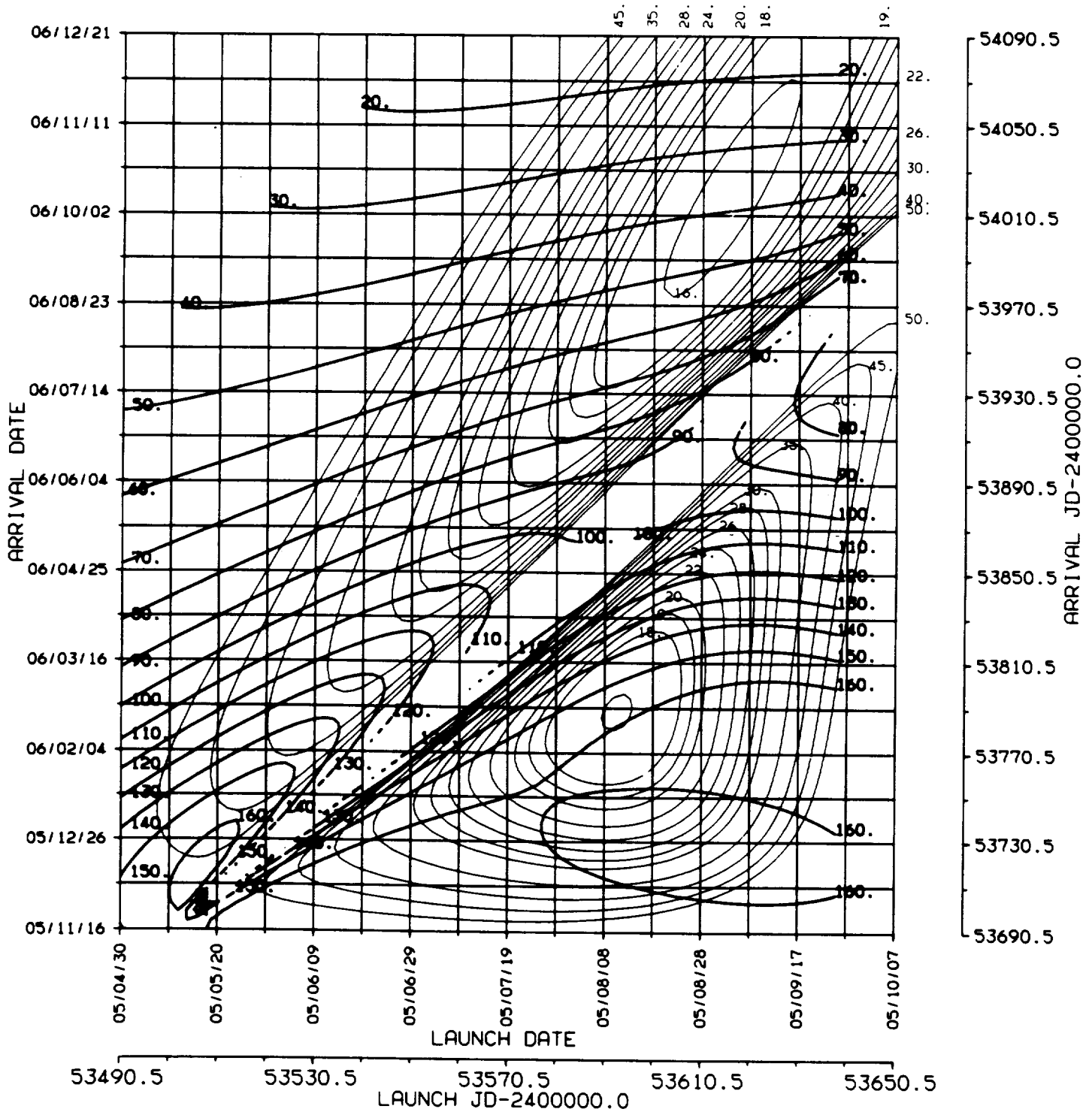
ORIGINAL PAGE 19
OF POOR QUALITY

8.
ZAPS
♂
2005

EARTH - MARS 2005 , C3L , ZAPS
* BALLISTIC TRANSFER TRAJECTORY

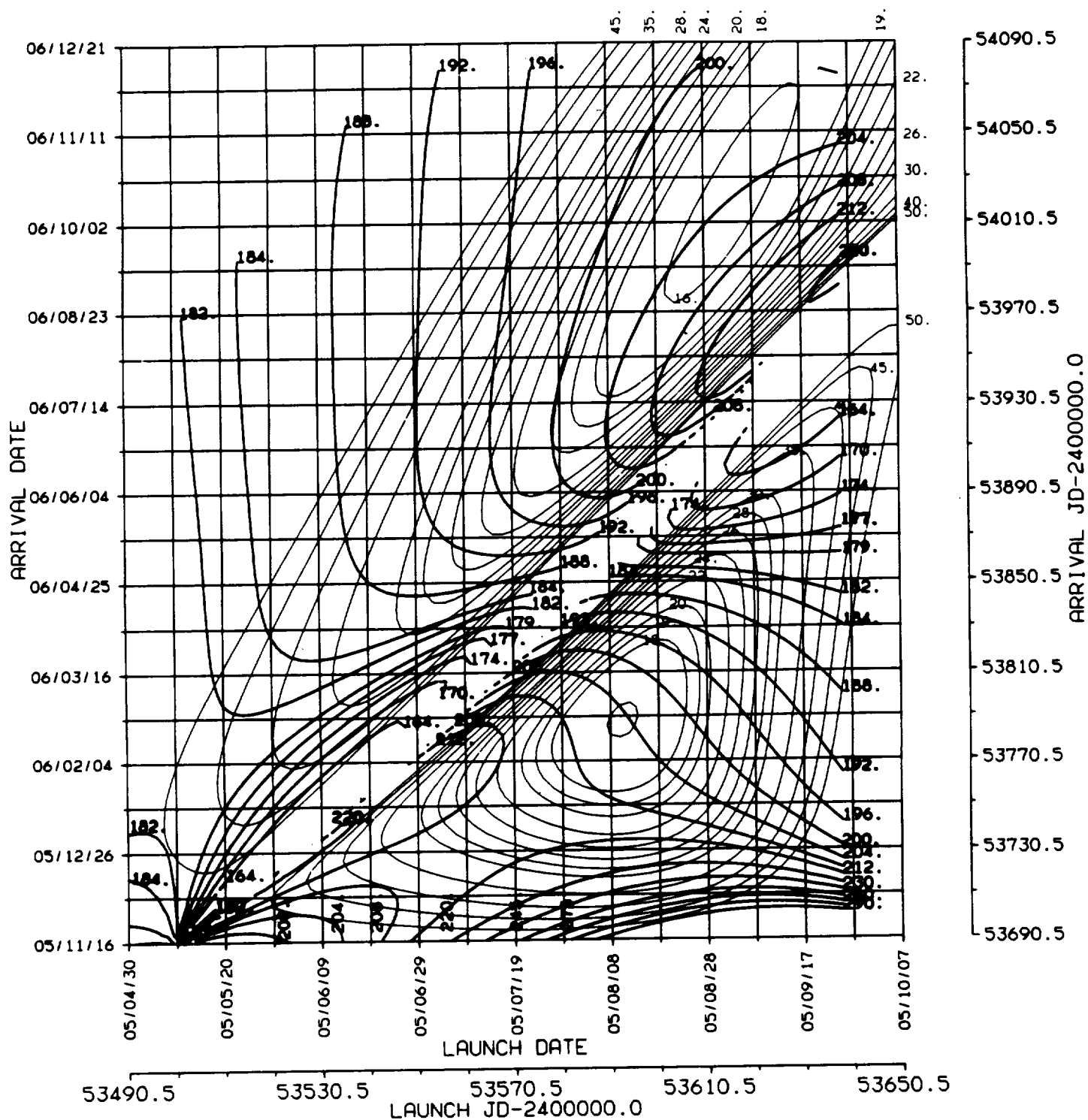


EARTH - MARS 2005 , C3L , ZAPE
* BALLISTIC TRANSFER TRAJECTORY



ORIGINAL PAGE IS
OF POOR QUALITY

EARTH - MARS 2005 , C3L , ETSP
* BALLISTIC TRANSFER TRAJECTORY



EARTH - MARS 2005 , C3L , ETEP
* BALLISTIC TRANSFER TRAJECTORY

